VIBRATION ENERGY HARVESTING, BIOMIMETIC ACTUATION, AND CONTACTLESS ACOUSTIC ENERGY TRANSFER IN A QUIESCENT FLUID DOMAIN

A Dissertation

Presented to

The Academic Faculty

By

Shima Shahab

In Partial Fulfillment

of the Requirements for the Degree

Doctor of Philosophy in the

George W. Woodruff School of Mechanical Engineering

Georgia Institute of Technology

December 2015

VIBRATION ENERGY HARVESTING, BIOMIMETIC ACTUATION, AND CONTACTLESS ACOUSTIC ENERGY TRANSFER IN A QUIESCENT FLUID DOMAIN

Approved by:

Prof. Alper Erturk, Committee Chair
Mechanical Engineering
Georgia Institute of Technology

Prof. Kenneth Cunefare
Mechanical Engineering
Georgia Institute of Technology

Prof. Alper Erturk, Advisor
Mechanical Engineering
Georgia Institute of Technology

Prof. Karim Sabra
Mechanical Engineering
Georgia Institute of Technology

Prof. Aldo Ferri
Mechanical Engineering
Georgia Institute of Technology

Prof. Maurizio Porfiri
Mechanical and Aerospace Engineering
New York University

Date Approved: July 27, 2015

ACKNOWLEDGMENTS

I would like to express my deepest gratitude to my advisor, Dr. Alper Erturk. I cannot find words to express my sincere appreciation to Dr. Erturk for his precious guidance, motivation and immense support in all stages of this dissertation. My heartfelt appreciation goes to Dr. Erturk for all I have learned from him, his valuable comments, and creating an environment where I could develop my thinking and research skills.

I would also like to thank my committee members Dr. Kenneth Cunefare, Dr. Aldo Ferri, Dr. Karim Sabra, and Dr. Maurizio Porfiri for all their valuable insights and comments. In addition I would like to thank Dr. Michael Gray for kindly helping with UAET experiments, and also Dr. Peter Hesketh for providing access to the impedance analyzer in his lab. I also want to extend my gratitude to my fellow labmates in SSDSL and friends who made my life more enjoyable during my PhD studies. I express my sincere appreciation to Stephen Leadenham and David Tan for their help and support in the lab. I do believe that, Stephen is indeed the best teacher ever.

Above all I would like to give my special appreciation to my parents for their endless love, support and encouragement throughout my life and for all sacrifices they have made to give me the opportunity of chasing my dreams. I would also like to thank my brother and sister for supporting me spiritually throughout my life.

Last but not the least, I would like to thank my beloved husband Reza, whose role in my life was and remains immense, for his sacrifices, emotional support, encouragement, and patience throughout the long journey of my PhD studies.

This work was supported in part by the NSF CAREER award CMMI-1254262.

TABLE OF CONTENTS

LIST OF TABLES

LIST OF FIGURES

SUMMARY

This work is centered on low-frequency and high-frequency multiphysics problems of piezoelectric structures submerged in a quiescent fluid domain for the applications of vibration energy harvesting, biomimetic actuation, and contactless acoustic energy transfer. In the first part of this research, Macro-Fiber Composite (MFC)-based piezoelectric structures are employed for underwater mechanical base excitation and electrical biomimetic actuation in bending mode at low frequencies (the fundamental underwater bending resonance being in the infrasonic frequency range). The MFC technology (fiber-based piezoelectric composites with interdigitated electrodes) exploits the effective 33-mode of piezoelectricity, and strikes a balance between structural deformation and force levels for actuation to use in underwater locomotion, in addition to offering high power density for energy harvesting to enable battery-less aquatic sensors. Following in-air electroelastic composite model development, the fundamental research problem is to establish semi-analytical models that can predict the underwater dynamics of thin MFC cantilevers for different length-to-width aspect ratios. In-air analytical electroelastic dynamics of MFCs is therefore coupled with added mass and nonlinear hydrodynamic damping effects of fluid to describe the underwater electrohydroelastic dynamics in harvesting and actuation. To this end, passive plates of different aspect ratios are tested to extract and explore the repeatability of the inertia and drag coefficients in Morison's equation. The focus is placed on the first two bending modes in this semi-empirical approach. In particular, electrode segmentation is studied for performance enhancement in the second bending mode. Additionally, nonlinear dependence of the output power density to aspect ratio is characterized theoretically and experimentally in the underwater base excitation problem. In the second part of this work,

Ultrasonic Acoustic Energy Transfer via piezoelectric transduction is investigated theoretically and experimentally. Contactless energy transfer using acoustic excitation offers larger distances of power transmission as compared to well-studied inductive method. Various transmitter configurations (e.g. spherical, cylindrical, and focused) are explored for energy transfer to a piezoelectric receiver bar (operating in the longitudinal/thickness mode) that is shunted to a generalized resistive-reactive circuit. Fixed-free and free-free mechanical boundary conditions of the receiver are explored in detail. The resulting multiphysics analytical model framework is compared with finite-element simulations and experiments conducted in fluid (water and oil). Optimal piezoelectric receiver material and electrical loading conditions are sought for performance and bandwidth enhancement.

1 INTRODUCTION

This first chapter aims to provide with a literature review and research motivations of this theoretical and experimental dissertation work under four sections for the topics of low-frequency underwater vibration of Macro-Fiber Composite (MFC) piezoelectric structures for energy harvesting and biomimetic actuation, and high-frequency contactless ultrasound power transfer using piezoelectric transmitter and receiver concepts. In the following, the first section is centered on the bridging of mixing rules formulation and distributed-parameter global electroelastic dynamics of MFC structures for energy harvesting, sensing, and biomimetic actuation. The second and the third sections add semi-empirical aspect ratio-dependent fluid loading effects to this framework for the problems of energy harvesting and actuation, respectively. Finally, the fourth section discusses the problem of high-frequency contactless acoustic power transfer for wireless applications. This chapter ends with an outline of this dissertation.

1.1 Coupling of Experimentally Validated Electroelastic Dynamics and Mixing Rules Formulation for Piezoelectric Macro-Fiber Composites with Interdigitated Electrodes

Piezoelectric materials are well suited to a variety of tasks as the piezoelectric effect is a reversible process in the form of the direct effect (conversion of mechanical strain to electrical charge) and the converse effect (conversion of electric potential to mechanical strain). The most typical use of piezoelectric materials in bending is through the application of the 31-mode with uniform surface electrodes. The use of the 31-mode in bending has been well studied for sensing, energy harvesting and static or dynamic actuation [1] while the 33-

mode has been conventionally used for longitudinal operation through the use of piezoelectric monolithic layers and stacks [2-5].

The concept of Interdigitated Electrodes (IDEs) was first introduced by Hagood *et al.* [6] and Bent and Hagood [7] as the 33-mode tends to have piezoelectric constants 50-100% larger than those of the 31-mode, making it an intriguing option to exploit in bending mode. The Active Fiber Composite (AFC) structure was first characterized by Bent [8, 9] and its properties were later investigated by others [10-14] analytically and experimentally. However the AFC technology employed round piezoelectric fibers that limited the contact area between the fiber and the electrodes leading to low electromechanical coupling and high dielectric loss. Unlike conventional piezoelectric actuators, the Macro-Fiber Composite (MFC) piezoelectric technology, introduced by the NASA Langley Research Center [15, 16] in the last decade (and commercialized by the Smart Material Corp. [17]), offers flexible and robust piezoelectric actuators made from PZT (lead zirconate titanate) fibers and epoxy matrix sandwiched between interdigitated electrodes and assembled in Kapton (Figure 1.1). These actuators offer significant advantages over monolithic piezoceramic materials which have limitations such as their brittle nature and low allowable curvature. The MFC technology provides flexibility, endurance, ease of fabrication in various sizes, as well as high strain and stress performance based on the 33-mode of piezoelectricity (i.e. electric field and strain are in the same direction) [15, 16]. Furthermore, the MFCs use PZT fibers of rectangular cross section, yielding dramatically enhanced electrode contact and reduced dielectric loss as compared to their previous generation counterparts, such as the AFCs with circular fiber cross section [18]. Therefore the MFCs overcome the problem of small

displacement response associated with piezoelectric actuators without substantially compromising the high actuation force capability.

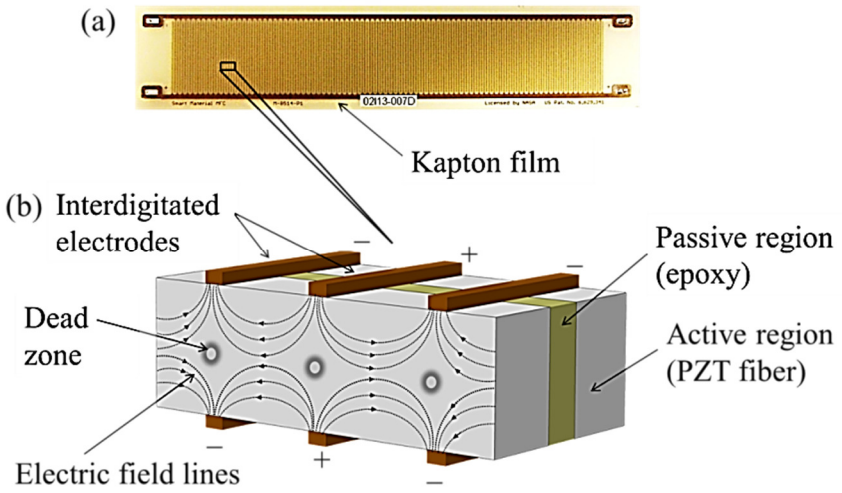

Figure 1.1. (a) Picture of an MFC actuator and (b) close-up volumetric (3-D) representation showing PZT fibers, epoxy matrix, and interdigitated electrodes with non-uniform electric field lines (the composite structure is embedded in Kapton film for robustness).

These unique properties of MFCs have led to their experimental applications including vibration control [19, 20], bio-inspired locomotion [21, 22], acoustic wave propagation [23, 24], morphing-wing aircraft [25-28], and in-air/underwater dynamic actuation or energy harvesting [29-31]. However, modeling of MFCs has not kept pace with the experimental applications, and there has been limited literature on the fully coupled electroelastic dynamics of the 33-mode configuration with IDEs. Meanwhile several attempts were made to obtain the effective electromechanical properties of 31-mode type MFCs using analytical and numerical approaches [32, 33]. Other than their use in AFCs and MFCs, IDEs have also found use in Micro Electro-Mechanical Systems (MEMS) as surface electrodes over monolithic plates. IDEs are useful to MEMS as the 33-mode coupling allows for larger

voltages to be produced in energy harvesting, overcoming the forward voltage requirements of diodes for DC rectification [34, 35]. Additionally, implementation of IDEs allows for an electrode surface on only side of a piezoelectric material, simplifying the microfabrication process. However, in the existing literature, modeling of the effect of 33-mode IDE actuators and harvesters in MEMS applications has been oversimplified or excluded completely.

In early constitutive modeling of 33-mode MFCs, Williams *et al.* [36-39] presented an experimentally validated analytical model for equivalent thermal expansion and mechanical properties of MFCs using modified classical mixing rules. Deraemaeker *et al.* [40, 41] reported analytical calculations against experiments and numerical results [42]. In another work, Deraemaeker and Nasser [43] proposed a finite-element method to evaluate the equivalent properties of MFCs. Recently, Prasath and Arockiarajan [44] presented analytical and numerical models to evaluate the effective thermo-electro-elastic properties of MFCs and the effect of thermal environment on the effective piezoelectric constants of MFCs.

In the present work (Chapter 2), building on the model presented by Deraemaeker *et al.* [40], the electroelastic and dielectric properties of a representative volume element (RVE; piezoelectric fiber and epoxy matrix) between two subsequent interdigitated electrodes are obtained using mixing rules, and then the RVE electroelastic mechanics modeling is coupled with the global electroelastic dynamics based on the Euler-Bernoulli kinematics of MFC bimorphs. A linear distributed-parameter model for a bimorph assuming Euler-Bernoulli beam theory for energy harvesting and actuation is extended to the 33-mode and employed for parameter identification. The identified physical parameters of the MFC bimorphs are validated experimentally for different MFC types with the same overhang length but different active widths. Comparison of this model with the experimental results allows for

effective electroelastic and dielectric constants to be found via mixing rules-based analysis and successfully bridged with the global dynamics in a high-fidelity modeling framework.

1.2 Underwater Vibration Energy Harvesting Using Macro-Fiber Composites

Among the fiber-based piezoelectric actuators/sensors, the MFC technology has received great interest for use in both energy harvesting and actuation systems. The unique construction of the MFC structures and their material properties (explained in Ref. [20], among others) offer benefits such as increased flexibility, improved anisotropic and potentially waterproof (custom made with polyester electrode sheets) behaviors. These advantages allow making the MFC laminates durable to damage and robust in relatively harsh environmental conditions. Furthermore, the MFCs are designed to use interdigitated electrodes which employ the effective 33-mode of piezoelectricity in bending operation with increased energy conversion efficiency. All these factors prove that the use of MFCs has its own merits for underwater energy harvesting purposes. However, presently there is limited literature on their electrohydroelastic modeling and underwater experimental applications especially with connection to previously mentioned mixing rules-based formulation in the sense of a first principles formulation that bridges the piece-wise defined electroelasto-mechanics of the fibers with interdigitated electrodes to the global electroelastic dynamics of the composite structure.

In their 2011 paper, Erturk and Delporte [21] performed in-air and underwater base excitation experiments of an MFC-based fish-like propulsor with a caudal fin. Comparing the in-air and underwater test results showed that maximum underwater power output is an order of magnitude larger than its in-air counterpart for the same base acceleration level.

More recently energy harvesting from base excitation of an MFC bimorph under water was investigated by Cha *et al.* [29] for a partially submerged piezoelectric composite beam through changing the submersion length. Electrohydroelastic dynamics of a fully submerged MFC bimorph propulsor was investigated by Cen and Erturk [22] for the theoretical and experimental analysis of fish-like aquatic robotics by accounting the hydrodynamic effects following the work by Sader and co-workers [45-48]. Likewise, for underwater operations, Brunetto *et al.* [49], Mbemmo *et al.* [50], and Aureli *et al.* [51, 52] used similar approaches to analyze the dynamics of ionic polymer-metal composite (IPMC) samples. In these efforts [21, 22, 29, 45-52], analyzing the force exerted on the oscillating structure by the fluid showed that the fluid effects can be taken as added mass and hydrodynamic damping. The hydrodynamic effect is to lower the resonance frequencies of the structure and to increase the damping ratio as compared to the resonance frequency and damping ratio of in-air vibrations. The linear hydrodynamic function developed based on Sader's theory [45-48] assumes infinitesimal small amplitudes of vibration and a large length-to-width ratio in order to accurately predict the response of the beam. Therefore, as the vibration amplitude increases or length-to-width ratio decreases, the reliability of Sader's theory is affected negatively [30, 53]. The results obtained by using Sader's model showed approximately 20% error in predicting fluid-loaded resonance frequencies and damping ratios when compared with the experimental results [30, 31] . Through extending the approach proposed by Sader [45], studies were performed by Aureli *et al.* [54, 55], Falcucci *et al.* [56], and Phan *et al.* [57] to establish a correction to Sader's hydrodynamic function by accounting for nonlinear hydrodynamic effects. The goal was to develop accurate models for predicting underwater response of flexible beams for a broad range of frequencies and aspect ratios undergoing

relatively large amplitude vibrations. Aureli *et al.* [54] and Phan *et al.* [57] performed computational fluid dynamics analyses to understand the effects of fluid physical parameters on the vibration of a submerged beam and ultimately form a nonlinear hydrodynamic correction term added to the classical hydrodynamic function. Facci and Porfiri [53] performed numerical investigation on the physics of 3-D fluid flow induced by the vibration of cantilevered beams with different aspect ratios. In this work [53], modeling results showed that the hydrodynamic function given by Sader [45], Bidkar *et al.* [58], and Aureli *et al.* [54] would accurately predict the distributed load experienced by oscillating beams for the length-to-width aspect ratio greater than three. It was found that, as the aspect ratio of the beam decreased, the 3-D hydrodynamic effects were responsible for significant difference in the distributed added mass loading due to vortex shedding from the edge of the beam while the actual loads were overestimated by these theories [45, 54]. However, the modeling approach proposed by Aureli *et al.* [54] was found to be effective in predicting hydrodynamic damping for a broad range of aspect ratios. Facci and Porfiri [53], Cha *et al.* [29] and Kopman and Profiri [59] adapted the nonlinear semi-empirical Morison's equation [60-64] to incorporate the effects of the surrounding fluid on the oscillating beams with small aspect ratios. Morison's equation was originally [60-64] used to calculate the fluid loading on a circular cylinder in viscous oscillatory flow by incorporating added mass and nonlinear damping as functions of the transverse velocity of the cantilever beam.

A particular task in Chapter 3 is to develop experimentally validated electrohydroelastic models for MFC bimorphs by adding Morison's hydrodynamic equation to the electroelastic in-air energy harvesting model [1] that is implemented for the homogenized interdigitated structure with non-uniform electric field. Both the first and the second bending modes are of

interest for broadband energy harvesting applications as shown by Erturk and Delporte [21] in their experimental study. In addition, parametric exploration for the repeatability of the inertia and drag coefficients in Morison's nonlinear equation extracted from base excitation tests for passive plates made from aluminum with different aspect ratios is of particular interest to have a useful model.

Erturk and Delporte [21] pointed out in their work that the results for the second bending mode in vibration energy harvesting of clamped MFC bimorphs (with uniform piezoelectrics and electrodes) are suboptimal because of undesired cancellation of electrical power output which happens due to the strain node where the dynamic strain distribution changes sign in the direction of beam length. In their paper, Erturk *et al.* [65] presented analytical modeling and experimental demonstration to show that there is strong cancellation of the electrical power output in cases where continuous electrodes cover strain nodes of vibration modes, and they presented dimensionless strain node positions for different boundary conditions of thin beams. In their results [65], they proved the feasibility of avoiding the cancellation problem in energy harvesting by using segmented electrode pairs in multimode vibrations of a cantilevered piezoelectric energy harvester. In that work [65], it was experimentally shown that using segmented electrodes instead of continuous electrodes enhanced the voltage output significantly for second mode excitation.

In Section 3.4, the electrode segmentation is applied for a cantilevered MFC bimorph to eliminate the cancellation so that the second bending mode can be used effectively in electrical power generation. An MFC bimorph (with extended aluminum substrate and MFC laminates attached on both sides) is designed as experimental case study for vibration-based energy harvesting purpose, both in linear and nonlinear response regimes. Two cases are

considered. First, the MFC laminates are wired in phase for the first mode where the voltage outputs are in phase for MFCs in the first mode. Secondly, the MFC laminates are wired 180 degree out of phase where the voltage outputs are in phase for MFCs in the second mode and cancellation is avoided. Tip velocity, voltage, and electrical power output Frequency Response Functions (FRFs) are shown for various external resistive loads to compare the response of the segmented MFC bimorph for these two wiring configurations.

1.3 Underwater Biomimetic Actuation Using Macro-Fiber Composites

Bio-inspired underwater vehicles have received growing interest over the last few years. As an alternative to conventional underwater vehicles with propeller-based propulsion systems, the research motivation for using bio-inspired structures in aquatic locomotion is to enable enhanced low-speed maneuverability, silent operation, signature reduction, lower weight, increased efficiency, and reduced power consumption [66]. The applications of fish-like biomimetic locomotion spans from underwater sensing and exploration for sustainable ecology to drug delivery and disease screening in medicine [66-68].

There exist various successful designs with motors and appropriate linkage systems or mechanisms to mimic biological creatures in the existing literature [67, 69]. Locomotion is typically obtained by creating an undulatory motion in the tail portion connected to a passive caudal fin [70-72]. Some of the other studies that employed motor-based actuation include pectoral fins for locomotion [73, 74]. Although motor-based biomimetic vehicles have relatively high swimming speeds, they are often noisy and not easy to miniaturize. To overcome this problem, various research groups have explored the use of smart materials as actuators in bio-inspired aquatic robotics especially in the last few years [75].

The commonly used smart material actuators in biomimetic applications are IPMCs, shape memory alloys and piezoelectric materials as discussed in a recent review article [76]. Among these three smart materials, the compliant IPMC technology offers the largest mechanical deformation for low voltage actuation, and has therefore become the most heavily researched smart material in bio-inspired aquatic robotics applications. The main tradeoff in the use of IPMCs is the resulting low actuation force in contrast to their large geometric deformation capabilities. Several studies have been conducted by actuating a tail embedded with IPMCs, as such as a cantilever beam, with or without a passive caudal fin attached, including tadpole like robot in undulatory motion to create thrust in [77], an untethered swimming robot in [78], among other centimeter-scale examples [79, 80]. This type of locomotion created by IPMCs has been modeled and analyzed by several authors [81-83].

As discussed in the previous sections, MFC introduced by the NASA Langley Research Center in last decade [84] offers benefits such as increased flexibility, improved actuation authority, and anisotropic behavior over monolithic piezoelectrics (see Figure 1.1 and the corresponding explanations about the construction and properties of MFCs). MFC actuators have been successfully used in *tethered* underwater robotic fish [85-87] and lately in active control and hydrodynamic performance enhancement of flexible fins actuated in an unsteady fluid flow [88]. Erturk and Delporte [21] investigated underwater thrust and power production using MFC bimorphs with and without a passive caudal fin (with a focus on the first two vibration modes). Recently, an *untethered* piezoelectric robotic fish was developed and a suboptimal swimming speed of 0.3 body length/second was reported by Cen and Erturk [22].

In Chapter 4, underwater electrohydroelastic dynamic actuation of MFC cantilevers with different aspect ratios (length-to-width ratio, L/b) is explored. The in-air piezo-electroelastic model is extended by combining the linear electromechanical model based on Euler-Bernoulli beam theory [22, 89, 90] with the classical nonlinear Morison's equation for the hydrodynamic loading [29, 59, 62, 63, 91] (the main drive for using Morison's equation to incorporate the effects of the surrounding fluid on the oscillating beams was extensively explained in Section 1.2). The hydrodynamic coefficients (inertia and drag coefficients) in Morison formula are extracted experimentally for MFC cantilevers with three aspect ratios and the resulting nonlinear mathematical framework is analyzed and simulated by using the method of harmonic balance.

The aspect-ratio dependence of the hydrodynamic coefficients shows the 3-D effects of the surrounding fluid on the vibration response of the beam. In addition, the variation of both inertia and drag coefficients with Keulegan-Carpenter (KC) number [92], defined as $\mathrm{KC} = 2\pi|w(L)|/b$ (where $|w(L)|$ is the maximum tip displacement amplitude of oscillating beam), have been shown in a number of experimental efforts over the past decades [55, 58, 59, 62, 63, 91-94]. Therefore the dependence of the drag and inertia coefficients on the KC number is also reported in this work for the first two bending modes. Finally the variations of empirical hydrodynamic coefficients with aspect ratio are shown and compared with the results reported in literature [29, 45, 47, 52-55, 59, 95, 96] . Specifically, the aspect-ratio dependent hydrodynamic coefficients from base-excited aluminum beams are identified experimentally and used in order to predict the electrohydroelastic dynamics of the first two bending modes with good accuracy for standard MFC cantilevers with three aspect ratios. The variation of identified hydrodynamic inertia and drag coefficients with KC number for

both aluminum and MFC cantilevers with different aspect ratios are shown and compared with experimental observations from the existing literature [59].

Employing MFCs in the design of untethered robotic fish and bio-inspired thrust generation has been proven to be fairly successful in our group [21, 22]. However, more research is required to investigate the effect of length-to-width (L/b) aspect ratio on the hydrodynamic thrust generation performance of MFC cantilever fins while accounting for the power consumption levels during actuation. Facci *et al.* [53] compared the thrust coefficient for different values of oscillatory Reynolds numbers and aspect ratios by using 3-D computational fluid dynamics simulations. They [53] showed that, while the dependence of the thrust coefficient on the Reynolds number was relatively small and linear, there was a significant nonlinear dependence on the aspect ratio due to 3-D fluid effects. In this work (Section 4.4) the developed electrohydroelastic model is used in conjunction with Lighthill's elongated-body theory [97-99] to calculate the thrust production as a function of tip velocity and virtual mass (corrected with aspect ratio dependence) for quiescent water condition. Experiments are then conducted for various actuation voltage levels to quantify the mean thrust resultant and power consumption levels for different aspect ratios. The hydrodynamic thrust coefficient of the propulsor is estimated based on the virtual mass and aspect ratio, and then validated experimentally for MFC bimorphs with different aspect ratios.

1.4 Contactless Ultrasonic Energy Transfer for Wireless Systems

The harvesting of ambient vibrations for powering wireless electronic components has been heavily researched over the last decade [100-104]. As long as sufficient vibrational energy is readily available in the neighborhood of small electronic devices, it is possible to achieve mechanical-to-electrical energy conversion by means of a proper transduction mechanism

and thereby enable self-powered wireless electronic systems. An alternative scenario is the case in which a wireless electronic component has little or no vibrational energy available in its environment, yet the wireless charging of its battery is still of great interest and possible by means of Contactless Energy Transfer (CET). Examples of this scenario range from biomedical implants (e.g. cardiac pacemakers) to sensors located beyond physical access or in hazardous environments (e.g. sensors in nuclear waste containers). As an alternative to relatively well-studied methods of CET, namely the inductive, far-field electromagnetic (or microwave), capacitive, and optical coupling methods [105], research in the field of Ultrasonic Acoustic Energy Transfer (UAET) has recently gained momentum for energy transmission to wireless electronic components in various applications.

Biomedical applications offer great potential for CET since battery charging for medical implants without a surgery is tremendously valuable, and vibration intensity available inside the body (from the organs that exhibit motion or dynamic strain) is usually very low for energy harvesting. It is worth mentioning that, although the acceleration levels of muscular organs, such as the heart, have appeared intriguing to some researchers for energy harvesting [106], unfortunately what matters is the available power (or intensity) because tissue and muscle are dramatically more compliant than standard lab shakers. In other words, kinematic measurement (e.g. acceleration, velocity, or displacement) in the absence of the harvester is insufficient information to simulate vibrational energy available from a compliant, low-impedance system, using an electrodynamic shaker in lab environment. Continuing with the example of heartbeat, therefore, the main limitation is the impedance mismatch to have the same heartbeat acceleration in the presence of a non-compliant harvester. If the original heart wall acceleration in the absence of the harvester is a_o, it is straightforward to show that

[107] the acceleration available in the presence of the harvester is $a_f = a_o / (1 + Z_{harvester} / Z_{heart\_wall})$, where $Z_{harvester}$ and Z_{heart_wall} are the individual mechanical point impedances of the harvester and heart wall at the mounting location, suggesting that the kinematic input available to the harvester will substantially diminish in the coupled system (after the harvester is mounted), since $Z_{harvester} / Z_{heart\_wall} >> 1$ for strongly coupled piezoceramic harvesters as in the cm-scale device reported in [106]. This leaves compliant materials (such as dielectric elastomers [108, 109] or ionic polymers-metal composites [52, 110]) as the only option to avoid mechanical impedance mismatch, at the expense of dramatically reduced power density (of electronic/ionic polymers) as the main trade off. On the other hand, using a proper CET method, such as UAET, it is possible to transfer usable energy (more than sufficient for pacemakers) within several centimeters range to charge the battery of a medical implant without surgery.

In UAET, ultrasonic waves carry acoustic energy from a vibrating source (also called the transmitter) to a piezoelectric receiver, which then converts the vibrational energy into electricity and delivers to an electrical load. Among the methods of CET [105, 111-113], the relatively less studied UAET approach is an effective method for biomedical applications toward powering implanted devices [114-120] due to a number of advantages it offers, while the most heavily investigated approach for CET remains inductive coupling [121-126]. In the latter method (inductive coupling), power transfer is realized by means of two inductive resonators. High efficiency is achieved only within distances of the same order of the size of transmitter and receiver coils as the inductive coupling reduces significantly with increased distance (requiring increased reactive currents, and therefore yielding high conduction losses). In addition, inductive coupling experiences losses at high frequencies involved

[105]. The less popular capacitive coupling method is limited to very short distances for voltage levels to be realistic since capacitance is inversely proportional to distance. Other two methods are far-field electromagnetic coupling [111] and optical coupling [127] for CET. Recent analytical and experimental studies in the fields of both ultrasonic and inductive CET show that UAET is more advantageous for power transfer at large distances and for small implants [105, 119, 128]. Moreover, UAET is well suited for biomedical applications where exposure to electromagnetic fields is not allowed.

A brief summary of the limited (and mostly experimental) literature on UAET follows next (more details can be found in a recent review article [105]). The first biomedical application of UAET for charging implants appears to be the early work by Cochran *et al.* [114, 115]. They presented a system based on an internal piezoelectric plate attached to the bone fracture site for providing mechanical stability. The piezoelectric element was excited by external ultrasonic waves and generated electrical current delivered to the electrodes in order to stimulate treating fractures. Remarkably, this [114, 115] early approach was also used for energy harvesting from the mechanical strain in the implanted device due to the body motion. Recently, Kawanabe *et al.* [116] and Suzuki *et al*. [117] demonstrated ultrasonic power and information transmission to implanted medical devices. They could achieve an energy transfer efficiency of 20 % and a 9.5 kb/s bit rate for a power supply operating at 1 MHz frequency. Ozeri and Shmilovitz [118] investigated ultrasonic transcutaneous energy transfer as a method for powering implanted devices. In this method, two ultrasonic piezoelectric transducers were used as the transmitter external to the body and receiver implanted inside the body. The measurements of ultrasonic radiation and energy transfer were conducted thorough a pig muscle tissue and the results show 27 % power

transfer efficiency (70 mW of power output at 5 mm distance) for excitation frequency of 673 kHz. After that Ozeri *et al.* [119] proposed an ultrasonic transcutaneous energy transfer system similar to [118] with the aim of minimizing the diffraction losses by using segmented electrodes in the driver transducer. More recently, Maleki *et al.* [120] presented an implantable micro-oxygen generator that is powered ultrasonically at 2.15 MHz. The experimental results obtained by the proposed method showed less directionality and greater power transmission efficiencies for larger penetration depth and smaller receiver dimensions as compared to inductive transmission. In 2013, Roes *et al.* [105] reviewed the methods of CET in detail along with available technologies of UAET. Specifically they [105] pointed out the lack of modeling efforts for UAET, which is the central theme of the present work, along with performance enhancement, as outlined next.

The schematic representations of various possible and potential concepts in UAET are demonstrated in Figure 1.2. The first one shown in Figure 1.2a represents energy transfer from a pulsating sphere to an array of piezoelectric receiver bars (which are separately shunted to electrical loads). Acoustic waves can be transmitted in various media, such as water, air, or tissue, as long as the vibrating source is well coupled to the medium, i.e. impedance mismatch between the source and the medium is minimized. For instance, in the absence of ambient energy to harvest, underwater sensor networks or other arrays of wireless electronic components can be powered by UAET as depicted in Figure 1.2a. The second schematic (Figure 1.2b) is analogous to the transcutaneous UAET concept studied by Ozeri *et al.* [118, 119] for transferring energy from an external piezoelectric source to a piezoelectric receiver inside the tissue (i.e. multiple domains are involved). Figure 1.2b may represent various other problems of more than one domain (medium). For instance, a third

domain is often introduced to minimize possible impedance mismatch between two domains of primary interest (e.g. which would be the domains of transmitter and receiver in UAET).

The schematic in Figure 1.2c is implemented from the HIFU (High-Intensity Focused Ultrasound) technology [129] to focus the transmitted energy in space, and thereby strongly excite the receiver with dramatically reduced energy input to the source. Focusing should obviously be employed in UAET with care since HIFU may yield substantial energy localization and heating, which is the basis of its use in hyperthermia therapy [129] to destroy diseased or damaged tissue. It is worth mentioning that, other than using curved piezoelectric transducers to create focusing as depicted in Figure 1.2c, mirroring concepts [130] can also be employed with point sources in order to focus the transmitted energy in space. Figure 1.2d shows the possible scenario for enhanced power transfer by using a parabolic mirror at the receiver to focus plane waves.

Chapters 5 and 6 explore the basic concept of Figure 1.2a, i.e. UAET from a pulsating spherical source to a receiver piezoelectric bar shunted to an electrical load. While the focusing concept (Figure 1.2c) is suitable for exciting a single receiver, radiation from a spherical source (Figure 1.2a) is a practical solution to power multiple wireless electronic components by using a single source. The application of the scenario in Figure 1.2a is not limited to underwater sensor networks and it could represent the powering of wireless electronic devices in another medium by means of a single source.

Although there has been growing interest in the field of UAET under the area of CET, fully coupled acoustic-piezoelectric structure interaction modeling that combines the source and the receiver dynamics with fluid coupling as well as the electrical load has not been covered in the existing literature. Analytical modeling and closed-form solution of this

electromechanically and acoustically problem can be used for design and performance optimization of UAET concepts with substantially improved computational efficiency as compared to multiphysics finite-element modeling.

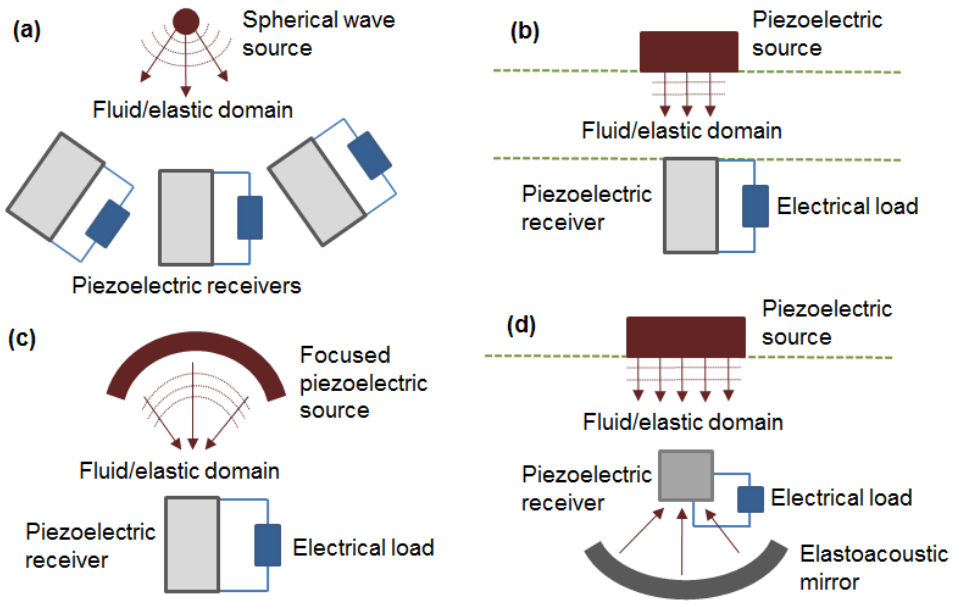

Figure 1.2. Various UAET concepts using piezoelectric transduction: (a) Excitation of an array of receivers by a pulsating sphere in the same domain (e.g. powering of an underwater sensor network); (b) excitation of a receiver in a separate domain (e.g. as in transcutaneous UAET[119]); (c) enhanced power transfer by focusing of the source; and (d) enhanced power transfer by using a parabolic mirror at the receiver to focus plane waves (3-D analog of our recent structure-borne energy harvesting concepts employing 2D elastoacoustic mirrors [130-132]).

To this end, in Chapter 5, a coupled model is developed for wireless acoustic energy transfer from a spherical wave source to the electrical load of a piezoelectric receiver (the special case of Fig. 1a with a single receiver). The fully coupled model relates the source strength to the electrical power output of the receiver through the acoustic-structure

interaction at the receiver-fluid interface. The receiver is a thickness-poled piezoelectric transducer located at a specific distance from the source and excited longitudinally by incident acoustic pressure waves. In the following, first an *in vacuo* electromechanical model is developed for linear longitudinal vibration of a fixed-free cylindrical piezoelectric bar with the fundamental vibration mode. Then, in order to account for acoustic-structure interaction, a lumped-parameter electromechanical piston representation of a fully submerged piezoelectric bar is used. The equivalent parameters are defined and the *in vacuo* model is extended by adding the radiation impedance terms to the equation of motion. Effects of various parameters such as the source strength, source-to-receiver distance, and receiver diameter are explored. Both resistive and resistive-reactive electrical loads are considered for the receiver bar. Soft (PZT-5H) and hard (PZT-8) piezoelectric materials are considered for performance comparison.

Next, an experimentally validated analytical modeling framework that relates the incident acoustic wave originating from a source of known strength to the electrical power output extracted by a free-free piezoelectric receiver is investigated. The effects of various parameters along with the optimal electrical loading conditions are reported. Among the various concepts summarized for UAET in Figure 1.2, this section is focused on the special case of Figure 1.2a with a single receiver (under electrical and fluid loading) excited by a spherical acoustic wave source.

As previously shown in Figure 1.2, one concept of UAET using piezoelectric receiver bar operating in the 33-mode of piezoelectricity is transferring energy from an external cylindrical piezoelectric source to a cylindrical piezoelectric receiver (i.e. multiple domains can be involved inherently or introduced for acoustic impedance matching). The primary

domains include the receiver, the transmitter and the intermediate domain (representing body tissue) all together submerged in a quiescent fluid [118, 119]. Both the transmitter and receiver surfaces can be modeled as unbaffled axially vibrating cylinders and the generated acoustic pressure by the source is obtained by solution of Helmholtz integral equation in space considering sommerfeld radiation and continuity condition on the surface of the source. To maximize the power output from the receiver, typically it is required to operate the transmitter/receiver close to its resonance frequency. On the other hand, the determination of operating frequency is of importance since it has effects on the attenuation, beam pattern and scattering of incident pressure wave at the leading surface of the cylindrical receiver. Acoustic-electroelastic structure interaction modeling efforts and experiments will explore these aspects for power transfer from a cylindrical source to a cylindrical receiver.

Focused UAET implemented from the HIFU (High-Intensity Focused Ultrasound) technology can be employed to concentrate the transmitted energy in space, and thereby strongly excite the receiver with dramatically reduced energy input to the source [133, 134]. Focusing should obviously be employed in UAET with care since HIFU may yield substantial energy localization and heating (FDA's requirement is the maximum temporal average intensity of 94 mW/cm^2 [118]), which is the basis of its use in hyperthermia therapy to destroy diseased or damaged tissue [135, 136]. It is worth mentioning that, other than using curved piezoelectric transducers to create focusing [134], mirroring concepts [137, 138] can also be employed with point sources in order to focus the transmitted energy in space. This work also briefly explores the possibility of focusing for improved power transfer efficiency in a quiescent fluid domain.

1.5 Outline of the Dissertation

This dissertation consists of two main subjects. The first subject (Chapters 2-4) is modeling and analysis of underwater vibration energy harvesting and biomimetic actuation of MFC-based piezoelectric structures with experimental validations. The second subject (Chapters 5-7) is theoretical and experimental studies on contactless acoustic energy transfer for various acoustic source and receiver configurations. The main body of this dissertation starts from Chapter 2 with the following components:

The second chapter of this dissertation bridges mixing rules formulation with distributed-parameter global electroelastic dynamics of MFC structures for energy harvesting, sensing, and biomimetic actuation in an analytical framework. Experimental validations are given to compare the parameters (such as modal electromechanical coupling term) obtained from analytical models with predictions of the homogenized formulation.

The third chapter presents modeling of underwater vibration energy harvesting from bimorph cantilevers made from piezoelectric MFCs with different aspect ratios. The formulation is obtained by adding the semi-empirical Morison's hydrodynamic function to the electroelastic in-air energy harvesting model given in the second chapter. Inertia and drag coefficients in Morison's equation are identified through a set of base excitation experiments on clamped passive aluminum strips and MFCs with similar aspect ratios for the first two vibration modes. Electrode segmentation is studied for power output enhancement in the second vibration mode for energy harvesting.

The fourth chapter provides an experimentally validated semi-empirical model for actuation of bimorph cantilevers made from piezoelectric MFCs with different aspect ratios. The model is derived by combining the in-air actuation model given in the second chapter

with Morison's nonlinear hydrodynamic function. For analysis of the coupled electrohydroelasctic equations, the method of harmonic balance is used. A set of rigorous experiments are conducted to identify inertia and drag coefficients. The repeatability of these two empirical coefficients is investigated in detail. Curve fit expressions are given for inertia and drag coefficients as functions of the aspect ratio alone. The thrust produced by MFC bimorphs is analyzed by using the developed electrohydroelastic model in combination with Lighthill's elongated-body theory. Experiments are then conducted to quantify the mean thrust resultant and power consumption levels for different aspect ratios. The hydrodynamic thrust coefficient is estimated and then validated experimentally for MFC bimorphs with different aspect ratios.

In Chapter 5, contactless ultrasonic acoustic energy transfer is investigated by analytical and numerical multiphysics modeling along with several case studies with an emphasis on analytical model validation and performance enhancement. The analysis is performed for UAET from a pulsating spherical source to a piezoelectric receiver bar (fixed-free boundary conditions) shunted to an electrical load. Soft and hard piezoelectric materials are considered for performance comparison.

In Chapter 6, contactless ultrasonic acoustic energy transfer is investigated analytically, numerically, and experimentally for a cylindrical receiver in free-free mechanical boundary conditions excited by a spherical wave source.

Chapter 7 presents an experimentally validated analytical model for contactless ultrasound acoustic energy transfer through acoustic-piezoelectric structure coupling of a cylindrical source and a cylindrical 33-mode receiver. Scattering effects are studied both

numerically and experimentally. The possibility of focusing for improved power transfer efficiency in a quiescent fluid domain is shown experimentally.

Finally, Chapter 8 summarizes the results of the work in this dissertation and draws conclusions from the aforementioned chapters.

2 COUPLING OF EXPERIMENTALLY VALIDATED ELECTROELASTIC DYNAMICS AND MIXING RULES FORMULATION FOR PIEZOELECTRIC MACRO-FIBER COMPOSITES

2.1 Introduction

Piezoelectric systems and structures have been used for decades in a variety of applications ranging from vibration control and sensing to morphing and energy harvesting. Conventional piezoelectric ceramics with uniform electrodes typically employ the 31-mode of piezoelectricity in bending, where the 3- and 1- directions are the directions of poling and strain, respectively. In order to employ the more effective 33-mode of piezoelectricity, IDEs have been used in the design of MFCs. In this chapter, an investigation into the two-way electroelastic coupling in bimorph cantilevers (in the sense of direct and converse piezoelectric effects) that employ IDEs for 33-mode operation is conducted. To this end, distributed-parameter electroelastic models are developed for the dynamic scenarios that involve two-way coupling, namely piezoelectric power generation and the problem of dynamic actuation. First, mixing rules formulation based on the plane-stress assumption is employed to evaluate equivalent and homogenous properties of MFCs from the constitutive properties. The electroelastic and dielectric properties of a representative volume element (piezoelectric fiber and epoxy matrix between two subsequent interdigitated electrodes) are then coupled with the global electroelastic dynamics based on the Euler-Bernoulli kinematics. Various MFC bimorph cantilevers that employ the 33-mode are tested under dynamic actuation, as well as power generation from base excitation (with resistive shunt damping) to identify their electromechanical properties which are then compared with the results obtained from analytical solution based on mixing rules formulation. The high fidelity

yet simple modeling framework presented and experimentally validated herein can be used for resonant sensing, actuation, and energy harvesting using MFC-based structures in their linear regime.

2.2 Electroelastic Equations of a Bimorph Cantilever with 33-Mode Piezoelectric Coupling

2.2.1 Electroelastic properties of an MFC laminate using mixing rules formulation and bimorph configurations

An MFC actuator laminate and interdigitated electrode configuration, which results in a complex electric field, are shown in Figure 2.1a-Figure 2.1c. The piezoelectric active material consists of commercial PZT fibers. A polymer coating (Kapton) keeps the electrodes attached on both faces of the piezoceramic layer isolated against possible electrical shorting and moisture in the environment. As depicted in Figure 2.1d, the strain axis and the electrical poling axis (the *x*-direction) are coincident, therefore the MFC laminate uses 33-mode of piezoelectricity.

The non-uniform electric field lines through the piezoelectric fibers and dead zones are depicted in Figure 2.1b [6, 139-141]. Because of the non-uniform electric field and heterogeneous complex structure involving active and passive regions (in Figure 2.1b; PZT fiber and epoxy, respectively) in MFCs, a direct integration over the volume of constitutive equation cannot be conducted easily to obtain the electromechanical coupling and capacitance parameters. However, it was experimentally shown that these two parameters act as global parameters for analysis of 33-mode MFC bimorphs, by Cacan and Erturk [142]. In the present work, mixing rules formulation is employed to evaluate equivalent and

homogenous properties of MFCs from the constitutive properties. To this end, the piezoelectric fibers and interdigitated electrodes are modeled as a series of piezoelectric segments combined in parallel. In Figure 2.1d each representative volume element (RVE) is a piezoelectric segment which is combined in parallel to the adjacent RVEs along the length and width of the MFC laminate. The following presents an analytical solution by combining the electroelastic and dielectric properties of an RVE for an MFC using the 33-mode of piezoelectricity (Figure 2.1d) based on distributed parameter electroelastic modeling.

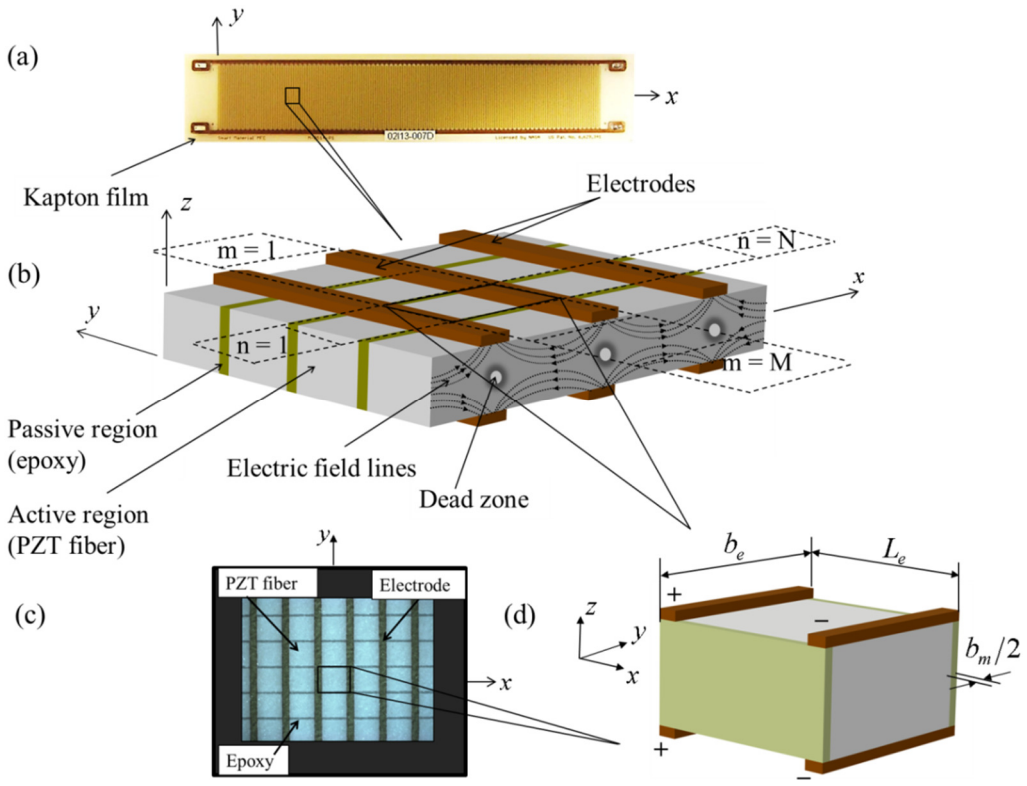

Figure 2.1. (a) MFC actuator laminate, (b) volumetric (3-D) representation of an MFC showing PZT fibers with electric field lines, polymer matrix (epoxy) and interdigitated electrodes, (c) digital image of the planar surface of an MFC actuator (M8514-P1 with polyester electrode sheets and approximately 90 % volume fraction of PZT fibers) under optical microscope and (d) RVE (in symmetric shape) for an MFC actuator using 33-mode of piezoelectricity.

The linear constitutive equations for a piezoelectric thin beam (RVE in Figure 2.1d) with 33-mode coupling are [1]

$$T_3 = c_{33,e}^E S_3 - e_{33,e} E_3 \tag{2.1}$$

$$D_3 = e_{33,e} S_3 + \varepsilon_{33,e}^S E_3 \tag{2.2}$$

where T_3 is the stress, S_3 is the strain, E_3 is the electric field, D_3 is the electric displacement, $c_{33,e}^E$ is the elastic modulus at constant electric field, $e_{33,e}$ is the effective piezoelectric stress constant and $\varepsilon_{33,e}^S$ is the effective permittivity component at constant strain, respectively (subscript *e* stands for effective properties).

Here, the elastic modulus ($c_{33,e}^E$), piezoelectric charge constant ($d_{33,e}$), and dielectric relative constant ($\varepsilon_{33,e}^S$) are defined based on the mixing rules formulation for RVE in Figure 2.1d as follows [40, 143]:

$$c_{33,e}^E = \nu c_{33,p}^E + (1-\nu) c_{33,m}^E \tag{2.3}$$

$$d_{33,e} = \frac{1}{c_{33,e}^E} \nu d_{33,p} c_{33,p}^E \tag{2.4}$$

$$\varepsilon_{33,e}^S = \left[\nu \varepsilon_{33,p}^T + (1-\nu) \varepsilon_{33,m}^T \right] - d_{33,e}^2 c_{33,e}^E \tag{2.5}$$

where ν is the PZT fiber volume fraction and is defined by the measurement done from the digital image of the planar surface of an MFC actuator (shown in Figure 2.1c) and ε_{33}^T is the permittivity component at constant stress. Subscripts *p* and *m* stand for PZT fiber and matrix (epoxy) properties in RVE, respectively. The mixing rules-based effective electroelastic parameters will be coupled with the electroelastic dynamics based on the Euler-Bernoulli

kinematics in the next section to obtain the resulting physical parameters (e.g. capacitance and electromechanical coupling term) of an MFC bimorph using 33-mode of piezoelectricity in bending operation. The analysis of an Euler-Bernoulli beam with piezoelectric layers has been thoroughly covered in previous work [1] for energy harvesting applications. The key concepts will be developed and applied later in this work.

Schematics of an MFC bimorph for dynamic actuation with fixed base and energy harvesting from base motion are shown in Figure 2.2. Each symmetric bimorph is composed of two MFC laminates (Figure 2.1a) which are processed by vacuum bonding system using high-shear-strength epoxy as the adhesive layer of negligible thickness.

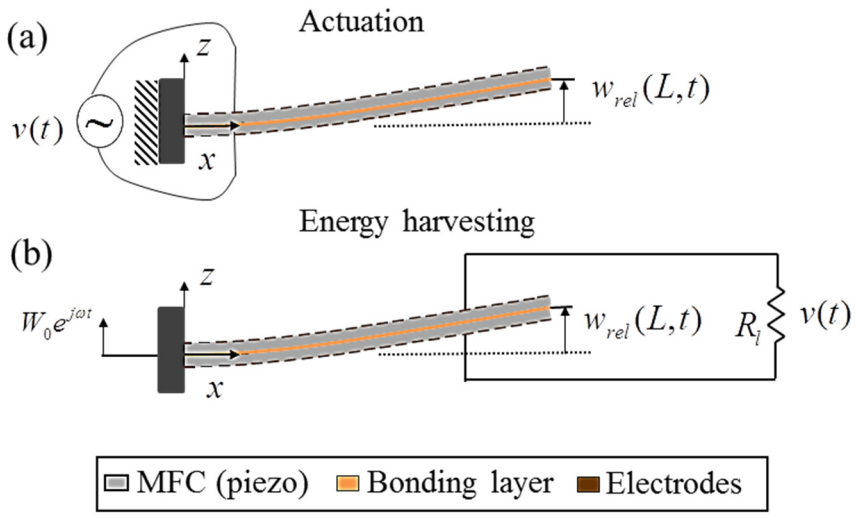

Figure 2.2 . Schematics of a cantilevered MFC bimorph composed of two bonded MFC laminates under (a) dynamic actuation and (b) transverse base excitation.

2.2.2 Coupled mechanical equation under base excitation

The MFC bimorph cantilever configurations shown in Figure 2.2 are modeled here based on the Euler-Bernoulli beam theory. Deformations are assumed to be small and the composite structure is assumed to exhibit linear material (elastic and electroelastic) behavior. The

partial differential equation governing the dynamics of the base-excited cantilevered bimorph is

$$-\frac{\partial^2 \mathrm{M}(x,t)}{\partial x^2} + c_\alpha \frac{\partial^5 w_{rel}(x,t)}{\partial x^4 \partial t} + c_\beta \frac{\partial w_{rel}(x,t)}{\partial t} + m_s \frac{\partial^2 w_{rel}(x,t)}{\partial t^2} = -m_s \frac{\partial^2 w_b(t)}{\partial t^2} \tag{2.6}$$

where $w_{rel}(x,t)$ is the transverse displacement of the beam (neutral axis) relative to its base at position x and time t, c_α is the stiffness-proportional damping coefficient, c_β is the mass-proportional damping coefficient[1], m_s is the mass per unit length of the beam, $\mathrm{M}(x,t)$ is the internal bending moment, and $w_b(t)$ is the transverse base displacement.

The internal bending term in Equation (2.6) is the first moment of the axial stress field over the cross-section of MFC bimorph (which has two laminates):

$$\mathrm{M}(x,t) = \int_A T_3 \, z \, dA = \sum_{m=1}^{M} b_e \left(\int_{-h_{\tilde{p}}-h_b/2}^{-h_b/2} T_3 \, z \, dz + \int_{h_b/2}^{h_{\tilde{p}}+h_b/2} T_3 \, z \, dz \right) \tag{2.7}$$

where in each RVE (Figure 2.1d), b_e is the summation of piezoceramic fiber and matrix layer width. In Equation (2.7), M is the number of RVEs in active width of the bimorph, b, yielding $b = Mb_e$. Furthermore, $h_{\tilde{p}}$ is the thickness of piezoceramic fiber, h_b is the thickness of bonding and Kapton layers, and T_3 is the stress component (in the x- direction) given in Equation (2.1). The stress component for bonding (epoxy) and Kapton layers are assumed to be negligible as their stiffness is much less than the stiffness of PZT fibers. The electric field in Equation (2.1) can be given in terms of voltage across the electrodes, $v(t)$. The voltage

[1] This combined generalized proportional damping form is assumed to account for the internal losses as a convenient mathematical representation. In-air infinitesimal vibrations in the experiments will be approximated with the *in vacuo* condition.

across each MFC laminate is $v(t)/2$ in the series connection of two MFC laminates and $v(t)$ for the parallel connection case. The electric field between two parallel plates can be defined as $E_3 = \pm v(t)/L_e$ where L_e is the distance between two subsequent electrode fingers (shown in Figure 2.1d). The $\pm$ is a result of the difference in poling of the piezoelectric material depending on series or parallel connection of the piezoelectric layers [1]. It is worth mentioning that, in Figure 2.1c each RVE is a piezoelectric segment which is linked in parallel to the adjacent RVEs along the length and width of the MFC laminate. Furthermore, based on plane-stress assumption, the piezoelectric stress constant $e_{33,e}$ in Equation (2.1) can be given in terms of the more commonly used piezoelectric strain constant $d_{33,e}$ as $e_{33,e} = d_{33,e} c_{33,e}^{E}$ [1]. For geometrically small oscillations, the axial strain at a certain level z from the neutral axis of the symmetric composite beam is simply proportional to the linear curvature of the beam at position x;

$$S_3(x,z,t) = -z\frac{\partial^2 w_{rel}(x,t)}{\partial x^2} \tag{2.8}$$

Substituting Equation (2.7) into Equation (2.6) and multiplying the electrical term by $\left[H(x-(n-1)L_e)-H(x-nL_e)\right]$, the internal bending moment term is then obtained from Equation (2.7) as

$$\mathrm{M}^s(x,t) = -D\frac{\partial^2 w_{rel}(x,t)}{\partial x^2} + \sum_{n=1}^{N} \vartheta_s v(t)\left[H(x-(n-1)L_e)-H(x-nL_e)\right] \tag{2.9}$$

$$\mathrm{M}^{p}(x,t) = -D\frac{\partial^2 w_{rel}(x,t)}{\partial x^2} + \sum_{n=1}^{N} \vartheta_p v(t)\left[H(x-(n-1)L_e) - H(x-nL_e)\right] \tag{2.10}$$

where D is the bending stiffness of the composite cross-section, $H(x)$ is the Heaviside function and n is the index number of an RVE at a distance x from the fixed end of the bimorph. Note that, here and hereafter, the subscripts and superscripts *s* and *p*, respectively, stand for the series and parallel connections of the MFC laminates. The coefficients of the backward coupling terms for the series and parallel connection cases (ϑ_s and ϑ_p, respectively) are

$$\vartheta_s = \sum_{m=1}^{M} \frac{e_{33} b_e}{2h_{\tilde{p}}}\left[\left(h_{\tilde{p}} + \frac{h_b}{2}\right)^2 - \frac{h_b^2}{4}\right] = \sum_{m=1}^{M} \frac{e_{33} b_e h_{\tilde{p}}}{2L_e}(h_{\tilde{p}} + h_b) = M d_{33,e} c_{33,e}^{E} \frac{A_e}{L_e} h_{pc} \tag{2.11}$$

$$\vartheta_p = 2\vartheta_s = 2M d_{33,e} c_{33,e}^{E} \frac{A_e}{L_e} h_{pc} \tag{2.12}$$

In Equations (2.9) and (2.10), N is the number of RVEs in active overhang length, L, as $L = NL_e$. For each RVE, A_e is the effective cross section area and h_{pc} is defined as the position of center of piezoceramic layer from the neutral axis (in the thickness direction). From Equations (2.6), (2.9) and (2.10), the coupled beam equation can be obtained as follows for parallel connection of MFC laminates:

$$\begin{aligned} &D\frac{\partial^4 w_{rel}(x,t)}{\partial x^4} + c_\alpha \frac{\partial^5 w_{rel}(x,t)}{\partial x^4 \partial t} + c_\beta \frac{\partial w_{rel}(x,t)}{\partial t} + m_s \frac{\partial^2 w_{rel}(x,t)}{\partial t^2} - \\ &\vartheta_p v(t)\left[\frac{d\delta(x)}{dx} - \frac{d\delta(x-L)}{dx}\right] = -m_s \frac{\partial^2 w_b(t)}{\partial t^2} \end{aligned} \tag{2.13}$$

For the series connection case, ϑ_s is used for the backward coupling term in Equation (2.13) .

2.2.3 *Electroelastically coupled and resistive shunted electrical circuit equation*

The electric current output is obtained from the integral form of Gauss's law as

$$\frac{d}{dt}\left(\int_A \mathbf{D}.\mathbf{n}\, dA\right) = \frac{v(t)}{R_l} \tag{2.14}$$

where $\mathbf{D}$ is the vector of electric displacement components, $\mathbf{n}$ is the unit outward normal, R_l is the resistive load across the device, and integration is performed over overall effective area, A, obtained from $A \cong MA_e$. The inner product of the integrand in Equation (2.14) is obtained using D_3 given in Equation (2.2). Employing Equation (2.8) for the average bending strain in terms of the curvature and the electric field in terms of the electric potential difference ($E_3 = -v(t)/L_e$), Equation (2.2) can be used in Equation (2.14) to obtain

$$C_p \frac{dv(t)}{dt} + \frac{v(t)}{R_l} + Md_{33,e}c^E_{33,e}\frac{A_e}{L_e}h_{pc}\int_0^L \frac{\partial^3 w_{rel}(x,t)}{\partial x^2 \partial t}dx = 0 \tag{2.15}$$

The internal capacitance is expressed as

$$C_p = \sum_{m=1}^{M}\sum_{n=1}^{N} \varepsilon^S_{33,e}\frac{A_e}{L_e} = MN\varepsilon^S_{33,e}\frac{A_e}{L_e} \tag{2.16}$$

2.2.4 *Modal analysis of base-excited and actuated MFC bimorph cantilever and equivalent representation of the electromechanical parameters*

The transverse deflection of the reference surface at position x and time t is

$$w_{rel}(x,t) = \sum_{r=1}^{\infty} \phi_r(x)\eta_r(t) \tag{2.17}$$

where $\phi_r(x)$ and $\eta_r(t)$ are the mass-normalized eigenfunction and the generalized modal coordinate for the *r*th vibration mode, respectively. The eigenfunctions denoted by $\phi_r(x)$ can be derived for the transverse vibration of a clamped-free beam as

$$\phi_r(x) = \sqrt{\frac{1}{m_s L}}\left[\cos\frac{\lambda_r}{L}x - \cosh\frac{\lambda_r}{L}x + \frac{\sin\lambda_r - \sinh\lambda_r}{\cos\lambda_r + \cosh\lambda_r}\left(\sin\frac{\lambda_r}{L}x - \sinh\frac{\lambda_r}{L}x\right)\right] \tag{2.18}$$

where λ_r is the eigenvalue of the *r*th mode obtained from the characteristic equation

$$1 + \cos\lambda\cosh\lambda = 0 \tag{2.19}$$

The expression given for $\phi_r(x)$ satisfies the companion orthogonality conditions as [22].

$$\int_0^L \phi_s(x) m_s \phi_r(x) dx = \delta_{rs} \tag{2.20}$$

$$\int_0^L \phi_s(x) D \frac{\partial^4 \phi_r(x)}{\partial x^4} dx = \omega_r{}^2 \delta_{rs} \tag{2.21}$$

where $\omega_r = \lambda_r^2\sqrt{D/m_s L^4}$ is the undamped natural frequency of the *r*th vibration mode and δ_{rs} is the Kronecker delta. The base displacement is assumed to be harmonic of the form $w_b(t) = W_0 e^{j\omega t}$ (where ω is the angular excitation frequency and j is the unit imaginary number). The modal forcing is expressed as $f_r(t) = F_r e^{j\omega t}$ where the amplitude F_r is

$$F_r = -\sigma_r \omega^2 W_0 \tag{2.22}$$

where

$$\sigma_r = -m_s \int_0^L \phi_r(x) dx \tag{2.23}$$

Assuming harmonic steady-state modal mechanical response and voltage response in the forms of $\eta_r(t) = H_r e^{j\omega t}$ and $v(t) = V e^{j\omega t}$, and using Equation (2.17) into Equations (2.13) and (2.15), multiplying by $\phi_s(x)$, and integrating over the length of the cantilever give the following electromechanically coupled linear equations for the modal coefficient

$$(\omega_r^2 - \omega^2 + j2\zeta_r \omega_r \omega) H_r - \theta_r V = F_r \tag{2.24}$$

$$(\frac{1}{R_l} + j\omega C^{eq}) V + j\omega \sum_{r=1}^{\infty} \theta_r H_r = 0 \tag{2.25}$$

where θ_r is the modal electromechanical coupling, ζ_r is the modal mechanical damping ratio, and C^{eq} is the equivalent capacitance. The modal electromechanical coupling and the equivalent capacitance depend on the way the MFC laminates are wired. The analytical expressions for the equivalent capacitance and modal electromechanical coupling are given in Table 2.1 for the series and parallel connections of the MFC laminates [1].

Table 2.1: Modal electromechanical coupling and equivalent capacitance of an MFC bimorph for the series and parallel connections of the MFC laminates.

	Series connection	Parallel connection
θ_r	$Md_{33,e} c_{33,e}^E \frac{A_e}{L_e} h_{pc} \left. \frac{d\phi_r(x)}{dx} \right\|_{x=L}$	$2Md_{33,e} c_{33,e}^E \frac{A_e}{L_e} h_{pc} \left. \frac{d\phi_r(x)}{dx} \right\|_{x=L}$
C^{eq}	$MN\varepsilon_{33,e}^S \frac{A_e}{2L_e}$	$2MN\varepsilon_{33,e}^S \frac{A_e}{L_e}$

The solution to the actuation case of the 33-mode cantilevered MFC bimorph can be derived using the governing linear coupled equations from Equations (2.24) and (2.25) by changing the input to $v(t)$ and setting F_r (modal mechanical forcing) equal to zero, yielding

$$\left(\omega_r^2 - \omega^2 + j2\zeta_r\omega_r\omega\right)\mathrm{H}_r = \theta_r V \tag{2.26}$$

$$-I + j\omega VC^{eq} + j\omega\sum_{r=1}^{\infty}\theta_r\mathrm{H}_r = 0 \tag{2.27}$$

where in Equation (2.25), V/R_l is replaced with $-i(t) = -Ie^{j\omega t}$. Here $i(t)$ is the electrical current input (negative sign implies current flow into the system).

2.2.5 Energy harvesting from base excitation: Voltage and velocity FRFs

Solutions of Equations (2.24) and (2.25) for energy harvesting from base excitation yield the analytical form of $v(t)$ and $w_{rel}(x,t)$. Yet as the input frequency can vary, the most general solutions are the steady-state transfer functions from the translational base acceleration to the voltage and displacement, simply FRFs, and given by $\alpha(\omega)$ and $\beta(\omega,x)$, respectively [1].

$$\alpha(\omega) = \frac{v(t)}{-\omega^2 W_0 e^{j\omega t}} = \frac{\sum_{r=1}^{\infty}\dfrac{-j\omega\theta_r\sigma_r}{\omega_r^2 - \omega^2 + j2\zeta_r\omega_r\omega}}{\dfrac{1}{R_l} + j\omega C^{eq} + \sum_{r=1}^{\infty}\dfrac{j\omega\theta_r^2}{\omega_r^2 - \omega^2 + j2\zeta_r\omega_r\omega}} \tag{2.28}$$

$$\beta(\omega,x) = \frac{w_{rel}(x,t)}{-\omega^2 W_0 e^{j\omega t}} = \sum_{r=1}^{\infty}\frac{\left[\sigma_r + \theta_r\alpha(\omega)\right]\phi_r(x)}{\omega_r^2 - \omega^2 + j2\zeta_r\omega_r\omega} \tag{2.29}$$

Finally, the displacement FRF relative to the fixed end is modified to express the absolute velocity response, i.e. tip velocity with respect to absolute reference frame, $\gamma(\omega,x)$

, in order to compare with experimental measurements (in which the laser Doppler vibrometer is in the absolute reference frame).

$$\gamma(\omega,x)=\frac{1}{j\omega}+j\omega\beta(\omega,x) \tag{2. 30}$$

2.2.6 Dynamic actuation due to voltage excitation: Velocity and admittance FRFs

Solving Equations (2.26) and (2.27) yield the displacement FRF, $\chi(\omega,x)$, and the admittance FEF, $\varphi(\omega)$.

$$\chi(\omega,x)=\frac{w_{rel}(x,t)}{Ve^{j\omega t}}=\sum_{r=1}^{\infty}\frac{\theta_r\phi_r(x)}{\omega_r^2-\omega^2+2j\zeta_r\omega_r\omega} \tag{2.31}$$

$$\varphi(\omega)=\frac{I}{V}=j\omega\left(C^{eq}+\sum_{r=1}^{\infty}\frac{\theta_r^2}{\omega_r^2-\omega^2+2j\zeta_r\omega_r\omega}\right) \tag{2.32}$$

To find the solution to the velocity FRF, multiplying $\chi(\omega,x)$ by $j\omega$ is sufficient since the base is not moving and harmonic excitation is assumed.

2.3 Case Study for Macro-Fiber Composite Bimorphs and Model Validation

For the experimental validation of the modeling framework presented in the previous section and for a comparative analysis into the properties of MFCs, three cantilever MFC bimorphs are tested focusing on the fundamental mode of vibration. The MFCs, acquired from the Smart Material Corp. [66], have active length of 85mm (active length and width define the portions which are covered with piezoelectric material) for all samples. Each bimorph is made from two identical custom-made MFC laminates (hydrophobic due to polyester

electrode sheets) labeled as M8507-P1, M8514-P1 and M8528-P1 (Figure 2.3a) with active widths of 7 mm, 14 mm, and 28 mm, respectively.

The MFCs are processed with a vacuum system to create symmetric bimorphs and cantilevered in an aluminum clamp, shown in Figure 2.3a. The overhang lengths of the MFC bimorphs are approximately 75.5mm while the total thicknesses are around 0.61mm. The electrode leads of the MFC bimorphs are connected in parallel throughout the experiments discussed in this section and the focus is placed on the energy harvesting and dynamic actuation problem for the fundamental bending vibration mode under geometrically, materially, and piezoelectrically linear behavior. Energy harvesting experiments (Figure 2.3b) are conducted through a Spectral Dynamics SigLab data acquisition device that received base acceleration data (Kistler accelerometer with a Kistler Signal Conditioner), absolute velocity data measured at the tip of the bimorph by a Laser Doppler Vibrometer (LDV, Polytec PDV 100), and voltage level across a resistive load (IET Decade Resistor). Harmonic excitation with 10 averages is fed to a B&K electromechanical shaker through an HP power amplifier for base excitation over a range of frequencies centered at the first mode. Actuation experiments (Figure 2.3c) are conducted in the same set up, but with a fixed mount instead of a shaker and a Trek High Voltage Amplifier (Trek, inc. Model 2220) from which one can extract reference voltage and current input to the system (for admittance calculation).

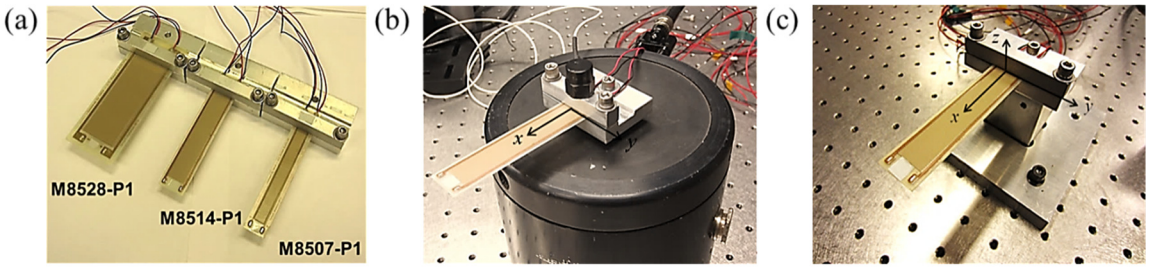

Figure 2.3. (a) MFC bimorphs in aluminum clamps, (b) close-up view of an M8514-P1 type bimorph cantilever mounted on electromechanical shaker with an accelerometer and (c) dynamic actuation test for sample bimorph (M8514-P1) cantilever mounted to a stiff fixture.

2.3.1 System parameters

The geometric properties and sequence of layers for the active (PZT fibers) and passive (epoxy, electrodes and Kapton film) layers of an MFC bimorph are shown in Figure 2.4 for both *x*-*z* and y-z (cross section area) planes. From the surface image (e.g. Fig 2b for M8514-P1 bimorph) the width of each piezoceramic fiber is approximately $355.5\,\mu m$ and each epoxy layer between the fibers has a width of $34.4\,\mu m$. Since the total active width is 14 mm, this sample (M8514-P1) has approximately 36 piezoceramic fibers (M = 36) and $\nu = 0.9$. The average spacing between two subsequent electrodes is $407.18\,\mu m$. Therefore, the number of RVE over the beam length is 185 (N = 185). Having the measured capacitance of the MFCs and using Equation (2.16), the average effective surface area of each RVE, A_e, is calculated as 0.02 mm^2 and h_{pc} is given as $157\,\mu m$. The MFCs use Navy II piezoceramics, for which the effective value of the piezoelectric constant for RVE is $e_{33,e} = 19.1 C/m^2$. In Table 2.2, properties of PZT fibers, epoxy, RVE (the effective properties for RVE are calculated based on mixing rules formulation), and MFC bimorph are given. It is important

to note that, as it is shown in Figure 2.4, for MFCs the electrode layers are made of an epoxy and copper fibers (volume fraction of copper is approximately 24%) which are perpendicular to the PZT fibers and then the composite structure is embedded in a Kapton film. The in-plane (*y-z* plane) sequence of layers for an MFC bimorph is shown in details in Figure 2.4b. The effective properties of electrode-Kapton layer are calculated using the mixing rules formulation. Then, the properties of an MFC bimorph are calculated from the properties of all the included layers (PZT-epoxy (RVE in Figure 2.1d) and electrode-Kapton layers). For example RVE has the effective Young's modulus as 48.3 GPa, by including the electrode-Kapton layers (c_{33}^{E} is 117.2 GPa and 2.8 GPa for copper and Kapton, respectively), the effective stiffness and piezoelectric constant are evaluated as 31.1 GPa and 13.6 C/m^2 for an MFC bimorph, respectively. The reported values in Table 2.2 are cross checked with the previously published numerical and experimental data as well as the data from the manufacturer [17, 40, 42] despite the uncertainty on the values of material and geometrical properties of MFCs under study.

Having mixing rules-based effective and homogenized properties of MFC bimorphs, the modal electromechanical coupling (θ) is obtained from Table 2.1 for fundamental vibration mode (r = 1) and parallel connection of MFC laminates. For each sample short-circuit resonance frequency, damping ratio and the equivalent capacitance (C^{eq}) are measured experimentally and employed in Equations (2.28) - (2.32). The energy harvesting and dynamic actuation models of MFC bimorphs (in Section 2.2) are validated experimentally in next sections along with the parameter identifications.

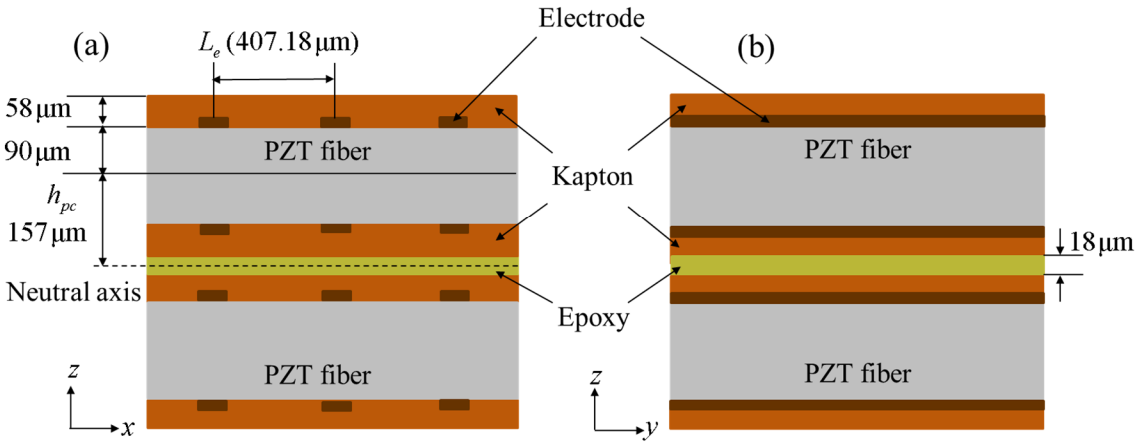

Figure 2.4. 2D representation of MFC bimorph (made from two identical MFC laminates bonded using high-shear-strength epoxy with electrodes (epoxy and copper fibers) perpendicular to the PZT fibers embedded in Kapton film); (a) Geometric parameters in x-y plane and (b) sequence of layers in cross section area (y-z plane). Approximate geometric data provided by the manufacturer [17] or measured under optical microscope.

Table 2.2. Properties of active layer (PZT fiber), passive layer or matrix (epoxy), RVE, and 33-mode MFCs using analytical mixing rules formulation (parameter x stands for the corresponding property).

	PZT fiber ($x_{,p}$)	Epoxy ($x_{,m}$)	RVE ($x_{,e}$)	MFC
c_{33}^{E} [GPa]	48.30	3.10	43.78	31.10
d_{33} [pm/V]	440	-	437	437
$\varepsilon_{33}^{T} / \varepsilon_{0}$ *	1850	4.25	1665	1665
ε_{33}^{S} ** [nF/m]	7.02	-	6.38	8.80

* $\varepsilon_0 = 8.854\,\text{pF/m}$ is the permittivity of free space.

** $\varepsilon_{33}^{S} = \varepsilon_{33}^{T} - d_{33}^{2} c_{33}^{E}$

2.3.2 Energy harvesting from base excitation

Figure 2.5a-Figure 2.5c show the voltage output and tip velocity FRFs obtained from Equations (2.26) and (2.27) for M8507-P1, M8514-P1, and M8528-P1 bimorphs, respectively. The tests are conducted at low base excitation levels around the fundamental frequency with varying electrical resistive loads from 100Ω to ~9.09MΩ ([0.1 1 10 99 909.1 5000 9082.6] kΩ). As the load resistance is increased, the resonance frequency shifts from the short-circuit resonance frequency to the open-circuit resonance frequency. It is seen that by changing the load resistance from short- to open-circuit conditions, the voltage output increases uniformly and the resonance frequency for moderate resistive loads can take a value between the short- and open-circuit resonance frequencies. With increasing load resistance the peak vibration amplitude decreases considerably from the peak of short-circuit condition to a certain value and then is amplified at the open-circuit resonance frequency. This phenomenon happens because of changing the electrical boundary condition of the bimorph and shunt damping effect of power generation due to Joule heating in the resistor for moderate resistance values.

An optimal electrical load resistance can be identified at each frequency for delivering the maximum power output, which is associated with resistive shunt damping.

The variations of the peak voltage output, electric current, power output, and tip velocity versus changing load resistance for excitations at the short and open-circuit resonance frequencies (44.6 and 46.1 Hz, respectively) are shown in Figure 2.6a-Figure 2.6d for M8507-P1. For brevity, the remaining samples are not graphically presented here.

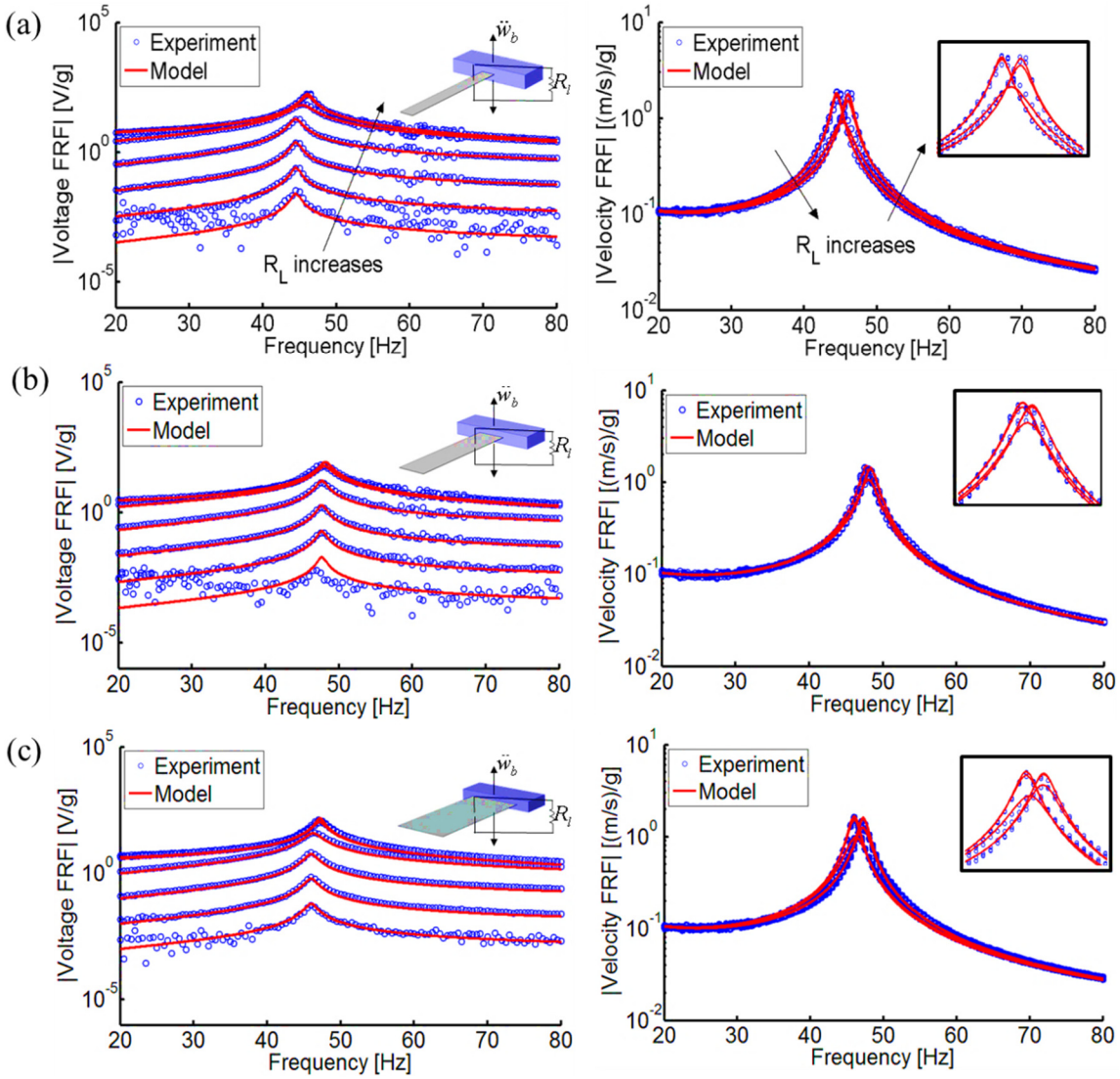

Figure 2.5. Experimental and analytical frequency response results for base-excited energy harvesting: Tip velocity FRFs (left side) and voltage FRFs for a set of resistors (right side) for (a) M8507-P1, (b) M8514-P1 and (c) M8528-P1.

It is observed that the variation of the voltage amplitude with load resistance has opposite trend as compared to that of the current amplitude. That is, as the load resistance increases the voltage output amplitude increases monotonically. The voltage for excitation at the short-circuit resonance frequency is higher when the system is close to short circuit

conditions. For a 0.74 MΩ load resistance, both excitation frequencies yield the same voltage amplitude (49.1 V/*g*).

The electrical power outputs versus load resistance graph for excitations at the fundamental short- and open- circuit resonance frequencies is plotted in Figure 2.6c. It is seen that the electrical power does not show monotonic change with load resistance. The maximum electrical power happens at the optimum resistive loads defined for the short- and open-circuit resonance frequency excitations. The optimum load resistance for excitation at 44.6 Hz is about 0.3 MΩ, yielding a maximum electrical power of about 4.6 mW/g^2 whereas the optimum resistive load for excitation at 46.1 Hz is 49.7 kΩ, yielding the same power output 4.6 mW/g^2. As in the case of voltage and current outputs, the electrical power output for excitation at the short circuit resonance frequency is higher when the system is close to short circuit conditions. Since the system is lightly damped and strongly coupled [144, 145] approximately the same power output is delivered to substantially different optimal resistance values. Figure 2.6d shows that, by increasing the load resistance, the vibration amplitude at the fundamental short- and open-circuit resonance frequencies is attenuated due to the power transfer to the electrical load at its maximum level. This is due to the effect of Joule heating in the resistor [146, 147] on the dynamics of the MFC bimorph as the generator. Very good agreement is observed between the empirical results and the proposed analytical model.

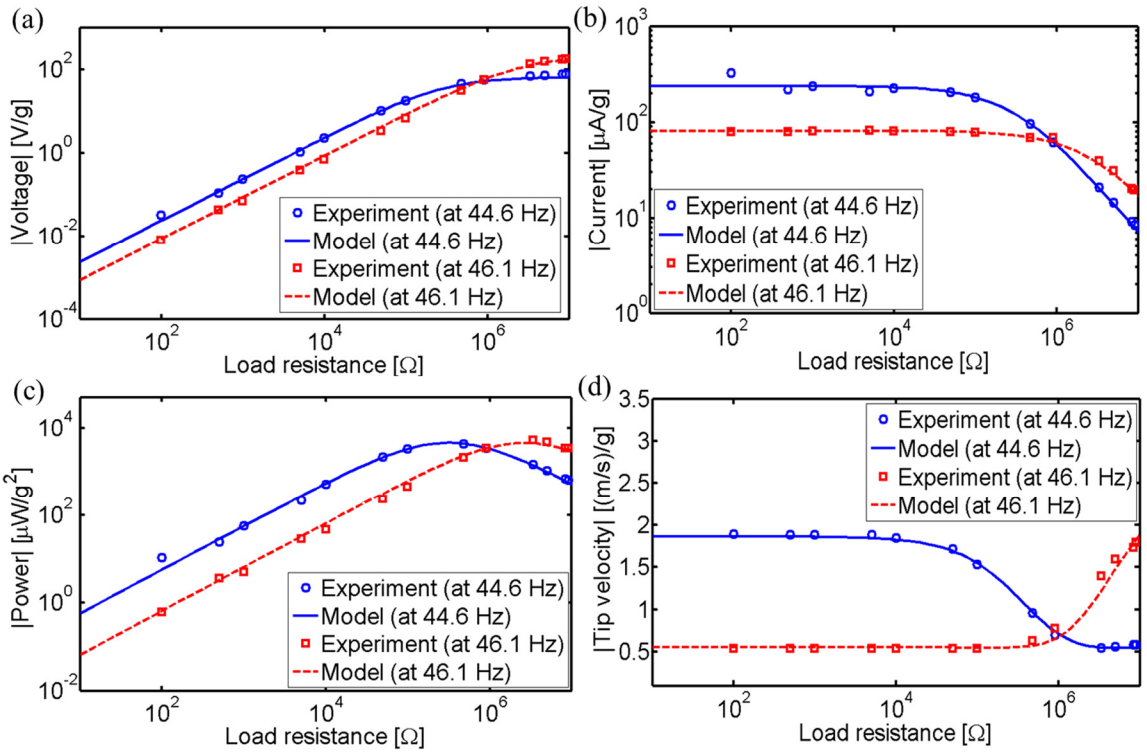

Figure 2.6. Variation of the (a) voltage, (b) current, (c) power, and (d) tip velocity amplitude (per base acceleration input for changing load resistance for excitation at fundamental short- and open-circuit resonance frequencies.

2.3.3 Dynamic actuation due to voltage excitation

Tip velocity and admittance FRFs for actuation experiments on the three bimorphs (M8507-P1, M8514-P1, and M8528-P1) are calculated by using Equations (2.31) and (2.32) and shown in Figure 2.7a to Figure 2.7c, respectively. The good agreement between the experimental results and analytical model validates the modeling framework. The model predictions from Figure 2.5 to Figure 2.7 are the application of Equations (2.28) – (2.32). The close match between experimental results and model predictions shows that modeling MFCs in the linear regime with analytical-based electromechanical properties is valid. The

identified parameters from actuation and energy harvesting experiments are summarized in Table 2.3.

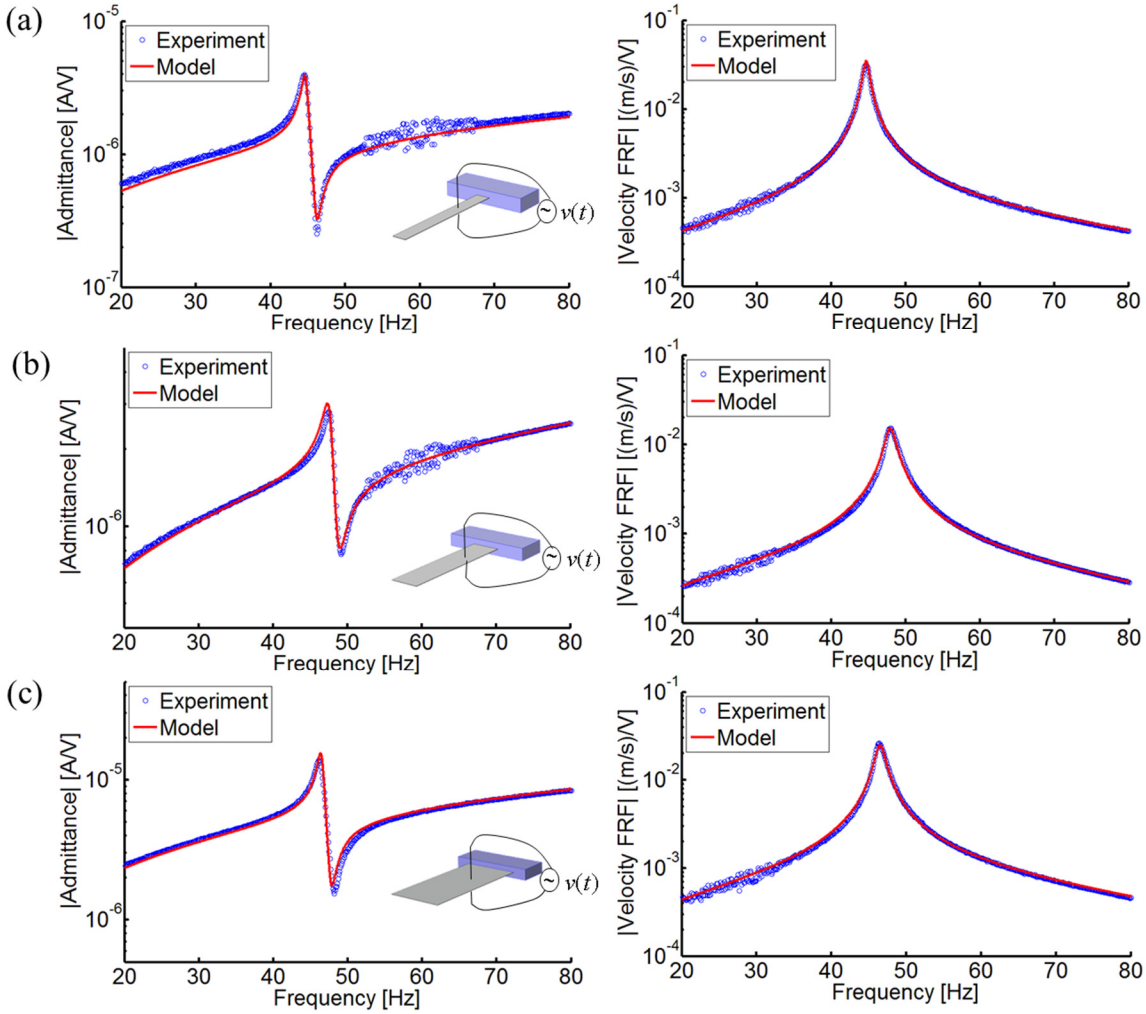

Figure 2.7. Experimental and analytical frequency response results for actuation: Admittance FRF (left side) and tip velocity FRF (right side) for (a) M8507-P1, (b) M8514-P1 and (c) M8528-P1.

Furthermore, the close match justifies the identification of system parameters through experimental results. Of particular importance is that the electromechanical parameters, all identified from the harvesting experiments in this case, lead to close matches for the

actuation FRFs. This illustrates the importance of analyzing piezoelectric systems with two-way coupling.

Table 2.3. Experimentally identified parameters from in-air actuation and energy harvesting experiments.

	M8507-P1	M8514-P1	M8528-P1
f_{sc} (Hz)	44.6	47.9	46.4
f_{oc} (Hz)	46.1	48.5	47.2
$\zeta(\%)$	1.8	2	1.5
θ (10^{-3} C/m$\sqrt{\text{kg}}$)	3.5	4.5	9
C^{eq} (nF)	3.8	5.5	17.5

2.3.4 Analytical and experimental modal electromechanical coupling and piezoelectric constant

In Figure 2.8, modal electromechanical coupling term and effective piezoelectric constant of the custom-made piezoelectric MFC bimorph with polyester electrode sheets are measured experimentally and compared with the effective properties obtained from the model employing mixing rules formulation (parallel wiring of MFC laminates). A good agreement is seen between the theoretical predictions and the experimental results. In addition, the results are well consistent with the empirical estimates given by Cacan and Erturk [142] for standard MFCs. In this way the mixing rules-based effective electroelastic, elastic, and dielectric properties of the MFCs are successfully bridged with the global electroelastic dynamics of the MFC laminates for energy harvesting and actuation.

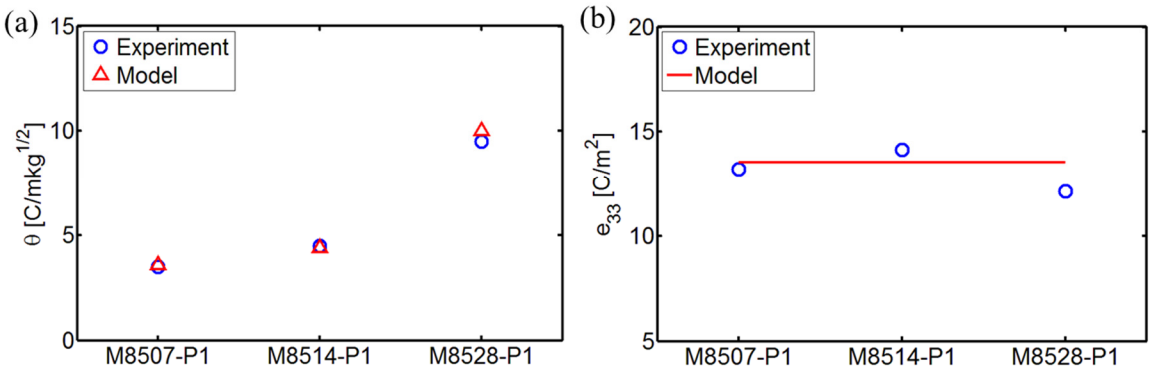

Figure 2.8. Experimental and analytical results for (a) modal electromechanical coupling term, θ, and (b) effective piezoelectric constant, e_{33} for MFC bimorph (parallel wiring of MFC laminates).

2.4 Summary and Conclusions

In this chapter, high-fidelity electroelastic modeling of 33-mode MFC bimorphs has been presented for resonant sensing, actuation, and energy harvesting applications. The piezoelectric fiber-based MFCs employ interdigitated electrode structure. Homogenized electromechanical constitutive properties are obtained using mixing rules formulation and then coupled with the distributed-parameter electroelastic model to obtain the global electroelastic parameters of MFCs with different aspect ratios. The parameters (such as modal electromechanical coupling term) obtained from theoretical analysis are compared with the experimentally identified parameters following a thorough analysis. Consistent results and very good predictions are obtained for samples of different active width values. The analytical modal electromechanical coupling terms are shown to depend directly on the width of the sample, yielding identical piezoelectric constants when normalized with respect to width. The modeling framework given in this chapter successfully connects mixing rules formulation with the continuum homogenized electroelastic dynamics for a variety of

applications of MFCs, such as underwater vibration energy harvesting and actuation as discussed in the next chapters.

3 UNDERWATER VIBRATION ENERGY HARVESTING USING MACRO-FIBER COMPOSITES

3.1 Introduction

Low-power electronic systems are used in various underwater applications ranging from naval sensor networks to ecological monitoring for sustainability. In the present chapter, underwater base excitation of bimorph cantilevers made of MFC piezoelectric structures are explored experimentally and theoretically to harvest energy for such wireless electronic components toward enabling self-powered underwater systems. Bimorph cantilevers made of MFCs with different length-to-width ratios and same thickness are tested in air and under water to characterize the change in natural frequency and damping ratio with a focus on the first two bending modes (since Erturk and Delporte [21] showed the favorable potential of the second vibration mode experimentally). A distributed-parameter electrohydroelastic model is developed by incorporating Morison's hydrodynamic equation added to the electroelastic in-air energy harvesting model given in Chapter 2. To this end, first the inertia and drag coefficients in Morison's equation are identified from an experiment conducted for underwater base-excited clamped aluminum beams of similar aspect ratios to explore the repeatability of the inertia and drag coefficients in Morison's equation. The variations of experimentally extracted hydrodynamic coefficients with aspect ratio are shown and compared with the results reported in the literature. The dependence of hydrodynamic coefficients on the aspect ratio is investigated. Finally, variations of the electrical power output with excitation frequency and load resistance are obtained for different length-to-width ratios. Additionally, nonlinear dependence of the output power density to the aspect ratio is characterized theoretically and experimentally in the underwater base excitation

problem. Electrode segmentation is studied as well for performance enhancement in the second bending mode.

3.2 Electrohydroelastic Modeling of MFC Bimorph Cantilevers

A schematic of the MFC bimorph for energy harvesting from base excitation in a quiescent fluid domain is shown in Figure 3.1. The in-air energy harvesting analysis of MFCs has been thoroughly covered in Chapter 2. The key concepts will be developed and applied later in this chapter.

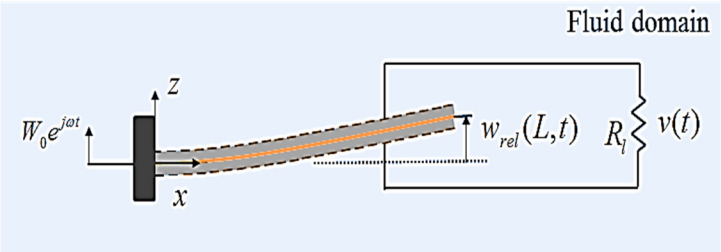

Figure 3.1. Schematic of a cantilevered MFC bimorph under transverse base excitation submerged in an unbounded quiescent fluid domain (air or water).

Electrohydroelastically coupled equations for dynamics of underwater base excitation of MFC cantilever can be obtained as

$$D\frac{\partial^4 w_{rel}(x,t)}{\partial x^4}+c_\alpha\frac{\partial^5 w_{rel}(x,t)}{\partial x^4\partial t}+c_\beta\frac{\partial w_{rel}(x,t)}{\partial t}+m_s\frac{\partial^2 w_{rel}(x,t)}{\partial t^2}+\Gamma(x,t) \\ -\vartheta v(t)\left[\frac{d\delta(x)}{dx}-\frac{d\delta(x-L)}{dx}\right]=-m_s\frac{\partial^2 w_b(x,t)}{\partial t^2} \tag{3.1}$$

$$C_p \frac{dv(t)}{dt} + \frac{v(t)}{R_l} + \vartheta \int_0^L \frac{\partial^3 w_{rel}(x,t)}{\partial x^2 \partial t} dx = 0 \tag{3.2}$$

where $w_{rel}(x,t)$ is the relative transverse displacement (in *z*-direction), $w_b(t)$ is the transverse base displacement, $v(t)$ is the voltage across the electrical load, *D* is the bending stiffness of the composite cross section, c_α is the stiffness-proportional structural damping coefficient, c_β is the mass-proportional structural damping coefficient, m_s is the mass per unit length of the beam, *L* is the overhang length, ϑ is the electromechanical coupling term, C_p is the capacitance of the bimorph, R_l is the resistive load across the device, and $\delta(x)$ is the Dirac delta function. Moreover, $\Gamma(x,t)$ is the hydrodynamic loading of the surrounding fluid per unit length and it is expressed by Morison's equation [29, 60-63] as follows:

$$\Gamma(x,t) = \frac{\pi}{4}\rho_w b^2 c_m \left[\frac{\partial^2 w_{rel}(x,t)}{\partial t^2} + \frac{\partial^2 w_b(t)}{\partial t^2}\right] + \frac{1}{2}\rho_w b c_d \left[\frac{\partial w_{rel}(x,t)}{\partial t} + \frac{\partial w_b(t)}{\partial t}\right]\left|\frac{\partial w_{rel}(x,t)}{\partial t} + \frac{\partial w_b(t)}{\partial t}\right| \tag{3.3}$$

where ρ_w is the mass density of water and b is the overall width of the bimorph. Moreover, c_m and c_d are the inertia and drag coefficients, respectively, which depend on the aspect ratio, $(\psi = L/b)$, and to be determined experimentally. Clearly, the damping component in Morison's equation introduces quadratic nonlinearity (different from the classical linearized hydrodynamic function presented by Sader [45]), therefore vibration modes need to be explored separately. The structural (geometric and electroelastic) behavior is assumed to be linear.

Assuming well-separated modes, i.e. no modal interaction, the transverse deflection of the reference surface at position *x* and time *t* for mode *r* is

$$w_{rel}(x,t) \cong \sum_{r=1}^{\infty} \phi_r(x)\eta_r(t) \tag{3.4}$$

where $\phi_r(x)$ and $\eta_r(t)$ are the mode shape (obtained from the corresponding linear *in vacu*o problem) and the generalized modal coordinate, respectively. Substituting w_{rel} into Equations (3.1) and (3.2), multiplying by the mass normalized eigenfunction $\phi_s(x)$, integrating over the length of the beam and applying the orthogonality conditions [75] one obtains (see Equations (2.18) to (2.21)).

$$(1+\mu_r)\ddot{\eta}_r(t) + (2\zeta_r\omega_r + \tau_r)\dot{\eta}_r(t) + \omega_r^2\eta_r(t) + \beta_r - \theta_r v(t) = F_r \tag{3.5}$$

$$C^{eq}\dot{v}(t) + \frac{v(t)}{R_l} + \theta_r\dot{\eta}_r(t) = 0 \tag{3.6}$$

where

$$\omega_r = \lambda_r^2\sqrt{D/m_sL^4} \tag{3.7}$$

is the *in vacuo* undamped natural frequency (λ_r is the eigenvalue of the *r*th mode obtained from the characteristic equation [1]), $\theta_r = \vartheta\left[d\phi_r(x)/dx\right]_{x=L}$ is the modal electromechanical term, $\mu_r = (\pi/4)(\rho_w b^2 c_{mr}/m_s)$ is the dimensionless added mass term, ζ_r is the modal mechanical damping ratio due to internal mechanical losses, C^{eq} is the equivalent capacitance of the bimorph cantilever, $F_r = \left(-m_s - m_s\mu_r\right)\ddot{w}_b(t)\int_0^L \phi_r(x)dx$ is the modal mechanical forcing function, $\tau_r = (1/2)\rho_w b c_{dr}\int_0^L \phi_r^2(x)\left|\dot{\eta}_r(t)\phi_r(x) + \dot{w}_b(t)\right|dx$ defines the

hydrodynamic damping associated with the transverse beam deflection and $\beta_r = (1/2)\rho_w b c_{dr} \dot{w}_b(t) \int_0^L \phi_r(x) \left| \dot{\eta}_r(t) \phi_r(x) + \dot{w}_b(t) \right| dx$ contributes to the hydrodynamic damping related to rigid body motion imposed to base excitation [29]. Here c_{mr} and c_{dr} are the inertia and drag coefficients for *r*th vibration mode. An over-dot represents differentiation with respect to time. It should be noted that, the modal electromechanical coupling and equivalent capacitance depend on the way the MFC laminates are wired [1] (see Section 2.2.4) . Solving Equations (3.6) and (3.7) for steady-state behavior gives the vibration and voltage FRFs of the base-excited bimorph. The results in the following are based on the numerical solution of Equations (3.5) and (3.6). In the present analysis, the electromechanical coupling in physical coordinates (ϑ) is obtained by using mixing rules [148, 149] formulation (see Section 2.2.4).

3.3 Experimental Results and Model Validation

Eight aluminum strips (Figure 3.2a) are tested in air (Figure 3.2b) and under water (Figure 3.2c) through base-excitation experiments performed for a frequency range which captures resonance frequencies of the strips for the first two bending modes. Three MFC bimorphs shown in Figure 3.3a are tested and characterized in air (Figure 3.3b) and under water (Figure 3.3c) using the clamps employed for in-air actuation FRF measurements. Each bimorph is made of two identical custom-made MFC laminates (hydrophobic due to polyester electrode sheets) labeled as M8507-P1, M8514-P1 and M8528-P1 (Figure 3.3a) by Smart Material Corp. [17].

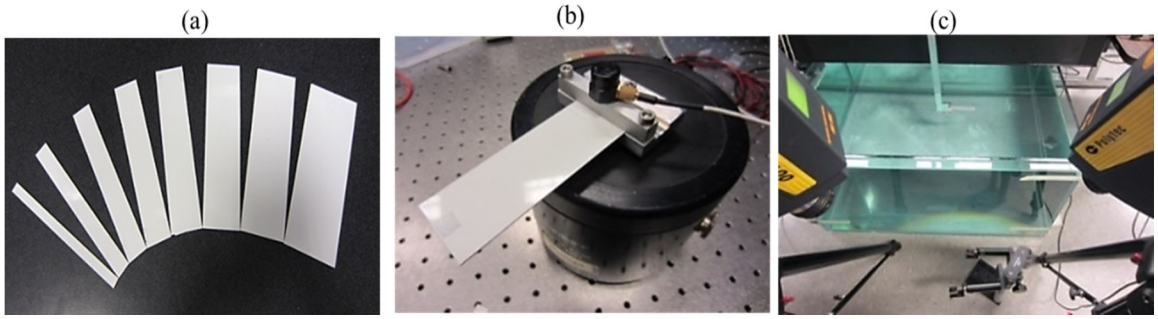

Figure 3.2. In-air and underwater base excitation tests for parameter identification: (a) Aluminum strips with different aspect ratios and same length (L = 89 mm), (b) close-up view of an aluminum cantilever mounted on the electromechanical shaker, and (c) underwater excitation of an aluminum cantilever

The electrode leads of the MFC bimorphs are connected in parallel throughout the experiments discussed in this chapter. The bimorphs are cantilevered in aluminum clamps with the basic geometry and structural properties given in Table 3.1.

Table 3.1: Geometric and structural properties of the MFC bimorphs (L: overhang length, b: width, h: total thickness, m_s: structural mass per length)

	L (mm) [active*, overall]	b (mm) [active, overall]	h (mm)	m_s (kg m^{-1})
M8507-P1	[75.5, 83.5]	[7, 16.5]	0.61	0.028
M8514-P1	[75.5, 83.5]	[14, 21.5]	0.61	0.045
M8528-P1	[75.5, 88.5]	[28, 43.5]	0.61	0.090

* Active length and width define the portions which are covered with piezoelectric material.

Both in-air and underwater energy harvesting (Figure 3.3b and Figure 3.3c) data are analyzed using a Spectral Dynamics SigLab data acquisition device. The absolute velocity at the tip of the bimorph is measured by an LDV (Polytec, PDV 100) thorough a small mirror that makes a 45^0 angle with horizontal plane. For in-air experiment, data acquisition device receives base acceleration from Kistler accelerometer with a Kistler signal conditioner. Harmonic excitation with 10 averages is applied to a B&K electromechanical shaker through an HP power amplifier/supply for base excitation over a range of frequencies covering the two fundamental bending modes.

For underwater experiments, the clamped bimorphs are mounted on an APS-113 long-stroke shaker connected to an APS-125 amplifier. In Figure 3.3c, an LDV is used for obtaining the base velocity whereas the other one is used to measure the absolute tip velocity of the bimorphs. Note that, the laser signal amplitude is divided by the refractive index of water (n = 1.333) in the underwater experiments [21, 22, 75].

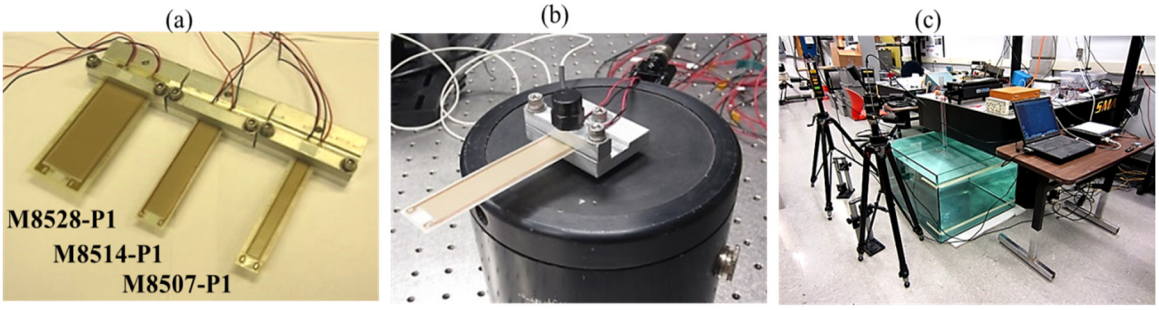

Figure 3.3. (a) MFC bimorphs in aluminum clamps, (b) close-up view of an M8514-P1 type bimorph cantilever mounted on electromechanical shaker with an accelerometer and (c) experimental setup for underwater base excitation experiments.

3.3.1 In-air and underwater velocity FRFs for aluminum strips

A sample velocity FRF for in-air base excitation experiments is shown in Figure 3.4. Good agreement between the experimental results and analytical model validates the approach and is used for parameter identification (given in Table 3. 2). Bending stiffness, *D*, is first identified by using the experimental fundamental resonance frequency of the bimorph, f_1, and then *D* is used in in the natural frequency equation ($\omega_r = \lambda_r^2 \sqrt{D / m_s L^4}$) to obtain the second resonance frequency, f_2 (λ_1 and λ_2 are given as 1.875 and 4.694, respectively). Comparing the experimental and analytical second resonance frequencies shows less than 4% error. Structural damping ratios for the first and second mode (ζ_1 and ζ_2) are obtained by using the half-power-point method [150]. In Figure 3.4, the low-amplitude peak around 220 Hz is the resonance frequency of the clamp that is attached to the shaker with a screw. This is verified very easily (not shown here) by pointing the laser vibrometer at the clamp.

Having validated the analytical model results for in-air aluminum vibration and having identified the resonance frequencies and damping ratios, the case studies for aluminum samples are analyzed for underwater excitation using Morison's hydrodynamic function.

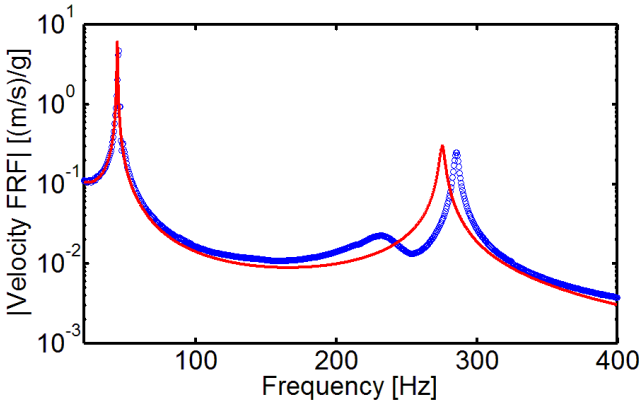

Figure 3.4. Experimental and analytical in-air tip velocity FRFs of aluminum cantilever with $(\psi = 2.1)$ for the first two bending modes.

Table 3. 2. Experimentally identified parameters of aluminum strips from in-air experiments.

L/b	f_1^{air} (Hz)	f_2^{air} (Hz)	$\zeta_1(\%)$	$\zeta_2(\%)$
14.5	46	281.7	0.5	0.7
8	44.5	286.4	0.4	0.7
5.5	44.7	295.5	0.5	0.8
4.2	44.7	286	0.5	0.7
3.4	44	279.5	0.4	0.6
2.8	44.5	283.3	0.5	0.7
2.5	44	281.8	0.5	0.6
2.1	44	292.3	0.6	0.8

As displayed in Figure 3.2c, each strip is submerged in quiescent water along with the same aluminum clamp used for in-air experiment. Figure 3.5 shows the tip velocity FRFs for a frequency range of 8-130Hz which captures underwater resonance frequency of the aluminum strips for the first two vibration modes. For brevity, the remaining samples are not graphically presented here.

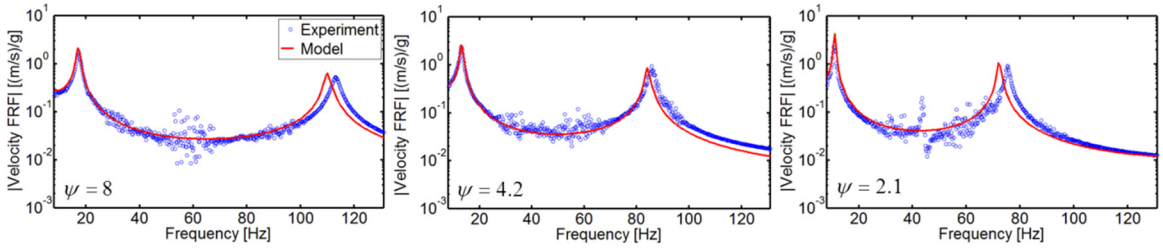

Figure 3.5. Experimental and analytical underwater tip velocity FRFs for cantilevered aluminum samples (solid red lines represent model predictions and blue dots represent experimental data).

3.3.2 *In-air and underwater voltage, velocity, and power output FRFs*

Resistor sweep in-air energy harvesting tests are conducted for three MFC bimorphs (Figure 3.3a) to measure voltage and velocity FRFs (shown in Figure 3.6 to Figure 3.8). The electrical load resistance values range from $100\,\Omega$ (close to short-circuit condition) to $9\,\mathrm{M}\Omega$ (close to open-circuit condition) are considered as $R_l = [100\,\Omega, 1\mathrm{k}\Omega, 10\,\mathrm{k}\Omega, 99\mathrm{k}\Omega, 0.9\,\mathrm{M}\Omega, 5\,\mathrm{M}\Omega$, and $9\,\mathrm{M}\Omega]$. In the voltage output plots it is observed that, with increasing load resistance, voltage magnitude increases uniformly and the resonance frequency shifts from the short-circuit resonance frequency to its open-circuit counterpart. From the velocity plots, one can see, with increasing load resistance the peak vibration amplitude decreases considerably from the peak of short-circuit condition to a certain value and then is amplified at the open-circuit resonance frequency. These observed behaviors are consistent with the results obtained in Section 2.3.2 for the energy harvesting tests. The identified parameters from in-air experiments are summarized in Table 3.3.

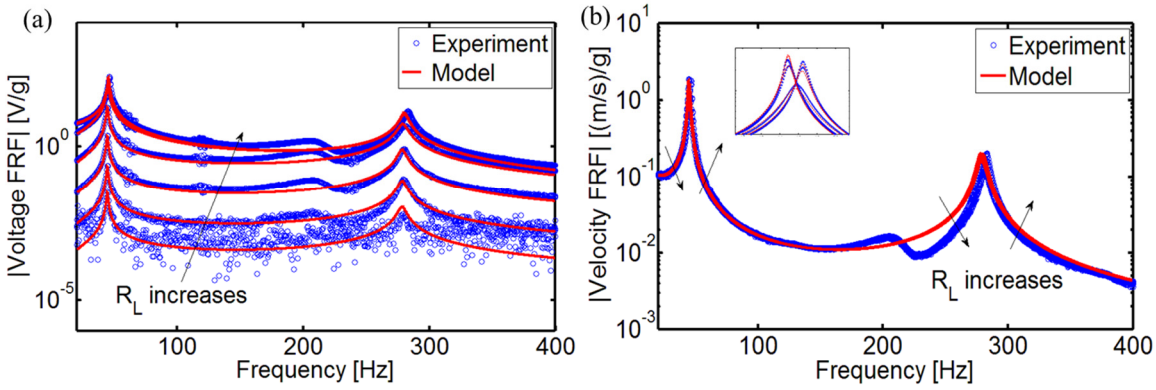

Figure 3.6. In-air experimental and analytical frequency response results; (a) Voltage FRFs and (b) tip velocity FRFs for a set of resistors for cantilevered M8507-P1 ($\psi = 5.1$).

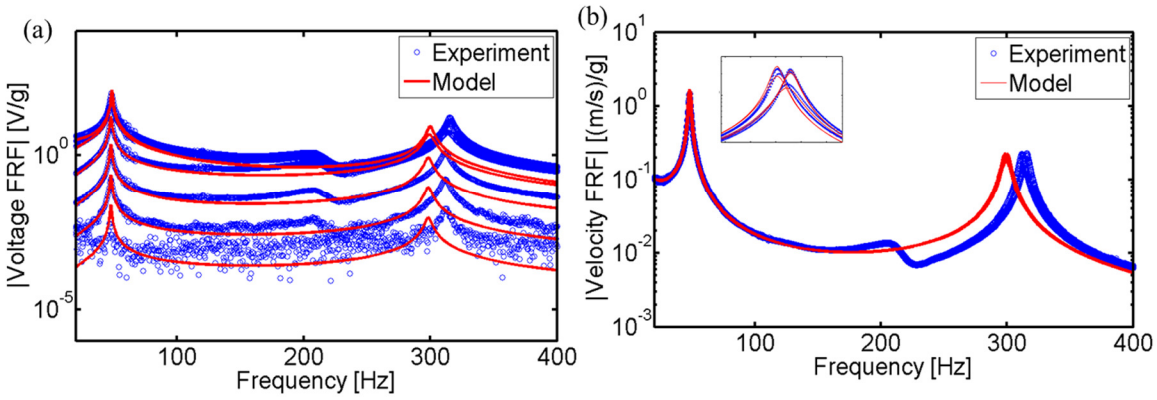

Figure 3.7. In-air experimental and analytical frequency response results; (a) Voltage FRFs and (b) tip velocity FRFs for a set of resistors for cantilevered M8514-P1 ($\psi = 3.9$).

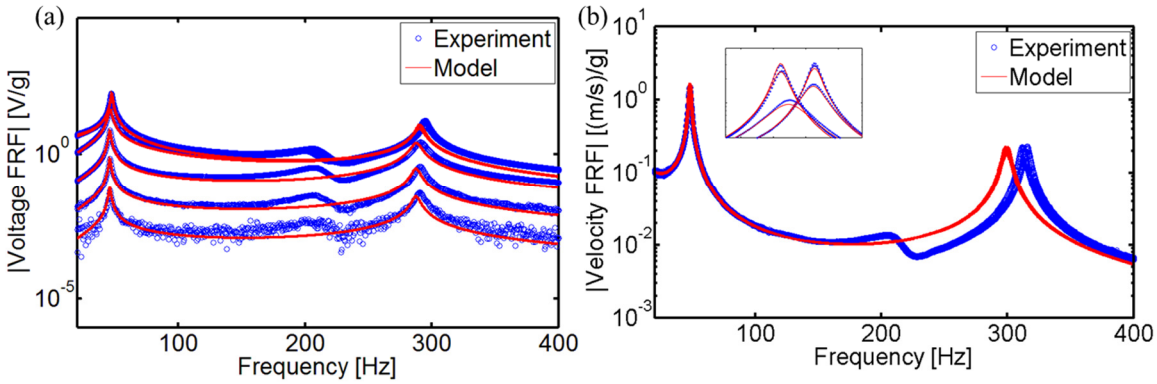

Figure 3.8. In-air experimental and analytical frequency response results; (a) Voltage FRFs and (b) tip velocity FRFs for a set of resistors for cantilevered M8528-P1 ($\psi = 2.1$).

After validating the analytical model results for in-air bimorph vibration and having identified the parameters, three MFC case studies are tested and analyzed for underwater base excitation. Seven electrical resistive loads are considered ($100\,\Omega$ to $9\,\mathrm{M}\Omega$) in the experiments. As the load resistance is increased, the resonance frequency shifts from the short-circuit resonance frequency to the open-circuit resonance frequency. Comparing the in-air and underwater experimental and analytical results, the decrease in the resonance frequencies and increase in the damping ratios are obvious. These changes are due to the

hydrodynamic fluid effects (added mass and nonlinear hydrodynamic damping) and consistent with the results given in the literature. In-air and underwater energy harvesting experimental FRFs are correlated with model simulations based on purely experimental parameters (plots are given in Appendix, Figure A and Figure B) for accurate identification of the first and second mode inertia and drag coefficients. These drag and inertia coefficients when used in the semi-empirical electrohydroelastic Euler-Bernoulli-Morison model result in the underwater FRF predictions given in Figure 3.9-Figure 3.11.

Table 3.3. Identified parameters from in-air experiments.

	M8507-P1	M8514-P1	M8528-P1
f_1 (Hz)	44.7	47.9	46.4
f_2 (Hz)*	[279.3 280.1]	[309.8 300.2]	[289.2 290.8]
D (N m^2)	0.0058	0.0107	0.0201
ζ_1, ζ_2 (%)	1.8, 1.5	2, 1.5	1.5, 1.2
ϑ [10^{-6} Nm V^{-1}]	4.53	6.89	22.73
C^{eq} (nF)	3.8	5.5	17.5

*f_2 is given in the form of [experimental analytical]

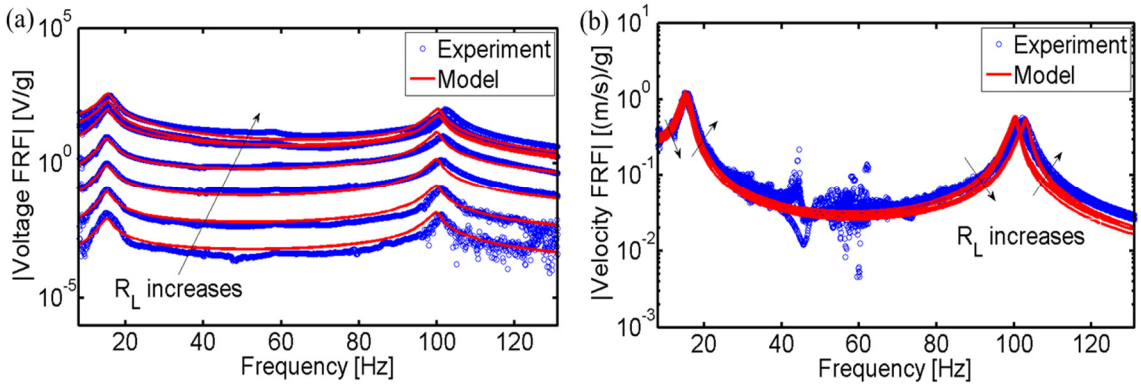

Figure 3. 9. Underwater experimental and analytical frequency response results; (a) Voltage FRFs and (b) tip velocity FRFs for a set of resistors for cantilevered M8507-P1 ($\psi = 5.1$).

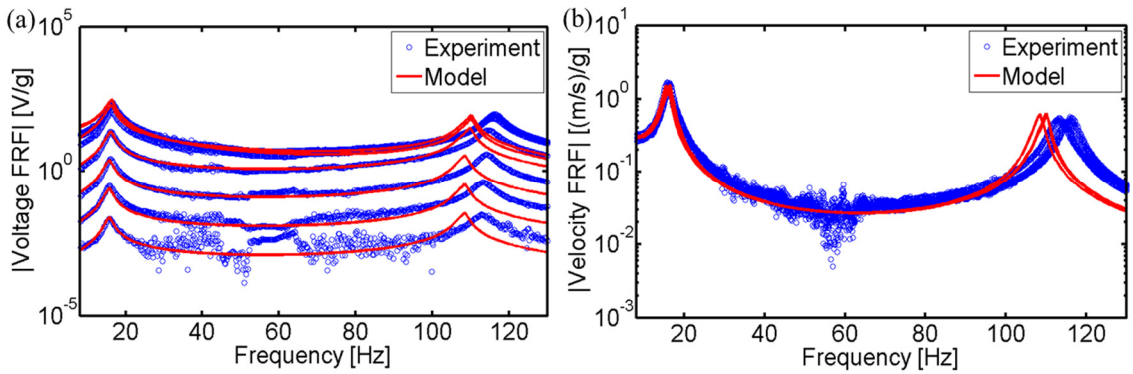

Figure 3.10. Underwater experimental and analytical frequency response results; (a) Voltage FRFs and (b) tip velocity FRFs for a set of resistors for cantilevered M8514-P1 ($\psi = 3.9$).

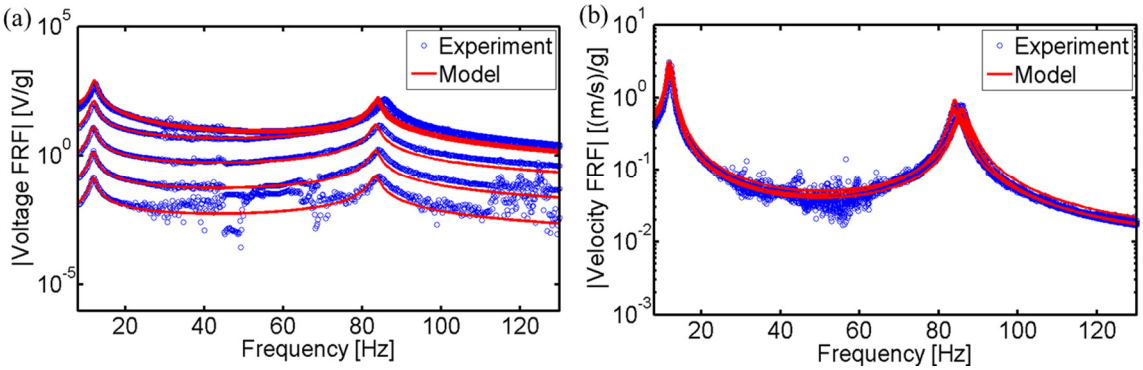

Figure 3.11. Underwater experimental and analytical frequency response results; (a) Voltage FRFs and (b) tip velocity FRFs for a set of resistors for cantilevered M8514-P1 ($\psi = 2.1$).

Theoretical in-air and underwater power output vs. load resistance and frequency diagrams are displayed in Figure 3.12 and Figure 3.13 for three MFC bimorphs. The power density plots reveal that the maximum values of power are delivered to the optimum electrical load of $0.9\text{M}\Omega$ (among the set of resistors used in the tests) at the fundamental resonances frequencies of three bimorphs. According to these graphs, for M8507-P1, M8514-P1, and M8528-P1 bimorphs, the maximum power output of about 5.1, 8.5, and 17.1 mW/g^2 are obtained for in-air test whereas the maximum power output of about 46.4, 73.9, and 355.3 mW/g^2 are delivered for underwater experiment, respectively. It is important to

note that, in these plots the active and overall widths are used for in-air and underwater experiments, respectively. In-air power output grows linearly with increased width, i.e. power density does not depend on the aspect ratio since fluid effects are negligible for small in-air oscillations. For underwater base excitation, the output power increases nonlinearly with increased width (for the same base acceleration level).

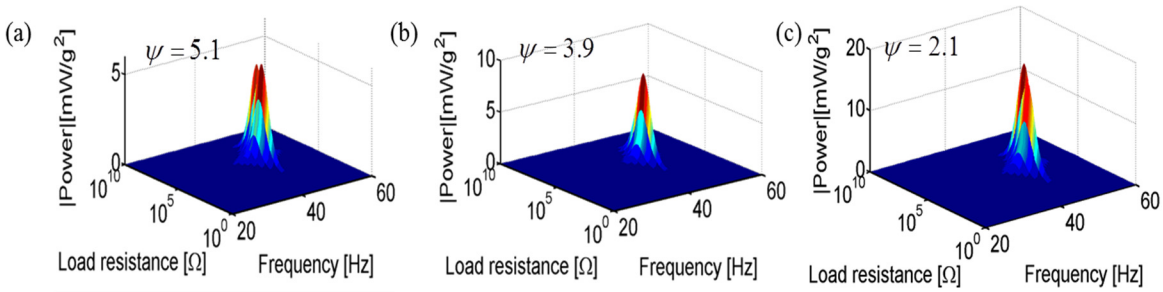

Figure 3.12. In-air simulated power output vs. load resistance and frequency diagrams focusing on the fundamental vibration mode of the (a) M8507-P1, (b) M8514-P1and (c) M8528-P1 bimorph.

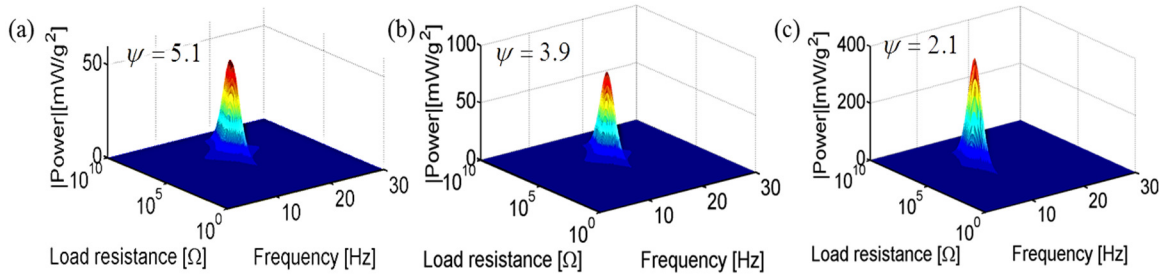

Figure 3.13. Underwater simulated power output vs. load resistance and frequency diagrams focusing on the fundamental vibration mode of the (a) M8507-P1, (b) M8514-P1and (c) M8528-P1 bimorph.

The output power density with respect to aspect ratio is characterized theoretically for the in-air and underwater base excitation problems in Figure 3.14. With increasing aspect

ratio, the power density decreases nonlinearly (due to nonlinear fluid damping effects) for the same base acceleration input to fully submerge cantilevers.

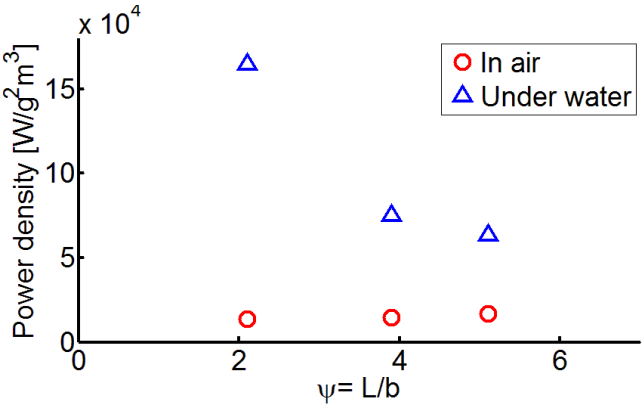

Figure 3.14. Theoretical in-air and underwater power output density (per base acceleration squared) for three MFC bimorphs.

3.3.3 Identification of hydrodynamic inertia and drag coefficients

Figure 3.15 displays the identified hydrodynamic inertia and drag coefficients focusing on the first two bending modes for both aluminum and MFC cantilevers with different aspect ratios. The identified c_m and c_d values exhibit convergence to certain values (with increased length-to-width aspect ratio), in good agreement with experimental and numerical observations presented in the relevant literatures [29, 59]. It is observed that the inertia and drag coefficients show asymptotic behavior for ψ greater than approximately 5, making inertia and drag coefficients insensitive to ψ (cases of ψ smaller than 5 are very sensitive to aspect ratio). Specifically, in Figure 3.15a and Figure 3.15b, $c_m(\psi)$ value converges to unity (for large ψ) in agreement with the predictions of classical flow solutions based on two dimensional fluid-structure problem in which the linear hydrodynamic forces are dominant. In Figure 3.15c and d, $c_d(\psi)$ converges to approximately 21 and 125 for the first

and second vibration modes, respectively, consistent with the range of experimental and numerical observations summarized in Figure 11 of Kopman and Porfiri [59]. In addition to the smooth trend and converging behavior with increased aspect ratio for the aluminum cantilevers, the agreement of the MFC and aluminum cantilever results for both modes is remarkable.

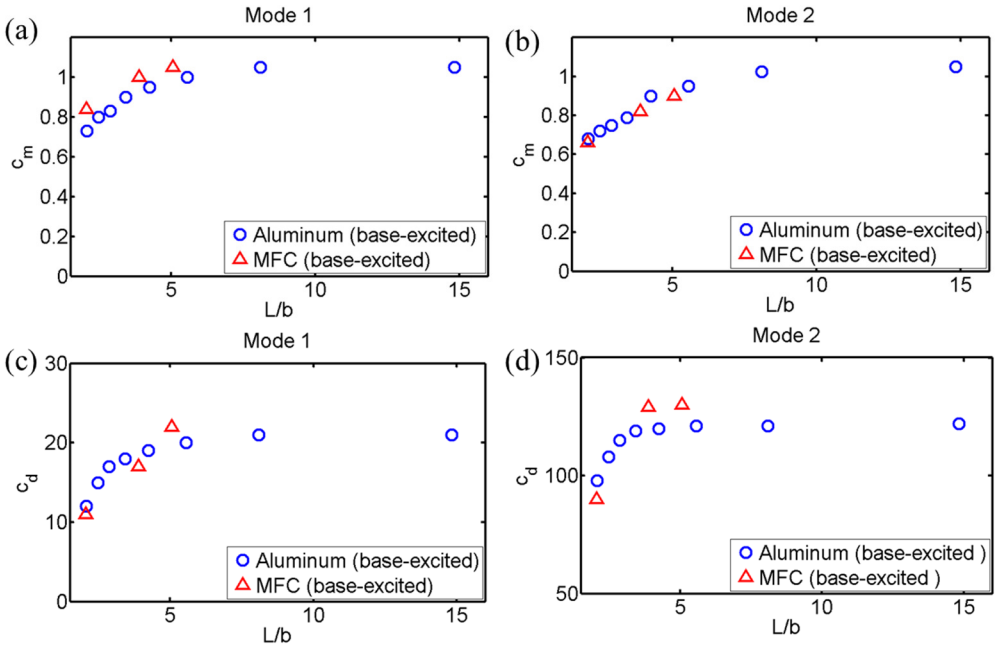

Figure 3.15. Hydrodynamic inertia coefficient (c_m) vs. aspect ratio for (a) mode 1 and (b) mode 2; Hydrodynamic drag coefficient (c_d) vs. aspect ratio for (c) mode 1 and (d) mode 2.

3.4 Electrode Segmentation for Broadband Performance Enhancement in Second Bending Mode

The results for the second bending mode in Section 3.3.2 are sub-optimal due to cancellations of power output in *strain node* resulting from the mode shape of second vibration mode. This phenomenon is related to the strain distribution over the length of the bimorph. The second bending mode of a cantilever has a *strain node* (i.e. inflection point

where the curvature changes sign) near the root [65] where cancellation of electrical outputs in harvesting energy occurs in case of using continuous electrodes at the strain node location. Therefore, it is required to apply electrode segmentation to eliminate the cancellation so that second bending mode can be used effectively in electrical power generations. In the following sections, experimental electrode segmentation is implemented for performance enhancement in the second bending mode.

3.4.1 Experimental setup

A segmented bimorph sample is fabricated using a 0.127 mm thick aluminum sheet as the substrate material and MFCs as the active material (M2814-P1 and M8514-P1 from Smart Material Corporation [17]). The MFC layers (single laminates are shown in Figure 3.16) are bonded onto both faces of the aluminum substructure using high-shear strength epoxy (3M DP460) in a vacuum bonding process. As it is shown in Figure 3.16, the length and width of aluminum substrate is extended outside the active region giving the total width and length for, 39.5 mm and 159.2 mm respectively. M2814-P and M8514-P1 have an active region of 28 mm x 14 mm and 85 mm x 14 mm and thickness of 0.30 mm. The clamped-free capacitances of MFCs are measured as 1.5 nF and 3.5 nF. The two MFC laminates in the top view (Figure 3.16a) from right to left side are labeled as MFC1 and MFC2 while the two MFCs in the bottom are labeled as MFC3 and MFC4, respectively (MFC1 and MFC3 are M2814-P1 and MFC2 and MFC4 are M8514-P1). Parallel connection is employed throughout the experiments in this section. The positions of velocity measurement are denoted by A and B (covered with reflective tape) in Figure 3.16b. The focus of this work is on the energy harvesting performance of the segmented MFC bimorph. Figure 3.17a shows

the base-excitation setup for harvesting energy from the two bending modes of the sample underwater. The segmented bimorph is cantilevered in an aluminum clamp. The clamped bimorph is mounted on an APS-113 long-stroke shaker connected to an APS-125 amplifier. In Figure 3.17a, an LDV (Polytec, PDV 100) is used for obtaining the base velocity at point B, while another LDV (Polytec, PDV 100) is used to measure the absolute velocity of the bimorph at point A. The tests are conducted for nine load resistance values ranging from 100 $\mathrm{k}\Omega$ to $10\,\mathrm{M}\Omega$. During the experiments, low to moderately high intensity mechanical excitation are applied in energy harvesting. The voltage across the cantilever electrodes are shunted to a load resistance box (IET Labs, Inc. RS-201W). Data is collected using National Instruments NI 9223 data acquisition unit. Low intensity chirp excitation is used in the experiments where linear behavior is expected. During nonlinear tests, forward and reverse frequency sweeps at constant base acceleration amplitude ($0.1g$ RMS) are conducted using a vibration control system (APS Dynamics, Inc. VCS201).

For excitation at the fundamental natural frequency (approximately 2.5 Hz), the dynamic strain distribution in MFC1 and MFC2 (the same for MFC3 and MFC4) is expected to be in phase throughout its length since the first mode has no strain nodes. For excitation at the second natural frequency (about 19.5 Hz), the voltage outputs of MFC1 and MFC2 (the same for MFC3 and MFC4) are 180 degree out of phase with each other where the voltage cancellation occurs.

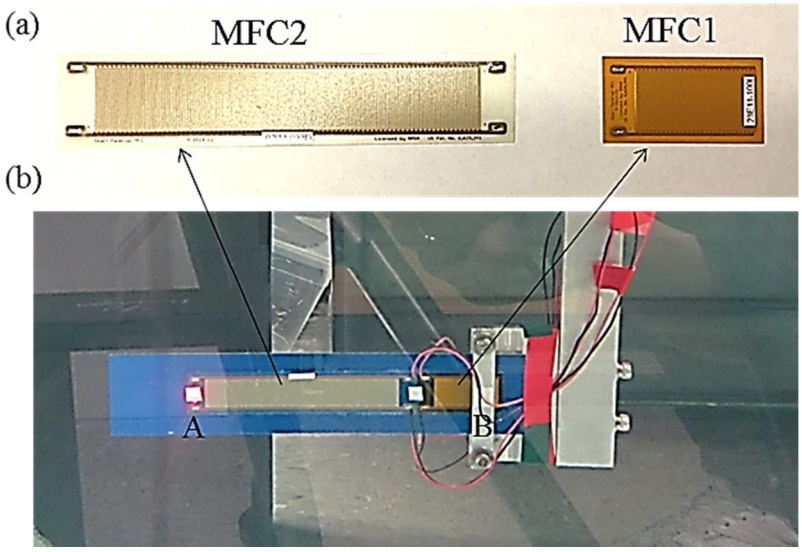

Figure 3.16. (a) MFC laminates (M8514-P1 (left side) and M2814-P1 (right side) and segmented MFC bimorph in aluminum clamp.

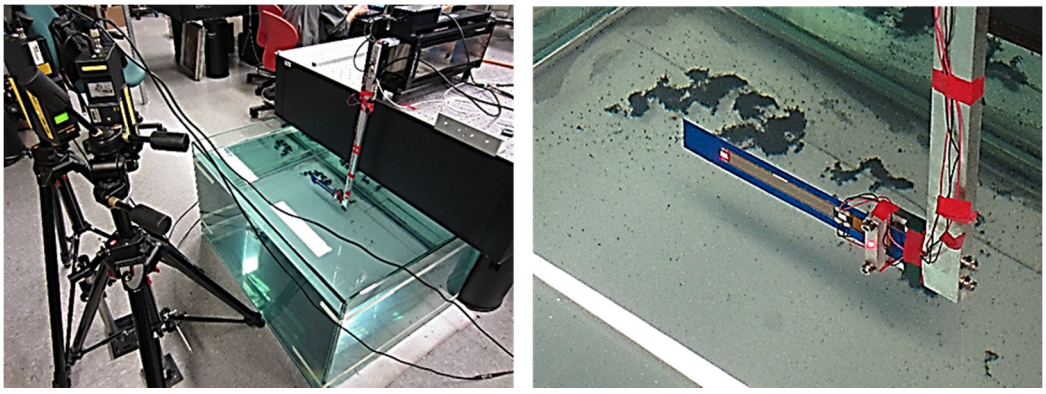

Figure 3.17. (a) Experimental setup for underwater base excitation experiments and (b) close-up view for underwater testing of the segmented MFC bimorph sample.

To compensate voltage cancellation in second mode excitation (where the second mode is dominating), the wires are connected as demonstrated in the diagram shown in Figure 3.18: Two cases considered in the schematic are referred as in-phase and out-of-phase wiring hereafter. In-phase wiring: For the first mode excitation (where dynamic strain and voltage

output are in phase throughout the length of the beam) the voltage output from MFC1 and MFC2 (the same for MFC3 and MFC4) are in phase whereas for the second mode excitation (where dynamic strain and voltage output change the phase at the strain node near root) the voltage output from MFC1 and MFC2 (the same for MFC3 and MFC4) are out of phase (cancellation is happening). Out-of-phase wiring: For the first mode excitation, voltage output from MFC1 and MFC2 (the same for MFC3 and MFC4) are out of phase whereas for the second mode excitation, voltage output from MFC1 and MFC2 (the same for MFC3 and MFC4) are in phase (cancellation is avoided).

It is worth adding that (as explained in [65]), the summed voltage response of MFC3 and MFC4 is 180 degree out of phase with that of MFC1 and MFC2 since the lower face of cantilever bimorph is in tension when the upper face is in compression, and vice versa.

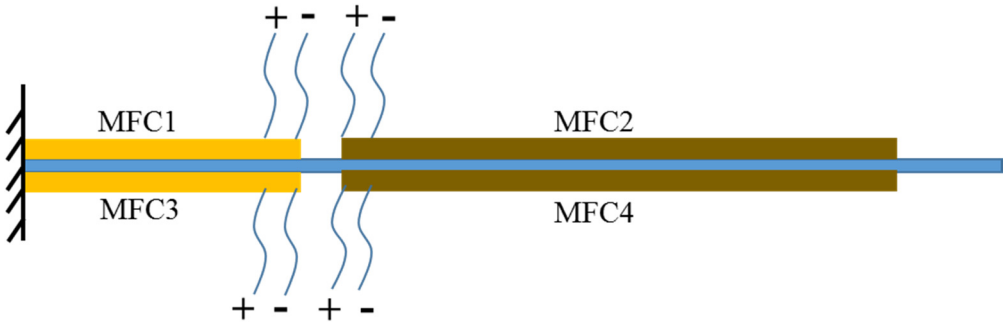

In-phase wiring	$MFC1^{+}$ $MFC2^{+}$ $MFC3^{-}$ $MFC4^{-}$	$MFC1^{-}$ $MFC2^{-}$ $MFC3^{+}$ $MFC4^{+}$
Out-of-phase wiring	$MFC1^{+}$ $MFC2^{-}$ $MFC3^{-}$ $MFC4^{+}$	$MFC1^{-}$ $MFC2^{+}$ $MFC3^{+}$ $MFC4^{+}$

Figure 3.18. Diagram of wiring configuration for segmented electrode demonstration.

3.4.2 *Underwater velocity, voltage, and power output FRFs: Linear response for low intensity excitation*

Velocity (measured at point A) and voltage output per base acceleration FRFs (where *g* stands for gravitational acceleration) for underwater energy harvesting experiments on the segmented MFC bimorph are shown in Figure 3.19 and Figure 3.21 for in-phase and out-of-phase wiring cases, respectively. The tests are conducted for a set of resistive loads between short- and open-circuit conditions and a broad range of frequencies which cover the first two transverse vibration modes. The electrical load resistance values range from 100 kΩ (close to short-circuit condition) to 10 MΩ (close to open-circuit condition) are considered. In agreement with well-suited in-air vibration-based piezoelectric bimorphs for energy harvesting [89], the plots show that as the load resistance is increased, the resonance frequency shifts from the short-circuit resonance frequency to its open-circuit counterpart. It is observed that by changing the load resistance from short- to open-circuit conditions, the voltage output increases uniformly and the resonance frequency for moderate resistive loads can take a value between the short- and open-circuit resonance frequencies. The experimental power output vs. load resistance and frequency diagrams are shown in Figure 3.20 and Figure 3.22 for in-phase and out-of-phase wiring cases, respectively. For the same mechanical excitation input, the results exhibit substantially increased power output for the out-of-phase case in the second vibration mode.

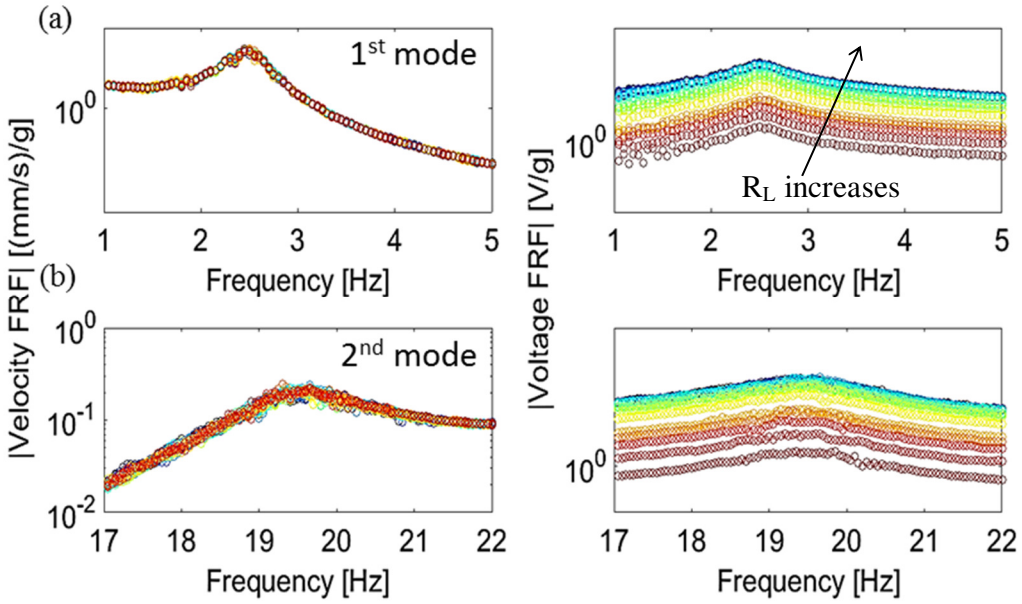

Figure 3.19. Experimental velocity (left side) and voltage (right side) frequency response results for the segmented MFC bimorph; (a) First and (b) second bending mode for in-phase wiring of the MFC laminates.

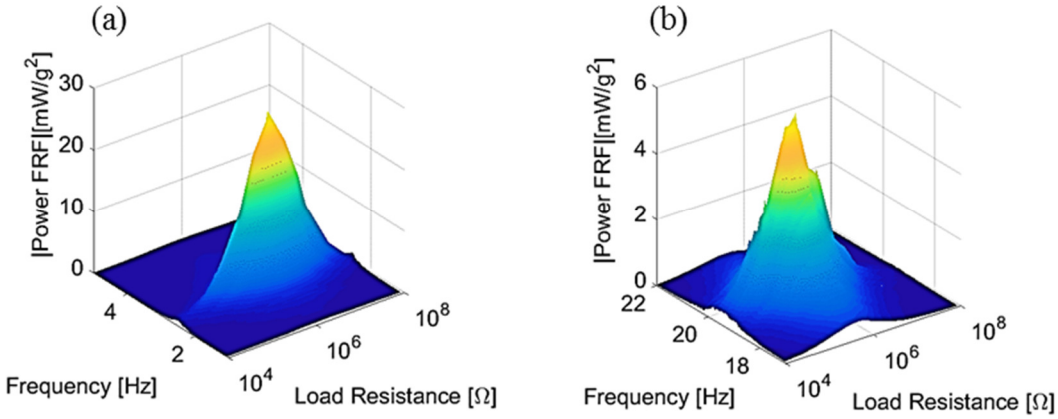

Figure 3.20. Experimental power output vs. load resistance and frequency diagrams focusing on the (a) first and (b) second vibration mode for in-phase wiring of the MFC laminates.

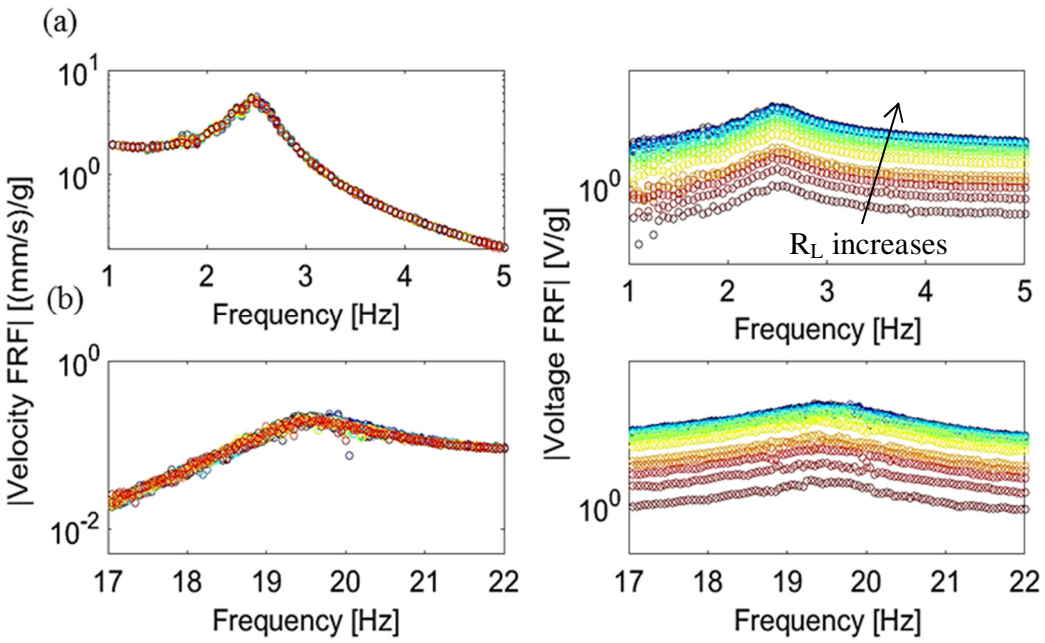

Figure 3.21. Experimental velocity (left side) and voltage (right side) frequency response results for the segmented MFC bimorph; (a) First and (b) second bending mode for out-of-phase wiring of the MFC laminates.

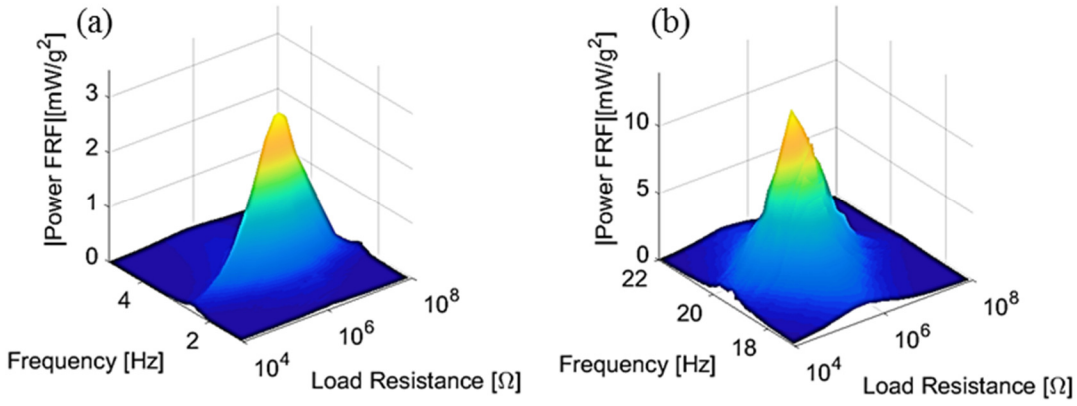

Figure 3.22. Experimental power output vs. load resistance and frequency diagrams focusing on the (a) first and (b) second vibration mode for out-of-phase wiring of the MFC laminates.

Variations of the average power output versus changing load resistance for excitations at the first (Figure 3.23a) and the second (Figure 3.23b) natural frequencies (2.2 Hz and 19.5 Hz, respectively) are shown for in-phase and out-of-phase wiring cases. The electrical power

output for excitation at the first mode is higher when the system is wired in phase. For the second mode excitation, power output is higher for the out-of-phase wiring case; Voltage amplitude of the preferable out-of-phase wiring is approximately 2.4 times greater than the amplitude of the voltage response for in-phase wiring case (where cancellation at strain node happens). Results in Figure 3.23 show that the proposed design of segmented MFC bimorph results in power enhancement in second vibration mode, successfully.

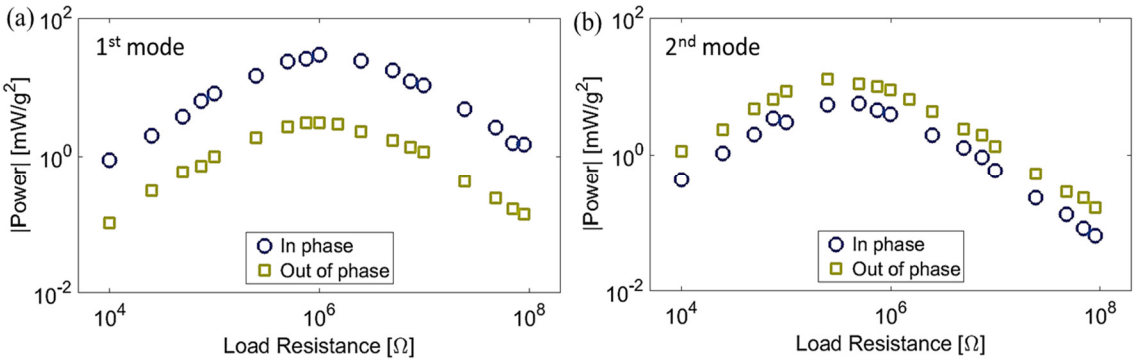

Figure 3.23. Power output versus load resistance for excitation at the (a) first (2.5 Hz) and (b) second (19.5 Hz) resonance frequency (comparing in-phase and out-of-phase cases).

3.4.3 Underwater velocity, voltage, and power output FRFs: Nonlinear response for moderately high intensity excitation

Resistor sweep energy harvesting tests are conducted at moderately high intensity base-excitation (0.1 *g* RMS base acceleration level) for in-phase and out-of-phase wiring cases. Figure 3.24 and Figure 3.26 show RMS velocity (measured at point B) and voltage output for the broad range of frequencies which cover the first two vibration modes. It should be noted that applying high intensity base excitation results in nonlinear response (nonlinear softening; shifting of resonance frequency to the left) of the bimorph due to the

electroelastic, geometric, and dissipative nonlinear effects. The electrical load resistance values range from 100 kΩ (close to short-circuit condition for these samples) to 10 MΩ (close to open-circuit condition) are considered. The average power output vs. load resistance and frequency diagrams are given in Figure 3.25 and Figure 3.27 for in-phase and out-of-phase cases, respectively. For the same mechanical input, the results exhibit substantially increased power output for out-of-phase case in the second vibration mode.

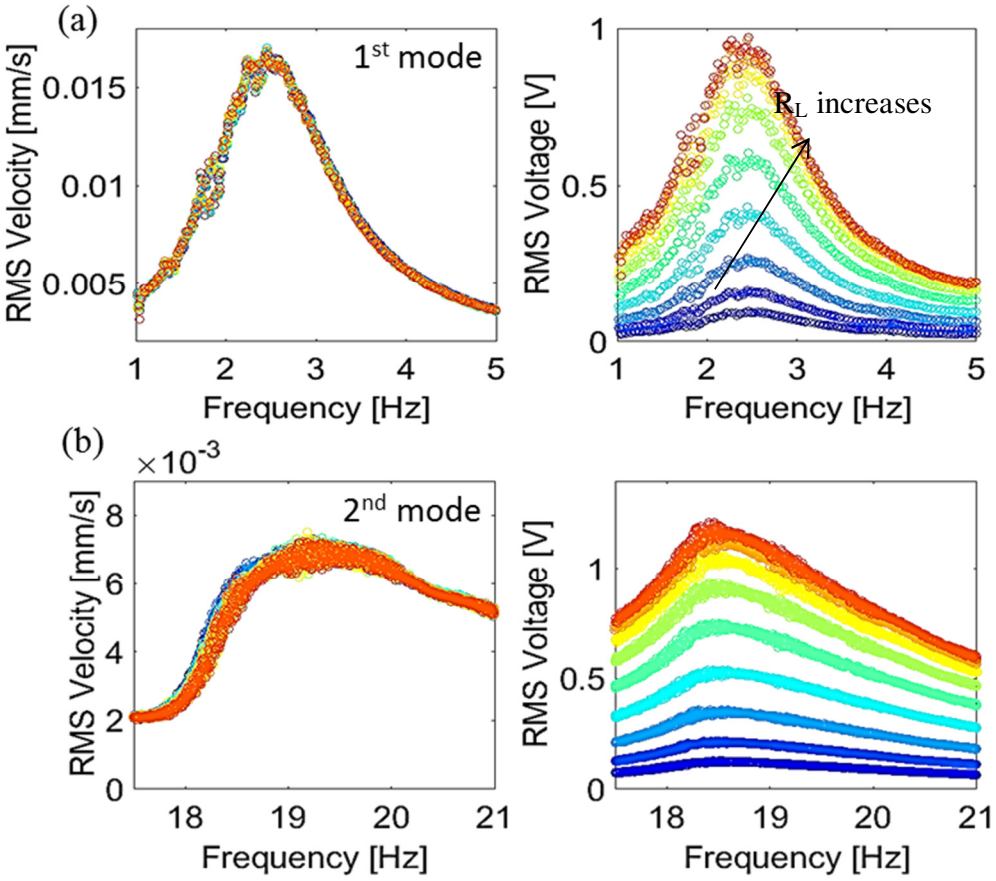

Figure 3.24. Resistor sweep energy harvesting test at 0.1 *g* RMS base acceleration level for in-phase case; (a) First and (b) second vibration mode.

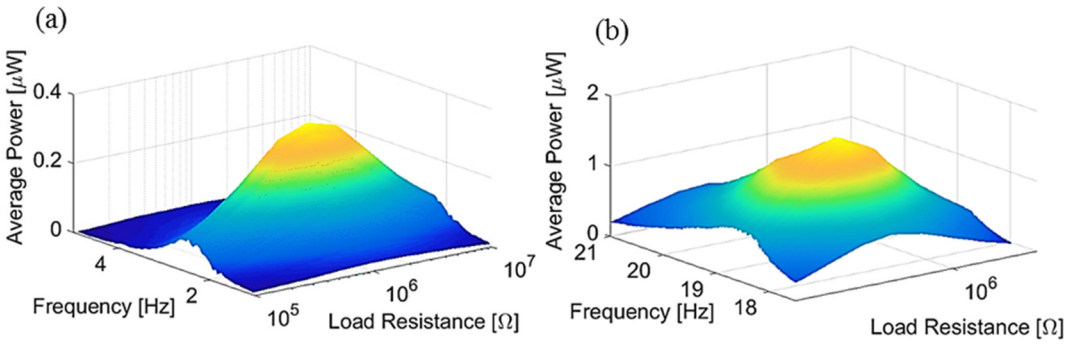

Figure 3.25. Experimental power output vs. load resistance and frequency diagrams at 0.1 *g* RMS base acceleration level and in-phase wiring of MFC laminates; (a) First and (b) second vibration mode.

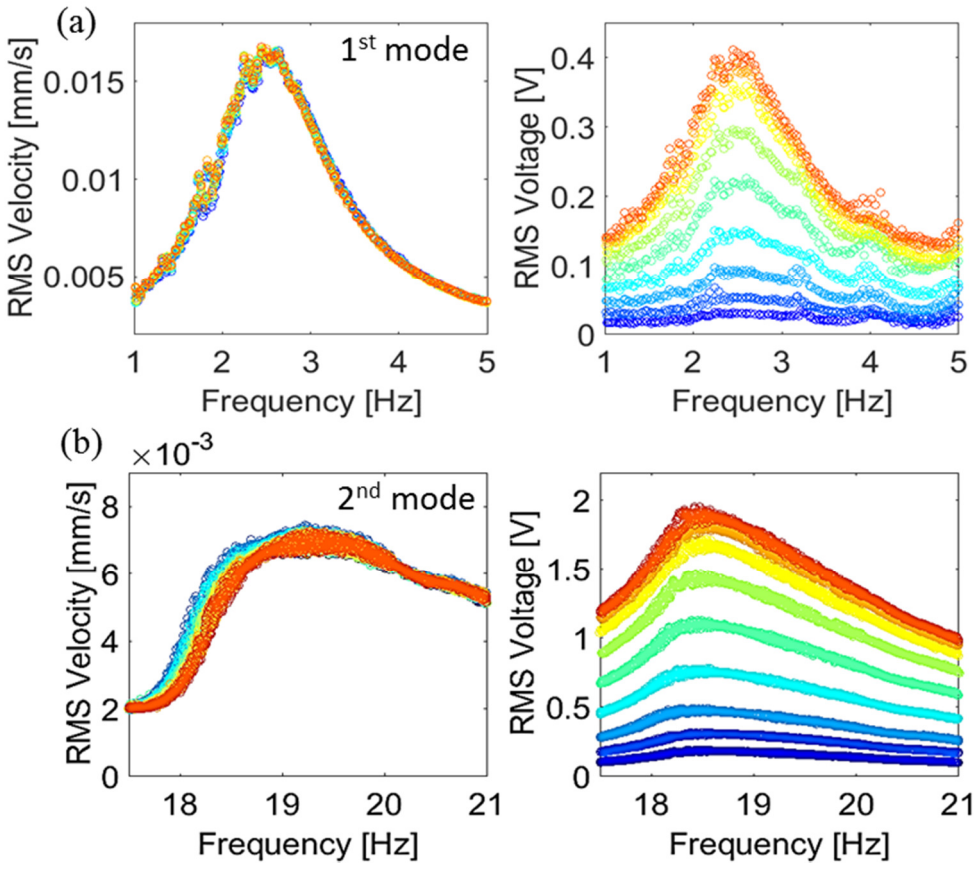

Figure 3.26. Resistor sweep energy harvesting test at 0.1 *g* RMS base acceleration level for out-of-phase case; (a) First and (b) second vibration mode.

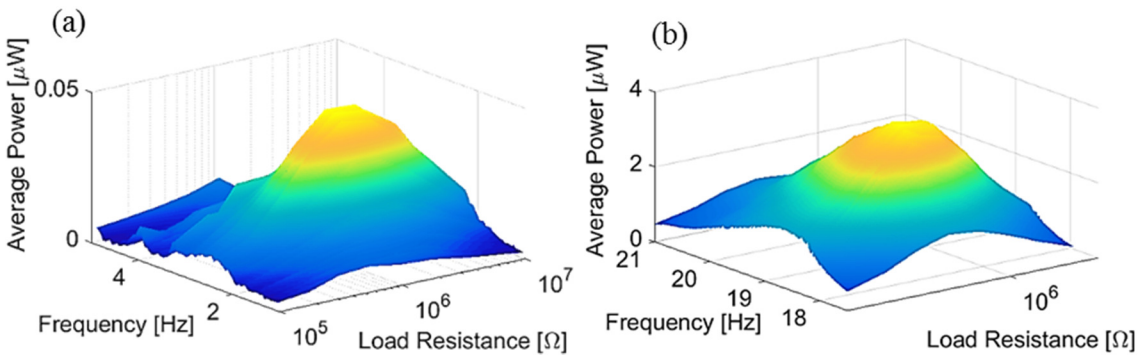

Figure 3.27. Experimental power output vs. load resistance and frequency diagrams at 0.1 *g* RMS base acceleration level and out-of-phase wiring of MFC laminates; (a) First and (b) second vibration mode.

Variations of the average power output versus changing load resistance for excitations at around the first (Figure 3.28a) and the second (Figure 3.28b) natural frequencies are shown for in-phase and out-of-phase wiring cases. The electrical power output for excitation at the first mode is higher when the system is wired in phase. For the second mode excitation, average power output is higher for out-of-phase wiring case; voltage amplitude of the out-of-phase wiring is approximately 2 times greater than the amplitude of the voltage response for in-phase case (where cancellation at strain node happens).

Using segmentation method, the second bending mode is used effectively in energy harvesting both linear and nonlinear regimes. The results show that power output has been enhanced significantly for second mode excitation.

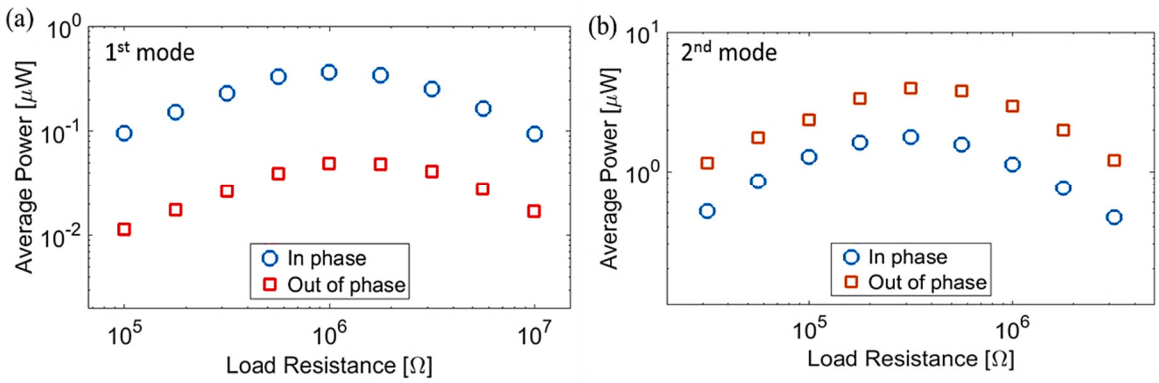

Figure 3.28. Power output versus load resistance at 0.1 *g* RMS base acceleration level and the (a) first and (b) second resonance frequency (comparing in-phase and out-of-phase cases).

3.5 Summary and Conclusions

Underwater base excitation of cantilevers made from piezoelectric MFCs with different length-to-width ratios and same thickness is explored experimentally and theoretically in this chapter. A semi-empirical model is employed and experimentally validated for predicting the power delivered to an electrical load as well as the underwater vibration response for base excitation of fully submerged cantilevers. Inertia and drag coefficients are identified and asymptotic behavior for $L/b>5$ has been observed. Strong dependence of the inertia and drag coefficients on the aspect ratio for $L/b<5$ is reported with good agreement between MFC and aluminum samples of the same aspect ratios. Variations of the electrical power output with excitation frequency and load resistance are obtained for different length-to-width ratios. Theoretical underwater output power density results are reported and compared with their in-air counterparts. It is shown that, for underwater base excitation, due to the effects of nonlinear fluid damping the output power increases nonlinearly with increased width (for the same base acceleration level) whereas in-air power output grows linearly with increased

width. Specifically for underwater cases, power density analysis reveals strong nonlinear dependence on the aspect ratio that can be exploited in design. Low values of L/b ratio are preferred to obtain large power density for the same base acceleration input to fully submerged cantilevers. Electrode segmentation is also performed for a cantilevered MFC bimorph to eliminate the cancellation due to strain node existing in the second mode shape. The results from the experiments for both linear and nonlinear responses of the segmented bimorph show that using segmented electrodes can enhance the power output significantly (approximately two times more power output) for second mode excitation.

4 UNDERWATER BIOMIMETIC ACTUATION USING MACRO-FIBER COMPOSITES

4.1 Introduction

In this chapter of dissertation, in order to develop high-fidelity models to predict the electrohydroelastic dynamics of MFC structures, mixing rules-based electroelastic mechanics modeling is coupled with the global electroelastic dynamics based on the Euler-Bernoulli kinematics and the nonlinear fluid loading based on Morison's semi-empirical model. The focus is placed on the dynamic actuation problem for the first two bending vibration modes under geometrically, materially, and piezoelectrically linear, and hydrodynamically nonlinear behavior. The physical parameters of MFC bimorphs are obtained based on mixing rules formulation and validated for different MFC types that have the same overhang length but different active widths. Following this process of in-air electroelastic model development and validation, underwater experiments are conducted for different length-to-width aspect ratios (L/b), empirical drag and inertia coefficients are extracted for Morison's equation. The repeatability of these empirical coefficients is demonstrated for experiments conducted using aluminum cantilevers of different aspect ratios. The convergence of nonlinear electrohydroelastic Euler-Bernoulli-Morison model to its hydrodynamically linear counterpart with increased L/b values is also reported. The proposed model, its harmonic balance analysis, and experimental results can be used for parameter identification as well as aspect ratio optimization for underwater piezoelectric actuation, sensing, and energy harvesting problems.

4.2 Electrohydroelastic Dynamic Actuation of an Underwater Bimorph Cantilever

The in-air dynamic actuation analysis of MFCs has been thoroughly covered in Chapter 2. Electrohydroelastically coupled equations for underwater actuation of an MFC cantilever bimorph (Figure 4.1) can be expressed as follows:

$$D\frac{\partial^4 w(x,t)}{\partial x^4}+c_\alpha\frac{\partial^5 w(x,t)}{\partial x^4\partial t}+c_\beta\frac{\partial w(x,t)}{\partial t}+m_s\frac{\partial^2 w(x,t)}{\partial t^2}+\Gamma(x,t) = \vartheta\left[\frac{d\delta(x)}{dx}-\frac{d\delta(x-L)}{dx}\right]v(t) \tag{4.1}$$

$$-i(t)+C_p\frac{dv(t)}{dt}+\vartheta\int_0^L\frac{\partial^3 w(x,t)}{\partial x^2\partial t}dx=0 \tag{4.2}$$

Here $\Gamma(x,t)$ is the hydrodynamic loading of the surrounding fluid per unit length ($L=L_o$ is the overall overhang length) and it is expressed by semi-empirical Morison's equation as [29, 60, 61]:

$$\Gamma(x,t)=\frac{\pi}{4}\rho_w b^2 c_m\frac{\partial^2 w(x,t)}{\partial t^2}+\frac{1}{2}\rho_w b c_d\frac{\partial w(x,t)}{\partial t}\left|\frac{\partial w(x,t)}{\partial t}\right| \tag{4.3}$$

where ρ_w is the mass density of water and b is the overall width of the bimorph. Moreover, c_m and c_d are the inertia and drag coefficients, respectively, which depend on the aspect ratio and to be determined experimentally. The damping component in Morison's equation introduces quadratic nonlinearity (different from the classical linearized hydrodynamic function presented by Sader [45]), therefore vibration modes need to be explored separately. The structural behavior is assumed to be linear.

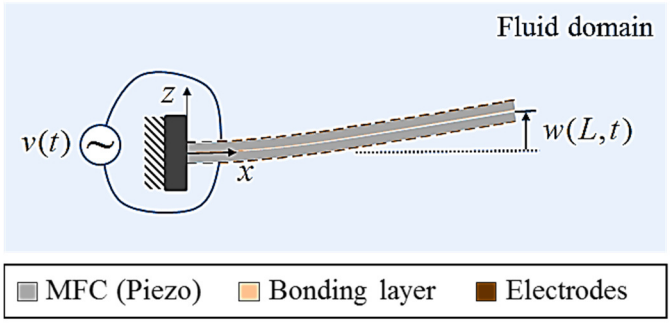

Figure 4.1. Schematic representation of a geometrically bimorph cantilever under dynamic actuation in an unbounded quiescent fluid domain (air or water).

Assuming well separated modes, the transverse deflection of the reference surface at position x and time t is

$$w(x,t) \cong \sum_{r=1}^{\infty} \phi_r(x)\eta_r(t) \tag{4.4}$$

where $\phi_r(x)$ and $\eta_r(t)$ are the respective eigenfunction (from the linear *in vacuo* solution) and modal coordinate.

Substituting the expression for $w(x,t)$ into Equations (4.1) and (4.2), multiplying by the mass normalized eigenfunction $\phi_s(x)$, integrating over the length of the beam, and applying the orthogonality conditions (Equations (2.20) and (2.21)) one obtains

$$(1+\mu_r)\ddot{\eta}_r(t) + (2\zeta_r\omega_r + \gamma_r|\dot{\eta}_r(t)|)\dot{\eta}_r(t) + \omega_r^2\eta_r(t) = \theta_r v(t) \tag{4.5}$$

$$-i_r(t) + C^{eq}\dot{v}(t) + \theta_r\dot{\eta}_r(t) = 0 \tag{4.6}$$

where $\mu_r = (\pi/4)(\rho_w b^2 c_{mr}/m_s)$ and $\gamma_r = (1/2)\rho_w b c_{dr}\int_0^L \phi_r^2(x)|\phi_r(x)|dx$. Here c_{mr} and c_{dr} are the inertia and drag coefficients for rth vibration mode.

Notably, Equation (4.5) shows that the problem in this case is nonlinear different from the given in-air electromechanical model in Equations (2.31) and (2.32). Therefore, the

method of harmonic balance is used to analyze periodic solutions of nonlinear ordinary Equations (4.5) and (4.6). Using this method, a Fourier series solution is assumed and the ordinary differential equations are replaced with algebraic equations (the details of harmonic balance analysis have been extensively explained elsewhere [151-153]). In this work, a single-term harmonic balance solution is found to be adequate for approximating the steady-state response to harmonic input voltage.

The input voltage, $v(t)$, is assumed to be of the form:

$$v(t) = V\cos(\omega t) \tag{4.7}$$

The unknown modal coordinate $\eta_r(t)$ is given as and the current flow through the piezoelectric bimorph, $i_r(t)$, are assumed to be of the form:

$$\eta_r(t) = H_{0r}\cos(\omega t) + H_{1r}\sin(\omega t) \tag{4.8}$$

$$i_r(t) = I_{0r}\cos(\omega t) + I_{1r}\sin(\omega t) \tag{4.9}$$

Substituting Equations (4.7)-(4.9) into Equations (4.5) and (4.6) and the use of harmonic balance method give the following set of algebraic equations in H_{0r}, H_{1r}, I_{0r}, and I_{1r} for the *r*th vibration mode.

$$-(1+\mu_r)\omega^2 H_{0r} + (2\zeta_r\omega_r + \frac{8}{3\pi}\gamma_r\omega\sqrt{H_{0r}^2 + H_{1r}^2})\omega H_{1r} + \omega_r^2 H_{0r} - \theta_r V = 0 \tag{4.10}$$

$$-(1+\mu_r)\omega^2 H_{1r} - (2\zeta_r\omega_r + \frac{8}{3\pi}\gamma_r\omega\sqrt{H_{0r}^2 + H_{1r}^2})\omega H_{0r} + \omega_r^2 H_{1r} = 0 \tag{4.11}$$

$$-I_{0r} + \theta_r\omega H_{1r} = 0 \tag{4.12}$$

$$I_{1r} + C^{eq}\omega + \theta_r\omega H_{0r} = 0 \tag{4.13}$$

Note that, following the simplification suggested by Sarpkaya [63] and later be used by Aureli *et al.* [54] and Cha *et al.* [29] the nonlinear hydrodynamic damping term in Equation (4.5) is simplified by considering the fact that

$$|\hat{H}\,\mathrm{Im}[e^{(j\omega t)}]|\hat{H}\,\mathrm{Im}[e^{(j\omega t)}] = \frac{8}{3\pi}|\hat{H}|\hat{H}\,\mathrm{Im}[e^{(j\omega t)}] \tag{4.14}$$

where $\hat{H}$ is any complex number. The resulting system of algebraic equations (Equations (4.5)-(4.8)) is solved numerically using the solve function in MATLAB®.

4.3 Experimental Validations

Three MFC bimorphs shown in Figure 4.2a are tested and characterized in air and under water using the clamps employed for in-air actuation FRF measurements. Each bimorph is made of two identical custom-made MFC laminates (hydrophobic due to polyester electrode sheets) labeled as M8507-P1, M8514-P1 and M8528-P1 (Figure 4.2a) by Smart Material Corp. [17]. The piezoelectric laminates are assembled by using high shear strength epoxy through vacuum bonding (process described elsewhere [154]). The electrode leads of the MFC bimorphs are connected in parallel throughout the experiments discussed in this work. The bimorphs are cantilevered in aluminum clamps with the basic geometry and structural properties given in Table 4.1.

A sample bimorph (M8514-P1) cantilever in fixture mounted rigidly to an optical table is shown in Figure 4.2b for in-air actuation test. During actuation experiments, the actuation voltage signal (harmonic excitation with 10 averages) is generated by a Spectral Dynamics SigLab data acquisition device and a Trek High Voltage Amplifier (Trek, inc. Model 2220) provides reference driving voltage and current. An LDV (Polytec PDV 100) is used along

with the monitored actuation signal to obtain the tip velocity-to-actuation voltage FRFs of the MFC bimorphs in air and under water.

Table 4.1. Geometric and structural properties of the MFC bimorphs (L: overhang length, b: width, h: total thickness, m_s: structural mass per length)

	L (mm) [active*, overall]	b (mm) [active, overall]	h (mm)	m_s (kg m^{-1})
M8507-P1	[75.5, 83.5]	[7, 16.5]	0.61	0.028
M8514-P1	[75.5, 83.5]	[14, 21.5]	0.61	0.045
M8528-P1	[75.5, 88.5]	[28, 43.5]	0.61	0.090

* Active length and width define the portions which are covered with piezoelectric material.

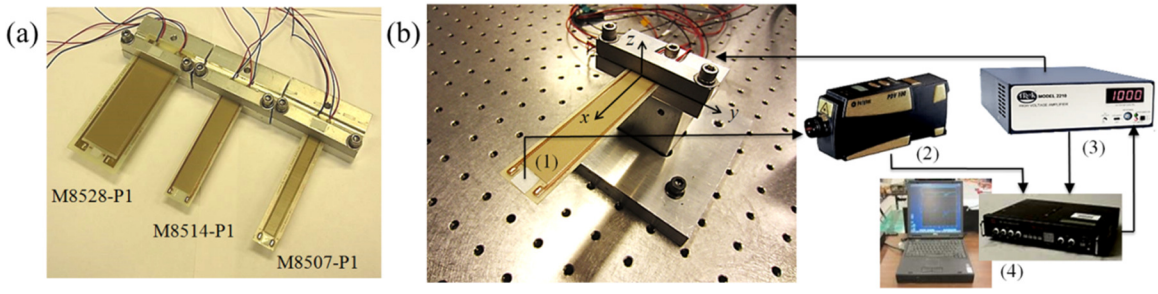

Figure 4.2. (a) MFC bimorphs in aluminum clamps, and (b) in-air dynamic actuation test setup: (1) sample bimorph (M8514-P1) cantilever in fixture mounted rigidly to table, (2) LDV for the measurement of the bimorph tip velocity-to-actuation voltage FRF, (3) power amplifier, and (4) data acquisition system.

Underwater experiments are conducted in the same setup as in-air (Figure 4.3a) and an LDV is used for obtaining the transverse tip velocity under dynamic actuation (Figure 4.3b).

Note that, the laser signal amplitude is divided by the refractive index of water ($n = 1.333$) in the underwater experiments [21, 22].

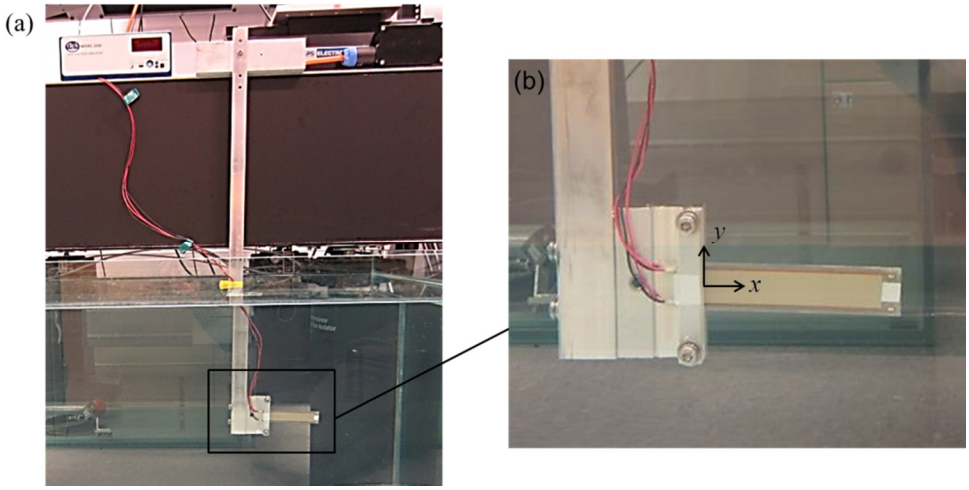

Figure 4.3. (a) Underwater configuration of the bimorph MFC cantilever for the measurement of its tip velocity-to-actuation voltage FRF and (b) close-up view of a clamped M8514-P1 type bimorph cantilever fixed to the aluminum bar.

4.3.1 In-air admittance and velocity FRFs and parameter identification

Tip velocity and admittance FRFs for in-air actuation experiments and modeling for three bimorphs (M8507-P1, M8514-P1, and M8528-P1) are shown in Figure 4.4 to Figure 4.6, respectively. The identified parameters from in-air actuation experiments are summarized in Table 4.2. Bending stiffness, *D*, is first identified by using the experimental fundamental resonance frequency of the bimorph, f_1, then is used Equation (3.7) to obtain the second resonance frequency, f_2 (note that in Equation (3.7), λ_1 and λ_2 are the roots of Equation (2.19) given as 1.875 and 4.694, respectively). Comparing the experimental and analytical second resonance frequency show less than 4% error. Damping ratios for the first and second mode (ζ_1 and ζ_2) are obtained by using the half-power-point method [150],

electromechanical coupling in physical coordinate (ϑ) is obtained from Equation (2.12) using mixing rules formulation (parallel connections of single MFC laminates) for each sample and the equivalent capacitance (C^{eq}) is measured experimentally.

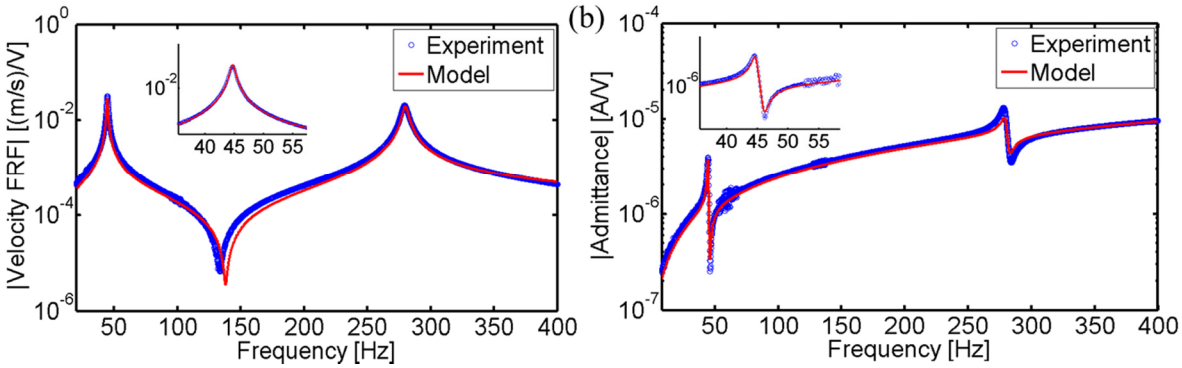

Figure 4.4. Experimental and analytical results for in-air actuation of bimorph M8507-P1 cantilever: (a) Tip velocity-to-actuation voltage and (b) admittance FRFs.

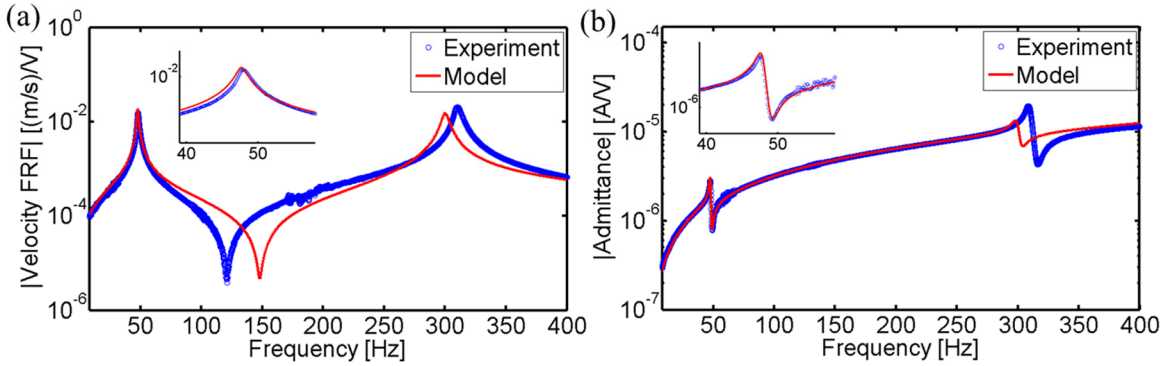

Figure 4.5. Experimental and analytical results for in-air actuation of bimorph M8514-P1 cantilever: (a) Tip velocity-to-actuation voltage and (b) admittance FRFs.

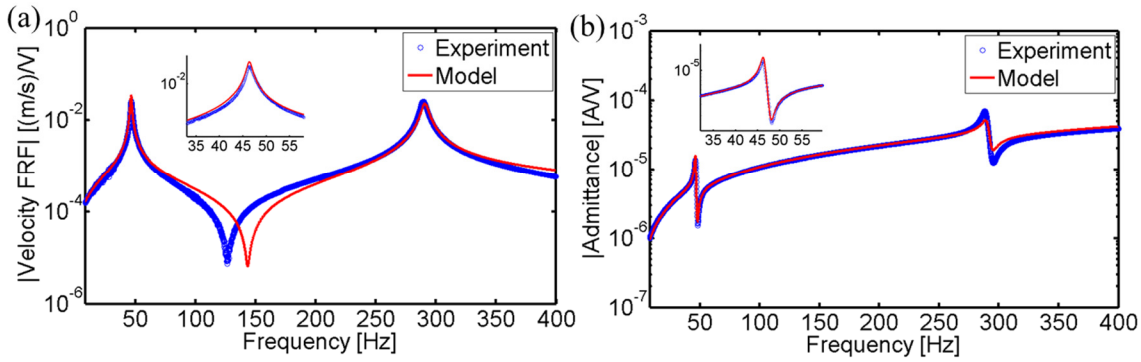

Figure 4.6. Experimental and analytical results for in-air actuation of bimorph M8528-P1 cantilever: (a) Tip velocity-to-actuation voltage and (b) admittance FRFs.

Table 4.2**:** Identified parameters from in-air actuation experiments

	M8507-P1	M8514-P1	M8528-P1
f_1 (Hz)	44.7	47.9	46.4
f_2 (Hz) *	[279.3 280.1]	[309.8 300.2]	[289.2 290.8]
D (N m^2)	0.0058	0.0107	0.0201
ζ_1, ζ_2 (%)	1.8, 1.5	2, 1.5	1.5, 1.2
ϑ [10^{-6} Nm V^{-1}]	4.53	6.89	22.73
C^{eq} (nF)	3.8	5.5	17.5

* f_2 is given in the form of [experimental analytical]

The good agreement between the experimental results and analytical model validates the approach. All the identified parameters are used in the next section for the actuation analysis of MFC bimorphs under water.

4.3.2 *Analytical and experimental system parameters*

In Figure 4.7, modal electromechanical coupling (θ_r) and piezoelectric stress constant (e_{33}) of the custom-made piezoelectric MFCs are calculated from experimental data and compared with the effective properties obtained from the model employing mixing rules formulation (Equations (2.3), (2.5) and (2.12)). Details about the geometric and homogeneous properties of the active (PZT fibers) and passive (epoxy) layers can be found in in Chapter 2. Using mixing rules-based formulation and following the analysis extensively explained previously, the experimental and analytical results for modal electromechanical coupling and equivalent piezoelectric constant are given for MFCs with three aspect ratios and for two first vibration modes.

A good agreement is seen between the theoretical predictions and the experimental results in Figure 4.7. In addition, the results are well consistent with the empirical estimates given by Cacan and Erturk [142] for standard MFCs. In this way the effective electroelastic, elastic, and dielectric properties of the MFCs will be fully bridged to the global electrohydroelastic dynamics of the MFC laminates explored in this work for dynamic actuation under water.

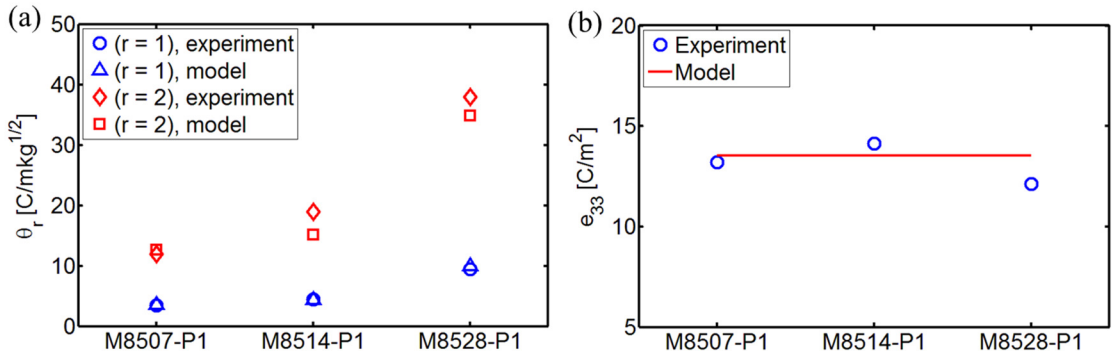

Figure 4.7. Experimental and analytical results for (a) modal electromechanical coupling, θ_r, and (b) equivalent piezoelectric constant, e_{33} for MFC.

4.3.3 Underwater velocity and admittance FRFs

Having validated the analytical model results for in-air actuation of the bimorphs and identified parameters, three case studies are tested and analyzed for underwater actuation. As displayed in Figure 4.3, each MFC bimorph is submerged in quiescent water along with the same aluminum clamp used for in-air experiment.

Figure 4.8 to Figure 4.10 show the experimental and semi-empirical (using Morison hydrodynamic function) tip velocity and admittance FRFs for a frequency range of 12 to 130Hz which captures underwater two resonance frequencies of the bimorphs. For this analysis, inertia and drag coefficients, c_m and c_d, are obtained by the analysis done for in-air and underwater purely experimental data (plots are given in Appendix, Figure C and Figure D). Then c_m and c_d are used in the analytical modeling to give Figure 4.8 to Figure 4.10.

In Table 4.3, the experimental underwater fundamental frequencies and total damping ratios (ζ_T in Table 4.3 includes structural damping ratio and the added fluid damping) are listed. It is therefore detected that, the effect of fluid is to lower the resonance frequencies of the MFCs (for both modes) approximately by amount of 35% and to increase the damping ratio by amount of 45% as compared to in-air results reported in Table 4.2. The electromechanical coupling term, ϑ, is the same as the one obtained from in-air experiment.

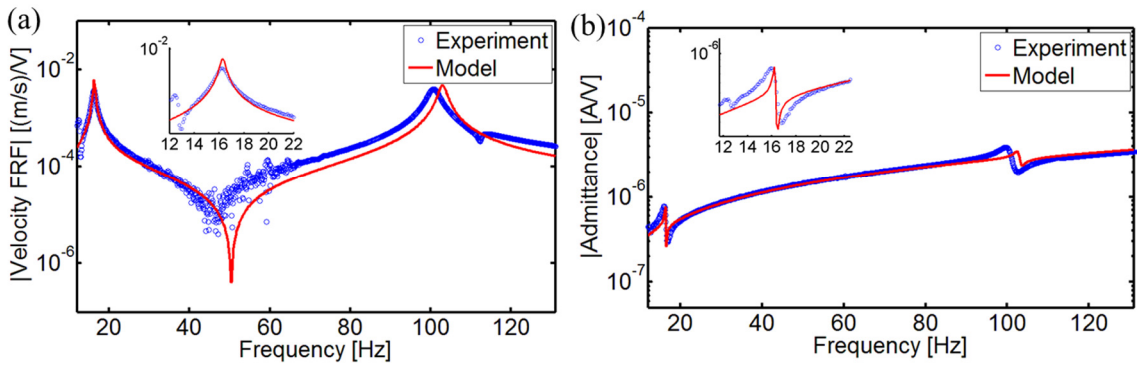

Figure 4.8. Experimental and analytical results for underwater actuation of bimorph M8507-P1 cantilever: (a) Tip velocity-to-actuation voltage and (b) admittance FRFs.

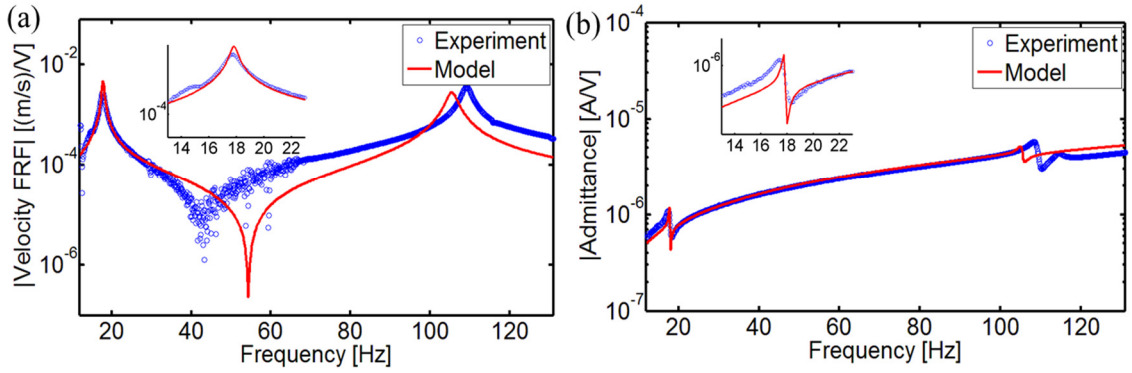

Figure 4.9. Experimental and analytical results for underwater actuation of bimorph M8514-P1 cantilever: (a) Tip velocity-to-actuation voltage and (b) admittance FRFs.

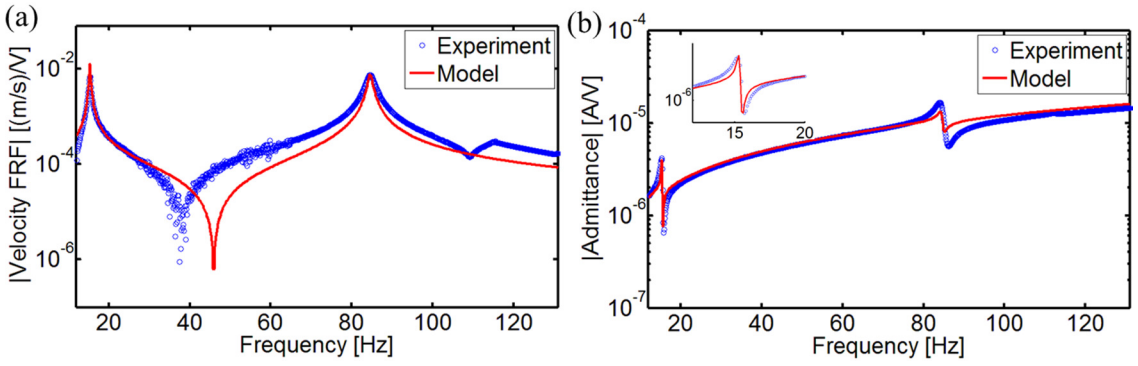

Figure 4.10. Experimental and analytical results for underwater actuation of bimorph M8514-P1 cantilever: (a) Tip velocity-to-actuation voltage and (b) admittance FRFs.

Table 4.3. Experimental identified parameters for underwater studies.

	M8507-P1	M8514-P1	M8528-P1
f_1 (Hz)	15.9	17.5	15.2
f_2 (Hz) *	[100.7 103]	[109.2 105.5]	[84.6 84.5]
ζ_{T_1} , ζ_{T_2} (%)	3.3, 2.5	4.3, 3.2	3.3, 2.4

* f_2 is given in the form of [experimental analytical]

4.3.4 Analysis of hydrodynamic inertia and drag coefficients in Morison's equation

Figure 4.11a - Figure 4.11d display the identified hydrodynamic inertia and drag coefficients (c_m and c_d in Morison's hydrodynamic function are determined experimentally) focusing on the first two bending modes for both base-excited aluminum and actuated MFC cantilevers with different aspect ratios ($\psi = L/b$). Experimental vibration characteristics of the aluminum strips considered in this study are explained in details in Chapter 3. In Figure 4.11, the identified inertia and drag coefficients from actuation tests show smooth variation and converging behavior (to linear hydrodynamics) by increasing the aspect ratio. This trend is consistent with the results observed in Chapter 3 and Figure 3.15 for base-excited MFC bimorphs. The obtained values for inertia and drag coefficients are to be found in the same order of magnitude.

Figure 4.11 shows the quadratic increase of coefficients c_m and c_d with respect to aspect ratio for each mode separately. In order to represent the curves given in Figure 4.11, the curve fitting toolbox of MATLAB® is used. The following quadratic curve fitting

polynomial ratio expressions are given for the dimensionless inertia and drag coefficients focusing on the two first bending modes.

$$c_{m1} = \frac{\psi^2 - 0.701\psi + 0.3745}{\psi^2 - 1.111\psi + 2.637},\ c_{m2} = \frac{\psi^2 + 6.99\psi - 1.658}{\psi^2 + 5.36\psi + 11.46}$$

$$c_{d1} = \frac{\psi^2 + 0.1432\psi + 0.5618}{0.04983\psi^2 - 0.03946\psi + 0.2674}, \tag{4.15}$$

$$c_{d2} = \frac{\psi^2 - 0.412\psi + 0.4096}{0.008492\psi^2 - 0.007883\psi + 0.01853}$$

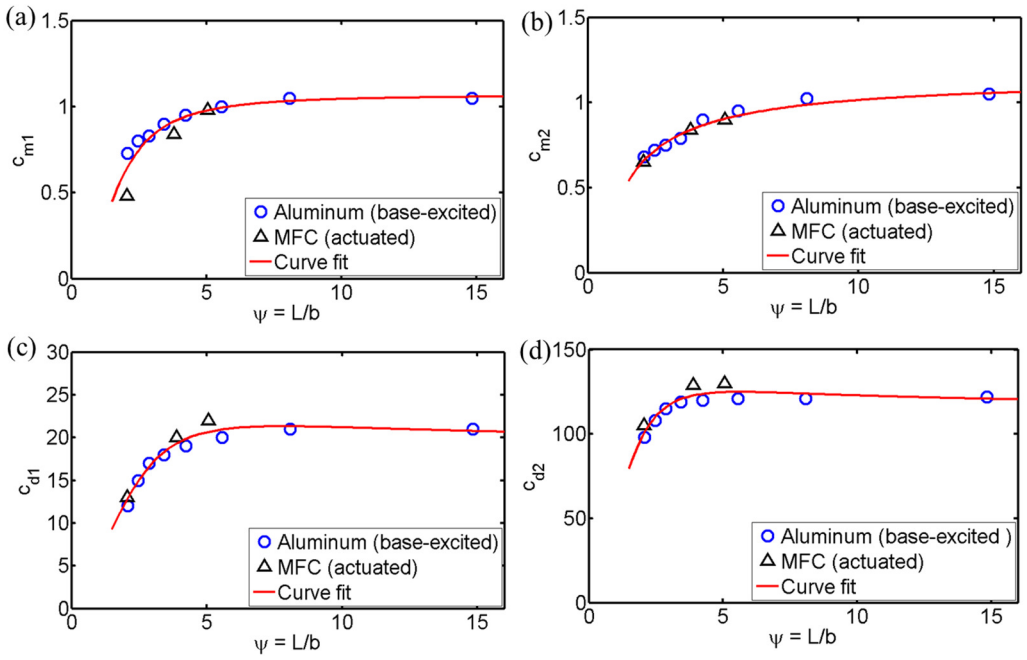

Figure 4.11. Hydrodynamic inertia coefficient (c_m) vs. aspect ratio (ψ) for (a) mode 1 and (b) mode 2; Hydrodynamic drag coefficient (c_d) vs. ψ for (c) mode 1 and (d) mode 2.

Comparing c_m and c_d values that belong to the first and the second modes in Figure 4.11 shows that not only aspect ratio but also vibration frequency, therefore the vibration mode (especially for the drag coefficient), is determinant of fluid loading effects. This observation justifies the dependence of inertia and drag coefficients (especially the drag coefficient) in Morison's semi-empirical equation on the KC number ($\mathrm{KC} = 2\pi \left| w(L) \right| / b$). Figure 4.12 displays the identified hydrodynamic inertia and drag coefficients versus KC for both aluminum and MFC cantilevers with different aspect ratios. The underwater vibration characteristics of aluminum strips and MFCs show that, resonance frequencies of these two groups keep close values for the same aspect ratio while the maximum displacement amplitudes for base-excited aluminum cantilevers are larger than the MFC ones. Therefore, the results for aluminum in Figure 4.12 are given for larger KC numbers. Figure 4.12a shows that, for both aluminum and MFC samples, inertia coefficients for the first and second modes are in the same order of magnitude (tend to converge to unity), relatively insensitive to KC range in this study ($0.008 < \mathrm{KC} < 1.5$). This observation is consistent with the experimental [55] and numerical [54, 56, 58] data for $\mathrm{KC} < 1.5$ reported in Figure 11 of Kopman and Porfiri [59]. In Figure 4.12b, KC number's dependency is significant for drag coefficient (c_d decreases as KC increases; previously predicted by experimental and numerical efforts summarized by [59]). For each mode, aluminum strips and MFCs give the drag coefficients in the same order of magnitude. In contract to the behavior of inertia coefficient, drag coefficient shows great sensitivity to vibration mode such that the drag coefficient increases from mode 1 to mode 2.

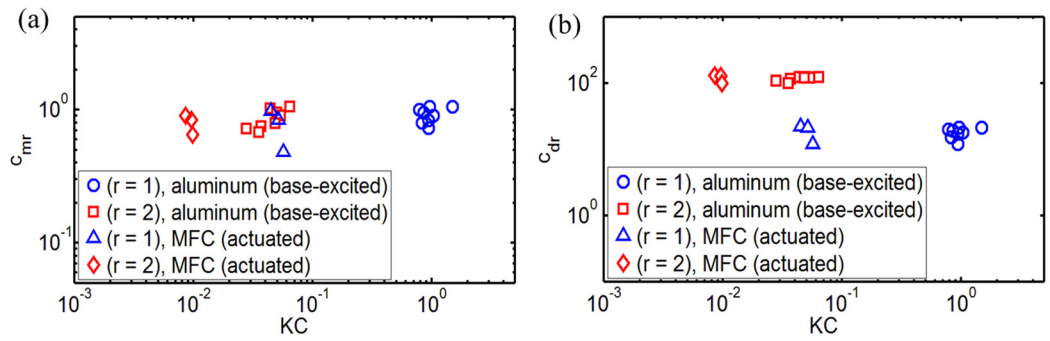

Figure 4.12. (a) Hydrodynamic inertia coefficient (c_{mr}) vs. KC number and (b) hydrodynamic drag coefficient (c_{dr}) vs. KC number.

4.4 Hydrodynamic Thrust Generation and Power Consumption Investigations for Piezoelectric Fins with Different Aspect Ratios

This section of dissertation investigates the effect of length-to-width (L/b) aspect ratio on the hydrodynamic thrust generation performance of MFC cantilever fins by accounting for the power consumption level. From the results shown in section 4.3, it is known that the hydrodynamic inertia and drag coefficients are controlled by the aspect ratio especially for L/b<5. The three MFC bimorph fins explored in this work have the aspect ratios of 2.1, 3.9, and 5.4. The developed nonlinear electrohydroelastic model in section 4.2 is employed to extract the inertia and drag coefficients from the vibration response to harmonic actuation for the first bending mode. Experiments are then conducted for various actuation voltage levels to quantify the mean thrust resultant and power consumption levels for different aspect ratios. Variation of the thrust coefficient of the MFC fins with aspect ratio is also modeled and validated.

4.4.1 *Hydrodynamic mean thrust and identification of the thrust coefficient based on Lighthill's theory of elongated-body propulsion*

Among the resistive [155, 156] and reactive [75, 97, 98] methods used to predict thrust for robotic fish, Lighthill's theory [75, 97, 98, 157] is applied in the present work to estimate the mean thrust in quiescent water. This method employs Lighthill's theory of elongated-body theory [157], which is based on the reactive forces between the virtual mass of the surrounding fluid and the vibrating slender body. The mean thrust, *T*, produced by the cantilever MFC bimorph is calculated as

$$T = \frac{1}{2} m_v \left[\overline{\left(\frac{\partial w(x,t)}{\partial t} \right)^2} - U^2 \overline{\left(\frac{\partial w(x,t)}{\partial x} \right)^2} \right]_{x=L} \tag{4.16}$$

where U is relative speed of external free stream (or the swimming speed of propulsor) which is neglected for quiescent water conditions (i.e. $U \to 0$ is assumed). The overbar denotes the mean values for the time derivative and the spatial derivative of the transverse deflection, $w(x,t)$, and m_v is the virtual mass density at $x = L$ which is estimated as

$$m_v = \frac{\pi \rho_w b^2}{4} c_m \tag{4.17}$$

In most instances of thrust calculation using Lighthill's theory [22, 50, 158], the virtual mass coefficient (or inertia coefficient used in Equation (4.3)), c_m, is taken as unity based on two-dimensional fluid-structure analysis for slender beams [45, 99]. Based on the analysis performed in Section 4.2, accurate values of the virtual mass coefficient to calculate the thrust stemming from the actuation of various MFC bimorphs with different aspect ratios are implemented in Equation (4.16). To identify c_m, each MFC bimorph is clamped and placed

in both in-air and underwater actuation experiments. The in-air and underwater experimental FRFs are correlated with model simulations (Sections 2.2.6 and 4.2) that used only experimental parameters for the identification of the inertia coefficients for the fundamental mode, and are then used in the semi-empirical electrohydroelastic Euler-Bernoulli-Morison model for experimental validations.

4.4.2 Experimental validations

4.4.2.1 Details of experimental setup

Three MFC bimorphs are formed by bonding pairs of MFCs of varying aspect ratios (M8528-P1, M8514-P1, and M8507-P1 from the Smart Material Corporation [17], shown in Figure 4.13a) using high shear strength epoxy and a vacuum bonding process. Table 4.4 summarizes the physical properties of the MFC bimorphs. The MFC pairs are wired in parallel for all of the experiments, and the equivalent capacitances of the bimorphs are measured experimentally via a capacitance meter. These three bimorphs are then rigidly clamped at one end (shown in Figure 4.13b) and linearly actuated in-air with a low-voltage sinusoidal input. During actuation experiments, the actuation voltage signal is generated by a National Instruments NI USB-4431 and amplified using a power amplifier (Trek, Inc. Model 2220). Output voltage and current data are collected from the amplifier, as well as tip velocity measurements from an LDV (Polytec PDV 100) and recorded using the NI USB-4431. To measure the mean hydrodynamic thrust, each sample is attached to the free end of a fixed-free 254mm x 25.4mm x 6.35mm elastic aluminum transducer cantilever and submerged underwater, as seen in Figure 4.13c and Figure 4.13d. The deflection of the

aluminum cantilever in response to the thrust of each sample during actuation is measured by an optical displacement sensor (Micro-Epsilon optoNCDT 2300-50), as shown in Figure 4.13d, and the thrust force is extracted using the calibration curve seen in Figure 4.14, as explained next.

Table 4.4. Geometric and structural properties of the MFC bimorphs (L: overhang length, b: width, h: total thickness, m_s: structural mass per length)

	L (mm) [active*, overall]	b (mm) [active, overall]	h (mm)	m_s (kg m^{-1})
M8507-P1	[75.5, 85.5]	[7, 16.5]	0.61	0.028
M8514-P1	[75.5, 83.5]	[14, 21.5]	0.61	0.045
M8528-P1	[75.5, 90.6]	[28, 43.5]	0.61	0.075

* Active length and width define the portions which are covered with piezoelectric material.

The hydrostatic pressure effects are canceled out in the underwater experiments, so the mean thrust is assumed to be a point force applied to the transducer cantilever through the center of the clamp holding the MFC, which results in a deflection of the free end of the transducer cantilever. The transducer is calibrated horizontally and in air, where weights are gradually added to the location of the point force with the aid of gravity while the static displacement of the free end of the transducer is measured. The resulting calibration curve, shown in Figure 4.14, is determined to be linear for the range of deflections seen in these experiments. Since the stiffness of the transducer cantilever is unchanged in air and underwater, the in-air calibration can be utilized for the underwater experiments. Impact hammer testing is performed on this transducer cantilever to ensure that the first mode of the

transducer is well separated from the first mode of the MFC bimorphs, both in air and underwater.

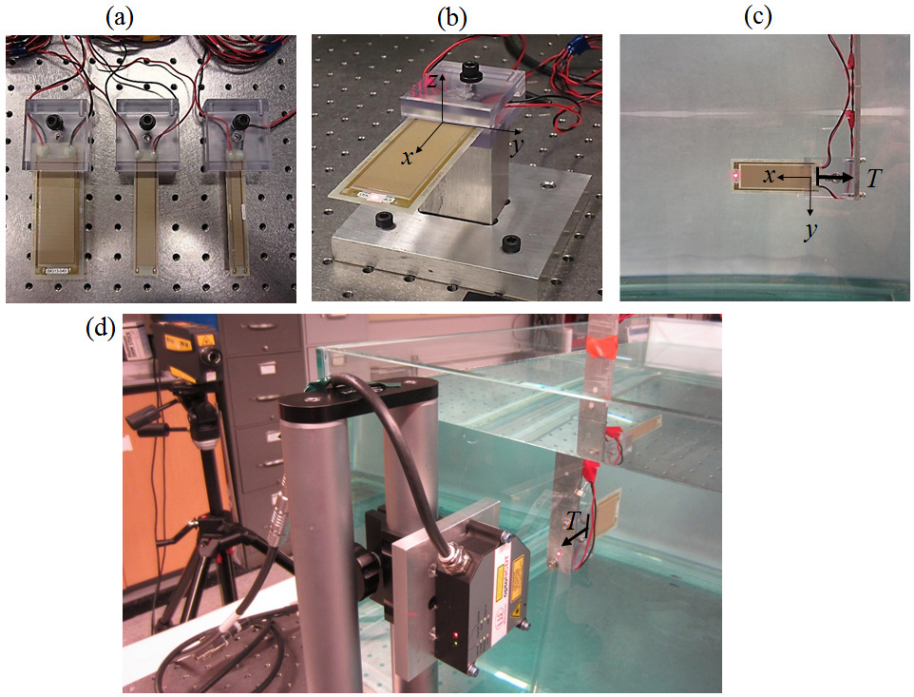

Figure 4.13. (a) Clamped MFC bimorphs (from left to right side: M8528-P1, M8514-P1, and M8507-P1), (b) in-air dynamic actuation test setup, (c) side view of the underwater configuration of the MFC bimorph for the measurement of its tip velocity-to-actuation voltage FRF and (d) front view of underwater configuration of MFC bimorph for mean thrust measurement.

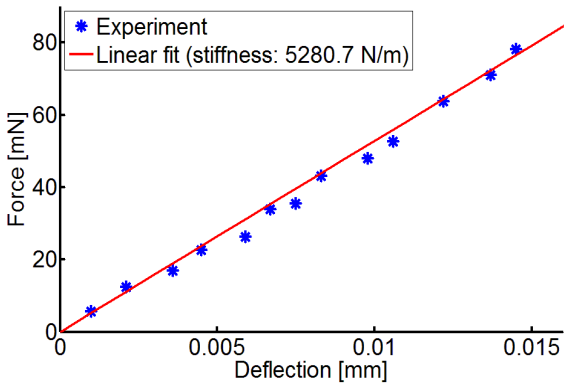

Figure 4.14. Linear calibration curve for the aluminum transducer cantilever.

4.4.2.2 In-air and underwater velocity FRFs and parameter identification

Tip velocity-to-actuation voltage FRFs for in-air and underwater actuation experiments and modeling on M8528-P1 are shown in Figure 4.15a and Figure 4.15b, respectively. For brevity, the remaining samples are not graphically presented here. During the actuation experiments, low-voltage harmonic excitation is applied, resulting in a linear response. The identified parameters based on the in-air actuation experiments are summarized in Table 4.5. Bending stiffness, D, is identified by using the experimental fundamental resonance frequency of the bimorph. Damping ratio, ζ, is obtained by using the half-power-point method [150]. The identified modal electromechanical coupling coefficient, θ, for each sample is in agreement with the predicted values obtained by using the mixing rules formulation (for the parallel connection of MFC laminates) presented in Chapter 2. The equivalent capacitance, C^{eq}, of each bimorph is measured experimentally.

Once the analytical model for in-air actuation of the bimorphs is validated (using Equations (2.31) and (2.32)) and the parameters are identified, three case studies are tested and analyzed (using Morison's hydrodynamic function) for linear underwater actuation. The identified inertia coefficient for each sample is well matched with the prediction made by Equation (4.15). The drag coefficient is found by matching the analysis and experimental data, considering the clamping imperfections.

It is important to note that, in this section the electrohydroelastic model given in Section 4.2 is used only for excitations around the fundamental natural frequency since higher vibration modes are not studied here. In addition, the derivation neglects the geometric, material, and dissipative nonlinearities [159-161] and is strictly valid for linear vibrations only. Therefore, the linear model predictions would fail under high actuation voltage levels

(e.g. peak-to-peak voltage input: 400 V to 800 V) due to geometric and electroelastic nonlinearities [159-161]. Modeling of MFC dynamics under high voltage actuation and incorporating hydrodynamic effects [162] in such a nonlinear model are of interest for future work.

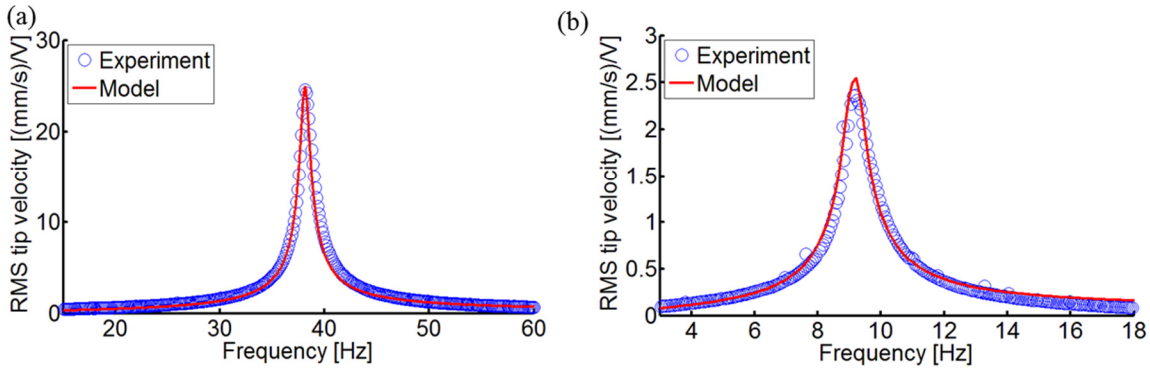

Figure 4.15 (a) In-air and (b) underwater experimental and analytical tip velocity FRF for M8528-P1.

Table 4.5. Experimentally identified parameters from in-air actuation experiments

	M8507-P1	M8514-P1	M8528-P1
f_{sc} (Hz)	35.5	46.4	38.1
D (N m^2)	0.0045	0.0101	0.0125
ζ(%)	1.6	1.8	1.3
θ (10^{-3} C/m$\sqrt{\text{kg}}$)	4.5	7.5	10
C^{eq} (nF)	5.5	6.7	19.3

4.4.2.3 Mean thrust and tip velocity correlation, and power consumption analysis

The experimental tip velocity and mean thrust measurements for M8528-P1 are shown in the frequency range of 1-11 Hz, which captures the resonance frequency of the bimorph for peak-peak actuation voltage levels of 400, 600, and 800 V (Figure 4.17a and Figure 4.17b). For a given actuation frequency and amplitude, the bimorphs were excited as per Figure 4.16a, where there is 10 seconds of pre-actuation where no voltage is applied, then 10 seconds of a sinusoidal voltage input at the given frequency and amplitude, and finally 10 seconds of post-actuation where there is again no input voltage. The tip velocity of the bimorph, displacement of the transducer cantilever, input voltage and current for the bimorph were measured as the bimorph is excited, and subsections where the response of the bimorph is in quasi-steady state during the pre-actuation, actuation, and post-actuation phases are extracted from the time histories. These quasi-steady state subsections are used to determine the RMS tip velocity, mean thrust, RMS current, and mean power consumed for each actuation frequency and amplitude. The mean displacement of the transducer cantilever caused by the thrust is the difference between the mean value during actuation and the average of the mean values during the pre-actuation and post-actuation phases. Figure 4.16 shows a representative time trace of input actuation voltage, transverse tip velocity, and transducer cantilever displacement in the direction of positive thrust (in Figure 4.13c and Figure 4.13d) during pre-actuation, actuation, and post-actuation phases at 5.5 Hz under a peak-to-peak input actuation voltage of 800 V.

The analytical thrust curves shown in Figure 4.17b use Lighthill's theory for a bimorph propulsor in quiescent water conditions based on the measured tip velocity shown in Figure 4.17a. For M8528-P1 ($\psi = 2.1$), M8514-P1 ($\psi = 3.9$), and M8507-P1 ($\psi = 5.4$), the inertia

coefficients (c_m) in Equation (4.17) (as it is equivalent to virtual mass coefficient in [22]) are defined as 0.069, 0.91, and 1.02, respectively, based on the semi-empirical Euler-Bernoulli-Morison electrohydroelastic analysis presented in Section 4.2 and plotted in Figure 4.11a.

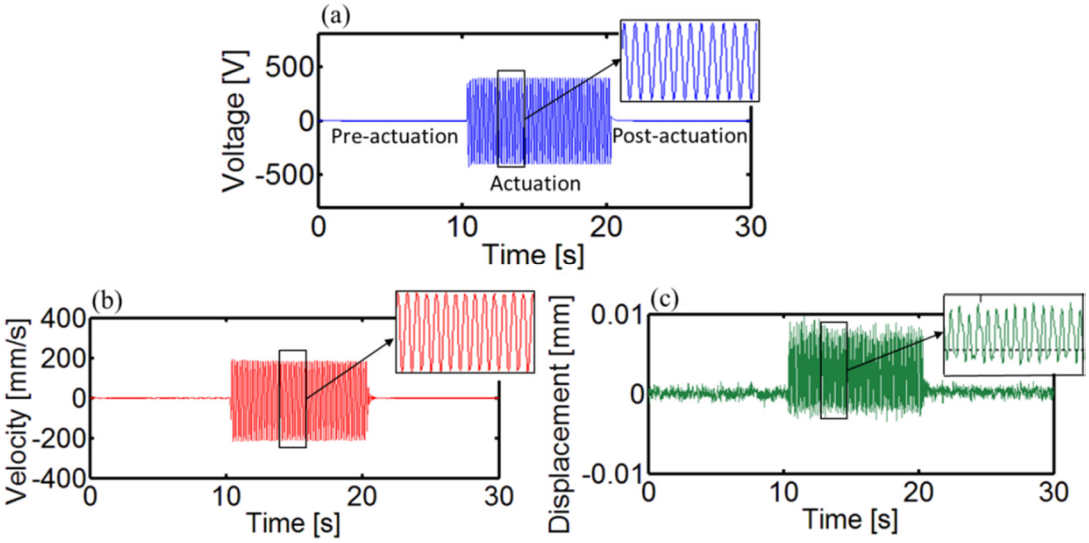

Figure 4.16. Representative time trace of (a) input actuation voltage (800V), (b) measured transverse tip velocity, and (c) head displacement during pre-actuation, actuation, and post-actuation at 5.5 Hz.

The experimental current amplitude and average power plots for the MFC bimorph at various actuation frequencies and voltages are shown in Figure 4.17c and Figure 4.17d. The data obtained for the thrust and power consumption is used later to analyze the effect of aspect ratio on the thrust generated per unit power consumption.

In Figure 4.17b, the agreement between the experimental thrust measurements and the analytical model validates the use of the reduced form of Lighthill's theory [97, 98] (which uses the measured tip velocity and predicted virtual mass by the Euler-Bernoulli-Morison electrohydroelastic model) for the bimorph under three different high-level input voltages.

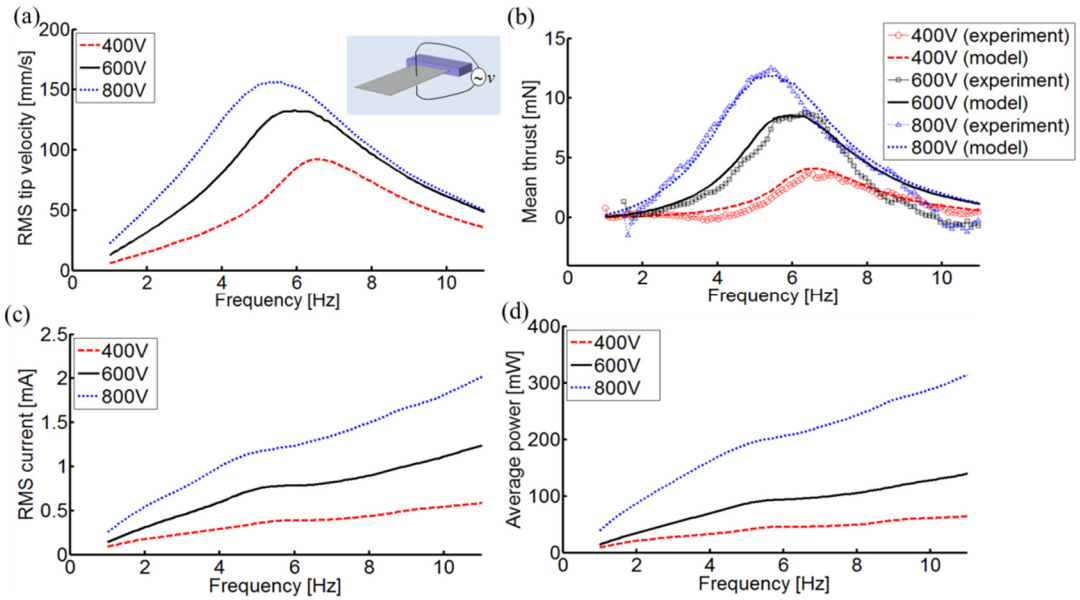

Figure 4.17. (a) Experimental tip velocity, (b) measured and predicted thrust curves, (c) experimental current amplitude, and (d) average power curves for M8528-P1 ($\psi = 2.1$).

Next, Lighthill's theory is employed for two more case studies with larger aspect ratios where the thrust levels, which are prone to noise, are difficult to accurately measure experimentally. In every cases, the correlation between measured tip velocity and predicted thrust shows that the thrust levels increase with increasing tip velocities, as is expected. Figure 4.18a and Figure 4.19a show the experimentally determined RMS tip velocity for the higher aspect ratio bimorphs under varying actuation frequencies and voltages, and Figure 4.18b and Figure 4.19b show the corresponding predicted thrust curves. In Figure 4.17, Figure 4.18 and Figure 4.19c-d, the current amplitude and average power plots for different actuation frequencies and voltages are given.

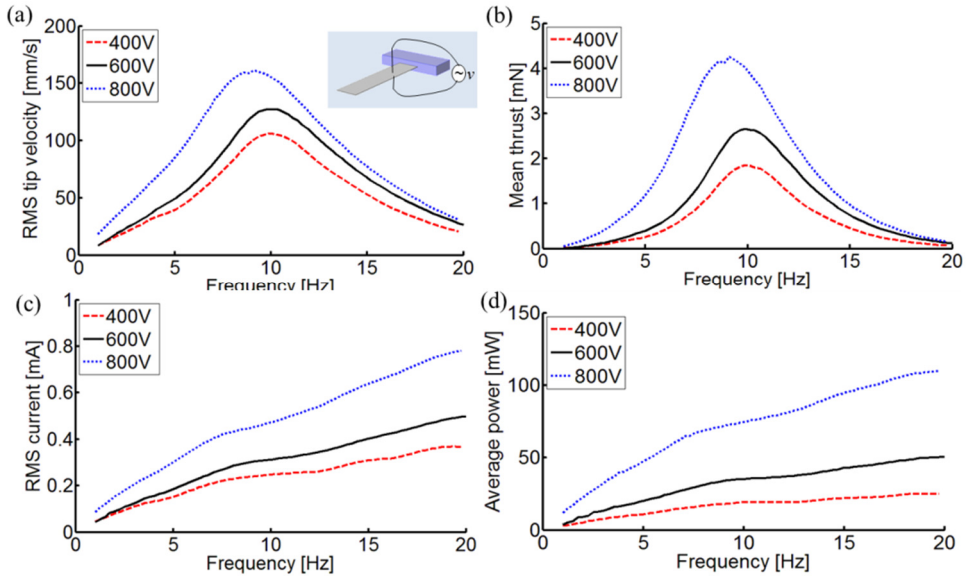

Figure 4.18. (a) Experimental tip velocity, (b) predicted thrust curves, (c) experimental current amplitude, and (d) average power curves for M8514-P1 ($\psi = 3.9$).

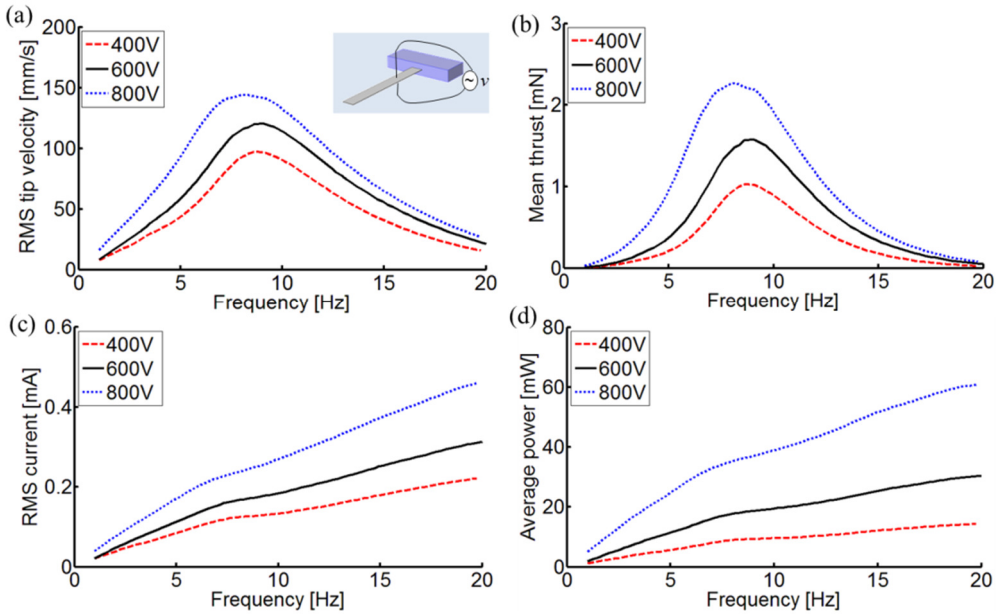

Figure 4.19. (a) Experimental tip velocity, (b) predicted thrust curves, (c) experimental current amplitude, and (d) average power curves for M8507-P1 ($\psi = 5.4$).

The ratio, Φ, between the mean thrust and power-consumption for the three aspect ratios using Lighthill's theory with the measured tip velocity for 800V peak-peak input voltage is shown in Figure 4.20a.

Maximum mean thrust to power-consumption ratio vs. aspect ratio is displayed in Figure 4.20b. Despite having differing aspect ratio, the maximum mean thrust resultant to power consumption level for three MFCs is approximately a constant average value of 60.7 mN/W.

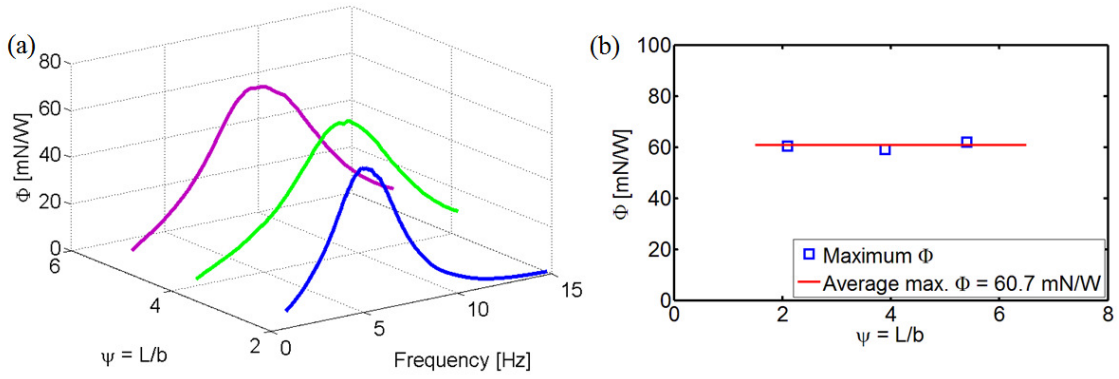

Figure 4.20. (a) Mean thrust to power-consumption ratio for three aspect ratios using Lighthill's theory with the measured tip velocity at an 800V peak-to-peak input voltage and (b) maximum mean thrust to power-consumption ratio vs. aspect ratio.

4.4.2.4 Identification of the thrust coefficient

In order to parametrically study the effects of the cantilever geometry, oscillation frequency, and oscillation tip displacement amplitude on the resultant thrust, the nondimensional thrust coefficient, c_τ, is defined as [163]

$$c_\tau = \frac{T}{\frac{1}{2}\rho_w \omega^2 \mid w(L,t) \mid^2 bL} \tag{4.18}$$

Substituting Equations (4.16) and (4.17) into Equation (4.18) yields an expression for c_t in terms of the virtual mass coefficient, c_m, and aspect ratio, ψ. Combining this expression with the expression given in Equation (4.15) for c_m results in an expression for c_τ as a function dependent only on the aspect ratio.

$$c_\tau = 0.3927 \frac{c_m}{\psi} = \frac{0.3927\psi^2 - 0.2753\psi + 0.1471}{\psi^3 - 1.111\psi^2 + 2.637\psi} \tag{4.19}$$

Figure 4.21 displays the experimental thrust coefficients of the actuated MFC cantilevers with different aspect ratios ($\psi = L/b$) along with the curve obtained from Equation (4.19). By increasing the aspect ratio, thrust coefficient is significantly reduced, which is attributed to the reduction of the overall fluid loading on the structure.

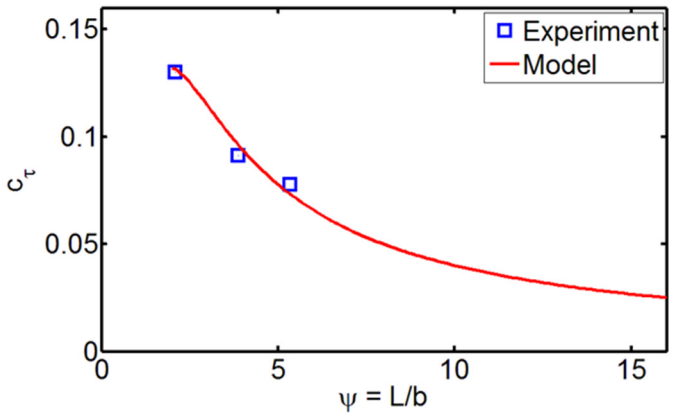

Figure 4.21. Identified experimental and analytical thrust coefficient in Equation (4.19) vs. aspect ratio (ψ).

4.5 Summary and Conclusions

MFC piezoelectric structures strike a balance between actuation force and deformation as recently demonstrated in underwater locomotion efforts [22]. Cantilevers made from MFC bimorphs with different aspect ratios can be employed for underwater actuation, sensing, and power generation, among other aquatic applications of direct and converse piezoelectric effects. In an effort to develop an electrohydroelastic modeling framework for such cantilevers, the work in this chapter investigates MFC bimorphs with three different aspect ratios under dynamic actuation. Tip velocity and admittance FRFs are successfully modeled for in-air actuation and validated experimentally for all aspect ratios. Underwater tip velocity and admittance FRFs are then derived by combining their in-air counterparts with Morison's nonlinear hydrodynamic function. The inertia and drag coefficients in Morison's equation are identified experimentally and compared (see Figure 4. 22) with the ones obtained from base-excited aluminum cantilevers of similar aspect ratios and base-excited energy harvesting (in Chapter 3) for the same MFC bimorphs used in actuation experiments. In these three cases, in addition to the smooth trend and converging behavior (to linear hydrodynamics) with increased aspect ratio for the aluminum cantilevers, the agreement of the MFC and aluminum cantilever results for both modes is found remarkable. The repeatability of the inertia and drag coefficients in Morison's equation was observed for samples with the same aspect ratio, and curve fit expressions are reported to use with the presented model. For the KC number (period number) range in this study ($0.008 < KC < 1.5$), the inertia coefficient is observed to be relatively insensitive to the KC number, whereas a significant increase is reported for the drag coefficient with increased vibration mode number.

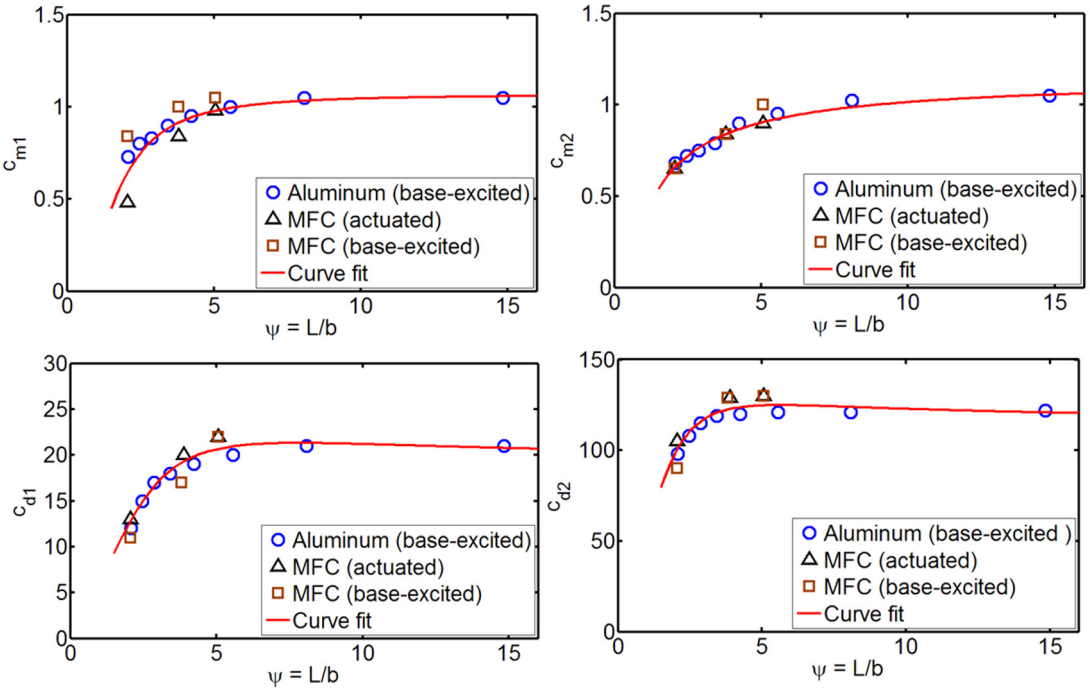

Figure 4. 22. Hydrodynamic inertia (c_m) and drag (c_d) coefficients of MFC samples (under actuation and base excitation) and aluminum samples (under base excitation) vs. aspect ratio.

Following the electrohydroelastic modeling given for underwater dynamic actuation of MFC bimorphs in this chapter, bio-inspired thrust generation using piezoelectric transduction is investigated theoretically and experimentally for MFC bimorphs with three aspect ratios. In-air experiments are conducted for model validation and for the characterization of the bimorph propulsors. Underwater tip velocity FRFs are then derived by combining their in-air counterparts with Morison's hydrodynamic function. The inertia and drag coefficients in Morison's equation are identified experimentally. The hydrodynamic effects added to the electroelastic in-air model successfully predict the underwater dynamics for small oscillations. However, the high actuation voltage levels during the experiments that included thrust measurements cause nonlinear electrohydroelastic behavior due to electroelastic,

geometric, and dissipative nonlinear effects. For future work, considering nonlinear electroelastic dynamics [159-161] with nonlinear hydrodynamic effects [162] are required to predict the dynamics of the propulsor for large oscillations and strong electric fields. In this work (Section 4.4), the experimentally obtained vibration response and the virtual mass coefficient (defined in Morison's hydrodynamic function) are coupled with Lighthill's elongated-body theory [164-166] to predict the thrust output. Although the inertia and drag coefficients are found to be highly dependent on the aspect ratio for $\psi < 5$, the maximum mean thrust to power consumption ratio is found to be insensitive to the aspect ratio. Trends of dimensionless thrust coefficient with respect to aspect ratio are reported and experimentally validated.

5 CONTACTLESS ULTRASONIC ENERGY TRANSFER FOR WIRELESS SYSTEMS: ACOUSTIC-PIEZOELECTRIC STRUCTURE INTERACTION MODELING AND PERFORMANCE ENHANCEMENT

5.1 Introduction

There are several applications of wireless electronic components with little or no ambient energy available to harvest, yet wireless battery charging for such systems is still of great interest. Example applications range from biomedical implants to sensors located in hazardous environments. Energy transfer based on the propagation of acoustic waves at ultrasonic frequencies is a recently explored alternative that offers increased transmitter-receiver distance, reduced loss, and elimination of electromagnetic fields. As this research area receives growing attention, there is increased need for fully coupled model development to quantify the energy transfer characteristics with a focus on the transmitter, receiver, medium, geometric, and material parameters. Multiphysics modeling and case studies of contactless ultrasonic energy transfer for wireless electronic components submerged in fluid are presented. The source is a pulsating sphere and the receiver is a piezoelectric bar operating in the 33-mode of piezoelectricity with a fundamental resonance frequency above the audible frequency range. The goal is to quantify the electrical power delivered to the load (connected to the receiver) in terms of the source strength. Both analytical and finite-element models are developed for the resulting acoustic-piezoelectric structure interaction problem. Resistive and resistive-reactive electrical loading cases are presented and optimality conditions are discussed. Broadband power transfer is achieved by optimal resistive-reactive load tuning for performance enhancement and frequency-wise robustness. Significant enhancement of power output is reported due to using a hard piezoelectric receiver (PZT-8)

instead of a soft counterpart (PZT-5H) as a result of reduced material damping. The analytical multiphysics modeling approach given in this work can be used to predict and optimize the coupled system dynamics with very good accuracy and dramatically improved computational efficiency as compared to using commercial finite-element packages.

5.2 Coupled Modeling of UAET from a Spherical Wave Source to a 33-Mode Receiver

5.2.1 In vacuo electromechanical dynamics of a 33-mode receiver

The linear constitutive equations for a thickness-poled (i.e. longitudinally poled) piezoelectric bar operating in 33-mode are [1, 167, 168]

$$S_3 = s_{33}^E T_3 + d_{33} E_3 \tag{5.1}$$

$$D_3 = d_{33} T_3 + \varepsilon_{33}^T E_3 \tag{5.2}$$

where S_3 is the strain, T_3 is the stress, D_3 is the electric displacement, and E_3 is the electric field, while s_{33}^E is the elastic compliance at constant electric field, d_{33} is the piezoelectric strain constant, and ε_{33}^T is the permittivity component at constant stress. Based on Equations (5.1) and (5.2), it is assumed that the excitation of the receiver is such that the elastic, coupling, and dissipative nonlinearities [161, 169-171] are not pronounced, i.e. linear piezoelectricity is assumed.

The coupled partial differential equation for longitudinal vibrations of the receiver and the electrical circuit equation (Figure 5.1) can be derived as

$$-YA\frac{\partial^2 u(\xi,t)}{\partial \xi^2} - c_\alpha \frac{\partial^3 u(\xi,t)}{\partial \xi^2 \partial t} + c_\beta \frac{\partial u(\xi,t)}{\partial t} + m\frac{\partial^2 u(\xi,t)}{\partial t^2} + \theta v(t)[\delta(\xi) - \delta(\xi - L)] = f(t)\delta(\xi - L) \tag{5.3}$$

$$C_p \frac{dv(t)}{dt} + Y_l v(t) + \int_0^L \theta \frac{\partial^2 u(\xi,t)}{\partial t \partial \xi} d\xi = 0 \tag{5.4}$$

where $u(\xi,t)$ is the displacement response of the bar at the axial position ξ and time t, Y is the Young's modulus at constant electric field, m is the mass per unit length, c_α is the stiffness-proportional damping coefficient, c_β is the mass-proportional damping coefficient,[2] A is the cross sectional area, θ is the electromechanical coupling term in physical coordinates, and $f(t) = Fe^{j\omega t}$ is the external harmonic force resultant at the free-end surface of the bar (where F is the force amplitude, ω is the frequency, and j is the unit imaginary number). Furthermore, C_p and Y_l are the internal capacitance of the piezoelectric receiver and the admittance of the external load, respectively, $v(t)$ is the voltage output across the electrical load, and $\delta(\xi)$ is the Dirac delta function. As depicted in Figure 5.1, the mechanical strain axis and the electrical poling axis (perpendicular to the surface electrodes) are coincident, and therefore the receiver bar is employed in the 33-mode of piezoelectricity. The dielectric loss is neglected, although it can easily be included by using a complex permittivity including the loss tangent of the piezoelectric material. Two types of electrical loading are to be considered in this work: purely resistive (yielding $Y_l = 1/R_l$, where R_l is the load resistance) and resistive-reactive (yielding, under harmonic excitation at frequency

[2] Proportional damping is assumed to represent *in vacuo* material dissipation (which can be merely due to the stiffness-proportional damping term c_α in the Kelvin-Voigt approximation).

ω, $Y_l(\omega) = 1/R_l + 1/j\omega L_l$ for resistive-inductive loading, and $Y_l(\omega) = 1/R_l + j\omega C_l$ for resistive-capacitive loading, where L_l is the load inductance connected to the load resistance in parallel and C_l is the load capacitance connected to load resistance in parallel).

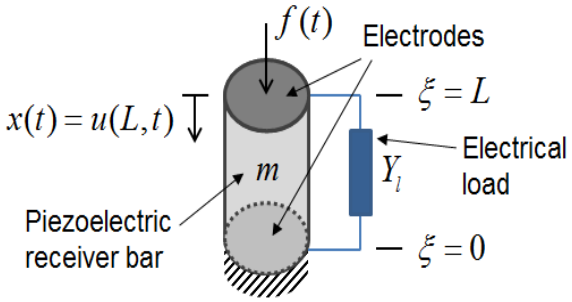

Figure 5.1. Longitudinal excitation of a fixed-free cylindrical piezoelectric receiver bar connected to an electrical load for power generation.

The linear displacement at the free end of piezoelectric bar ($x(t)$ in Figure 5.1, where $x(t) = u(L,t)$) due to harmonic excitation at or around the fundamental longitudinal (axial) vibration mode is obtained by modal analysis of the distributed-parameter electromechanical system with a focus on the first mode only (i.e. higher modes are excluded in the following). The longitudinal tip displacement of the bar at time *t* is then

$$x(t) = u(\xi,t)\big|_{\xi=L} = \phi(L)\eta(t) \tag{5.5}$$

where $\phi(L)$ and $\eta(t)$ are, respectively, the mass-normalized eigenfunction evaluated at $\xi = L$ (in Figure 5.1) and the generalized modal coordinate of the longitudinal vibration mode for a fixed-free uniform bar. The mass normalized eigenfunction evaluated at the tip is obtained as $\phi(L) = \sqrt{2/\rho AL}\sin(\pi\xi/2L)\big|_{\xi=L} = \sqrt{2/\rho AL}$ (where ρ is the mass density of the piezoelectric bar) which satisfies the companion mass and stiffness forms of the orthogonally

conditions (see, for instance, Appendix C.2 in Erturk and Inman [1] for standard modal analysis derivations in short-circuit conditions).

The electromechanically coupled equations of forced vibration and current balance are expressed for this lumped-parameter model (reduced from distributed-parameter solution) as

$$\ddot{x}(t) + 2\zeta\omega_n \dot{x}(t) + \omega_n^2 x(t) - \phi^2(L)\theta v(t) = \phi^2(L) f(t) \tag{5.6}$$

$$C_p \dot{v}(t) + Y_l v(t) + \theta \dot{x}(t) = 0 \tag{5.7}$$

where $\omega_n = (\pi/2)\sqrt{1/s_{33}^E \rho L^2}$ is the fundamental short-circuit natural frequency, ζ is the viscous damping ratio (that is due to internal mechanical losses only in the *in vacuo* problem), and an over-dot represents differentiation with respect to time.

Substituting $x(t) = Xe^{j\omega t}$ and $v(t) = Ve^{j\omega t}$ for the steady state response, the single-mode tip displacement $x(t)$ and voltage response $v(t)$ of the longitudinal 33-mode configuration (Figure 5.1) can be extracted from Equations (5.6) and as (5.7).

$$x(t) = \frac{(Y_l(\omega) + j\omega C_p) F \phi^2(L)}{(\omega_n^2 - \omega^2 + j2\zeta\omega\omega_n)(Y_l(\omega) + j\omega C_p) + j\omega\theta^2\phi^2(L)} e^{j\omega t} \tag{5.8}$$

$$v(t) = \frac{-j\omega\theta F \phi^2(L)}{(\omega_n^2 - \omega^2 + j2\zeta\omega\omega_n)(Y_l(\omega) + j\omega C_p) + j\omega\theta^2\phi^2(L)} e^{j\omega t} \tag{5.9}$$

which are valid for vibrations with the fundamental longitudinal vibration mode, i.e. for excitations at or around the first longitudinal resonance frequency.

5.2.2 Acoustic-piezoelectric structure coupling and receiver power output

The fluid-loaded longitudinal vibration of the piezoelectric bar is based on a lumped-parameter electromechanical piston representation of the fully submerged piezoelectric

receiver excited by incident acoustic pressure waves originating from a spherical source of known strength Q (Figure 6.2). Therefore the model development in this section is compatible with the lumped-parameter model reduced from the distributed-parameter formulation given in the previous section. Linear acoustics is assumed in the fluid (i.e. neither kinematic nor medium nonlinearities exist) and negligible loss in the fluid domain. Scatter pressure effects are also assumed to be negligible for the wavelength, reciever dimensions, and alignment in this setting (which is validated in a set of experiments conducted separately).

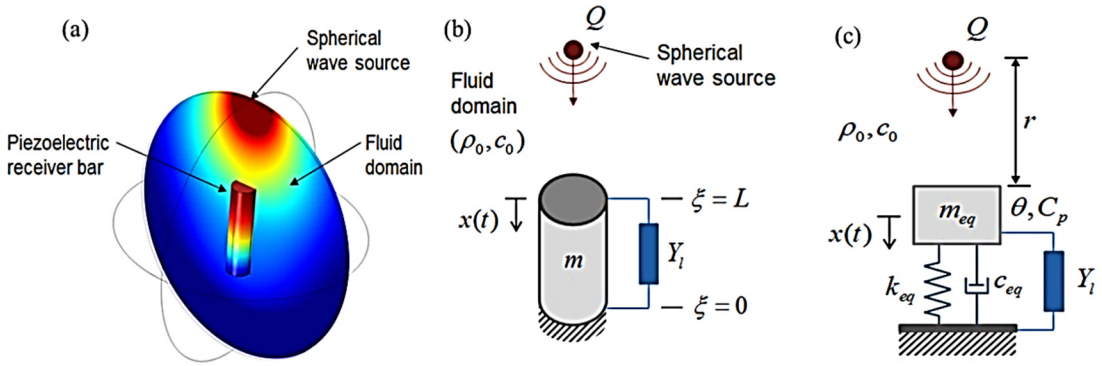

Figure 6.2. (a) Finite-element simulation snapshot, (b) schematic representation, and (c) lumped-parameter model of electrical power generation from spherical acoustic waves.

The electromechanically and acoustically coupled mechanical equation of motion for the lumped model in x coordinate (Figure 6.2c) can be written in the form of [1, 172]

$$m_{eq}\ddot{x}(t) + c_{eq}\dot{x}(t) + k_{eq}x(t) + F_r(t) - \chi v(t) = f(t) \tag{5.10}$$

where m_{eq}, c_{eq}, k_{eq} and χ are the equivalent *in vacuo* mass, damping coefficient, stiffness, and electromechanical coupling of the receiver, respectively. Multiplying both sides of

Equation (5.6) by m_{eq} and using the expression for short-circuit natural frequency ω_n, one can obtain the lumped-parameter terms as $m_{eq} = \rho AL/(\pi/2)^2$, $c_{eq} = 2m_{eq}\zeta\omega_n$, $k_{eq} = m_{eq}\omega_n^2$, and $\chi = m_{eq}\theta\phi^2(L)$. Furthermore, $f(t) = p(t)A$ is the force resultant due to the incident acoustic pressure wave evaluated at the piston surface as $p(t) = Pe^{j\omega t}$ (where P is the complex pressure amplitude and A is the piston area), and $F_r(t) = Z_r\dot{x}(t)$ is the force exerted by the fluid on the piston (where Z_r is the radiation impedance due to the acoustic-structure interaction at the free end of the receiver bar). The radiation impedance is given by $Z_r = R_r + jX_r$, where R_r and X_r are the resistive and reactive components for an unbaffled piston estimated using [168, 172]:

$$R_r = \sigma_R(ka)\rho_0 c_0 A\left(1 - \frac{J_1(2ka)}{ka}\right) \tag{5.11}$$

$$X_r = \sigma_X(ka)\rho_0 c_0 A\left(\frac{H_1(2ka)}{ka}\right) \tag{5.12}$$

Here, $J_1(2ka)$ and $H_1(2ka)$ are the first order Bessel and Struve functions of the first kind, respectively [172], while $\sigma_R(ka)$ and $\sigma_X(ka)$ account for the modifications relative to the baffled piston (see, for instance, figure 10.19 in [168] . Moreover, $k = \omega/c_0$ is the wave number, c_0 is the speed of sound in fluid (e.g. water) surrounding the piston, ρ_0 is the mass density of the surrounding fluid, and a is the radius of the piston (i.e. radius of the receiver's cross section: $a = \sqrt{A/\pi}$). The pressure field created by a pulsating spherical harmonic wave source in an infinite, homogeneous, and isotropic medium is [172, 173]

$$p(t) = \rho_0 c_0 \frac{-jkQ}{4\pi r(1-jk\bar{a})} e^{j(\omega t + k(r-\bar{a}))} \tag{5.13}$$

where r is source-to-receiver distance and $\bar{a}$ is the source radius. Moreover, Q is the acoustic source strength which is defined as a product of surface velocity U_0 and surface area ($4\pi\bar{a}^2$) of the pulsating spherical wave source, i.e. $Q = 4\pi\bar{a}^2 U_0$.

The single-mode tip displacement, voltage response, and power output (normalized with respect to source strength) frequency response functions for longitudinal vibrations of the fluid-loaded piezoelectric receiver are obtained by using Equations (5.10) and (5.7) as follows

$$\left|\frac{x(t)}{Qe^{j(\omega t + k(r-\bar{a}))}}\right| = \left|\frac{-\rho_0 c_0 A(Y_l(\omega) + j\omega C_p)\left(\frac{jk}{4\pi r(1-jk\bar{a})}\right) m_{eq}\phi^2(L)}{\left[-(m_{eq}+m_r)\omega^2 + m_{eq}\omega_n^2 + j\omega(2\xi m_{eq}\omega_n + R_r)\right](Y_l(\omega) + j\omega C_p) + j\omega m_{eq}\theta^2\phi^2(L)}\right| \tag{5.14}$$

$$\left|\frac{v(t)}{Qe^{j(\omega t + k(r-\bar{a}))}}\right| = \left|\frac{\rho_0 c_0 Aj\omega\theta\left(\frac{jk}{4\pi r(1-jk\bar{a})}\right) m_{eq}\phi^2(L)}{\left[-(m_{eq}+m_r)\omega^2 + m_{eq}\omega_n^2 + j\omega(2\xi m_{eq}\omega_n + R_r)\right](Y_l(\omega) + j\omega C_p) + j\omega m_{eq}\theta^2\phi^2(L)}\right| \tag{5.15}$$

$$\left|\frac{\Pi(t)}{(Qe^{j(\omega t + k(r-\bar{a}))})^2}\right| = \frac{1}{R_l}\left|\frac{\rho_0 c_0 Aj\omega\theta\left(\frac{jk}{4\pi r(1-jk\bar{a})}\right) m_{eq}\phi^2(L)}{\left[-(m_{eq}+m_r)\omega^2 + m_{eq}\omega_n^2 + j\omega(2\xi m_{eq}\omega_n + R_r)\right](Y_l(\omega) + j\omega C_p) + j\omega m_{eq}\theta^2\phi^2(L)}\right|^2 \tag{5.16}$$

where $m_r = X_r / \omega$ is the radiation mass, i.e. added mass, due to the reactive term given by Equation (5.12) and Π stands for the electrical power output (to avoid confusion with the pressure amplitude *P*). In the above formulation, the dielectric loss can easily be added by changing the real-valued capacitance C_p to the complex form of $C_p(1 - j\tan\delta)$, where $\tan\delta$ is the loss tangent of the piezoelectric material.

5.3 Optimal Power and Performance Enhancement by Resistive-Reactive Loading

5.3.1 Purely resistive electrical loading

The electrical load admittance in the presence of a purely resistive load of R_l is simply $Y_l = 1/R_l$. Then the expression for the power output normalized with respect to the incident acoustic pressure amplitude on the surface is obtained from Equation (6.16) as

$$\left|\frac{\Pi}{P^2}\right| = \frac{\omega_{n,fluid}}{k_{eq}} \frac{\alpha A^2 \kappa^2 \tilde{\omega}^2}{[(1-\tilde{\omega}^2) - 2\zeta_t \alpha \tilde{\omega}^2]^2 + [(1+\kappa^2-\tilde{\omega}^2)\alpha\tilde{\omega} + 2\zeta_t \tilde{\omega}]^2} \tag{5.17}$$

where $\omega_{n,fluid}$ is the natural frequency of the receiver bar submerged in fluid, and the remaining parameters are dimensionless load resistance α, dimensionless system electromechanical coupling term κ^2, dimensionless excitation frequency $\tilde{\omega}$, and total damping ratio (in fluid) ζ_t:

$$\alpha = R_l C_p \omega_{n,fluid},\ \kappa^2 = \frac{\theta^2}{k_{eq} C_p},\ \tilde{\omega} = \frac{\omega}{\omega_{n,fluid}},\ \zeta_t = \zeta_s + \frac{R_r}{2(m_{eq}+m_r)\omega_{n,fluid}} \tag{5.18}$$

The optimal electrical load [141] that gives the maximum power output can then be obtained as

$$\alpha_{opt}^2 = (R_{l,opt} C_p \omega_{n,fluid})^2 = \frac{1}{\tilde{\omega}^2} \frac{(1-\tilde{\omega}^2) + (2\zeta_t \tilde{\omega})^2}{(1+\kappa^2-\tilde{\omega}^2)^2 + (2\zeta_t \tilde{\omega})^2} \tag{5.19}$$

which can be substituted into Equation (5.17) to yield

$$\left| \frac{\Pi_{opt}}{P^2} \right| = \frac{\omega_{n,fluid}}{k_{eq}} \frac{\alpha_{opt} A^2 \kappa^2 \tilde{\omega}^2}{[(1-\tilde{\omega}^2) - 2\zeta_t \alpha_{opt} \tilde{\omega}^2]^2 + [(1+\kappa^2-\tilde{\omega}^2)\alpha_{opt} \tilde{\omega} + 2\zeta_t \tilde{\omega}]^2} \tag{5.20}$$

5.3.2 Resistive-inductive electrical loading

For the case of resistive-inductive loading (the resistive load, R_l, and the inductive load, L_l, are connected in parallel), $Y_l(\omega) = 1/R_l + 1/j\omega L_l$, and the power output normalized with respect to the incident pressure amplitude on the surface is:

$$\left| \frac{\Pi}{P^2} \right| = \frac{k_{eq} \alpha \beta^2 A^2 \kappa^2 \tilde{\omega}^4 / (m_{eq} + m_r)^2}{\omega_{n,fluid}^3 \left\{ \left[(\beta + 2\alpha\zeta_t)\tilde{\omega} - \beta(1+2\alpha\zeta_t)\tilde{\omega}^3 \right]^2 + \left[\alpha - (2\beta\zeta_t + \alpha(1+\beta+\beta\kappa^2))\tilde{\omega}^2 + \alpha\beta\tilde{\omega}^4 \right]^2 \right\}} \tag{5.21}$$

where

$$\alpha = R_l C_p \omega_{n,fluid}, \ \beta = L_l C_p \omega_{n,fluid}^2 \tag{5.22}$$

Following an optimization process in the same vein as Renno *et al.* [174], the optimal resistive and inductive loads are obtained as:

$$\alpha_{opt} = R_{l,opt} \omega_{n,fluid} C_p = \frac{\tilde{\omega}^4 + (4\zeta_t^2 - 2)\tilde{\omega}^2 + 1}{2\zeta_t \kappa^2 \tilde{\omega}^2} \tag{5.23}$$

$$\beta_{opt} = L_{l,opt}\omega_{n,fluid}^2 C_p = \frac{\tilde{\omega}^4 + (4\zeta_t^{\,2} - 2)\tilde{\omega}^2 + 1}{\tilde{\omega}^2(\tilde{\omega}^4 - (2 + \kappa^2 - 4\zeta_t^{\,2})\tilde{\omega}^2 + \kappa^2 + 1)}, \quad \tilde{\omega} < \tilde{\omega}_{sc} \text{ and } \tilde{\omega} > \tilde{\omega}_{oc} \tag{5.24}$$

Substituting Equations (5.23) and (5.24) in Equation (5.21) yields

$$\left|\frac{\Pi_{opt}}{P^2}\right| = \frac{k_{eq}A^2}{8\zeta_t\omega_{n,fluid}^3(m_{eq} + m_r)^2}, \quad \tilde{\omega} < \tilde{\omega}_{sc} \text{ and } \tilde{\omega} > \tilde{\omega}_{oc} \tag{5.25}$$

(for resistive-inductive loading)

It should be noted that, β_{opt} given by Equation (5.24) is valid only outside the short- and open-circuit resonance frequencies [174], i.e. for $\tilde{\omega} < \tilde{\omega}_{sc}$ and $\tilde{\omega} > \tilde{\omega}_{oc}$, therefore Equation (5.25) is valid only for this range under optimal resistive-inductive loading. The optimal inductance given by Equation (5.24) would be negative between the short- and open-circuit resonance frequencies, implying that optimal capacitive tuning should be performed for $\tilde{\omega}_{sc} < \tilde{\omega} < \tilde{\omega}_{oc}$, as discussed next.

5.3.3 Resistive-capacitive electrical loading

For the case of resistive-capacitive loading (the resistive load, R_l, and the capacitive load, C_l, are connected in parallel), $Y_l(\omega) = 1/R_l + j\omega C_l$, and the power output normalized with respect to the incident pressure amplitude on the surface is

$$\left|\frac{\Pi}{P^2}\right| = \frac{k_{eq}\alpha A^2\kappa^2\tilde{\omega}^4/(m_{eq} + m_r)^2}{\omega_{n,fluid}^3\left\{\left[(2\alpha\gamma\zeta_t\tilde{\omega}^2 - 1)\tilde{\omega} + (1 + 2\alpha\zeta_t)\tilde{\omega}^3\right]^2 + \left[\alpha\gamma(1 - \tilde{\omega}^2) + 2\zeta_t + \alpha(1 + \kappa^2 - \tilde{\omega}^2)\right]^2\tilde{\omega}^4\right\}} \tag{5.26}$$

where

$$\alpha = R_l C_p \omega_{n,fluid}\,,\ \gamma = C_l / C_p \tag{5.27}$$

yielding the following optimal parameters:

$$\alpha_{opt} = R_{l,opt}\omega_{n,fluid} C_p = \frac{\tilde{\omega}^4 + (4\zeta_t^{\,2} - 2)\tilde{\omega}^2 + 1}{2\zeta_t \kappa^2 \tilde{\omega}^2} \tag{5.28}$$

$$\gamma_{opt} = C_{l,opt} / C_p = \frac{-(\tilde{\omega}^4 - (2 + \kappa^2 - 4\zeta_t^{\,2})\tilde{\omega}^2 + \kappa^2 + 1)}{\tilde{\omega}^4 + (4\zeta_t^{\,2} - 2)\tilde{\omega}^2 + 1},\quad \tilde{\omega}_{sc} < \tilde{\omega} < \tilde{\omega}_{oc} \tag{5.29}$$

Using Equations (5.28) and (5.29) in Equation (5.26) leads to

$$\left|\frac{\Pi_{opt}}{P^2}\right| = \frac{k_{eq} A^2}{8\zeta_t \omega_{n,fluid}^3 (m_{eq} + m_r)^2},\quad \tilde{\omega}_{sc} < \tilde{\omega} < \tilde{\omega}_{oc} \text{ (for resistive-capacitive loading)} \tag{5.30}$$

which is identical to Equation (5.25) but valid for frequencies between the short- and open-circuit resonance values, i.e. for $\tilde{\omega}_{sc} < \tilde{\omega} < \tilde{\omega}_{oc}$, in capacitance tuning. Briefly, the optimal resistive-inductive loading results in broadband power output for $\tilde{\omega} < \tilde{\omega}_{sc}$ and $\tilde{\omega} > \tilde{\omega}_{oc}$, while the optimal resistive-capacitive loading yields broadband power output for $\tilde{\omega}_{sc} < \tilde{\omega} < \tilde{\omega}_{oc}$. Note that the resulting broadband power output (Π_{opt} / P^2) will not have a flat spectrum due to frequency-dependent fluid loading effects.

5.4 Case Studies, Model Validation, and Performance Enhancement

5.4.1 Receiver properties and finite-element model simulations

Analytical model results are compared with numerical simulations performed by 3-D finite-element modeling (FEM) in COMSOL Multiphysics 4.2 for model validation using fixed-free conditions. The receiver investigated in this case study is a cylindrical PZT-5H bar

submerged in water (with thickness L = 20 mm and diameter d = 6 mm). The material properties are listed in Table 5.1 Among the standard parameters of PZT-5H, the mechanical quality factor is assumed to be the only source of *in vacuo* dissipation, this is a reasonable assumption (since external fluid damping is already incorporated by the model). Therefore the purely mechanical (material) damping ratio is approximated as 0.77% based on the mechanical quality factor of PZT-5H in this table. The dielectric loss is neglected although it can easily be included. Figure 5.3 shows a typical demonstration of spherical wave excitation for a fixed-free fully submerged piezoelectric receiver bar over one period of excitation at its fundamental resonance frequency in open-circuit condition (47.7 kHz). The details of the spherical source location and the piezoelectric bar were previously shown in Figure 6.2a. The acoustic pressure field in the fluid domain and the piezoelectric longitudinal displacements are shown in each subgraph.

Table 5.1. Material properties of the PZT-5H receiver bar used in analytical and FEM simulations ($\varepsilon_0 = 8.854$ pF/m is the permittivity of free space and $Q_m = 65$ is the mechanical quality factor).

Material	PZT-5H
Elastic compliance, s_{33}^E [pm^2/N]	20.7
Mass density, ρ [kg/m^3]	7500
Piezoelectric constant, d_{33} [pm/V]	593
Relative permittivity, $\varepsilon_{33}^T/\varepsilon_0$	3400
Equivalent capacitance, $C_p = \varepsilon_{33}^T$A/L [pF]	42.5
Electromechanical coupling, θ [C/m]	0.067
Mechanical damping ratio, $\zeta = 1/2Q_m$	0.0077

In the following sections, the goal is first to validate the analytical model with comparisons against finite-element simulations for different parameter values in open-circuit conditions. Then the analytical model is employed to extract and optimize the transmitted power for finite values of load impedance under resistive and resistive-reactive electrical loading.

5.4.2 Analytical vs. finite-element model frequency response results

The longitudinal displacement at the top end of the bar (x in the analytical derivation) and voltage output are obtained from COMSOL as frequency response functions and compared with the analytical results.

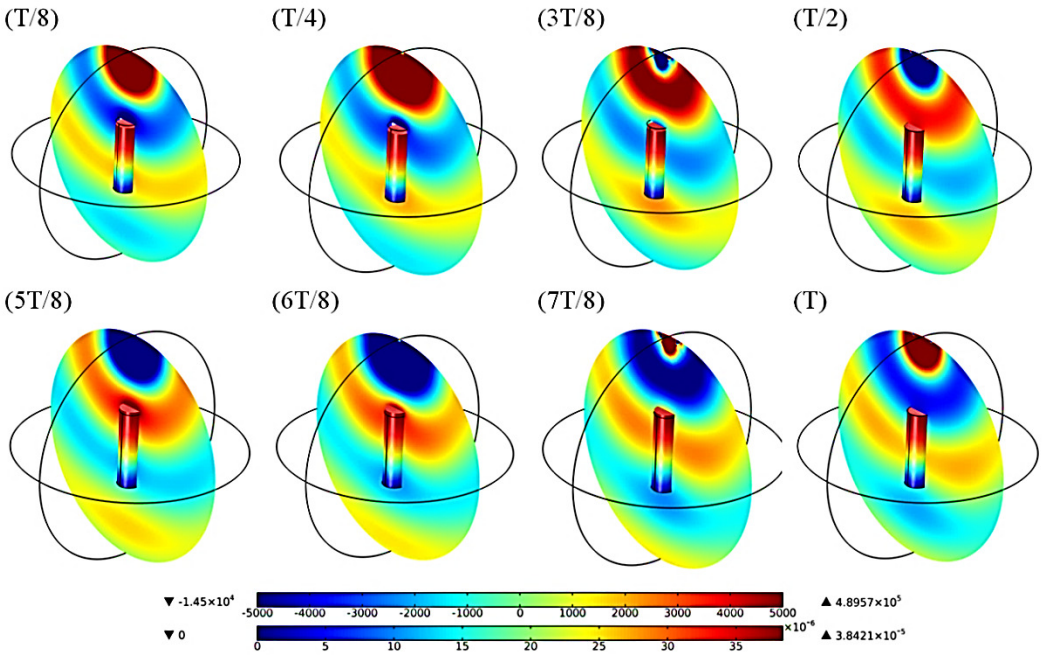

Figure 5.3. Multiphysics finite-element simulation for spherical wave excitation of a fixed-free piezoelectric receiver bar submerged under water in open-circuit condition. Acoustic pressure in fluid domain (first color bar, in Pa) and longitudinal displacement of the piezoelectric bar at its free end (second color bar, in mm) are shown for one period (T) of harmonic excitation at the fundamental open-circuit resonance frequency (47.7 kHz).

The relationships between the electromechanical outputs and system parameters, such as the distance of the receiver from the source (r), the level of source strength (Q), and the receiver diameter (d), are explored and shown in Figure 5.4 to Figure 5.6 .

Figure 5.4 shows that the mechanical and electrical response amplitudes decrease monotonically as the source-to-receiver distance increases. The dependence of the response amplitude to the distance from the source is nonlinear (which makes sense from the analytical standpoint due to the hyperbolic dependence of the pressure to distance r in Equation (5.13)). The results show very good agreement between the analytical and numerical (FEM) predictions.

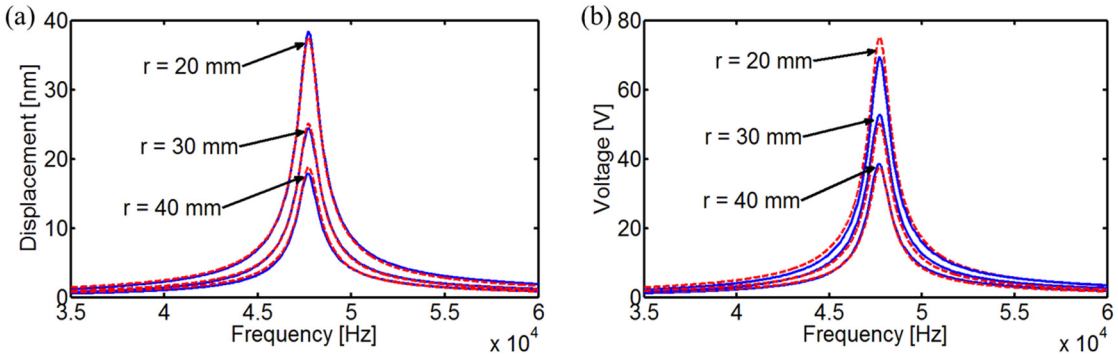

Figure 5.4. Comparison of the analytical (red dashed lines) and FEM (blue solid lines) frequency response curves for different values of source-to-receiver distance (r) in open-circuit conditions: (a) Longitudinal tip displacement and (b) voltage output of the receiver bar (Q = 5.65 cm^3/s; d = 6 mm).

Next, the variations of vibration (longitudinal tip displacement) and voltage frequency response magnitudes of the receiver with source strength are shown in Figure 5.5. The results indicate that increasing source strength amplifies the response of the receiver significantly. It is worth mentioning that the small-amplitude approximation [172] (the assumption used in

Equation (5.13)) requires that the displacement of the source surface should be much less than the radius of the source ($U_0/\omega \ll \bar{a}$).

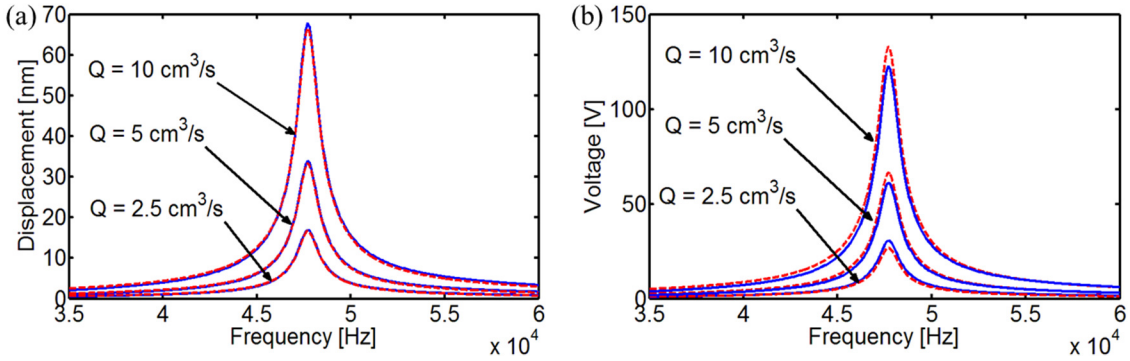

Figure 5.5. Comparison of the analytical (red dashed lines) and FEM (blue solid lines) frequency response curves for different values of source strength (Q) in open-circuit conditions: (a) Longitudinal tip displacement and (b) voltage output of the receiver bar (r = 20 mm; d = 6 mm).

Figure 5.6 shows the effects of receiver diameter on the electromechanical frequency response functions. It is observed that, with increased cross-sectional area of the receiver, the underwater resonance frequency shifts to the left slightly; additionally the peak vibration and voltage amplitudes decrease significantly. This is because the acoustic radiation resistance (or added damping) and reactance (or radiation added mass) are amplified in Equations (5.11) and (5.12) due to increased piston area (i.e. cross-sectional area) that vibrates against the fluid loading at the free end of the receiver bar. Therefore, in order to minimize, in particular, the radiation damping of the receiver bar, it may be preferable to reduce the cross-sectional area of the surface that interacts with the fluid. It should be noted that, while the voltage output decreases with increased receiver diameter, the capacitance increases, yielding increased current extraction.

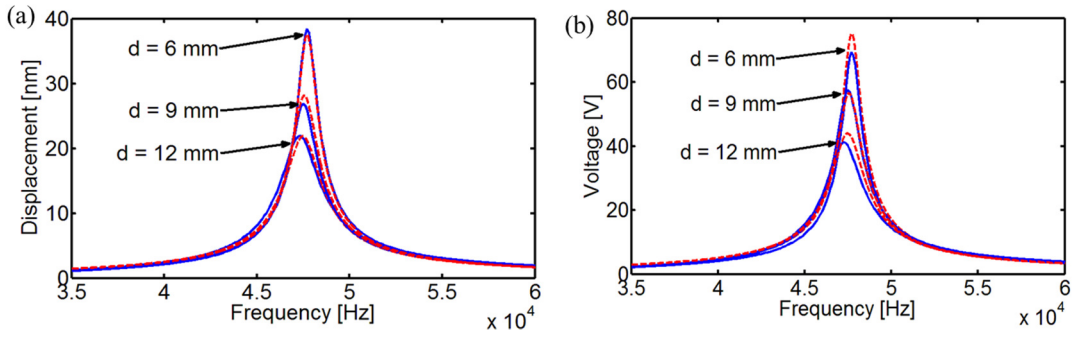

Figure 5.6. Comparison of the analytical (red dashed lines) and FEM (blue solid lines) frequency response curves for different values of receiver diameter (d) in open-circuit conditions: (a) Longitudinal tip displacement and (b) voltage output of the receiver bar (Q = 5.65 cm^3/s, r = 20 mm).

5.4.3 Power output for resistive and resistive-reactive loading

Having validated the analytical model results for open-circuit conditions against 3-D FEM simulations, finite load resistance cases are considered next (which cannot easily be simulated in standard FEM environment). The purely resistive loading case is considered first ($Y_l = 1/R_l$ is the load admittance). Figure 5.7a shows the longitudinal tip displacement FRFs obtained from Equation (6.14) for a set of resistors and a broad range of frequencies which cover the fundamental vibration mode and for fixed values of distance from the source (r = 20mm) and diameter of the piezoelectric receiver (d = 6mm). The frequency response curves are given per source strength in agreement with Equation (6.14). The electrical load resistance values range from 100 Ω (close to short-circuit conditions) to 100 MΩ (close to open-circuit conditions). As the load resistance is increased, the resonance frequency shifts from the short-circuit resonance frequency (31.4 kHz) to the open-circuit resonance frequency (47.7 kHz).

From Figure 5.7a, one can observe that with the increased load resistance, the peak vibration amplitude decreases significantly from the peak of short-circuit condition to a certain value, and then is amplified toward the open-circuit resonance frequency with a further increase load resistance. This phenomenon happens because of changing the electrical boundary condition of the receiver (which alters the elastic modulus) and Joule heating (for moderate values of load resistance), as in standard vibration-based piezoelectric energy harvesters [1, 147]. In Figure 5.7b, by changing the electrical load resistance from short- to open-circuit conditions, the voltage output obtained from Equation (6.15) increases monotonically at each frequency, and the resonance frequency of each finite load resistance takes a value between the short- and open-circuit resonance frequencies.

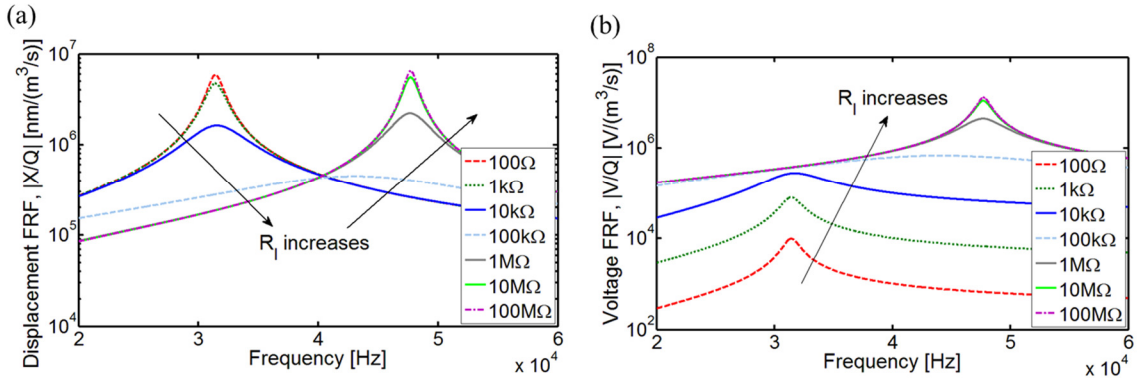

Figure 5.7. (a) Tip displacement-to-source strength FRFs and (b) voltage output-to-source strength FRFs of the receiver for broad range of load resistance (r = 20mm, d = 6mm).

The electrical power FRFs obtained from Equation (6.16) are plotted in Figure 5.8 for the same set of resistors. An optimal resistive load can be found at each excitation frequency. Among the finite set of resistance values in this graph, the maximum power output is obtained for the load resistance of 1 MΩ close to open-circuit resonance frequency. However, the optimal electrical load changes dramatically with changing excitation

frequency. A more global picture is explored next by using Equation (6.16) to construct a surface plot.

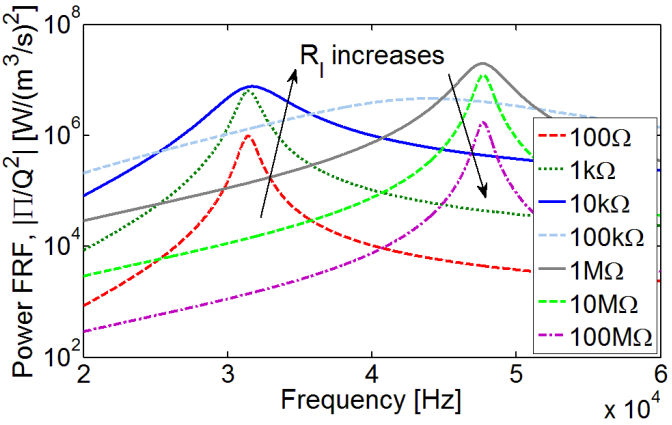

Figure 5.8. Power output-to-source strength FRFs of the receiver for a set of electrical load resistance values (r = 20mm, d = 6mm).

Power output of the receiver bar normalized with respect to source strength squared versus load resistance and excitation frequency is plotted in Figure 5.9 for fixed values of distance from the source (r = 20mm) and diameter of the piezoelectric receiver (d = 6mm). The resonance frequency smoothly shifts from the short-circuit value (31.4 kHz) to the open-circuit value (47.7 kHz). The local peak power at 31.4 kHz is 8.82 μW/(cm^3/s)^2 for the electrical load of 2.5 kΩ while the global peak at 47.7 kHz is 18.8 μW/(cm^3/s)^2 for the optimal load of 2.5 MΩ. It is important to note that the short- and open-circuit resonance excitations with the same source strength do not yield the same power output for the PZT-5H receiver, as a result of significant damping effects in fluid (soft piezoelectric receiver combined with fluid damping).

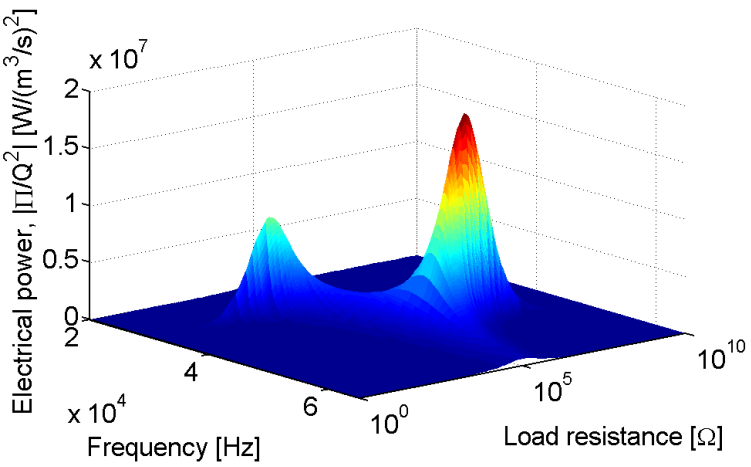

Figure 5.9. Power output (normalized with respect to source strength squared) for the PZT-5H receiver versus excitation frequency and load resistance (r = 20mm, d = 6mm).

The resistive and resistive-reactive load optimization results (for power output normalized by the incident acoustic pressure squared acting on the free end surface of the receiver) discussed in Section 6.3 are plotted in Figure 5.10 for the optimal purely resistive circuit, for the optimal resistive-inductive circuit (for frequencies less than 31.4 kHz and greater than 47.7 kHz), and for the optimal resistive-capacitive circuit (for frequencies in between 31.4 kHz and 47.7 kHz). It is clearly demonstrated that, by optimizing the inductor/capacitor and resistor values simultaneously, broadband power generation is successfully achieved over a range of frequencies. The broadband power amplitude behavior is not flat (unlike the case of optimal resistive-inductive loading in vibration-based energy harvesters [174]) is because the fluid loading effects. It is worth adding that the inductance value required for conjugate matching is inversely proportional to capacitance and frequency squared in Equation (5.24). As long as the inductance requirement is low enough, a passive inductor can be employed for broadband behavior. To keep the inductance requirement low, a high-capacitance piezoelectric stack transducer [175] can be used instead of a monolithic

receiver (so that μF-level capacitance is achieved instead of pF/nF-level capacitance) for which the above formulating still applies without loss of generality by using the effective values of d_{33}^{eff} and C_p for the entire cylindrical stack [175]. Alternatively the excitation frequency can be kept high to reduce the inductance requirement. Otherwise, in the case of a large inductance requirement, a synthetic inductor (or synthetic impedance) circuit [176, 177] would be necessary (and part of the transmitted power would have to be used for that).

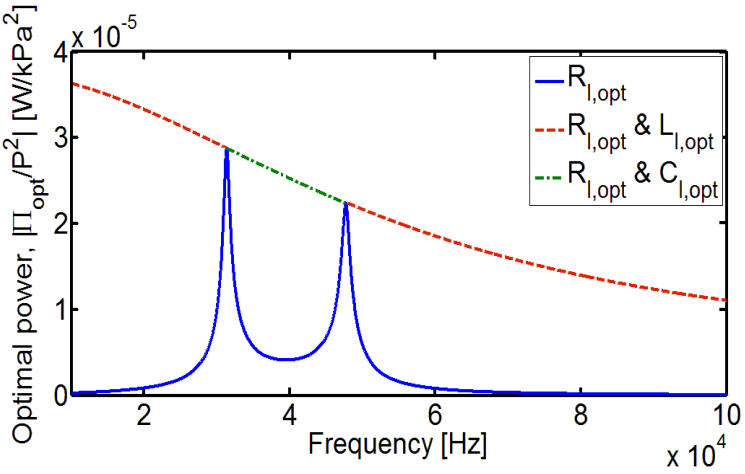

Figure 5.10. Optimal receiver power output frequency response curves (normalized by the incident acoustic pressure squared acting on the free end surface of the receiver) for the optimal resistive and resistive-reactive electrical loading cases.

5.4.4 The effect of receiver material: Case study for PZT-8

As the last case study, it is intended to explore the same problem (with a focus on purely resistive electrical loading) for an alternative piezoelectric material: PZT-8. The material properties for the PZT-8 receiver bar are listed in Table 5.2.

The dimensions of the receiver, source-to-receiver distance, fluid parameters, etc. are all kept the same as in the previous case study for PZT-5H; only the material properties are changed. The mechanical quality factor of PZT-8 ($Q_m = 1000$) is more than an order of magnitude larger than that of PZT-5H ($Q_m = 65$), whereas the piezoelectric constant of PZT-8 ($d_{33} = 225$ pm/V) is lower as compared to PZT-5H ($d_{33} = 593$ pm/V). The capacitance and stiffness values also differ, resulting in the system coupling term (κ^2) values of 0.88 and 1.54 for PZT-8 and PZT-5H, respectively.[3] Therefore, PZT-8 offers reduced mechanical loss (which is favorable) at the expense of reduced electromechanical coupling as compared to PZT-5H.

Table 5.2. Material properties of the PZT-8 receiver bar ($Q_m = 1000$) used for performance comparison against the PZT-5H receiver.

Material	PZT-8
Elastic compliance, s_{33}^E [pm^2/N]	13.5
Mass density, ρ [kg/m^3]	7600
Piezoelectric constant, d_{33} [pm/V]	225
Relative permittivity, $\varepsilon_{33}^T/\varepsilon_0$	1000
Equivalent capacitance, $C_p = \varepsilon_{33}^T$A/L [pF]	12.5
Electromechanical coupling, θ [C/m]	0.034
Mechanical damping ratio, $\zeta = 1/2Q_m$	0.0005

[3] The receiver's system level coupling term (κ^2) should not be confused with the piezoelectric material's extensional coupling factor ($k_{33}^2 = d_{33}^2 / s_{33}^E \varepsilon_{33}^T$), although they are related to each other.

The surface plot of the PZT-8 receiver's power output (normalized with respect to source strength squared) versus excitation frequency and load resistance is given in Figure 5.11. As compared to the PZT-5H counterpart of this graph previously given by Figure 5.9, two things are noteworthy. First, the overall resonant power output of the PZT-8 receiver is larger than that of the PZT-5H receiver. Second, the short- and open-circuit resonance power outputs of the PZT-8 receiver (which has lower mechanical, and therefore, lower total damping) are very similar to each other as in strongly coupled and lightly damped piezoelectric energy harvesters [1]. The short- and open-circuit resonance power output values are around 39 μ W/(cm^3/s)^2 (for 3.5 kΩ and at 38.7 kHz) and 41 μ W/(cm^3/s)^2 (for 15 MΩ and at 50.9 kHz), respectively. These resonant power outputs for the PZT-8 receiver are larger than those of the PZT-5H counterpart by factors of 4 and 2, respectively. Therefore, the hard ceramic PZT-8 (with reduced material loss at the expense of lower electromechanical coupling) should be preferred to the soft ceramic PZT-5H as the receiver material for resonant excitation. The same conclusion applies to soft versus hard single crystals [178, 179], e.g. PMN-PZT-Mn should be preferred to PMN-PT or PMN-PZT.

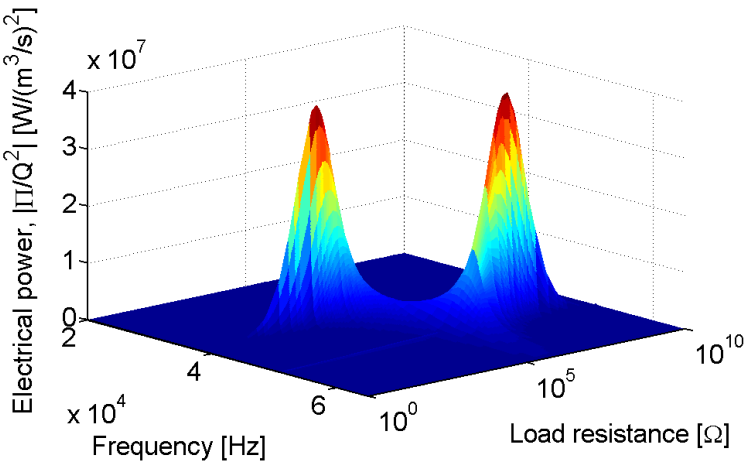

Figure 5.11. Power output (normalized with respect to source strength squared) for the PZT-8 receiver versus excitation frequency and load resistance (r = 20mm, d = 6mm).

5.5 Summary and Conclusions

As an alternative to widely used methods of contactless energy transfer (such as inductive coupling), the use of piezoelectric transduction for ultrasonic energy transfer to wireless electronic components (such as medical implants or sensors located in hazardous environments) has received growing attention over the last few years. However, fully coupled acoustic-piezoelectric structure interaction modeling that combines the source and the receiver dynamics with fluid domain as well as the electrical load has not been covered in the existing literature. In this chapter of the dissertation, contactless ultrasonic acoustic energy transfer is investigated by analytical and numerical multiphysics modeling along with several case studies with an emphasis on analytical model validation and performance enhancement. *In vacuo* and underwater dynamics of a cylindrical piezoelectric receiver are modeled for longitudinal vibrations under harmonic acoustic excitation. The fluid loading effects (resistive and reactive radiation impedance components) are added to the *in vacuo* electromechanical model to predict the underwater electromechanical response forms of the piezoelectric receiver. In addition to successful model validations against 3-D finite-element simulations, a study on the effects of several system parameters (e.g. source strength, receiver dimensions, and source-to-receiver distance) is performed. Optimal resistive-reactive electrical loading results in substantially enhanced broadband power transfer compared to the purely resistive electrical loading case. Soft (PZT-5H) and hard (PZT-8) piezoelectric receivers are considered and significant performance enhancement is reported due to using PZT-8. Therefore, receivers made from hard piezoelectric ceramics (e.g. PZT-8, PZT-4) and single crystals (e.g. PMN-PZT-Mn) outperform those made from soft piezoelectric ceramics (e.g. PZT-5H, PZT-5A) and single crystals (e.g. PMN-PT, PMN-PZT)

for resonant contactless power transfer. The electromechanically and acoustically coupled analytical model developed in this work can be used to predict and optimize the coupled system dynamics with very good accuracy and substantially improved computational efficiency as compared to using commercial finite-element simulation packages.

6 ULTRASONIC POWER TRANSFER FROM A SPHERICAL ACOUSTIC WAVE SOURCE TO A FREE-FREE PIEZOELECTRIC RECEIVER: MODELING AND EXPERIMENT

6.1 Introduction

This chapter investigates analytical modeling and experimental validation of UAET for low-power electricity transfer to exploit in wireless applications ranging from medical implants to underwater sensor systems. A piezoelectric receiver bar is excited by incident acoustic waves originating from a source of known strength located at a specific distance from the receiver. The receiver is a free-free piezoelectric cylinder operating in the 33-mode of piezoelectricity with a fundamental resonance frequency above the audible frequency range. In order to extract the electrical power output, the piezoelectric receiver bar is shunted to a generalized resistive-reactive circuit. The goal is to quantify the electrical power delivered to the load (connected to the receiver) in terms of the source strength. Experimental validations are presented along with parameter optimization studies. Sensitivity of the electrical power output to the excitation frequency in the neighborhood of the receiver's underwater resonance frequency, source-to-receiver distance, and source-strength level are reported. Resistive and resistive-reactive electrical loading cases are discussed for performance enhancement and frequency-wise robustness. Simulations and experiments reveal that the presented multiphysics analytical model for UAET can be used to predict the coupled system dynamics with very good accuracy.

6.2 Theory: Acoustic-Piezoelectric Structure Coupling of a Spherical Wave Source and a 33-Mode Receiver

6.2.1 Governing distributed-parameter equations

Figure 6.1 displays a schematic and a finite-element simulation snapshot of a piezoelectric receiver fully submerged in fluid (e.g. water) and excited by incident acoustic waves originating from a spherical source of known strength Q. The receiver is a free-free piezoelectric cylinder operating in the 33-mode of piezoelectricity (3-direction is the axial direction, i.e. ξ-axis) with a fundamental resonance frequency above the human audible frequency range. The top and bottom faces of the receiver have perfectly conductive electrodes of negligible thickness. In order to quantify the electrical power output, an external electrical load with the admittance Y_l is connected to the electrodes (in the case of purely resistive electrical loading $Y_l = 1/R_l$, where R_l is the load resistance – note that complex conjugate loading for broadband performance will be discussed later following the work done in Chapter 5).

For the fluid-loaded and electrically-loaded free-free piezoelectric bar excited by the acoustic wave, the coupled partial differential equation for longitudinal vibrations of the receiver and the AC electrical circuit equation can be derived as

$$\begin{aligned} &-YA\frac{\partial^2 u(\xi,t)}{\partial \xi^2} - c_\alpha \frac{\partial^3 u(\xi,t)}{\partial \xi^2 \partial t} + c_\beta \frac{\partial u(\xi,t)}{\partial t} + R_r[\delta(\xi)]\frac{\partial u(\xi,t)}{\partial t} + R_r[\delta(\xi - L)]\frac{\partial u(\xi,t)}{\partial t} \\ &+m\frac{\partial^2 u(\xi,t)}{\partial t^2} - \theta v(t)[\delta(\xi - L) - \delta(\xi)] = f_t(t)[\delta(\xi)] - f_b(t-\tau)[\delta(\xi - L)] \end{aligned} \tag{6.1}$$

$$C_p \frac{dv(t)}{dt} + Y_l v(t) + \int_0^L \theta \frac{\partial^2 u(\xi,t)}{\partial t \partial \xi} d\xi = 0 \tag{6.2}$$

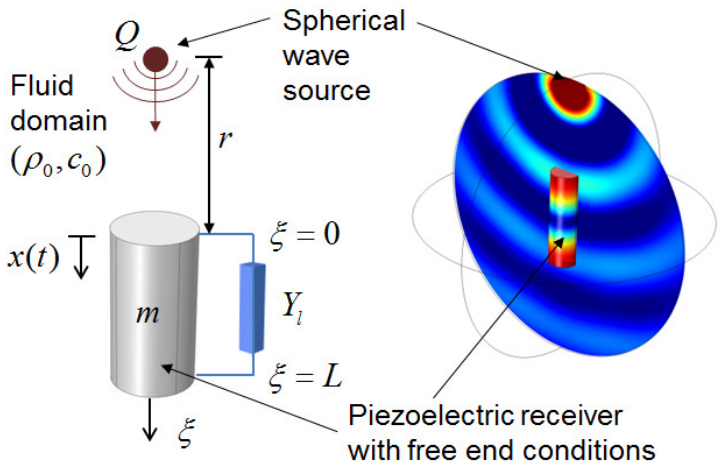

Figure 6.1. Schematic representation (left) and 3-D finite-element simulation snapshot (right) of contactless acoustic energy transfer from a spherical wave source to an axially-poled cylindrical piezoelectric receiver bar shunted to an electrical load from its surface electrodes (which cover the top and bottom faces).

where $u(\xi,t)$ is the displacement response of the bar at the axial position ξ and time t, $v(t)$ is the voltage output across the electrical load, Y is the Young's modulus at constant electric field, A is the cross sectional area (therefore YA is the axial rigidity of the receiver under short-circuit condition), m is the mass per unit length, c_α is the stiffness-proportional damping coefficient, c_β is the mass-proportional damping coefficient (c_α and c_β represent the generalized *in vacuo* dissipation in the proportional damping form – the fluid damping is accounted for separately), θ is the electromechanical coupling term in physical coordinates, and $\delta(\xi)$ is the Dirac delta function. Furthermore, in Equation (6.2), C_p and Y_l are the internal capacitance of the piezoelectric receiver and the admittance of the external load, respectively. The excitation forces due to the incident acoustic pressure are $f_t(t) = p(t)A$ at $\xi = 0$ and $f_b(t-\tau) = \mu p(t-\tau)A$ at $\xi = L$, given in terms of the acoustic pressure

$p(t) = Pe^{j\omega t}$ evaluated at the top surface ($\xi = 0$) and the bottom surface ($\xi = L$) of the receiver, where *P* is the complex pressure amplitude, ω is the excitation frequency, j is the unit imaginary number, μ is the ratio of the acoustic pressure on the bottom surface to that on the top surface, and τ is the time delay of f_b relative to f_t (therefore, τ depends of the wave propagation speed in fluid and the receiver length, *L*). Moreover, the dissipative term R_r in Equation (6.1) is the resistive component of the fluid radiation impedance [172] (for a circular piston oscillating on one side with no baffle) defined as $R_r = \sigma_R(ka)\rho_0 c_0 A\left(1 - J_1(2ka)/ka\right)$, where J_1 is the first-order Bessel function of the first kind, $k = \omega/c_0$ is the wave number, c_0 is the speed of sound in the surrounding fluid, ρ_0 is the mass density of the surrounding fluid, a is the radius of the piston, and $\sigma_R(ka)$ accounts for the modification relative to baffled piston (see figure 10.19 in [168]).[4] The pressure field created by a pulsating spherical harmonic wave source in an infinite, homogeneous, and isotropic medium is $p(t) = \rho_0 c_0 \left[-jkQ/4\pi r(1 - jk\bar{a})\right] e^{j(\omega t + k(r - \bar{a}))}$ [173, 180], where r is source-to-receiver distance, $\bar{a}$ is the source radius, and Q is the acoustic source strength of the spherical wave generator (transmitter). As depicted in Figure 6.1, the longitudinal strain axis and the electrical poling axis (perpendicular to the surface electrodes) are coincident, and therefore the receiver bar is employed in the 33-mode of piezoelectricity. The dielectric loss is neglected, although it can easily be included by using a complex permittivity including the loss tangent of the piezoelectric material so that C_p becomes $C_p(1 - j\delta_\varepsilon)$. While the present work is focused on AC electrical output of the receiver, it is possible to

[4] Therefore the added damping due to fluid loading is directly given in Equation (6.1) whereas the added mass at the free ends is to be accounted for as boundary conditions.

account for AC-DC conversion and rectification in the circuit dynamics [1, 102, 181] with a piecewise form of Equation (6.2).

6.2.2 Fluid-loaded fundamental mode shape and natural frequency

The linear displacement at the free end of piezoelectric receiver bar ($x(t)$ in Figure 6.1, where $x(t)=u(0,t)$) due to harmonic excitation at or around the fundamental longitudinal (axial) vibration mode is obtained by modal analysis of the distributed-parameter electromechanical system with a focus on the first mode only (i.e. higher modes are excluded in the following). The longitudinal tip displacement of the piezoelectric receiver bar at time t is then

$$x(t)=u(\xi,t)\big|_{\xi=0}=\phi(0)\eta(t) \tag{6.3}$$

where $\phi(0)$ and $\eta(t)$ are, respectively, the mass-normalized eigenfunction evaluated at $\xi=0$ (in Figure 6.1) and the generalized modal coordinate for the longitudinal vibration mode of a free-free uniform bar. The mass normalized elastic-mode eigenfunction is obtained from the corresponding undamped and electromechanically uncoupled (short-circuit) free vibration problem (which satisfies the companion mass and stiffness forms of the orthogonally conditions) is obtained as[5]

$$\phi(\xi)=\frac{\left[\cos(\alpha\xi/L)-\alpha\beta\sin(\alpha\xi/L)\right]}{\sqrt{\int_0^L m\left[\cos(\alpha\xi/L)-\alpha\beta\sin(\alpha\xi/L)\right]^2 d\xi+m_r\left[\cos(\alpha)-\alpha\beta\sin(\alpha)\right]^2+m_r}} \tag{6.4}$$

[5] Note that the rigid-body mode resulting from the positive semi-definite nature of the system (with free-free boundary conditions) is not of interest.

Here, the eigenvalue (α) of the fundamental mode is the first non-zero root of the transcendental equation $(\alpha^2\beta^2 - 1)\tan\alpha - 2\alpha\beta = 0$, while the radiation mass – to – receiver mass ratio is $\beta = m_r/mL$ (where $m_r = X_r/\omega$ is the radiation mass, i.e. added mass, due to reactive component of fluid radiation impedance, $X_r = \sigma_X(ka)\rho_0 c_0 A\left(H_1(2ka)/ka\right)$, H_1 is the Struve function of the first kind, and $\sigma_X(ka)$ is the modification relative to baffled piston (e.g. figure 10.19 in [168])). The fundamental short-circuit natural frequency is $\omega_n = \alpha\sqrt{1/s_{33}^E \rho L^2}$ (obtained for the first non-zero eigenvalue α), where s_{33}^E is the longitudinal elastic compliance at constant electric field and ρ is mass density of piezoelectric receiver bar.

6.2.3 Lumped-parameter form and response to harmonic excitation

The electromechanically coupled equations of forced vibration and current balance are expressed for the fundamental mode in lumped-parameter form (reduced from distributed-parameter solution) as

$$\begin{aligned}&\ddot{x}(t) + \left[2\zeta\omega_n + R_r\phi^2(0) + R_r\phi^2(L)\right]\dot{x}(t) + \omega_n^2 x(t) - \theta[\phi(0)\phi(L) - \phi^2(0)]v(t)\\ &= f_t(t)\phi^2(0) - f_b(t-\tau)\phi(0)\phi(L)\end{aligned} \tag{6.5}$$

$$C_p\phi(0)\dot{v}(t) + Y_l\phi(0)v(t) + \theta[\phi(L) - \phi(0)]\dot{x}(t) = 0 \tag{6.6}$$

Here, $\phi(0)$ and $\phi(L)$ are, respectively, the mass-normalized fundamental elastic mode eigenfunction evaluated at $\xi = 0$ and $\xi = L$ (in Figure 6.1) for the longitudinal vibration mode of a free-free uniform fully submerged bar (Equation (6.4)), and an over-dot represents differentiation with respect to time. Fluid absorption and scattering effects on the incident

pressure are assumed to be negligible for the frequency range of interest and receiver dimensions (confirmed with the experiments).

The steady-state electromechanical response to harmonic excitation is also harmonic and is of the form $x(t) = Xe^{j\omega t}$ and $v(t) = Ve^{j\omega t}$ based on the linear system assumption. Then the fundamental-mode voltage output per source strength frequency response function (FRF) can be obtained as

$$\frac{v(t)}{Qe^{j(\omega t + k(r-\bar{a}))}} = \frac{j\omega\theta\left(\rho_0 c_0 A \frac{jk}{4\pi r(1-jk\bar{a})}\right)[\phi(0) - \mu\phi(L)e^{-j\varphi}][\phi(L) - \phi(0)]}{\left\{\omega_n^2 - \omega^2 + j\omega\left[2\zeta\omega_n + R_r[\phi^2(0) + \phi^2(L)]\right]\right\}\left(Y_l(\omega) + j\omega C_p\right) + j\omega\theta^2[\phi(L) - \phi(0)]^2} \tag{6.7}$$

where $\varphi = \omega\tau$ is the phase angle between the excitation forces at the top and bottom surfaces of the cylindrical receiver.

6.2.4 Electromechanical impedance of the fluid-loaded receiver

Deriving an expression for the impedance of the fluid-loaded receiver is useful for identification of its parameters under electrical excitation. In Equation (6.5), changing the input to $v(t) = Ve^{j\omega t}$ and setting $f_t(t) = f_b(t-\tau) = 0$, while in Equation (6.6), replacing the current output $Y_l v(t)$ by the actuation current input $-i(t) = -Ie^{j\omega t}$, yields the following expression for the fluid-loaded receiver's electromechanical impedance $Z = V/I$:

$$Z(\omega) = \left\{ j\omega\left[C_p + \frac{\theta^2[\phi(L) - \phi(0)]^2}{\omega_n^2 - \omega^2 + j\omega\left[2\zeta\omega_n + R_r\phi^2(0) + R_r\phi^2(L)\right]}\right]\right\}^{-1} \tag{6.8}$$

which includes the fundamental longitudinal vibration mode only.

6.2.5 *Optimal power output and performance enhancement by resistive-reactive loading*

6.2.5.1 *Purely resistive electrical loading*

The electrical load admittance in the presence of a purely resistive load of R_l is simply $Y_l = 1/R_l$. Then the expression for the power output normalized with respect to the incident acoustic pressure amplitude on the top surface is obtained from Equation (6.7) as

$$\left|\frac{\Pi}{P^2}\right| = \frac{\omega_n}{k_{eq}} \frac{\chi A^2 \kappa^2 \tilde{\omega}^2}{[(1-\tilde{\omega}^2) - 2\zeta_t \chi \tilde{\omega}^2]^2 + [(1+\kappa^2-\tilde{\omega}^2)\chi\tilde{\omega} + 2\zeta_t \tilde{\omega}]^2} \tag{6.9}$$

where ω_n is the natural frequency of the receiver bar submerged in fluid, $k_{eq} = A/s_{33}^E L$ is the stiffness, and the remaining dimensionless parameters are load resistance χ, system-level electromechanical coupling term κ^2, excitation frequency $\tilde{\omega}$, and total damping ratio (in fluid) ζ_t:

$$\chi = R_l C_p \omega,\ \kappa^2 = \frac{\theta^2}{k_{eq} C_p}, \tilde{\omega} = \frac{\omega}{\omega_n},\ \zeta_t = \zeta + \frac{R_r[\phi^2(0) + \phi^2(L)]}{2\omega_n} \tag{6.10}$$

The optimal electrical load [141] that gives the maximum power output can then be obtained as

$$\chi_{opt} = R_{l,opt} C_p \omega_n = \frac{1}{\tilde{\omega}} \sqrt{\frac{(1-\tilde{\omega}^2) + (2\zeta_t \tilde{\omega})^2}{(1+\kappa^2-\tilde{\omega}^2)^2 + (2\zeta_t \tilde{\omega})^2}} \tag{6.11}$$

which can be substituted into Equation (6.9) to yield the optimal power FRF:

$$\left|\frac{\Pi_{opt}}{P^2}\right| = \frac{\omega_n}{k_{eq}} \frac{\chi_{opt} A^2 \kappa^2 \tilde{\omega}^2}{[(1-\tilde{\omega}^2) - 2\zeta_t \chi_{opt} \tilde{\omega}^2]^2 + [(1+\kappa^2-\tilde{\omega}^2)\chi_{opt}\tilde{\omega} + 2\zeta_t \tilde{\omega}]^2} \tag{6.12}$$

6.2.5.2 Resistive-inductive electrical loading

For the case of resistive-inductive loading (the resistive load, R_l, and the inductive load, L_l, are connected in parallel), $Y_l(\omega) = 1/R_l + 1/j\omega L_l$, and the power output normalized with respect to the incident pressure amplitude on the top surface is

$$\left|\frac{\Pi}{P^2}\right| = \frac{k_{eq}\chi\nu^2 A^2\kappa^2\tilde{\omega}^4/(m_{eq}+m_r)^2}{\omega_n^3\left\{\left[(\nu+2\chi\zeta_t)\tilde{\omega}-\nu(1+2\chi\zeta_t)\tilde{\omega}^3\right]^2+\left[\chi-(2\nu\zeta_t+\chi(1+\nu+\nu\kappa^2))\tilde{\omega}^2+\chi\nu\tilde{\omega}^4\right]^2\right\}} \tag{6.13}$$

where

$$\chi = R_l C_p \omega_n, \nu = L_l C_p \omega_n^2 \tag{6.14}$$

and $m_{eq} = \rho AL/\alpha^2$. Following an optimization process in the same vein as Renno *et al.* [174], the optimal resistive and inductive loads are obtained as

$$\chi_{opt} = R_{l,opt}\omega_n C_p = \frac{\tilde{\omega}^4 + (4\zeta_t^2 - 2)\tilde{\omega}^2 + 1}{2\zeta_t\kappa^2\tilde{\omega}^2} \tag{6.15}$$

$$\nu_{opt} = L_{l,opt}\omega_n^2 C_p = \frac{\tilde{\omega}^4 + (4\zeta_t^2 - 2)\tilde{\omega}^2 + 1}{\tilde{\omega}^2(\tilde{\omega}^4 - (2+\kappa^2-4\zeta_t^2)\tilde{\omega}^2 + \kappa^2 + 1)}, \quad \tilde{\omega} < \tilde{\omega}_{sc} \text{ and } \tilde{\omega} > \tilde{\omega}_{oc} \tag{6.16}$$

Substituting Equations (6.15) and (6.16) in equation (6.13) yields

$$\left|\frac{\Pi_{opt}}{P^2}\right| = \frac{k_{eq}A^2}{8\zeta_t\omega_n^3(m_{eq}+m_r)^2}, \quad \tilde{\omega} < \tilde{\omega}_{sc} \text{ and } \tilde{\omega} > \tilde{\omega}_{oc} \text{ (for resistive-inductive loading)} \tag{6.17}$$

It should be noted that, ν_{opt} given by Equation (6.16) is valid only outside the short- and open-circuit resonance frequencies [174], i.e. for $\tilde{\omega} < \tilde{\omega}_{sc}$ and $\tilde{\omega} > \tilde{\omega}_{oc}$, therefore Equation (6.17) is valid only for this range under optimal resistive-inductive loading. The optimal inductance given by Equation (6.16) would be negative between the short- and open-circuit

resonance frequencies, implying that optimal capacitive tuning should be performed for $\tilde{\omega}_{sc} < \tilde{\omega} < \tilde{\omega}_{oc}$, as discussed next.

6.2.5.3 Resistive-capacitive electrical loading

For the case of resistive-capacitive loading (the resistive load, R_l, and the capacitive load, C_l, are connected in parallel), $Y_l(\omega) = 1/R_l + j\omega C_l$, and the power output normalized with respect to the incident pressure amplitude on the end surfaces is

$$\left|\frac{\Pi}{P^2}\right| = \frac{k_{eq}\chi A^2\kappa^2\tilde{\omega}^4/(m_{eq}+m_r)^2}{\omega_n^3\left\{\left[(2\chi\gamma\zeta_t\tilde{\omega}^2-1)\tilde{\omega}+(1+2\chi\zeta_t)\tilde{\omega}^3\right]^2+\left[\chi\gamma(1-\tilde{\omega}^2)+2\zeta_t+\chi(1+\kappa^2-\tilde{\omega}^2)\right]^2\tilde{\omega}^4\right\}} \tag{6.18}$$

where

$$\chi = R_l C_p \omega_n, \ \gamma = C_l / C_p \tag{6.19}$$

yielding the following optimal parameters:

$$\chi_{opt} = R_{l,opt}\omega_n C_p = \frac{\tilde{\omega}^4+(4\zeta_t^2-2)\tilde{\omega}^2+1}{2\zeta_t\kappa^2\tilde{\omega}^2} \tag{6.20}$$

$$\gamma_{opt} = C_{l,opt}/C_p = \frac{-(\tilde{\omega}^4-(2+\kappa^2-4\zeta_t^2)\tilde{\omega}^2+\kappa^2+1)}{\tilde{\omega}^4+(4\zeta_t^2-2)\tilde{\omega}^2+1}, \quad \tilde{\omega}_{sc} < \tilde{\omega} < \tilde{\omega}_{oc} \tag{6.21}$$

Using Equations (6.20) and (6.21) in Equation (6.18) leads to

$$\left|\frac{\Pi_{opt}}{P^2}\right| = \frac{k_{eq}A^2}{8\zeta_t\omega_n^3(m_{eq}+m_r)^2}, \quad \tilde{\omega}_{sc} < \tilde{\omega} < \tilde{\omega}_{oc} \text{ (for resistive-capacitive loading)} \tag{6.22}$$

which is identical to Equation (6.17) but valid for frequencies between the short- and open-circuit resonance values, i.e. for $\tilde{\omega}_{sc} < \tilde{\omega} < \tilde{\omega}_{oc}$, in capacitance tuning.

Briefly, the optimal resistive-inductive loading results in broadband power output for $\tilde{\omega} < \tilde{\omega}_{sc}$ and $\tilde{\omega} > \tilde{\omega}_{oc}$, while the optimal resistive-capacitive loading yields broadband power output for $\tilde{\omega}_{sc} < \tilde{\omega} < \tilde{\omega}_{oc}$. Note that the resulting broadband power output (Π_{opt} / P^2) will not have a flat spectrum since the total damping ratio ζ_t includes frequency-dependent fluid loading effects.

6.3 Experimental Results and Model Validation

6.3.1 Experimental setup and fluid-loaded receiver impedance

Experiments are conducted for an axially-poled monolithic cylindrical piezoelectric bar (modified PZT from PI Ceramic GmbH) of length $L = 20$ mm and radius $a = 3$ mm, which is employed as the receiver (Figure 6.2). The receiver has silver electrodes covering its top and bottom faces. For the experimental configuration, orientation, and receiver dimensions in Figure 6.2, the hydrophone (B&K 8103) employed in reverse operation as a source is a reasonable representation of a spherical source for model validation. The incident pressure field ($p(t)$ at the leading surface of the receiver) can be obtained from an experiment (in a water tank) through pressure-to-source strength correlation in frequency domain for an open-loop burst signal from a projector to a hydrophone. Hence, by means of a second hydrophone used for calibration, the acoustic strength of the source is extracted using $Q = p(r)(-2j\lambda r)/\rho_0 c_0$, where $p(r)$ is the pressure at distance r from the projector and λ is the acoustic wavelength in fluid.

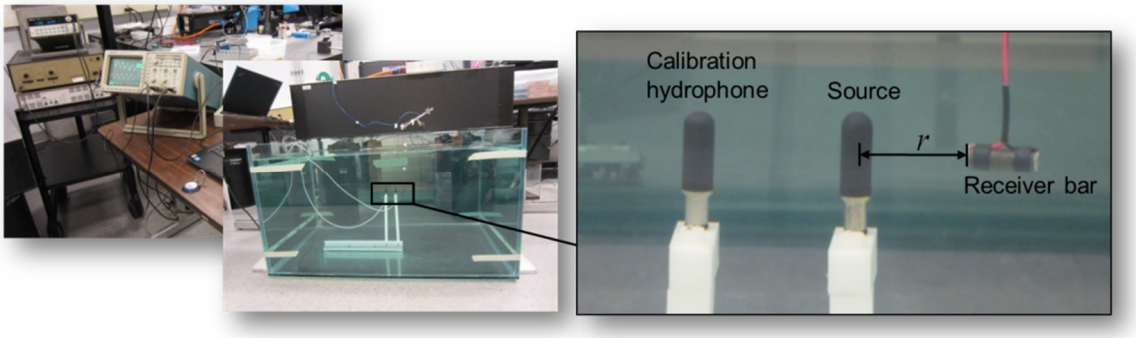

Figure 6.2. Experimental setup and close-up pictures showing the source (transmitter) and the receiver bar submerged in tap water.

The receiver is coated with a thin layer of electrically insulating, acoustically transparent material to avoid shorting under water. The analytical and experimental impedance FRFs for in-air and underwater actuation are shown in Figure 6.3. The impedance measurement captures the fundamental resonance and anti-resonance frequencies of the receiver bar, which are also called the short- and open-circuit resonance frequencies, and they have the values of 75 kHz and 79 kHz, respectively. Added mass and damping effects due to water loading are clearly observed in Figure 6.3, and the model successfully represents the underwater dynamics of the receiver near resonance. It should be noted that the resistive and reactive components of the radiation impedance determine the fluid-induced damping and fluid-loaded resonance frequency, and they depend on the dimensions (e.g. diameter) of the receiver (as a design parameter). The model was evaluated using receiver parameters of $s_{33}^{E} = 14.2\,\mathrm{pm^2/N}$, $\rho = 7800\,\mathrm{kg/m^3}$, $C_p = 5.5$ pF, $\theta = 0.0085\,\mathrm{C/m}$, and $\zeta = 0.01$, and with water parameters $\rho_0 = 1000\,\mathrm{kg/m^3}$ and estimated $c_0 = 1490.5$ m/s [168, 180, 182]. It is expected that the identified in-air damping ratio ($\zeta = 0.01$) is dominated by the material loss

(therefore this is taken to be an approximation to *in vacuo* damping). Fluid damping in the underwater case is taken into account by the model as described in Section 6.2.1.[6] Note that the speed of sound in water and piezoelectric bar are different (1490.5 m/s vs. 3004.5 m/s). The wavelength is 38mm in the fluid-loaded piezoelectric receiver. Therefore for the maximum power at resonance, approximately half wavelength is achieved in the receiver (since L = 20mm).

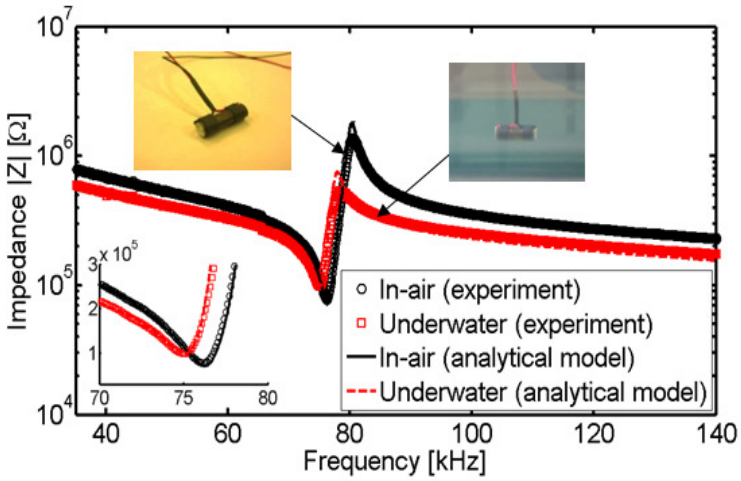

Figure 6.3. In-air and underwater electromechanical impedance FRFs of the piezoelectric receiver bar in free-free boundary conditions showing the agreement between experimental data and model prediction.

6.3.2 Finite-element vs. analytical model simulations

Multiphysics finite-element simulations are performed in COMSOL to explore the 3-D behavior of the receiver and fluid (water) under harmonic excitation. The relevant simulation tool in finite-element modeling is limited to open-circuit conditions unless it is coupled with a circuit simulator tool. Acoustic waves excite the free-free piezoelectric bar submerged in

[6] For the case of a very high mechanical quality factor receiver (such that $\zeta \sim 0.001$), which is preferred for larger power output, the total underwater damping would be dominated by the fluid (acoustic radiation) damping. That is, even for the extreme of $\zeta \to 0$ the underwater response would be bounded due to fluid damping.

fluid domain and boundaries of the fluid domain are defined to allow no reflection. For excitation at the fundamental open-circuit resonance frequency (79 kHz), Figure 6.4a shows the acoustic pressure field in fluid domain and longitudinal displacement field in the receiver bar at two instants of the period (T) of excitation for the extreme compressive and tensile deformations of the receiver during a cycle of harmonic excitation. The result shown in Figure 6.4b is given for finite-element simulations of incident pressure in unobstructed field and total pressure at the leading surface of the cylindrical receiver. At each frequency, scattered pressure is obtained by subtracting the incident pressure magnitude from total pressure magnitude. Percentage of scattered pressure over incident pressure ratio for a broad range of frequency is given Figure 6.4b. The result exhibits negligible effects of scattered pressure, the ratio is less than 5%, for the frequency range of interest in this work (around open-circuit resonance frequency, 79kHz) as the acoustic wave length (wave length = 19.5mm) in fluid is approximately 3.25 times larger than to the receiver diameter (6mm).

In Figure 6.5a and Figure 6.5b, the longitudinal tip displacement (at $\xi = 0$ in Figure 6.1) and open-circuit voltage output FRFs are extracted and plotted using the finite-element and the analytical models. Very good agreement is observed between 3-D finite-element simulations and the proposal analytical multiphysics model. Since the default version of the finite-element software is limited to open-circuit simulations, comparisons of frequency-domain analytical and time-domain numerical simulations will be limited to open-circuit electrical boundary conditions. However, the analytical model can easily accommodate the addition of finite electrical load impedance, as discussed next prior to the experimental validations.

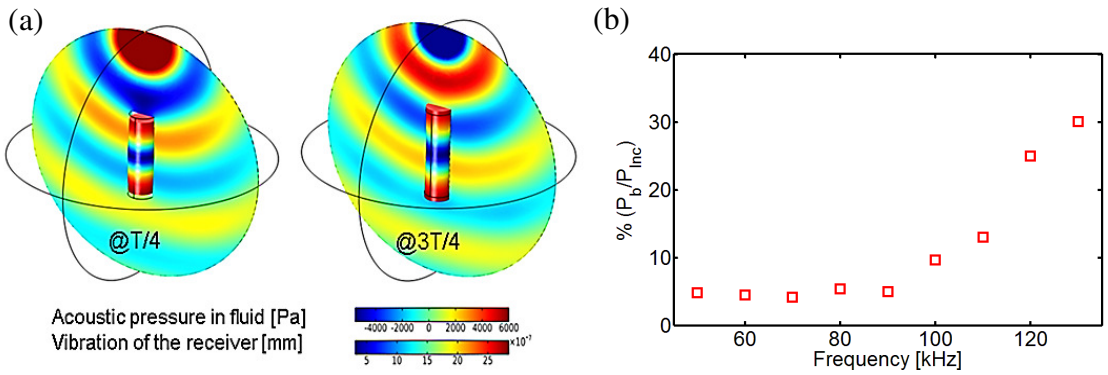

Figure 6.4. (a) Finite-element simulation for spherical acoustic wave excitation of the free-free piezoelectric receiver bar in water with a focus on the acoustic pressure field in fluid and the vibration (displacement) field of the receiver at two instants of one period (T) at the fundamental open-circuit resonance frequency (79 kHz) and (b) percentage of scattered pressure over incident pressure in a broad range of frequency.

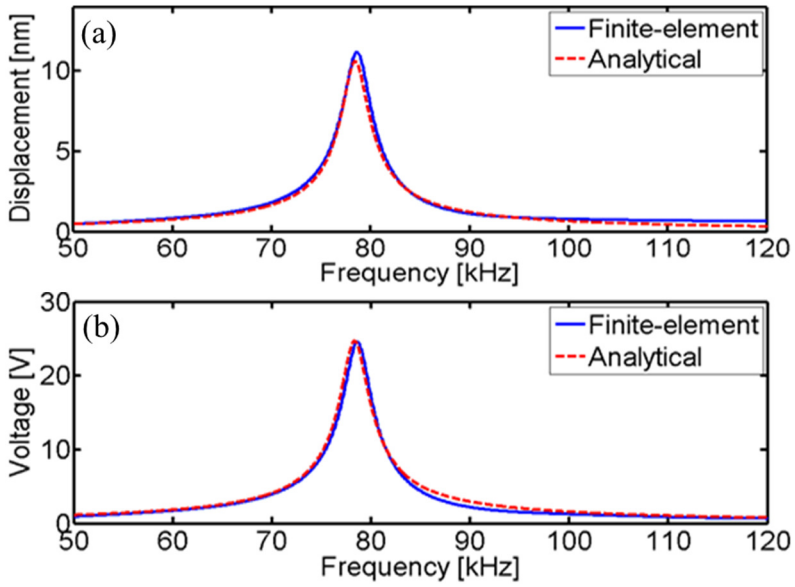

Figure 6.5. Finite-element vs. analytical model simulations of the open-circuit (a) tip displacement and (b) voltage output FRFs (for $Q = 5.65$ µm3/s, $a = 3$ mm and $r = 30$ mm).

Using the analytical model, further simulations are conducted for a broad range of resistive electrical load R_l (such that $Y_l = 1/R_l$ in Equation (6.2)) and excitation frequency

values to extract the optimality conditions of the receiver. The source-to-receiver distance r = 30.2 mm is based on the identified experimental value as a preliminary analysis for the next section. Using Equation (6.7) in the power expression $\Pi = v^2/R_l$, the power output FRF normalized with source strengths squared (Π/Q^2) is calculated, and plotted versus frequency in Figure 6.6 (note that $\Pi \propto Q^2$, since $v \propto Q$).

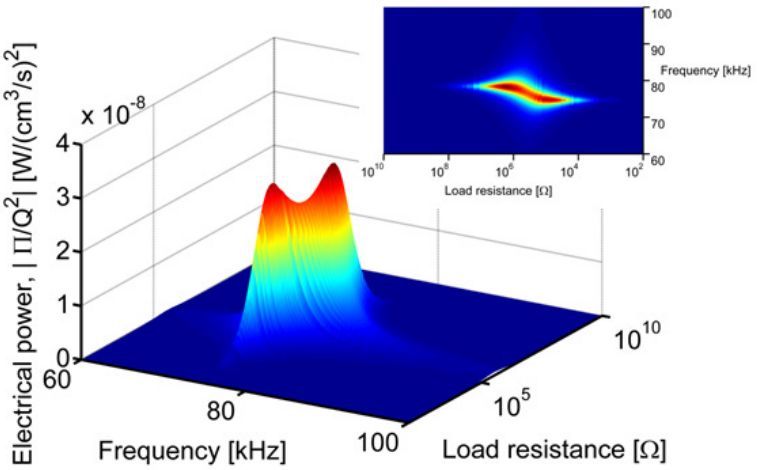

Figure 6.6. Power output (normalized with respect to source strength squared) for the piezoelectric receiver vs. excitation frequency and load resistance by using the analytical model (for r = 30.2 mm).

In agreement with typical piezoelectric energy harvesting problems [1], two peaks of power output are observed at the fundamental short- and open-circuit resonance frequencies. The first peak gives the local maximum power at 75 kHz as 0.0294 mW/(cm3/s)^2 for the optimal electrical load of 150 $\text{k}\Omega$, while the second and the global peak at 79 kHz is 0.0314 mW/(cm^3/s)^2 for the optimal load of 1.5 $\text{M}\Omega$. The peak power outputs at the short- and open-circuit resonance frequencies are not identical since the receiver is not very lightly damped

especially in the presence of fluid effects [4]; nevertheless, they are relatively similar. Therefore, a lower matched electrical load resistance is achieved at 75 kHz with larger current, whereas the opposite (larger optimal load with lower current) is the case at 79 kHz.

6.3.3 Experimental results and analytical model validation

Experiments are performed to excite the free-free receiver bar as shown in Figure 6.2 for validating the analytical model and to gain a detailed understanding of the coupled system dynamics.

The acoustic excitation source is a hydrophone (under reverse operation as a source) and the receiver is the free-free cylindrical piezoelectric bar operating in 33-mode of piezoelectricity and shunted to an electrical load as described previously and characterized in Figure 6.3. For the geometric alignment, distance, and frequencies used in the experiments, the experimental source device behaves as a spherical source. The strength of the source transducer under open-loop voltage excitation is calibrated with a separate hydrophone, itself calibrated using reciprocity [183]. In all cases, the source is excited by sinusoidal burst (3 cycles) at selected frequencies by means of a function generator and amplifier. Burst excitation is preferred to continuous excitation to properly track the signal and avoid excitation of the receiver by undesired reflections (although the water tank used in the experiments is sufficiently large). The electrodes of the piezoelectric receiver bar are shunted to a resistance substitution box and the voltage output is recorded by the data acquisition system. In the following, the Fast Fourier Transform (FFT) of the burst excitation originating from the source is used in conjunction with the voltage FRF given by Equation (6.7) to eventually obtain the inverse FFT of the voltage output for each resistive load.

Typical time histories of the voltage output across the electrical load connected to the receiver bar are shown in figure 8 in response to 3-cycle burst excitations at two different frequencies (fundamental short- and open-circuit resonance frequencies) as the two separate cases. In the experiments corresponding to this figure, the receiver is located at r = 30.2 mm and an electrical load of $R_l = 1.5\,\mathrm{M}\Omega$ is applied. The distance between the source and the receiver is extracted using the delay of approximately 20.3 μs between their time signals and the estimated speed of sound, 1490.5 m/s. The two graphs in Figure 6.7 show both experimental measurements and model predictions of the response histories for excitations at 75 kHz and 79 kHz, respectively. By keeping the load resistance at $R_l = 1.5\,\mathrm{M}\Omega$, burst excitations are performed at different frequencies. The resulting root-mean-square voltage output and average power output FRFs over a broad range of excitation frequencies are shown in Figure 6.8. Clearly, for this electrical load resistance value, the maximum power output takes place around 79 kHz, in agreement with Figure 6.6. Very good agreement is observed between the model predictions and experimental measurements in Figure 6.7 and Figure 6.8.

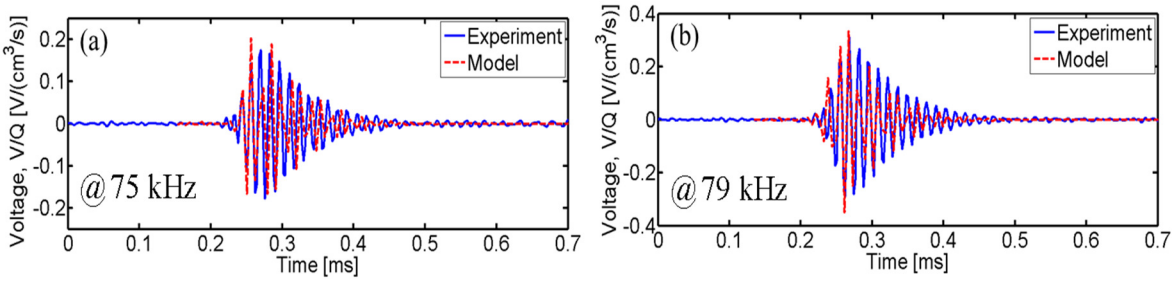

Figure 6.7. Voltage response of the receiver to 3-cycle burst excitations at the fundamental (a) short-circuit and (b) open-circuit resonance frequencies of 75 kHz and 79 kHz (for a source-to-receiver distance of r = 30.2 mm and load resistance of $R_l = 1.5\,\mathrm{M}\Omega$).

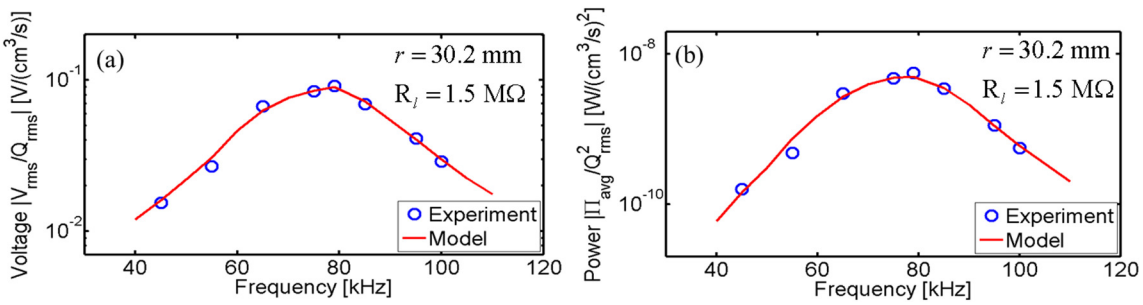

Figure 6.8. Root-mean-square (a) voltage output and (b) average power output FRFs of the receiver normalized with respect to source strength (for a source-to-receiver distance of $r =$ 30.2 mm and load resistance of $R_l = 1.5\,\mathrm{M\Omega}$).

6.3.4 *Effects of various system parameters*

Next, resistor sweep experiments are performed for 3-cycle burst excitations at the fundamental short- and open-circuit resonance frequencies while keeping the source-to-receiver distance fixed (at r = 30.2 mm). The tests are conducted for a set of load resistance values ranging from $100\,\mathrm{k\Omega}$ to $9\,\mathrm{M\Omega}$, covering a broad range that is expected to include the optimal loads at 75 kHz and 79 kHz. As shown in Figure 6.9a, very good agreement is observed between experimental data and analytical model predictions of the power output normalized with respect to source strength squared. The load resistance is then fixed to $R_l = 1.5\,\mathrm{M\Omega}$ and the effect of source-to-receiver distance is studied as given in Figure 6.9b. The hyperbolic dependence of the power output to distance is expected since $v_{rms} \propto 1/r$ in Equation (6.7), and therefore, $\Pi_{avg} = v_{rms}^2 / R_l \propto 1/r^2$ for a fixed Q_{rms} value. With increased source-to-receiver distance, the power output of the receiver decreases monotonically and hyperbolically. Finally, the dependence of the average power output on the root-mean-square

source strength is displayed in Figure 6.9c, validating the previously mentioned quadratic relationship $\Pi_{avg} \propto Q_{rms}^2$ with good accuracy.

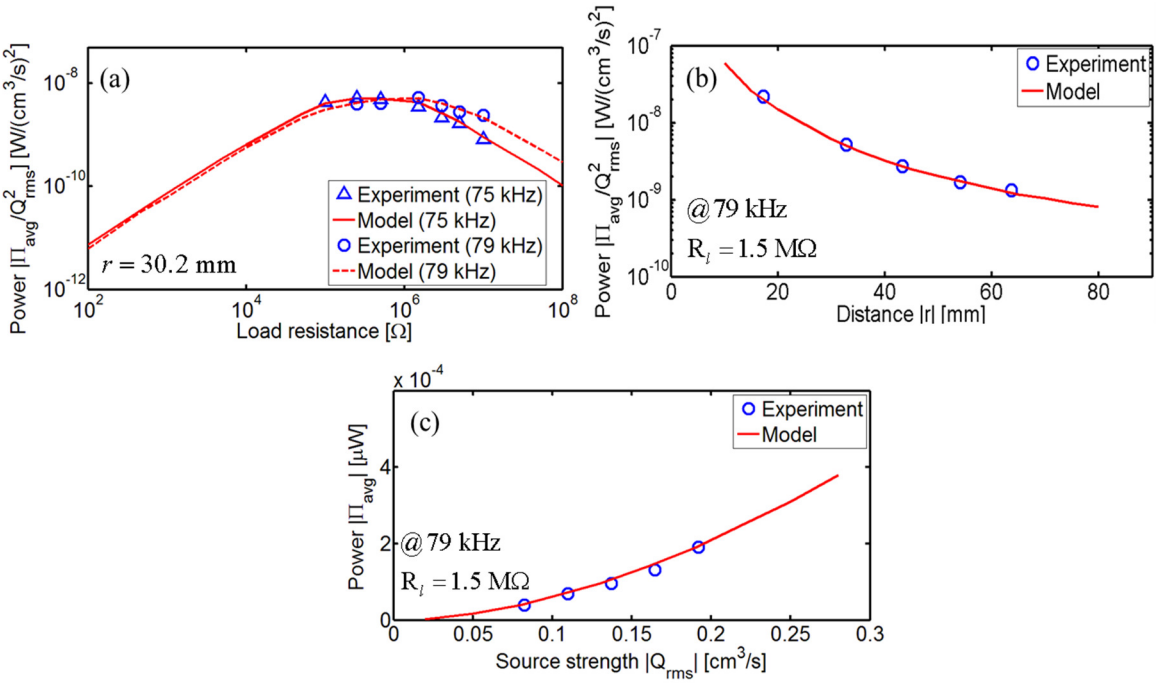

Figure 6.9. (a) Power output (normalized with respect to source strength squared) vs. electrical load resistance at the fundamental underwater short- and open-circuit resonance frequencies (for $r = 30.2$ mm); (b) Power output (normalized with respect to source strength squared) vs. source-to-receiver distance (for $R_l = 1.5\,\mathrm{M\Omega}$ excitation at 79 kHz); (c) Power output vs. source strength (for $R_l = 1.5\,\mathrm{M\Omega}$ excitation at 79 kHz).

6.3.5 Bandwidth enhancement by resistive-reactive electrical loading

In this last section, the analytical multiphysics model (that has been validated experimentally) is used for a purely theoretical simulation case study. The optimal resistive and resistive-reactive electrical loading conditions (for power output normalized by the incident acoustic pressure squared acting on the top end surface of the receiver) discussed in section 2.5 are plotted in Figure 6.10 for the optimal purely resistive circuit, the optimal

resistive-inductive circuit (for frequencies less than 75 kHz and greater than 79 kHz), and the optimal resistive-capacitive circuit (for frequencies in between 75 kHz and 79 kHz).

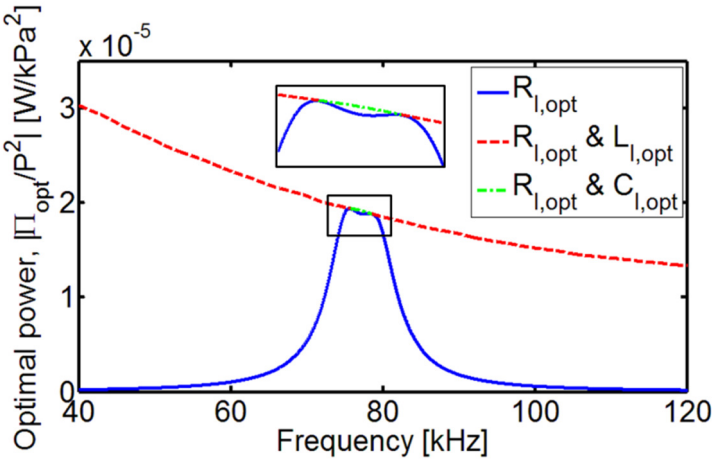

Figure 6.10. Optimal receiver power output frequency response curves (normalized by the incident acoustic pressure squared acting on end surfaces of the receiver) for optimal resistive and resistive-reactive electrical loading cases.

It is clearly demonstrated that, by optimizing the load inductance/capacitance and resistance values simultaneously, broadband power extraction from the receiver is successfully achieved over a range of frequencies. The fact that the broadband power amplitude behavior is not flat (unlike the case of optimal resistive-inductive loading in vibration-based energy harvesters [174]) is because of the fluid loading effects. It is worth adding that the inductance value required for conjugate matching is inversely proportional to piezoelectric capacitance and frequency squared in Equation (6.16). As long as the inductance requirement is low enough, a passive inductor can be employed for broadband behavior. To keep the inductance requirement low, a high-capacitance piezoelectric stack transducer [175] can be used instead of a monolithic receiver (so that μF-level capacitance is achieved instead of pF/nF-level capacitance) for which the above formulation still applies

without loss of generality by using the effective values of d_{33}^{eff} and C_p for the entire cylindrical stack [175]. Alternatively the excitation frequency can be kept high to reduce the inductance requirement. Otherwise, in case of large inductance requirement, a synthetic inductor (or synthetic impedance) circuit [176, 177] would be necessary (and part of the transmitted power would have to be used for that).

6.4 Summary and Conclusions

In this chapter, contactless ultrasonic acoustic energy transfer is investigated analytically, numerically, and experimentally for a cylindrical receiver in free-free mechanical boundary conditions excited by a spherical wave source. Specifically, a fully-coupled multiphysics analytical model (that accounts for the acoustic-piezoelectric structure interaction and the fluid-loaded receiver's electrical load) is developed and successfully validated. Optimal electrical loading conditions are shown and experimentally validated to be at the fundamental short- and open-circuit resonance frequencies of the receiver bar, which are associated with larger current and larger voltage, respectively, yielding similar power outputs. Effects of various system parameters, such as the source strength and the source-to-receiver distance, are also presented and validated. Optimal resistive-reactive electrical loading results in substantially enhanced broadband power transfer as compared to purely resistive electrical loading.

7 ULTRASONIC ENERGY TRANSFER USING A CYLINDRICAL SOURCE-CYLINDRICAL RECEIVER COMBINATION

7.1 Introduction

This chapter investigates a UAET method to effectively power devices implanted in deep distances. The receiver is a piezoelectric bar (free-free boundary conditions) operating in the 33-mode of piezoelectricity. Acoustic energy is being transferred from an axially vibrating cylindrical piezoelectric source to a cylindrical piezoelectric receiver. The acoustic domain includes the receiver and the transmitter submerged in a quiescent fluid (e.g. vegetable oil). Both the transmitter and receiver are modeled as unbaffled axially vibrating cylinders and the generated acoustic pressure from the source is obtained by the solution of Helmholtz integral equation in space considering Sommerfeld radiation and continuity condition on the surface of the source. To maximize the power output from the receiver, typically it is required to operate the transmitter/receiver close to its resonance frequency. On the other hand, the determination of operating frequency is of importance since it has effects on the attenuation, beam pattern and scattering of incident pressure wave at the leading surface of the cylindrical receiver. Acoustic-electroelastic structure interaction modeling efforts and experiments explore these aspects for power transfer from a cylindrical source to a cylindrical receiver. Focused UAET implemented from the HIFU is employed as a method to concentrate the transmitted energy in space and thereby strongly excite the receiver. An array of piezoelectric piston transducers on a curved cylindrical panel is designed to create focusing in the receiver location. Acoustic mirroring concept also is employed with a spherical point source in order to focus the transmitted energy in space. The possibility of focusing for improved power transfer efficiency in a quiescent fluid domain is shown experimentally.

7.2 Theory: Acoustic-Piezoelectric Structure Coupling of a Cylindrical Source and a Cylindrical 33-Mode Receiver

Figure 7.1 displays a schematic of a piezoelectric receiver fully submerged in fluid (e.g. water or oil) and excited by incident acoustic waves originating from a free-free piezoelectric cylindrical bar of known strength Q and vibrating in longitudinal direction ($\bar{\xi}$ -axis in Figure 7.1). The receiver is a free-free piezoelectric cylinder operating in the 33-mode of piezoelectricity (3-direction is the axial direction, i.e. ξ-axis) with a fundamental resonance frequency above the human audible frequency range. In order to quantify the electrical power output, an external electrical load with the admittance Y_l is connected to the electrodes (in the case of purely resistive electrical loading $Y_l = 1/R_l$, where R_l is the load resistance).

The fluid-loaded and electrically-loaded free-free piezoelectric bar receiver is excited by the acoustic pressure wave created by an axially vibrating piezoelectric bar. The coupled partial differential equation for longitudinal vibrations of the receiver and the AC electrical circuit equation are given in Chapter 6, Equations (6.1) and (6.2). The pressure field created by the source bar in an infinite, homogeneous, and isotropic medium is extensively described in the following sections.

7.2.1 Sound pressure generated by an axially vibrating cylindrical bar and directivity

The acoustic pressure generated by a cylinder oscillating harmonically in the axial direction ($\bar{\xi}$ -axis in Figure 7.2) is determined from Helmholtz integral equation as follows [173, 184].

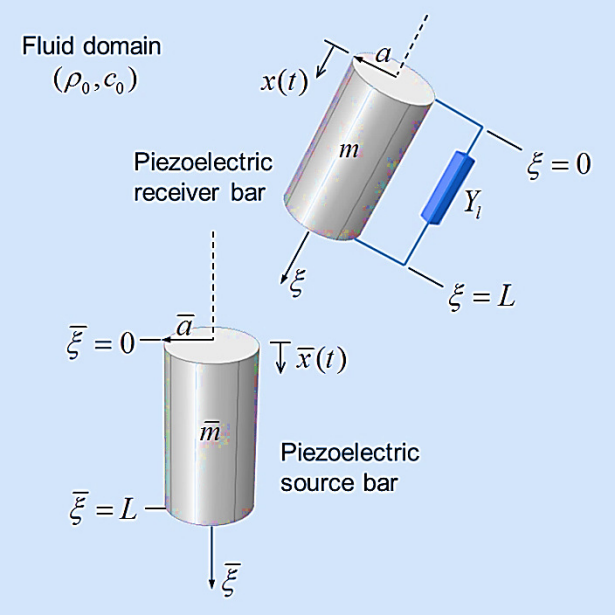

Figure 7.1. Schematic representation of contactless acoustic energy transfer from an axially vibrating cylindrical source to an axially-poled cylindrical piezoelectric receiver bar shunted to an electrical load from its surface electrodes (which cover the top and bottom faces).

$$p(Z,t) = \int_A \left[p(Z_t,t)\nabla G(z_t) + \rho_0 \frac{\partial^2 u(Z_t,t)}{\partial t^2} G(z_t) \right] dA + \int_A \left[p(Z_b,t)\nabla G(z_b) + \rho_0 \frac{\partial^2 u(Z_b,t)}{\partial t^2} G(z_b) \right] dA \tag{7.1}$$

where u is the longitudinal displacement of the bar. Equation (7.1) is obtained by considering Sommerfeld radiation condition [185] (the acoustic energy which is radiated from the acoustic source scatters to infinity) and applying the continuity boundary condition (continuity of pressure and the velocity normal to the end cross section area [173]). It is assumed that the resulting acoustic radiation is due to the motion of end surfaces of the vibrating bar as the contribution due to the side surface of the cylinder is negligible [184, 186].

The first and the second terms in Equation (7.1) give the pressure due to the top and bottom surfaces, respectively. Z, Z_t, and Z_b are the vectors all originating from the reference fixed frame (X-Y frame in Figure 7.2) and terminating at the reception point (leading surface of receiver), top and bottom end surfaces of the source bar, respectively.

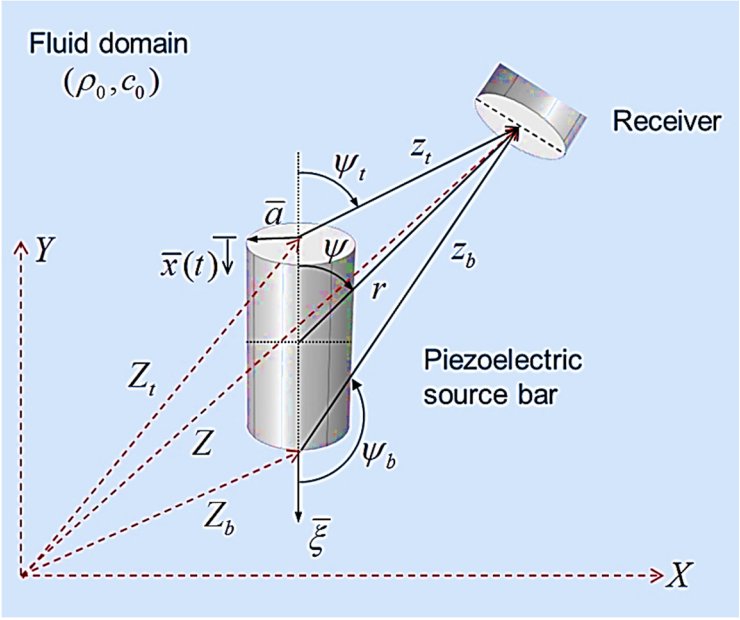

Figure 7.2. Geometric properties of the axially vibrating cylindrical source and receiver location.

In Equation (7.1), the free-field Green's functions for the top and bottom source leading surfaces are defined as [173]

$$G(z_t) = \frac{1}{4\pi z_t} e^{jkz_t},\ G(z_b) = \frac{1}{4\pi z_b} e^{jkz_b} \tag{7.2}$$

where $z_t = |Z - Z_t|$, $z_b = |Z - Z_b|$ are defined as the distance between top and bottom end surfaces of the source to the receiver location (as shown in Figure 7.2).

The acceleration of the source surfaces at the top and bottom ends are defined as

$$\frac{\partial^2 u(Z_t)}{\partial t^2} = -\frac{\partial^2 u(Z_b)}{\partial t^2} = \ddot{\bar{x}}(t) \tag{7.3}$$

where $\bar{x}(t)$ is the linear displacement at the top end of source bar (shown in Figure 7.2)

The pressures at the end surfaces of the bar source are defined as

$$p(Z_t, t) = p(Z_b, t) = p_s(t) \tag{7.4}$$

The surface gradient of Green's function with respect to outward unit surface normal for top surface (n_t) and bottom surface (n_b) are defined as follows [184]

$$\nabla G(z_t) = \frac{\partial G(z_t)}{\partial n_t} = \frac{\partial G(z_t)}{\partial z_t}\cos\psi_t \tag{7.5}$$

$$\nabla G(z_b) = \frac{\partial G(z_b)}{\partial n_b} = \frac{\partial G(z_b)}{\partial z_b}\cos\psi_b \tag{7.6}$$

where the following equations are used to obtain Equations (7.5) and (7.6).

$$\frac{\partial}{\partial n_t} = \frac{\partial}{\partial z_t}\frac{\partial z_t}{\partial n_t} \text{ and } \frac{\partial z_t}{\partial n_t} = \cos\psi_t \tag{7.7}$$

$$\frac{\partial}{\partial n_b} = \frac{\partial}{\partial z_b}\frac{\partial z_b}{\partial n_b} \text{ and } \frac{\partial z_b}{\partial n_b} = \cos\psi_b \tag{7.8}$$

Substituting Equations (7.2)-(7.6) into Equation (7.1) gives the expression for the pressure at leading surface of the receiver as considering the fact that $\cos\psi \simeq \cos\psi_t \simeq -\cos\psi_b$

$$p(Z,t) = \rho_0 \ddot{\bar{x}}(t)\int_A \left[G(z_t) - G(z_b)\right] dA + p_s(t)\int_A \left[\frac{\partial G(z_t)}{\partial z_t}\cos\psi - \frac{\partial G(z_b)}{\partial z_b}\cos\psi\right] dA \tag{7.9}$$

Considering the reference origin at geometric center of the cylindrical source bar gives $Z = r$. Therefore Equation (7.9) is defined as

$$p(r,\psi,t) = \rho_0 \ddot{x}(t) \Upsilon(r,\psi) + p_s(t) \Theta(r,\psi) \tag{7.10}$$

where $\Upsilon(r,\psi)$ and $\Theta(r,\psi)$ are defined as

$$\Upsilon(r,\psi) = \frac{A}{4\pi r} e^{jkr} \mathrm{D_p}(\psi) \mathrm{D_d}(r,\psi) \tag{7.11}$$

$$\Theta(r,\psi) \simeq \frac{jkr-1}{r} \cos\psi \int_A \left[\partial G(z_t) - \partial G(z_b)\right] dA \tag{7.12}$$

In Equation (7.11), $\mathrm{D_p}(\psi)$ represents directivity for baffled piston

$$\mathrm{D_p}(\psi) = \frac{2J_1(ka\sin\psi)}{ka\sin\psi} \tag{7.13}$$

and $\mathrm{D_d}(r,\psi)$ is the summation of out-of-phase and in-phase dipole source directivity as follows

$$\mathrm{D_d}(r,\psi) = \frac{L}{r}\cos\psi\cos\left(\frac{kL}{2}\cos\psi\right) - 2j\sin\left(\frac{kL}{2}\cos\psi\right), \quad L < r \tag{7.14}$$

Considering the fact that $\cos\psi \simeq \cos\psi_t \simeq -\cos\psi_b$ as shown in Figure 7.2 , and noting that

$$\frac{\partial G(z_t)}{\partial z_t} = \frac{jkz_t - 1}{z_t} G(z_t) \tag{7.15}$$

The second term given in Equation (7.10), Θ , is given as

$$\Theta(r,\psi) \simeq \frac{A(jkr-1)\cos\psi}{4\pi r^2} e^{jkr} \mathrm{D_p}(\psi) \mathrm{D_d}(r,\psi) \tag{7.16}$$

As it was mentioned previously, the resulting equation for pressure (Equation (7.9)) requires the average pressure on surface *A*. The average predicted pressure on the surface center is defined as [184]

$$p_s(t) = j\rho_0 \ddot{\bar{x}} \frac{(1-e^{jk\bar{a}})}{k} \tag{7.17}$$

Substitution of Equations (7.11) - (7.17) into Equation (7.10), the pressure generated by an axially oscillating cylinder in a free field and distance r is given as [184]

$$p(r) = \rho_0 (j\omega\dot{\bar{x}}) A \frac{e^{jkr}}{4\pi r} \mathrm{D_p}(\psi) \left[\mathrm{D}_d(\mathrm{r},\psi) + \frac{(1-e^{jk\bar{a}}).(j+kr)}{kr} \cos\psi \, \mathrm{D}_d(\mathrm{r},\psi) \right] \tag{7.18}$$

7.2.2 Lumped parameter form and piezoelectric receiver response to harmonic excitation

The electromechanically coupled equations of forced vibration and current balance are expressed for the fundamental mode in lumped-parameter form (reduced from distributed-parameter solution) as

$$\begin{aligned} &\ddot{x}(t) + \left[2\zeta\omega_n + R_r\phi^2(0) + R_r\phi^2(L) \right] \dot{x}(t) + \omega_n^2 x(t) - \theta[\phi(0)\phi(L) - \phi^2(0)]v(t) \\ &= f_t(t)\phi^2(0) - f_b(t-\tau)\phi(0)\phi(L) \end{aligned} \tag{7.19}$$

$$C_p\phi(0)\dot{v}(t) + Y_l\phi(0)v(t) + \theta[\phi(L) - \phi(0)]\dot{x}(t) = 0 \tag{7.20}$$

Here, $\phi(0)$ and $\phi(L)$ are, respectively, the mass-normalized fundamental elastic mode eigenfunction evaluated at $\xi = 0$ and $\xi = L$ (in Figure 7.1) for the longitudinal vibration mode of a free-free uniform fully submerged bar (see Equation (6.4)), and an over-dot represents differentiation with respect to time. Fluid absorption is assumed to be negligible for the frequency range of interest. Scattering effects will be studied in the following sections both numerically and experimentally.

The steady-state electromechanical response to harmonic excitation is also harmonic and is of the form $x(t) = Xe^{j\omega t}$ and $v(t) = Ve^{j\omega t}$ based on the linear system assumption. Then the fundamental-mode voltage output per source strength (product of surface velocity and leading surface area) frequency response function (FRF) can be obtained as

$$\frac{v(t)}{Qe^{j(\omega t + k(r-\bar{a}))}} = \frac{j\omega\theta\left(\frac{j\rho_0\omega}{8\pi r}\right)D(r,\psi)[\phi(0) - \mu\phi(L)e^{-j\varphi}][\phi(L) - \phi(0)]}{\left\{\omega_n^2 - \omega^2 + j\omega\left[2\zeta\omega_n + R_r[\phi^2(0) + \phi^2(L)]\right]\right\}\left(Y_l(\omega) + j\omega C_p\right) + j\omega\theta^2[\phi(L) - \phi(0)]^2} \tag{7.21}$$

where $\varphi = \omega\tau$ is the phase angle between the excitation forces at the top and bottom surfaces of the cylindrical receiver. In Equation (7.21), $D(r,\psi)$ is the directivity function and defined as

$$D(r,\psi) = \mathrm{D_p}(\psi)\left[\mathrm{D}_d(\mathrm{r},\psi) + \frac{(1-e^{jk\bar{a}}).(j+kr)}{kr}\cos\psi\,\mathrm{D}_d(\mathrm{r},\psi)\right] \tag{7.22}$$

7.2.3 Electromechanical impedance and velocity FRFs of the fluid-loaded receiver

Deriving an expression for surface velocity and impedance of the fluid-loaded receiver is useful for model validation and identification of its parameters under electrical excitation. In Equations (7.3), changing the input to $v(t) = Ve^{j\omega t}$ and setting $f_t(t) = f_b(t-\tau) = 0$, while in Equation (7.4), replacing the current output $Y_l v(t)$ by the actuation current input $-i(t) = -Ie^{j\omega t}$ and assuming $x(t) = Xe^{j\omega t}$, yields the following expressions for the fluid-loaded receiver's end surface velocity normalized to input voltage and electromechanical impedance $Z = V/I$:

$$\frac{\dot{x}(t)}{Ve^{j\omega t}} = \frac{j\omega\theta[\phi(0)\phi(L) - \phi^2(0)]}{\omega_n^2 - \omega^2 + j\omega\left[2\zeta\omega_n + R_r\phi^2(0) + R_r\phi^2(L)\right]} \tag{7.23}$$

$$Z(\omega) = \left\{ j\omega\left[C_p + \frac{\theta^2[\phi(L) - \phi(0)]^2}{\omega_n^2 - \omega^2 + j\omega\left[2\zeta\omega_n + R_r\phi^2(0) + R_r\phi^2(L)\right]} \right] \right\}^{-1} \tag{7.24}$$

Equations (7.23) and (7.24) include the fundamental longitudinal vibration mode only.

7.3 Experimental Validations

7.3.1 Experimental setup and fluid-loaded receiver parameter identification

Experiments are conducted for an axially-poled multilayer piezoelectric stack of length $L = 8$ mm and radius a = 3.5 mm, which is employed as the source (transmitter) and receiver (Figure 7.3). The piezoelectric stack (identical to the stack used as receiver) is employed as a representation of an axially vibrating cylindrical source for model validation. The incident pressure field ($p(t)$ at the leading surface of the receiver) can be given from the experimentally validated theoretical analysis in Section 7.2.1.

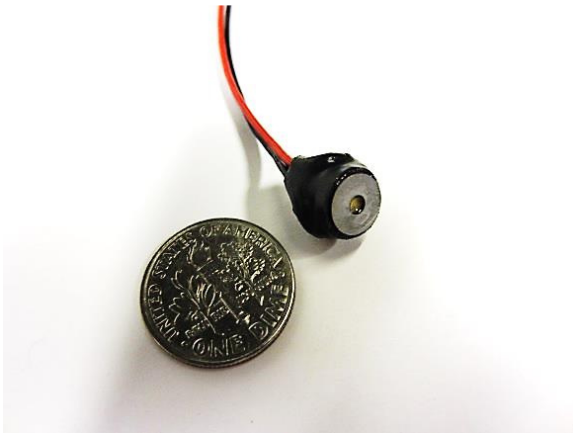

Figure 7.3. Piezoelectric multilayer stack

Figure 7.4. Experimental setup and close-up pictures showing the source bar (transmitter) and the receiver bar submerged in oil.

The analytical and experimental impedance FRFs for in-air and in-oil actuation are shown in Figure 7.5. The impedance measurement captures the fundamental resonance and anti-resonance frequencies of the receiver bar, which are also called the short- and open-circuit resonance frequencies, and they have the values of 150 kHz and 194 kHz, respectively. Added mass and damping effects due to oil loading are clearly observed in Figure 7.5a, and the model successfully represents the in-oil dynamics of the receiver near resonance. Added mass and damping (versus frequency) in the model are plotted in Figure 7.6. The model was evaluated using receiver parameters of $s_{33}^{E} = 6.02\,\mathrm{pm}^2/\mathrm{N}$, $\rho = 7800\,\mathrm{kg/m}^3$, $C_p = 12.1\,\mathrm{nF}$, $\theta = 1.3\,\mathrm{C/m}$, and $\zeta = 0.02$, and with oil parameters $\rho_0 = 910\,\mathrm{kg/m}^3$ and estimated $c_0 = 1492\,\mathrm{m/s}$ [168, 180, 182].

As it is shown in Equation (8.20), to obtain transmitted acoustic pressure, the source surface velocity is needed. Having identified parameters of the piezoelectric source bar, the analytical and experimental root-mean-square surface velocities for in-oil actuation are given in Figure 7.5b. During the experiments in this chapter, the source bar is excited by sinusoidal

burst (3 cycles at 18V peak-peak amplitude) at selected frequencies by means of a function generator and amplifier. The experimental surface velocity of the source is measured by an LDV (Polytec, Inc. OFV-505) and controller (Polytec, Inc. OFV-5000). For analytical results, Fast Fourier Transform (FFT) of the excitation voltage signal is used in conjunction with velocity FRF given by Equation (8.25) to eventually obtain the inverse FFT of the surface velocity at each frequency.

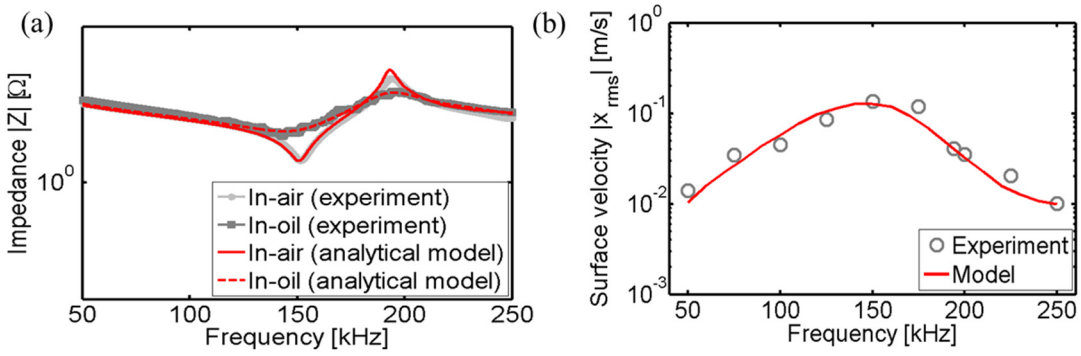

Figure 7.5. (a) In-air and in-oil electromechanical impedance FRF and (b) root-mean-square surface velocity of the piezoelectric source bar in free-free boundary conditions showing the agreement between experimental data and model prediction (Equations (7.23) and (7.24)).

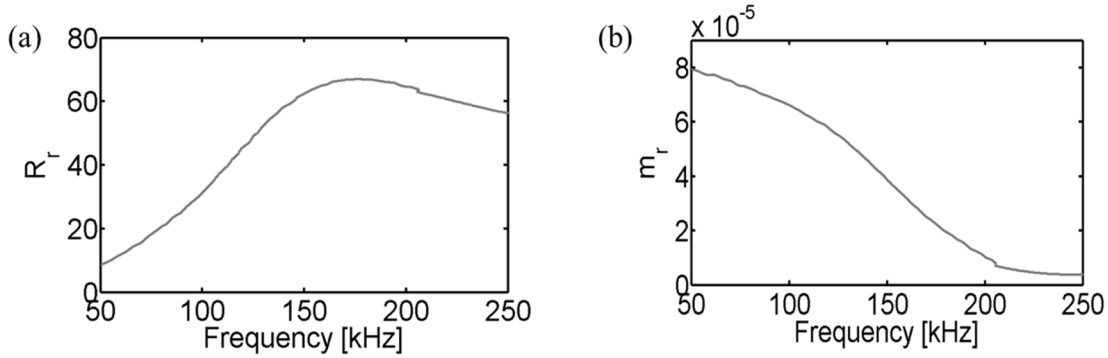

Figure 7.6. (a) Radiation damping (resistive component) and (b) radiation mass (reactive component) for a circular piston oscillating in one side with no baffle [168, 187].

Using the analytical model, further simulations are conducted for a broad range of resistive electrical load R_l and excitation frequency values to extract the optimality conditions of the receiver. The source-to-receiver distance is measured as r = 66.4 mm. Using Equation (7.21) in the power expression $\Pi = v^2 / R_l$, the power output FRF normalized with source strengths squared (Π / Q^2) is calculated and plotted in Figure 7.7. The surface plot shows that the maximum power happens around open-circuit resonance frequency (194 kHz) for the optimal electrical load of $210\,\Omega$.

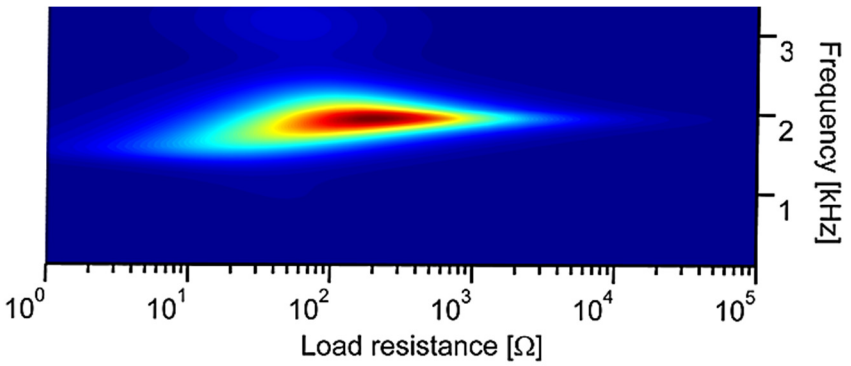

Figure 7.7. Surface plot for power output (normalized with respect to source strength squared) for the piezoelectric bar receiver vs. excitation frequency and load resistance by using the analytical model (for r = 66.4 mm).

7.3.2 Analytical and experimental investigations of directivity pattern for an unbaffled axially oscillating cylinder

Using the analytical model given in Equation (7.22), simulations are conducted and plotted in Figure 7.8 for directivity function versus orientation angle at various frequencies ($k\bar{a}$ is changing due to the change of frequency). The source is the piezoelectric bar with radius $\bar{a} = 3.5\,\text{mm}$.

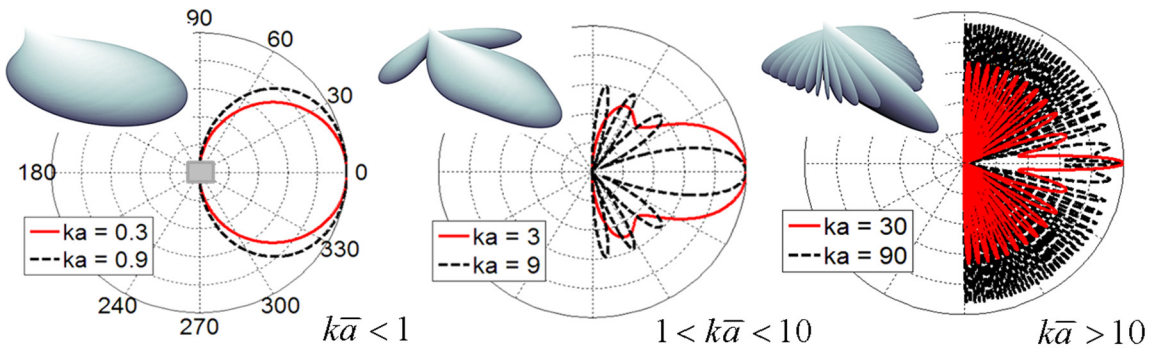

Figure 7.8. Directivity pattern for an unbaffled axially oscillating cylinder of radius $\bar{a}$ radiating sound at various $k\bar{a}$ values (for r = 66.4 mm).

It should be noted that $k\bar{a}$ can be defined in terms of wave length as $k\bar{a} = 2\pi\bar{a}\,(\text{circumference of source cross section})/\lambda$. If $k\bar{a} < 1$, when the cross-section circumference of the source is smaller than wave length, the directivity pattern in diverging similar to the case of spherical spreading of waves. In this case, only a small fraction of the generated acoustic energy is hitting the receiver due to existing spreading loss. By increasing $k\bar{a}$ (increasing frequency or radius of the source), the nodal surfaces (the surfaces on which transmitted acoustic pressure amplitude is approaching zero) are appearing. These nodal surfaces are disjointed by the *lobes*, where the acoustic energy is nonzero. The more increasing $k\bar{a}$ value results in the narrower major lobe and the greater number of minor lobes. It means that for larger $k\bar{a}$, the main transmitted acoustic energy is focused within a small angle sector around the source axis while energy emitted along the side lobes constitutes only a very small fraction of total energy emitted from the source.

To understand the effects of changing operating frequency on the directivity pattern, simulations are performed for the experimental source (unbaffled axially vibrating piezoelectric stack with radius $\bar{a}$ =3.5 mm) and plotted in Figure 7.9a and Figure 7.9b. It

should be reminded that, from Equation (7.21), at each excitation frequency, the incident pressure amplitude in proportional to the amplitude of directivity functions. The results in Figure 7.9 show that, in the most part of the frequency range, the major *lobe* which contains the main portion of the transmitted acoustic energy is found to be an axis ($\psi = 0$). By increasing frequency the directivity amplitude, for the three orientation angles, is increasing uniformly and approximately linearly up to about 100 kHz (where $k\bar{a} \cong 1$ in Figure 7.9b). For excitation higher than 100 kHz ($k\bar{a} > 1$), nonuniform fluctuation variations with multiple minima and maxima are seen for all the orientation angles.

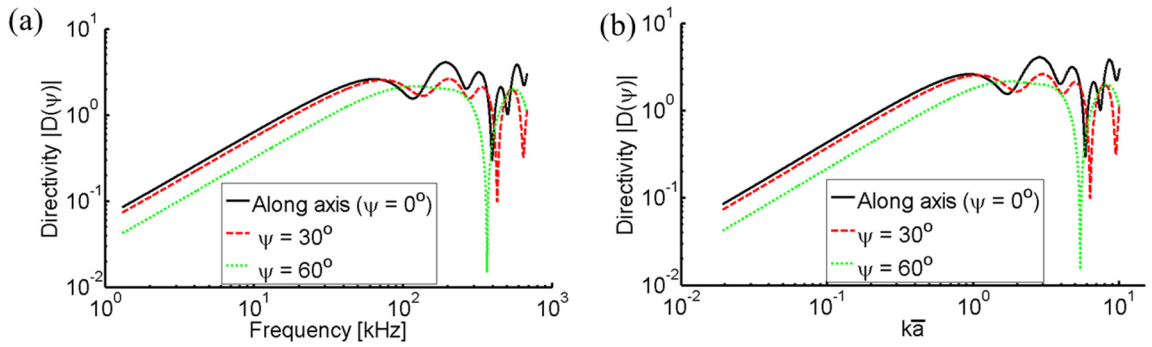

Figure 7.9. Directivity function amplitude versus (a) excitation frequncy and (b) $k\bar{a}$ at various orientation angles.

To validate the directivity model presented in the previous section (Equation (7.22)), experiments are performed for a free-free piezoelectric cylindrical stack (Figure 7.3) as transmitter and the acoustic pressure is measured by a hydrophone probe (B&k 8103) at distance r = 66.4 mm from the geometric center of radiating source (Figure 7.11b). The designed experimental set up allows the hydrophone to be easily moved at different orientation angles (shown in Figure 7.10) in order to represent the radiation pattern. The source bar is excited by sinusoidal burst (3 cycles at 18V peak-peak amplitude) at selected

frequencies by means of a function generator and amplifier. For the given analytical acoustic pressure in Equation (7.20), Equation (7.25) is used to calculate the surface velocity of the transmitted as its validity previously has been shown in Figure 7.5b.

Figure 7.11 shows the analytical and measured pressure amplitudes as a function of frequency at three orientation angles. For the whole frequency range, the results show greater pressure amplitude for the case that receiver (hydrophone) is located along the axis where the directivity is predicted to be maximum in Figure 7.9. In addition, for the three orientation angles, maximum pressure amplitude occurs at 150 kHz which is the short-circuit resonance frequency of the piezoelectric source bar (consistent with the resonance frequency predicted by impedance measurement in Figure 7.5). It should be note that, the results for $\psi = 90^{\circ}$ are not shown since the measured pressure amplitude is close to zero.

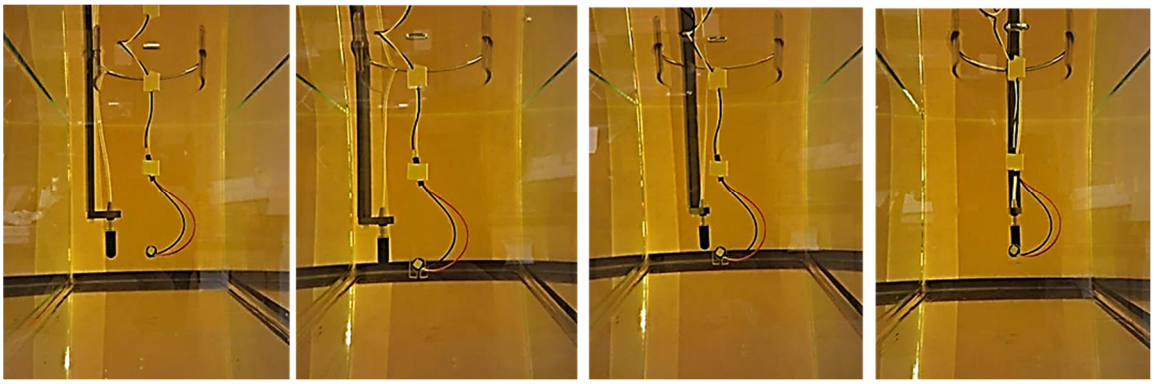

Figure 7.10. Experimental setup for representing directivity of acoutic pressure generated by a piezoelectric cylindircal stack at different orintation anlges (from left to rigth; $\psi = 90^{\circ}$ $\psi = 60^{\circ}$, $\psi = 30^{\circ}$, and $\psi = 0$).

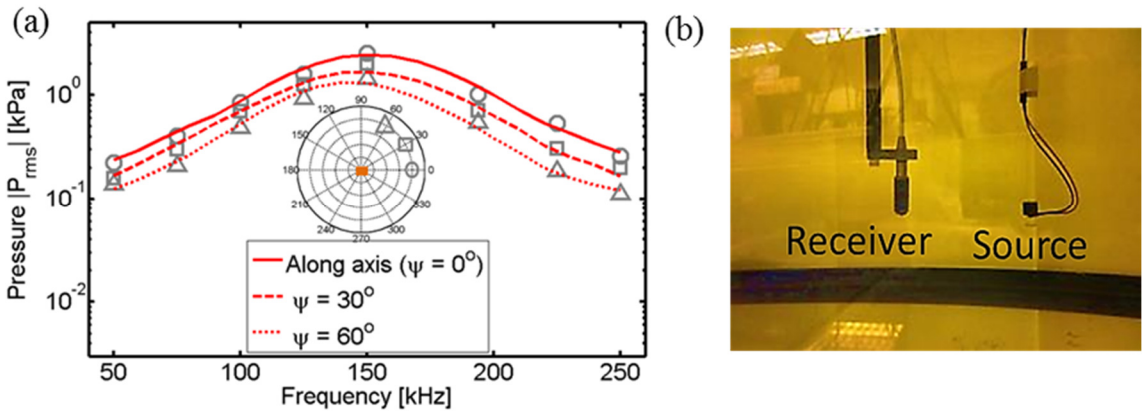

Figure 7.11. (a) Analytical (solid, dashed, and dotted lines) and measured (circle, square, and triangle markers) acoustic pressure versus excitation frequency at different orientation angles (ψ) and r = 66.4 mm, (b) close-up picture showing the source bar (transmitter) and the receiver hydrophone submerged in oil.

To understand the effects of directivity on the voltage response of the receiver (the receiver is an identical bar to the transmitter (shown in Figure 7.13b) which is operating in 33-mode of piezoelectricity) is shunted to an optimal electrical load (R_l=210Ω) and tested at different orientation angles with respect to the source bar. The designed experimental set up allows the receiver bar to be easily moved at different orientation angles (shown in Figure 7.12) at r = 90.1 mm.

Figure 7.13 shows the measured voltage output amplitudes normalized to source strength as a function of frequency at three orientation angles. For the whole frequency range, the results show greater voltage output for the case that receiver is located along the axis. In addition, for the three orientation angles, maximum pressure amplitude occurs at 194 kHz which is the open-circuit resonance frequency of the piezoelectric receiver bar (consistent with the optimal condition predicted in Figure 7.7).

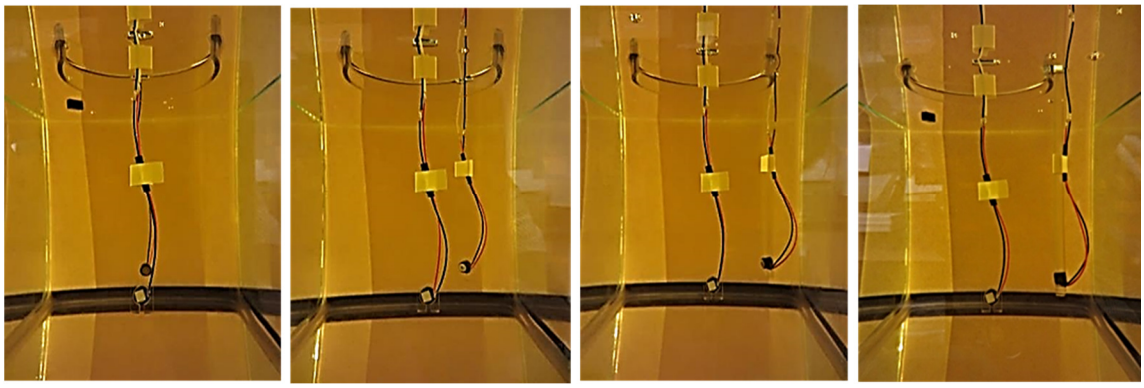

Figure 7.12. Experimental setup for studying the effects of incident pressure directivity on votage response of the reciever. Source and reciever are identical piezoelectric cylindircal stacks. The reciever is located at $r = 90.1$ mm and different orintation anlges; From left to rigth; $\psi = 90^{\circ}$, $\psi = 60^{\circ}$, $\psi = 30^{\circ}$, and $\psi = 0$).

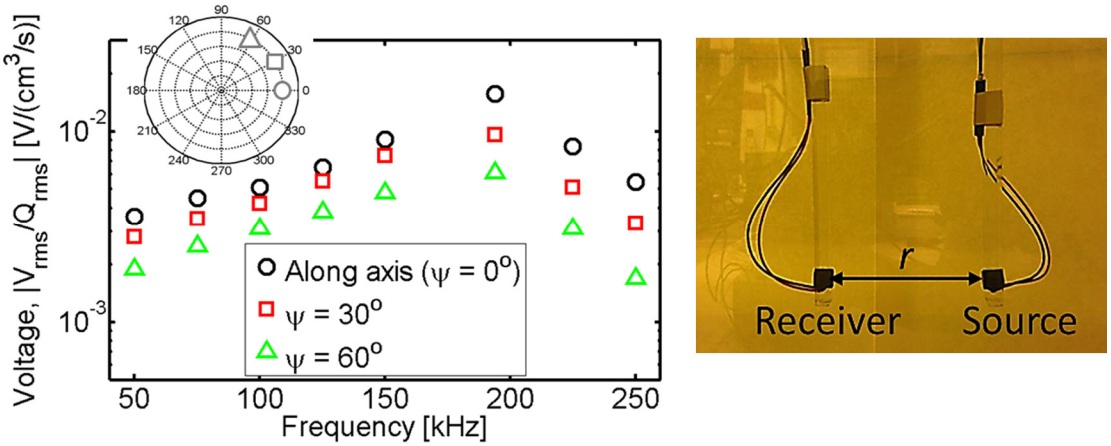

Figure 7.13. Voltage response of the receiver located at different orientation angles (for a source-to-receiver distance of $r = 90.1$ mm and load resistance of R_l=210Ω).

7.3.3 *Investigations on the effects of scattering on the incident pressure wave at the leading edge of the cylindrical receiver*

Multiphysics finite-element simulations are performed in COMSOL to explore the pressure field due to acoustic waves generated by the axially oscillating free-free piezoelectric bar submerged in fluid domain (in oil). The simulation is done in an unobstructed field (where the transmitted acoustic waves are not blocked by an obstacle/receiver inside the fluid domain) and boundaries of the fluid domain are defined to allow no reflection. The experimental and analytical (Equation (7.20)) pressure amlitudes versus frequency are given in for 18 V peak-to-peak actuation voltage at r = 90.1 mm in unobstructed acoustic field. Very good agreement is observed between finite-element simulations and the analytical model.

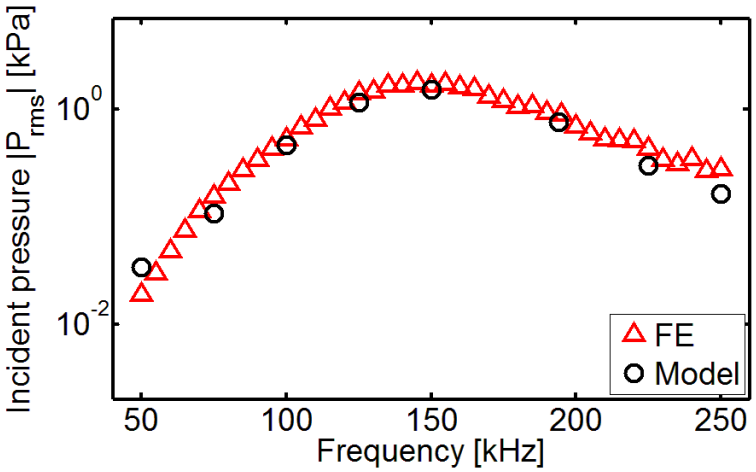

Figure 7.14. Finite-element vs. analytical model simulations for incident pressure in unobstructed sound field generated by an axially vibrating piezoelectric cylinder (r = 86.1 mm).

Having validated incident pressure amplitude at the leading surface of the receiver, resulting root-mean-square voltage output is given using Equation (7.23). By keeping the

load resistance at R_l=210Ω, burst excitations are performed at different frequencies. The experimental and analytical voltage output normalized to source strength FRFs over a broad range of excitation frequencies are shown in Figure 7.15a. Clearly, for this electrical load resistance value, the maximum power output takes place around 194 kHz, in agreement with Figure 7.7. Significant deviations are observed between experimental results and model predictions, especially at higher frequency range. The disagreements mainly reveal lacking of considering precise blocked pressure (incident pressure + scattered pressure) in the model. In other words, data obtained from the experiments confirms that scattering effects on the incident pressure must be considered in the modeling for the frequency range of interest and receiver dimensions. To show the dependency of the scattered pressure wave to excitation frequency and receiver dimension, percentage of the experimental voltage output over model prediction ratio is given in Figure 7.15b in terms of ka. For the source bar with constant radius $a = 3.5$ mm, these ratios grow by increasing frequency (ka is increasing) mainly around resonance frequency for $ka = 2.8$ up to approximately 200% . It means that, the magnitude of blocked pressure at receiver leading surface is approximately two times more than the magnitude of incident pressure used in model (Equation (7.23)).

Solving this problem and to gain a detailed understanding about the scattered pressure, multiphysics 3-D finite-element simulations are performed in COMSOL (Figure 7.16) to explore the pressure field generated by the axially oscillating free-free source bar submerged in fluid domain.

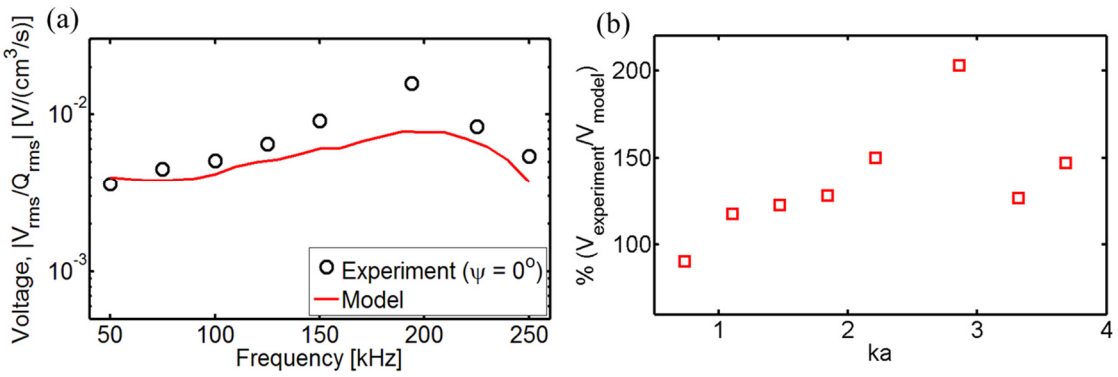

Figure 7.15. (a) Voltage response of the receiver to 3-cycle burst excitations for on-axis source-to-receiver distance of r = 90.1 mm and load resistance of R_l=210Ω) and (b) percentage of the experimental voltage output over model prediction ratio.

The simulation is done in an unobstructed (no receiver; Figure 7.16a) and obstructed (receiver is located along the source axis in distance r = 90.1 mm; Figure 7.16b) acoustic fields. Boundaries of the fluid domain are defined to allow no reflection. The results shown in Figure 7.17a are given for finite-element simulations of incident pressure in unobstructed field and total pressure at the leading surface of the cylindrical receiver. At each frequency, scattered pressure is obtained by subtracting the incident pressure magnitude from total pressure magnitude. Percentage of scattered pressure over incident pressure ratio for a broad range of ka are given Figure 7.17b. The results exhibit negligible effects of scattered pressure for ka<1.5 (the ratio is less than 5%) whereas these ratios grow by increasing ka predominantly around resonance frequency. Consistent with the results obtained from experiment, previously shown in Figure 7.15b, at some point the magnitude of scattered pressure at the receiver leading surface is comparable to the magnitude of incident pressure. For next section, at each frequency scattered pressure obtained from finite-element simulations is added to the predicted incident pressure by model in Equation (7.20) and the

total pressure is inserted to Equation (8.23) to accurately predict power output ($\Pi = v^2/R_l$) by the proposed model in this work.

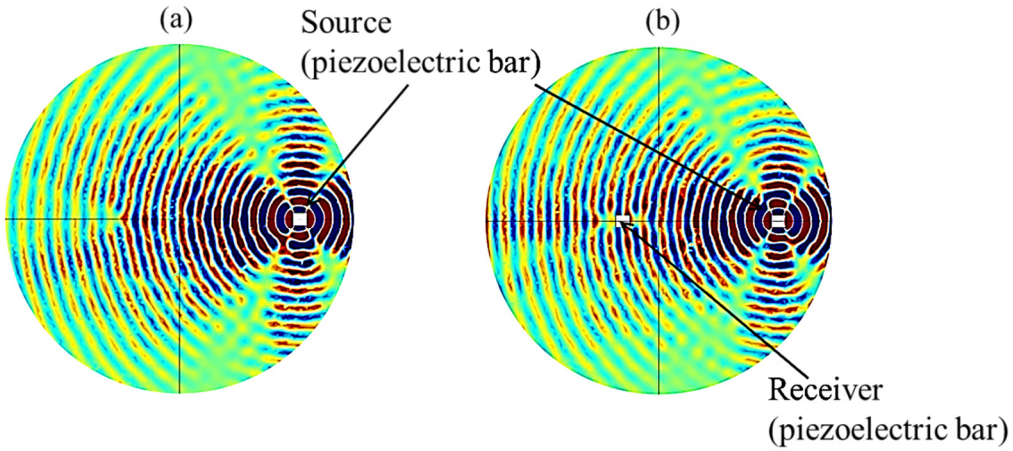

Figure 7.16. Finite-element simulation snapshot of (a) unobstructed and (b) obstructed (the receiver is a piezoelectric bar at $r = 86.1$ mm), acoustic pressure field generated by an axially vibrating piezoelectric cylindrical source.

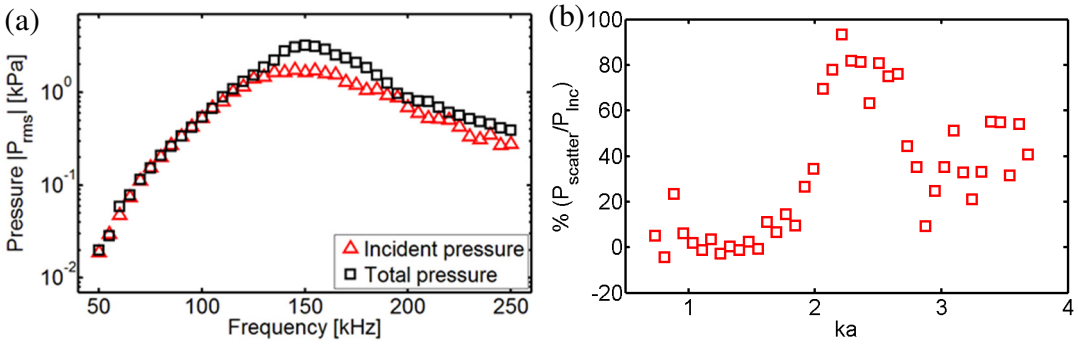

Figure 7.17. (a) Finite-element simulation of pressure amlitude versus frequency at $r = 90.1$ mm in unobstructed field (incident pressure) and obstructed field (total pressure is the pressure at the leading surface of the cylindrical receiver) and (b) percentage of scattered pressure over incident pressure ratio in terms of ka.

7.3.4 Effects of various system parameters

By keeping the load resistance at R_l=210Ω, burst excitations are performed at different frequencies. The resulting average power output FRFs over a broad range of excitation frequencies are shown in Figure 7.18a. Clearly, for this electrical load resistance value, the maximum power output takes place around 194 kHz, in agreement with Figure 7.7. Very good agreement is observed between the model predictions and experimental measurements in Figure 7.18a. Next, resistor sweep experiments are performed for 3-cycle burst excitations at the fundamental open-circuit resonance frequencies while keeping the source-to-receiver distance fixed (at r = 90.1 mm). The tests are conducted for a set of load resistance values ranging from 1Ω to 1kΩ, covering a broad range that is expected to include the optimal loads 194 kHz. As shown in Figure 7.18b, very good agreement is observed between experimental data and analytical model predictions of the power output normalized with respect to source strength squared. The load resistance is then fixed to $R_l = 210\Omega$ and the effect of source-to-receiver distance is studied as given in Figure 7.18c. The hyperbolic dependence of the power output to distance is expected since $v_{rms} \propto 1/r$ in Equation (7.21), and therefore, $\Pi_{avg} = v_{rms}^2 / R_l \propto 1/r^2$ for a fixed Q_{rms} value. With increased source-to-receiver distance, the power output of the receiver decreases monotonically and hyperbolically.

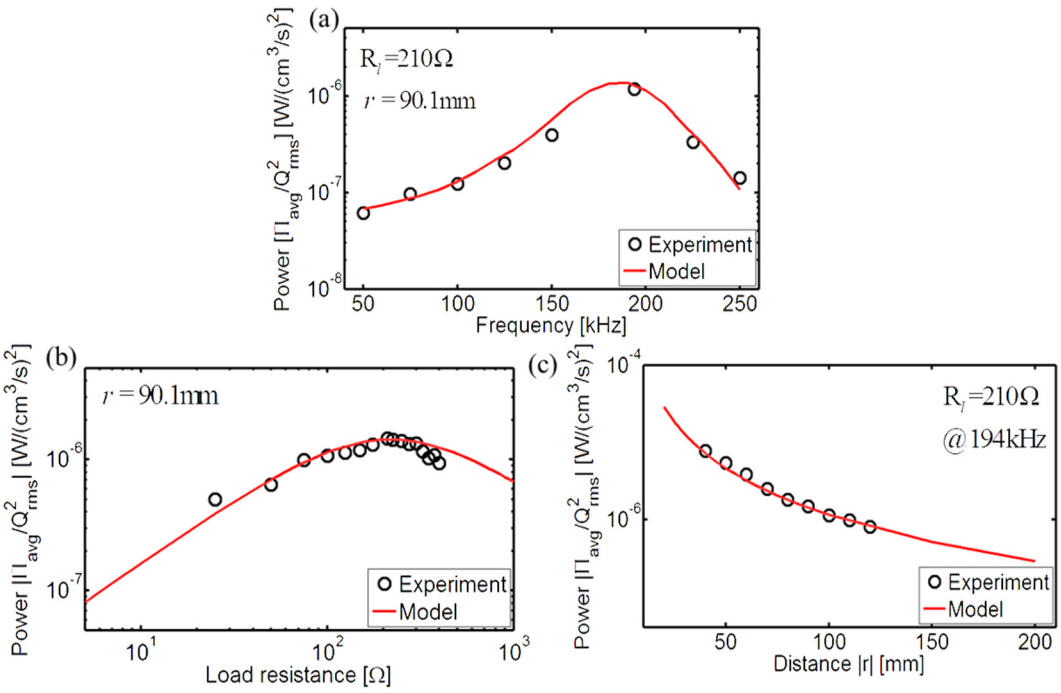

Figure 7.18. Average power output normalized with respect to source strength (a) FRFs for a source-to-receiver distance of $r = 90.1$ mm and load resistance of $R_l = 210\Omega$, (b) versus electrical load resistance at the fundamental in-oil open-circuit resonance frequency (for $r =$ 90.1 mm), and (c) versus source-to-receiver distance (for $R_l = 210\Omega$ excitation at 194 kHz).

7.4 Focused Ultrasonic Energy Transfer

Focused UAET is proposed in this section to locally concentrate the transmitted acoustic energy in space, and strongly excite the receiver for power output enhancement. In this section, focused UAET is investigated experimentally to enable efficient transmission of acoustic energy with two configurations.

Enhanced power transfer is achieved by focusing of the source (Figure 1.2, using curved piezoelectric transducer). To achieve this configuration, an array of piezoelectric cylindrical bars (for two sizes) is designed as shown in Figure 7.19 a and b. The parameter identification has been done for each piezoelectric bar through impedance measurement. The receiver is a

piezoelectric stack which is characterized in Section 7.3. The receiver is placed (with acceptable accuracy) at the focusing point located at geometric center of the cylindrical panel used to fix the source bars on a curved array. The receiver is connected to a load resistance at $R_l = 210\Omega$ (optimal load). Burst excitations are performed (18 V peak-to-peak magnitude) at different frequencies. The average power outputs over a broad range of excitation frequencies are shown in Figure 7.20 for the two experimental configurations. In Figure 7.20, the power outputs are compared for using single (receiver is located on the source axis) and multiple sources arranged in a curved configuration. The results show that using the curved arrays of source bars gave the amplitude of the power output 2-5 times greater than using single transmitter. Clearly, for this electrical load resistance value, the maximum power output takes place around 194 kHz consistent to the results shown in Figure 7.7.

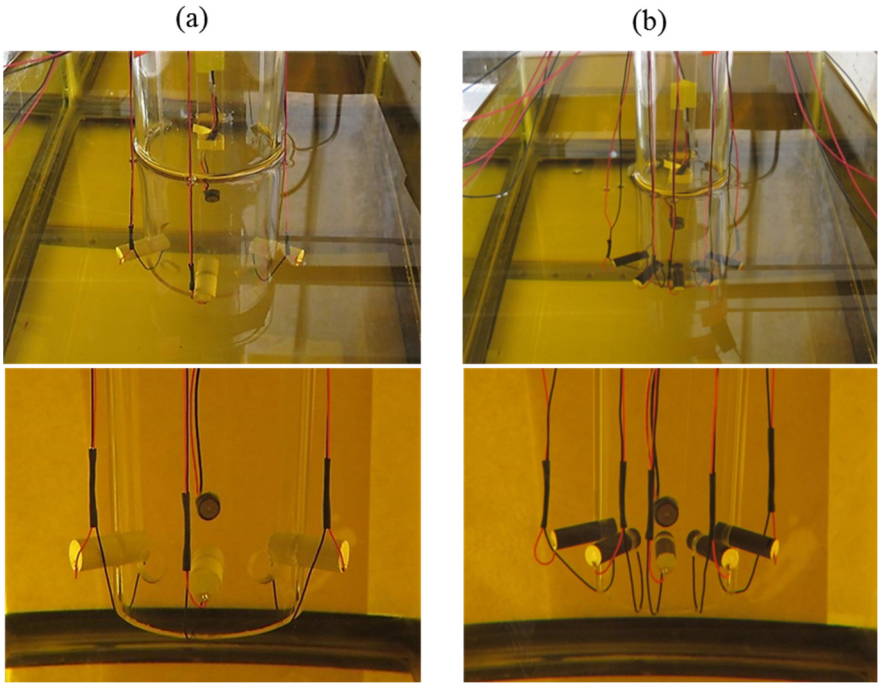

Figure 7.19. In-oil configurations for focusing of the source; Curved arrays of piezoelectric bars with two different sizes.

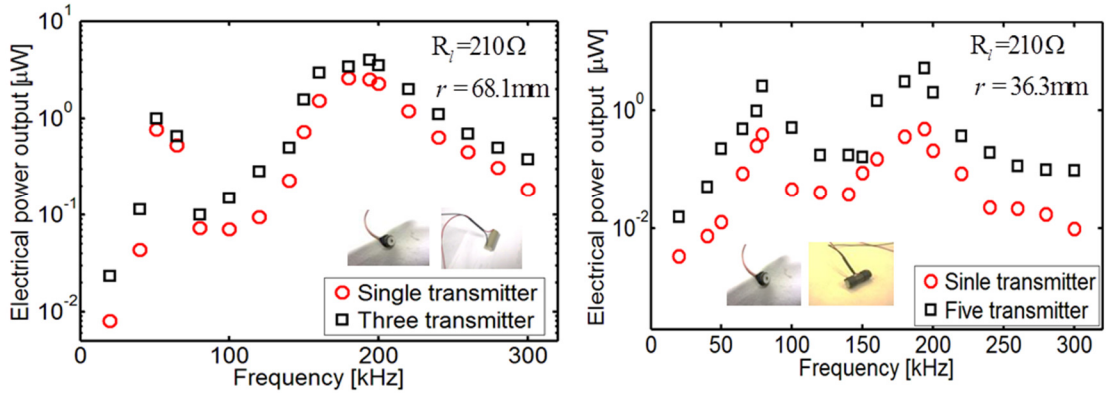

Figure 7.20. Average power output FRFs for (a) single and three sources (Figure 7.19a) and $r = 68.1$ mm, and (b) single and five sources (Figure 7.19b) $r = 36.3$ mm and load resistance of R_l=210Ω.

Other than using curved piezoelectric transducers to create focusing, mirroring concepts [137] can also be employed with using elliptical elastoacoustic mirrors, analogous to their 2D counterpart for elastoacoustic waves [138]. A spherical point source and a piezoelectric receiver are placed in an elliptical acoustic mirror domain. In order to accurately model the acoustic pressure field in fluid domain, 3-D multiphysics finite-element simulations are performed in COMSOL. The schematic in Figure 7.21 clearly exhibits the local focusing of acoustic wave energy inside the elliptical domain.

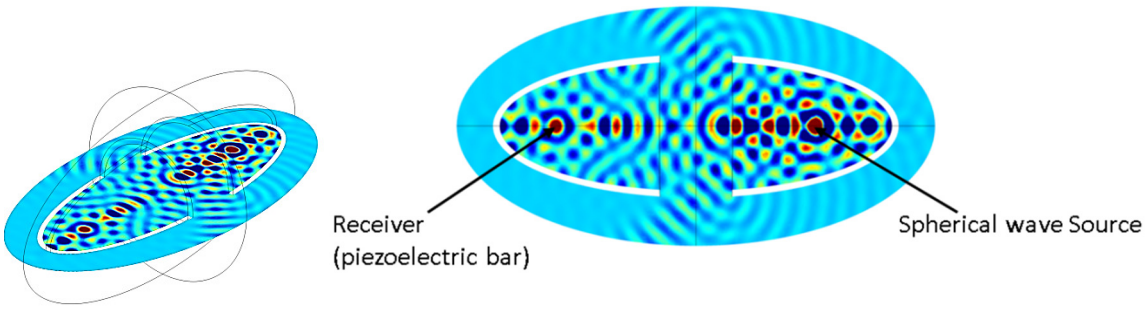

Figure 7.21. 3-D multiphysics finite-element simulation for spherical wave excitation (at 150 kHz) by a point source in an elliptical acoustic mirror configuration.

Figure 7.22 displays the experimental configuration employed to show the feasibility of focusing energy and thereby power transmission enhancement by using elliptical acoustic mirrors. Spherical acoustic waves are generated by a hydrophone (B&K 8103) and the receiver is a 33-mode piezoelectric stack (characterized in Section 7.3). The primary domains include the receiver and the transmitter placed in the elliptical mirrors (Figure 7.22b and Figure 7.22c) all together submerged in a quiescent fluid (e.g. oil). The accurate locations of the source and receiver have been defined by the finite-element simulation in COMSOL. The receiver is connected to a load resistance at $R_l = 100\Omega$ and located at distance 125.5 mm from the source. Burst excitations are performed (18 V peak-to-peak magnitude) at different frequencies.

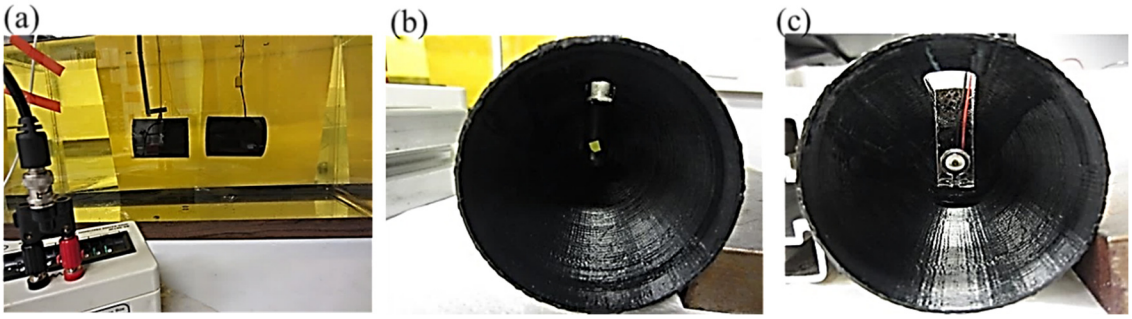

Figure 7.22. (a) In-oil configuration of transmitter, receiver, and acoustic mirrors, (b) transmitter (hydrophone) and (c) receiver located at distance 125.5 mm.

Figure 7.23 compares the average power output FRFs for the same actuation excitation (peal-to-peak voltage 18V) for the case of acoustic energy transfer by a hydrophone to the receiver without using elliptical mirrors and with using elliptical mirrors. The results show substantial power enhancement (approximately 300%) due to using the transmitter (hydrophone) and the receiver (piezoelectric stack) in the elliptical mirror domains.

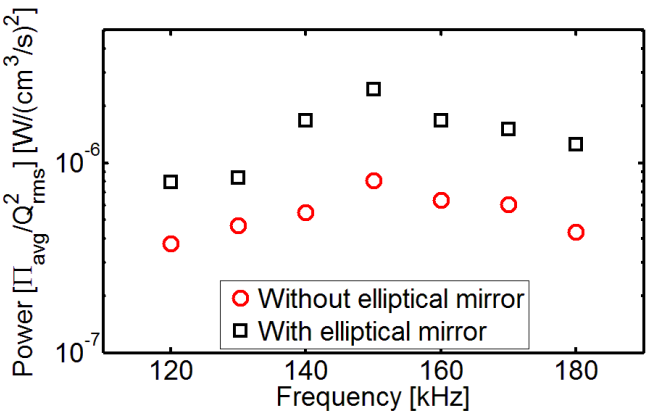

Figure 7. 23. Comparison of average power output for the same actuation excitation (peal-to-peak voltage 18V) showing the substantial power enhancement for using elliptical mirrors.

7.5 Summary and Conclusions

In this chapter of dissertation, UAET using a cylindrical source-cylindrical receiver combination (with free-free boundary conditions) is investigated theoretically and experimentally. Both the transmitter and receiver are modeled as unbaffled axially vibrating cylinders and the generated acoustic pressure from the cylindrical source is obtained by the solution of Helmholtz integral equation. The effects of increasing $k\bar{a}$ (where k is the wave number and $\bar{a}$ is the source bar radius) on directivity function are studied theoretically and experimentally. It is shown that with increasing $k\bar{a}$, the main transmitted acoustic energy is focused within a small angle sector around the source axis. Scattering phenomenon at the leading surface of the receiver bar (with radius a) and its effects on the incident pressure are investigated theoretically and numerically. The results exhibit negligible effects of scattered pressure for $ka < 1.5$ (scattered pressure-to-incident pressure ratio is less than 5%) whereas the scattering effects are found to be significant for $ka > 1.5$. Numerical simulations show that the magnitude of scattered pressure at the receiver leading surface is comparable to the

magnitude of incident pressure for excitations around resonance frequency of the receiver. Therefore for a receiver with constant radius, increasing excitation frequency (increasing *ka)* results in a favorable strong pressure field due to the scattering effects at surface of the receiver; however it is required to operate the transmitter/receiver close to its resonance frequency for maximum power output from the piezoelectric receiver. Optimal electrical loading conditions is shown and experimentally validated to be at the fundamental open-circuit resonance frequency of the receiver bar. Effect of source-to-receiver distance on the power output is also presented and validated.

The feasibility of power transmission enhancement using focused UAET is studied experimentally to enable efficient transmission of acoustic energy from acoustic sources with two configurations. Source focusing (curved array of piezoelectric source bars and free-free piezoelectric receiver bar) and elliptical electroacoustic mirrors (a hydrophone as a point source and free-free piezoelectric receiver bar) are employed in a set of proper experiments. The results show substantially power enhancement for using these proposed acoustic energy focusing methods.

8 CONCLUSIONS AND RECOMMENDED FUTURE RESEARCH

8.1 Summary, Conclusions, and Contributions

The first part of this research investigated underwater vibration energy harvesting and biomimetic dynamic actuation employing MFC-based piezoelectric structures. In the second part, contactless acoustic energy transfer using piezoelectric transduction was studied theoretically and experimentally for various transmitter configurations such as spherical, cylindrical, and focused. In this context, having introduced the main topics through a proper literature review in the first chapter, this dissertation covered the following two major topics starting from Chapter 2:

8.1.1 Vibration energy harvesting and dynamic actuation of MFCs in a quiescent fluid domain

In Chapter 2, an electroelastic modeling of 33-mode MFC bimorphs was developed for in-air energy harvesting and actuation applications. Homogenized electromechanical constitutive properties of MFCs were obtained based on mixing-rules formulation and coupled with the distributed-parameter electroelastic model to give the global elecrtroelastic parameters of MFCs with different aspect ratios. Experimentally validated equivalent analytical expressions for the capacitance and modal electromechanical coupling were given for the series and parallel connections of MFC laminates. The analytical modal electromechanical coupling terms were shown to depend directly on the width of the sample, yielding identical piezoelectric constants when normalized with respect to width. The successful modeling framework connected mixing rules formulation with the continuum homogenized

electroelastic dynamics for a variety of applications of MFCs, such as underwater vibration energy harvesting and actuation as discussed in the next two chapters.

Underwater vibration energy harvesting from piezoelectric MFCs with different length-to-width ratios and same thickness was explored experimentally and theoretically in Chapter 3. In order to develop high-fidelity models to predict the electrohydroelastic dynamics of base-excited MFC bimorphs in a quiescent fluid domain, mixing rules-based electroelastic mechanics modeling presented in Chapter 2 was coupled with the global electroelastic dynamics based on the Euler-Bernoulli kinematics and the nonlinear fluid loading based on Morison's semi-empirical model. The energy harvesting model was experimentally validated for predicting the power output delivered to an electrical load as well as the underwater vibration response for fully submerged MFC cantilevers. Inertia and drag coefficients were identified and asymptotic behavior for $L/b>5$ was observed. Strong dependence of the inertia and drag coefficients on the aspect ratio for $L/b<5$ was reported with good agreement between MFC and aluminum samples of the same aspect ratios. Variations of the electrical power output with excitation frequency and load resistance were obtained for different length-to-width ratios. For underwater cases, power density analysis revealed strong nonlinear dependence on the aspect ratio that can be exploited in design. Low values of L/b ratio were preferred to obtain large power density for the same base acceleration input to fully submerged cantilevers. To eliminate the cancellation due to strain node existing in the second mode shape, electrode segmentation was also performed for a cantilevered MFC bimorph. The results from the experiments for both linear and nonlinear responses of the segmented bimorph showed that using segmented electrodes could enhance the power output significantly for second mode excitation.

In Chapter 4, a modeling framework was presented for underwater biomimetic actuation of MFC bimorphs with three different aspect ratios. Following the experimentally validated model presented in Chapter 2, underwater tip velocity and admittance FRFs were derived by combining their in-air counterparts with Morison's nonlinear hydrodynamic function. Through a proper set of actuation tests, the inertia and drag coefficients in Morison's equation were identified and compared with the ones obtained from base-excited aluminum cantilevers of similar aspect ratios and base-excited energy harvesting (the experimental case studies in Chapter 3) for the same MFC bimorphs used in actuation experiments (Figure 4. 22). The repeatability of the inertia and drag coefficients in Morison's equation was observed for samples with the same aspect ratio. Curve fit expressions were reported to use with the presented model. The variations of inertia and drag coefficients with KC number were reported. The inertia coefficient was observed to be relatively insensitive to the KC number, whereas drag coefficient increased significantly with increased vibration mode number.

In Section 4.4, bio-inspired thrust generation was investigated theoretically and experimentally for MFC bimorphs with different aspect ratios. Experiments were conducted for various actuation voltage levels to quantify the mean thrust resultant and power consumption levels for different aspect ratios. The experimentally obtained vibration response and the virtual mass coefficient (defined in Morison's hydrodynamic function in Section 4.3) were coupled with Lighthill's elongated-body theory to predict the thrust output. The hydrodynamic thrust coefficient of the propulsor was estimated based on the virtual mass and aspect ratio, and then validated experimentally for MFC bimorphs with different aspect ratios. Although the inertia and drag coefficients were found to be highly dependent on the aspect ratio for small aspect ratios, the maximum mean thrust to power consumption

ratio was found to be insensitive to the aspect ratio, which directly influences the future design of untethered biomimetic robotic fish using MFCs. Trends of dimensionless thrust coefficient with respect to aspect ratio were reported and experimentally validated. It is expected that the experimental results and the modeling framework presented in this work can be applied in design of biomimetic robotic fish made from MFCs with thrust generation purposes.

8.1.2 Contactless acoustic energy transfer

In Chapter 5, multiphysics modeling of contactless ultrasound acoustic energy transfer was presented along with a detailed analysis. In UAET method, the ultrasound waves were generated by a spherical source and propagate through an acoustic medium (e.g. water). A piezoelectric bar (operating in 33-mode of piezoelectricity) as a receiver collected the acoustic energy and converted it to the electrical energy. An acoustic-electroelastic model of the fixed-free thickness-poled piezoelectric bar was presented analytically and validated numerically through FEM analysis. The multiphysics modeling of the acoustic-electroelastic structure interaction by FEM gave a comprehensive overview of the system dynamics. The effects of various parameters, such as the source strength, distance between the transmitter and the receiver, receiver size were explored by several case studies. The electrical power transmitted from the source to the receiver in terms of the source strength for a given distance between the transmitter and the receivers were quantified. Optimal resistive-reactive electrical loading results in substantially enhanced broadband power transfer compared to the purely resistive electrical loading case. Soft (PZT-5H) and hard (PZT-8) piezoelectric receivers were considered and significant performance enhancement was reported due to using PZT-8. The analytical electro-elasto-acoustic model derived in this work can give a

comprehensive description of ultrasonic energy transfer method for wirelessly charging low-power electronic devices.

In Chapter 6, contactless ultrasonic acoustic energy transfer was investigated analytically, numerically, and experimentally for a cylindrical 33-mode piezoelectric receiver in free-free mechanical boundary conditions excited by a spherical wave source. Experimental validations were presented along with parameter optimization studies. Effects of various system parameters, such as the source strength and the source-to-receiver distance, were presented and validated. Resistive and resistive-reactive electrical loading cases were discussed for performance enhancement and frequency-wise robustness. The presented multiphysics analytical model for UAET can be used to predict the coupled system dynamics with very good accuracy.

Theoretical, numerical, and experimental investigations on UAET were performed for a cylindrical source-cylindrical receiver combination in Chapter 7. Helmholtz integral equation was employed to obtain the acoustic pressure field from a axially oscillating source bar. Determination of operating frequency (with respect to source/receiver geometric properties) and its effects on the directivity pattern and scattering of incident pressure wave at the leading surface of the cylindrical receiver were investigated. The results showed that the main transmitted acoustic energy was focused within a small angle sector around the source axis with increased $k\bar{a}$. Scattering effects on the incident pressure were found to be significant for $ka > 1.5$. It was observed that increasing excitation frequency made a strong pressure field at the leading surface of the receiver. However, keeping the excitation frequency close to the receiver resonance frequency was of importance for maximum power output from the receiver. Employing source focusing and elliptical electroacoustic mirrors

showed substantially power enhancement for UAET. The experimental results and the multiphysics modeling framework presented in this work for UAET using a cylindrical source-cylindrical receiver combination can be used to accurately predict the coupled system dynamics.

8.2 Future Research

Some areas of potential future work are as follows:

- Considering nonlinear electroelastic dynamics [159-161] with nonlinear hydrodynamic effects [162] to predict the dynamics of the MFC propulsors for large oscillations and strong electric fields.
- Exploring energy focusing concepts [129, 130] and resulting acoustic nonlinearities [188] due to wave kinematics or medium, as well as transmitter/receiver electroelastic nonlinearities [161, 169-171], and advanced electrical power conditioning circuits [144, 189-194].

APPENDIX

In Chapter 3, in-air and underwater energy harvesting experimental FRFs are correlated with model simulations based on purely experimental parameters (given here in Figure A and Figure B) for accurate identification of the first and second mode inertia and drag coefficients (as summarized in Figure 3.15). These drag and inertia coefficients (Figure 3.15), when used in the semi-empirical electrohydroelastic Euler-Bernoulli-Morison model presented in the work in Chapter 3, result in the underwater FRF predictions given in Figure 3.9-Figure 3.11.

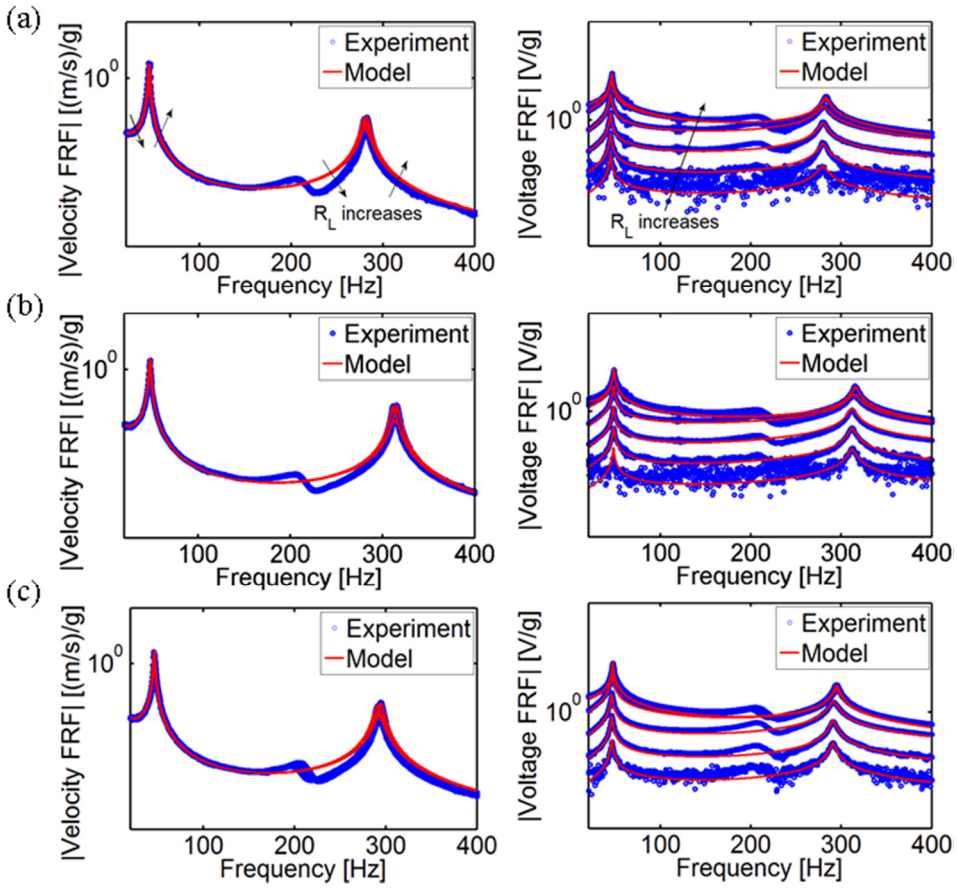

Figure A. In-air experimental and analytical frequency response results for base-excited energy harvesting of MFC bimorphs: Tip velocity (left-hand side) and voltage FRFs (right-hand side) for (a) M8507-P1, (b) M8514-P1 and (c) M8528-P1.

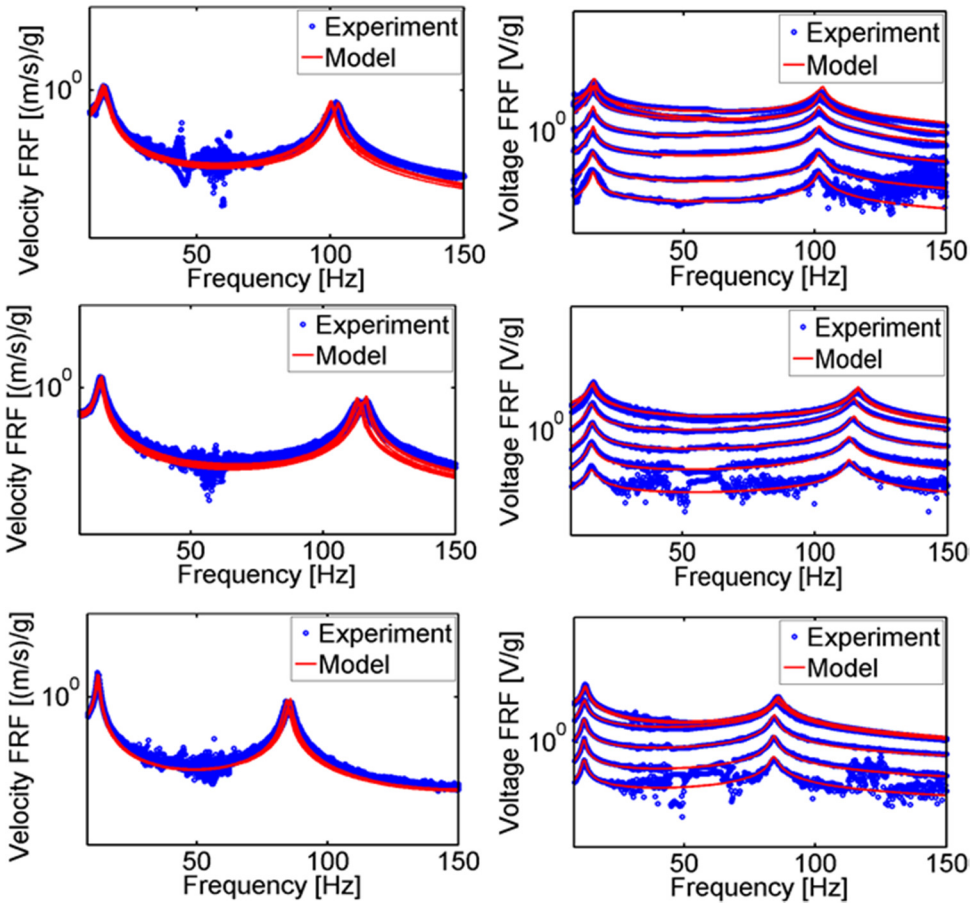

Figure B. Underwater experimental and analytical frequency response results for base-excited energy harvesting of MFC bimorphs: Tip velocity (left-hand side) and voltage FRFs (right-hand side) for M8507-P1, M8514-P1 and M8528-P1 from top to bottom, respectively.

In-air and underwater actuation experimental FRFs are correlated with model simulations based on purely experimental parameters in Chapter 4 (given here in Figure C and Figure D) for accurate identification of the first and second mode inertia and drag coefficients (as summarized in Figure 4.11). These drag and inertia coefficients (Figure 4.11), when used in the semi-empirical electrohydroelastic Euler-Bernoulli-Morison model presented in Chapter 4, result in the underwater FRF predictions given in Figure 4.8-Figure 4.10.

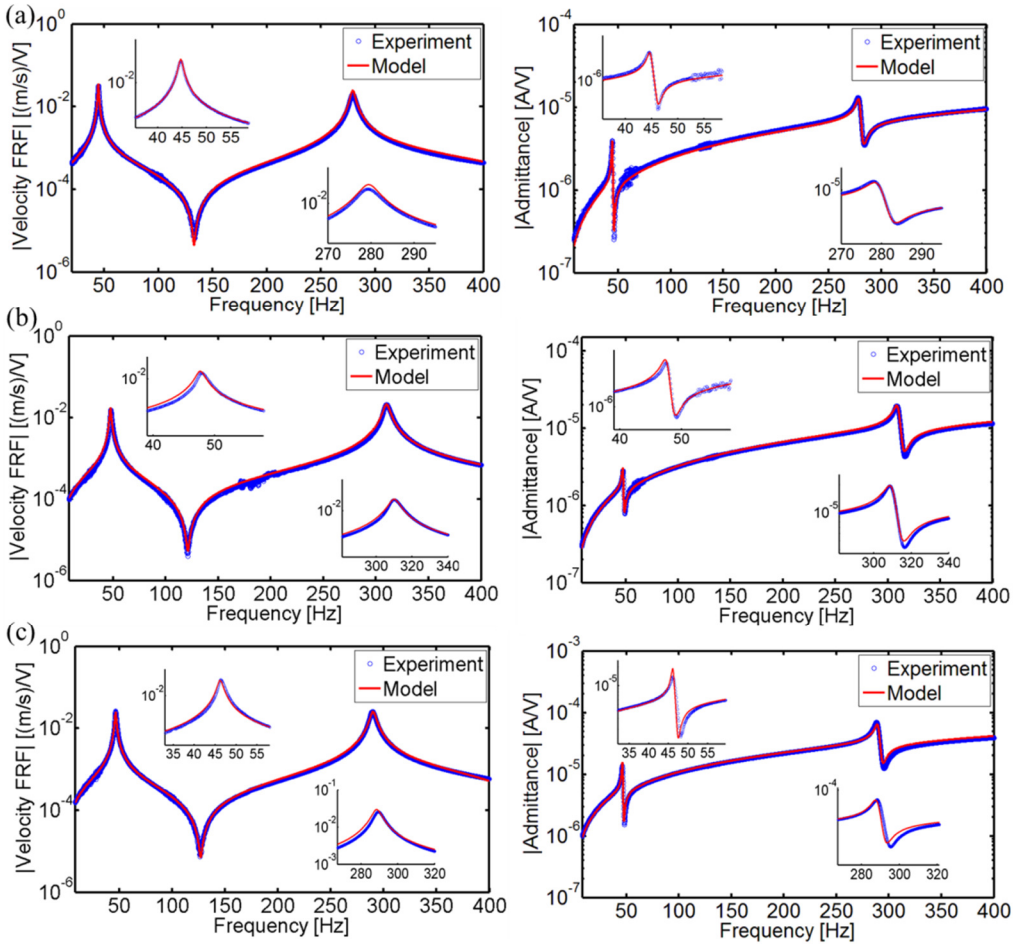

Figure C. In-air experimental and analytical frequency response results for actuation of MFC bimorphs: Tip velocity (left-hand side) and admittance FRFs (right-hand side) for (a) M8507-P1, (b) M8514-P1 and (c) M8528-P1.

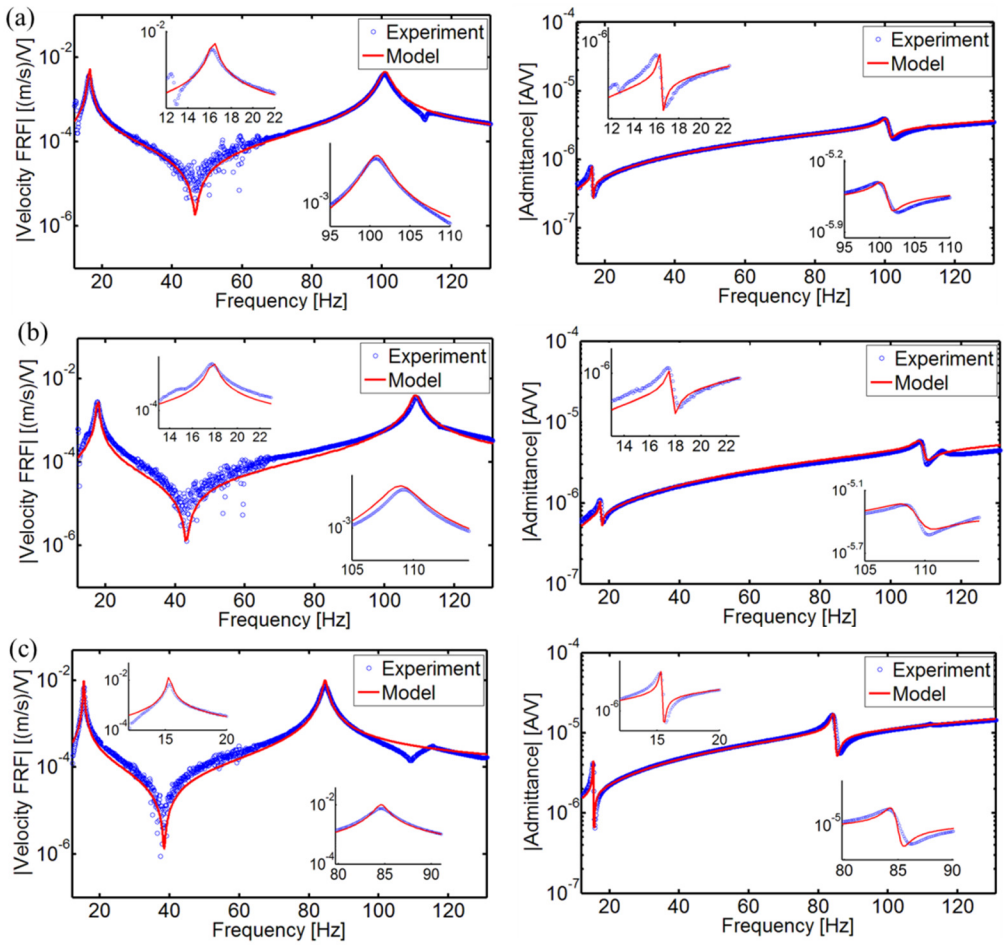

Figure D. Underwater experimental and analytical frequency response results for actuation of MFC bimorphs: Tip velocity (left-hand side) and admittance FRFs (right-hand side) for (a) M8507-P1, (b) M8514-P1 and (c) M8528-P1.

REFERENCES

[1] Erturk, A. and Inman, D. J., Piezoelectric Energy Harvesting, Chichester:: Wiley (2011).

[2] Feenstra, J., Granstrom, J., and Sodano, H., "Energy harvesting through a backpack employing a mechanically amplified piezoelectric stack," Mechanical Systems and Signal Processing. 22(3): 721-734 (2008).

[3] Masana, R. and Daqaq, M. F., "Electromechanical Modeling and Nonlinear Analysis of Axially Loaded Energy Harvesters," Journal of Vibration and Acoustics. 133(1) (2011).

[4] Shahab, S. and Erturk, A., "Contactless ultrasonic energy transfer for wireless systems: acoustic-piezoelectric structure interaction modeling and performance enhancement," Smart Mater. Struct. 23(12): 125032 (2014).

[5] Shahab, S., Gray, M., and Erturk, A., "Ultrasonic power transfer from a spherical acoustic wave source to a free-free piezoelectric receiver: Modeling and experiment," Journal of Applied Physics. 117(10): 104903 (2015).

[6] Hagood, N. W., Kindel, R., Ghandi, K., and Gaudenzi, P. "Improving transverse actuation of piezoceramics using interdigitated surface electrodes," in 1993 North American Conference on Smart Structures and Materials. International Society for Optics and Photonics 1993.

[7] Bent, A. A. and Hagood, N. W., "Piezoelectric fiber composites with interdigitated electrodes," Journal of Intelligent Material Systems and Structures. 8(11): 903-919 (1997).

[8] Bent, A. A., "Active Fiber Composites for Structural Actuation," (1997).

[9] Bent, A. A., Hagood, N. W., and Rodgers, J. P., "Anisotropic actuation with piezoelectric fiber composites," Journal of Intelligent Material Systems and Structures. 6(3): 338-349 (1995).

[10] Lin, Y. and Sodano, H. A., "Electromechanical characterization of a active structural fiber lamina for multifunctional composites," Composites Science and Technology. 69(11): 1825-1830 (2009).

[11] Brei, D. and Cannon, B. J., "Piezoceramic hollow fiber active composites," Composites Science and Technology. 64(2): 245-261 (2004).

[12] Lin, Y. and Sodano, H. A., "Concept and model of a piezoelectric structural fiber for multifunctional composites," Composites Science and Technology. 68(7): 1911-1918 (2008).

[13] Belloli, A., Niederberger, D., Pietrzko, S., Morari, M., and Ermanni, P., "Structural vibration control via RL shunted active fiber composites," Journal of Intelligent Material Systems and Structures. 18(3): 275-287 (2007).

[14] Belloli, A., Castelli, B., Kornmann, X., Huber, C., and Ermanni, P. "Modeling and characterization of active fiber composites," in Smart Structures and Materials. International Society for Optics and Photonics 2004.

[15] Wilkie, W. K., Bryant, R. G., High, J. W., Fox, R. L., Hellbaum, R. F., Jalink Jr, A., Little, B. D., and Mirick, P. H. "Low-cost piezocomposite actuator for structural control applications," in SPIE's 7th Annual International Symposium on Smart Structures and Materials. International Society for Optics and Photonics 2000.

[16] Bryant, R. G., "Overview of NASA Langley's Piezoelectric Ceramic Packaging Technology and Applications," National Aeronautics and Space Administration, Langley Research Center, (2007).

[17] http://www.smart-material.com/.

[18] Bent, A. A., Active fiber composites for structural actuation, 1997, Massachusetts Institute of Technology.

[19] Browning, J. S., Coff, R. G., Canfield, R. A., and Miller, S. K., "F-16 Ventral Fin Buffet Alleviation Using Piezoelectric Actuators," 50th AIAA/ASME/ASCE/AHS/ASC Structures, Structural Dynamics, and Materials Conference, (2009).

[20] Sodano, H. A., Park, G., and Inman, D. J., "An investigation into the performance of macro-fiber composites for sensing and structural vibration applications," Mechanical Systems and Signal Processing. 18(3): 683-697 (2004).

[21] Erturk, A. and Delporte, G., "Underwater thrust and power generation using flexible piezoelectric composites: an experimental investigation toward self-powered swimmer-sensor platforms," Smart Materials and Structures. 20(12): 125013 (2011).

[22] Cen, L. and Erturk, A., "Bio-inspired aquatic robotics by untethered piezohydroelastic actuation," Bioinspiration & Biomimetics. 8(1): 016006 (2013).

[23] Collet, M., Ruzzene, M., and Cunefare, K., "Generation of Lamb waves through surface mounted macro-fiber composite transducers," Smart Materials and Structures. 20(2): 025020 (2011).

[24] Matt, H. M. and di Scalea, F. L., "Macro-fiber composite piezoelectric rosettes for acoustic source location in complex structures," Smart Materials and Structures. 16(4): 1489 (2007).

[25] Kim, D.-K., "Smart flapping wing using macrofiber composite actuators." 6173: 61730F-61730F-9 (2006).

[26] Erturk, A., "Piezoelectric Energy Harvesting from Macro-Fiber Composites with an Application to Morphing-Wing Aircrafts," 19th International Conference on Adaptive Structures and Technologies, (2008).

[27] Paradies, R. and Ciresa, P., "Active wing design with integrated flight control using piezoelectric macro fiber composites," Smart Materials and Structures. 18(3): 035010 (2009).

[28] Arrieta, A. F., Bilgen, O., Friswell, M. I., and Ermanni, P., "Modelling and configuration control of wing-shaped bi-stable piezoelectric composites under aerodynamic loads," Aerospace Science and Technology. 29(1): 453-461 (2013).

[29] Cha, Y., Kim, H., and Porfiri, M., "Energy harvesting from underwater base excitation of a piezoelectric composite beam," Smart Materials and Structures. 22(11): 115026 (2013).

[30] Shahab, S. and Erturk, A. "Electrohydroelastic dynamics of macro-fiber composites for underwater energy harvesting from base excitation," in SPIE Smart Structures and Materials+ Nondestructive Evaluation and Health Monitoring. International Society for Optics and Photonics 2014.

[31] Shahab, S. and Erturk, A. "Underwater Dynamic Actuation of Macro-Fiber Composite Flaps With Different Aspect Ratios: Electrohydroelastic Modeling, Testing, and Characterization," in ASME 2014 Conference on Smart Materials, Adaptive Structures and Intelligent Systems. American Society of Mechanical Engineers 2014.

[32] Biscani, F., Nasser, H., Belouettar, S., and Carrera, E., "Equivalent electro-elastic properties of Macro Fiber Composite (MFC) transducers using asymptotic expansion approach," Composites Part B: Engineering. 42(3): 444-455 (2011).

[33] Berger, H., Kari, S., Gabbert, U., Rodriguez-Ramos, R., Guinovart, R., Otero, J. A., and Bravo-Castillero, J., "An analytical and numerical approach for calculating effective material coefficients of piezoelectric fiber composites," International journal of solids and structures. 42(21): 5692-5714 (2005).

[34] Choi, W. J., Jeon, Y., Jeong, J. H., Sood, R., and Kim, S. G., "Energy harvesting MEMS device based on thin film piezoelectric cantilevers," Journal of Electroceramics. 17(2-4): 543-548 (2006).

[35] Jeon, Y. B., Sood, R., Jeong, J. H., and Kim, S. G., "MEMS power generator with transverse mode thin film PZT," Sensors and Actuators a-Physical. 122(1): 16-22 (2005).

[36] Williams, R. B., Inman, D. J., and Wilkie, W. K., "Temperature-dependent thermoelastic properties for macro fiber composite actuators," Journal of Thermal Stresses. 27(10): 903-915 (2004).

[37] Williams, R. B., Grimsley, B. W., Inman, D. J., and Wilkie, W. K. "Manufacturing and mechanics-based characterization of macro fiber composite actuators," in ASME 2002 International Mechanical Engineering Congress and Exposition. American Society of Mechanical Engineers 2002.

[38] Williams, R. B., Inman, D. J., and Wilkie, W. K. "Nonlinear mechanical behavior of macro fiber composite actuators," in Proceedings of the Sixth International Conference on Sandwich Structures, March. 2003.

[39] Williams, R. B., Inman, D. J., Schultz, M. R., Hyer, M. W., and Wilkie, W. K., "Nonlinear tensile and shear behavior of macro fiber composite actuators," Journal of Composite Materials. 38(10): 855-869 (2004).

[40] Deraemaeker, A., Nasser, H., Benjeddou, A., and Preumont, A., "Mixing rules for the piezoelectric properties of macro fiber composites," Journal of Intelligent Material Systems and Structures. 20(12): 1475-1482 (2009).

[41] Deraemaeker, A., Benelechi, S., Benjeddou, A., and Preumont, A. "Analytical and numerical computation of homogenized properties of MFCs: Application to a composite boom with MFC actuators and sensors," in Proceedings of the III ECCOMAS thematic conference on Smart Structures and Materials. 2007.

[42] Williams, R. B., "Nonlinear mechanical and actuation characterization of piezoceramic fiber composites," PhD Thesis, Blacksburg (Va), USA, (2004).

[43] Deraemaeker, A. and Nasser, H., "Numerical evaluation of the equivalent properties of Macro Fiber Composite (MFC) transducers using periodic homogenization," International journal of solids and structures. 47(24): 3272-3285 (2010).

[44] Prasath, S. S. and Arockiarajan, A., "Experimental and theoretical investigation on the thermo-electro-elastic properties of Macro-Fiber Composites (MFC)," Composite Structures. 122: 8-22 (2015).

[45] Sader, J. E., "Frequency response of cantilever beams immersed in viscous fluids with applications to the atomic force microscope," Journal of Applied Physics. 84(1): 64-76 (1998).

[46] Van Eysden, C. A. and Sader, J. E., "Frequency response of cantilever beams immersed in viscous fluids with applications to the atomic force microscope: Arbitrary mode order," Journal of Applied Physics. 101(4): 044908-044908-11 (2007).

[47] Chon, J. W., Mulvaney, P., and Sader, J. E., "Experimental validation of theoretical models for the frequency response of atomic force microscope cantilever beams immersed in fluids," Journal of Applied Physics. 87(8): 3978-3988 (2000).

[48] Van Eysden, C. A. and Sader, J. E., "Resonant frequencies of a rectangular cantilever beam immersed in a fluid," Journal of Applied Physics. 100(11): 114916-114916-8 (2006).

[49] Brunetto, P., Fortuna, L., Graziani, S., and Strazzeri, S., "A model of ionic polymer–metal composite actuators in underwater operations," Smart Materials and Structures. 17(2): 025029 (2008).

[50] Mbemmo, E., Chen, Z., Shatara, S., and Tan, X. "Modeling of biomimetic robotic fish propelled by an ionic polymer-metal composite actuator," in Robotics and Automation, 2008. ICRA 2008. IEEE International Conference on. IEEE 2008.

[51] Aureli, M., Kopman, V., and Porfiri, M., "Free-locomotion of underwater vehicles actuated by ionic polymer metal composites," Mechatronics, IEEE/ASME Transactions on. 15(4): 603-614 (2010).

[52] Aureli, M., Prince, C., Porfiri, M., and Peterson, S. D., "Energy harvesting from base excitation of ionic polymer metal composites in fluid environments," Smart Materials and Structures. 19(1): 015003 (2010).

[53] Facci, A. L. and Porfiri, M., "Analysis of three-dimensional effects in oscillating cantilevers immersed in viscous fluids," Journal of Fluids and Structures. 38: 205-222 (2013).

[54] Aureli, M., Basaran, M., and Porfiri, M., "Nonlinear finite amplitude vibrations of sharp-edged beams in viscous fluids," Journal of Sound and Vibration. 331(7): 1624-1654 (2012).

[55] Aureli, M. and Porfiri, M., "Low frequency and large amplitude oscillations of cantilevers in viscous fluids," Applied Physics Letters. 96(16): 164102 (2010).

[56] Falcucci, G., Aureli, M., Ubertini, S., and Porfiri, M., "Transverse harmonic oscillations of laminae in viscous fluids: a lattice Boltzmann study," Philosophical Transactions of the Royal Society A: Mathematical, Physical and Engineering Sciences. 369(1945): 2456-2466 (2011).

[57] Phan, C. N., Aureli, M., and Porfiri, M., "Finite amplitude vibrations of cantilevers of rectangular cross sections in viscous fluids," Journal of Fluids and Structures, (2013).

[58] Bidkar, R. A., Kimber, M., Raman, A., Bajaj, A. K., and Garimella, S. V., "Nonlinear aerodynamic damping of sharp-edged flexible beams oscillating at low Keulegan–Carpenter numbers," Journal of Fluid Mechanics. 634: 269-289 (2009).

[59] Kopman, V. and Porfiri, M., "Design, modeling, and characterization of a miniature robotic fish for research and education in biomimetics and bioinspiration," Mechatronics, IEEE/ASME Transactions on. 18(2): 471-483 (2013).

[60] Morison, J., Johnson, J., and Schaaf, S., "The force exerted by surface waves on piles," Journal of Petroleum Technology. 2(05): 149-154 (1950).

[61] Morison, J., Johnson, J. W., and O'Brien, M. P., "Experimental studies of forces on piles," Coastal Engineering Proceedings. 1(4): 25 (1953).

[62] Graham, J., "The forces on sharp-edged cylinders in oscillatory flow at low Keulegan–Carpenter numbers," Journal of Fluid Mechanics. 97(02): 331-346 (1980).

[63] Sarpkaya, T., "Force on a circular cylinder in viscous oscillatory flow at low Keulegan—Carpenter numbers," Journal of Fluid Mechanics. 165: 61-71 (1986).

[64] Tuck, E., "Calculation of unsteady flows due to small motions of cylinders in a viscous fluid," Journal of Engineering Mathematics. 3(1): 29-44 (1969).

[65] Erturk, A., Tarazaga, P. A., Farmer, J. R., and Inman, D. J., "Effect of strain nodes and electrode configuration on piezoelectric energy harvesting from cantilevered beams," Journal of Vibration and Acoustics. 131(1): 011010 (2009).

[66] Bandyopadhyay, P. R., "Trends in biorobotic autonomous undersea vehicles," Oceanic Engineering, IEEE Journal of. 30(1): 109-139 (2005).

[67] Roper, D., Sharma, S., Sutton, R., and Culverhouse, P., "A review of developments towards biologically inspired propulsion systems for autonomous underwater vehicles," Proceedings of the Institution of Mechanical Engineers, Part M: Journal of Engineering for the Maritime Environment. 225(2): 77-96 (2011).

[68] Chu, W. S., Lee, K. T., Song, S. H., Han, M. W., Lee, J. Y., Kim, H. S., Kim, M. S., Park, Y. J., Cho, K. J., and Ahn, S. H., "Review of biomimetic underwater robots using smart actuators," International Journal of Precision Engineering and Manufacturing. 13(7): 1281-1292 (2012).

[69] Liu, F., Lee, K.-M., and Yang, C.-J., "Hydrodynamics of an undulating fin for a wave-like locomotion system design," Mechatronics, IEEE/ASME Transactions on. 17(3): 554-562 (2012).

[70] Wen, L., et al., "Quantitative Thrust Efficiency of a Self-Propulsive Robotic Fish: Experimental Method and Hydrodynamic Investigation," IEEE/ASME Transactions on,(Mechatronics): 1-12

[71] Liu, J. D., Dukes, I., and Hu, H. S., "Novel mechatronics design for a robotic fish," 2005 IEEE/RSJ International Conference on Intelligent Robots and Systems, Vols 1-4: 2077-2082 (2005).

[72] Liu, F. F., Lee, K. M., and Yang, C. J., "Hydrodynamics of an Undulating Fin for a Wave-Like Locomotion System Design," Ieee-Asme Transactions on Mechatronics. 17(3): 554-562 (2012).

[73] Crespi, A., Lachat, D., Pasquier, A., and Ijspeert, A. J., "Controlling swimming and crawling in a fish robot using a central pattern generator," Autonomous Robots. 25(1-2): 3-13 (2008).

[74] Zhou, C. L. and Low, K. H., "Design and Locomotion Control of a Biomimetic Underwater Vehicle With Fin Propulsion," Ieee-Asme Transactions on Mechatronics. 17(1): 25-35 (2012).

[75] Cen, L., Fish-like locomotion using flexible piezoelectric composites for untethered aquatic robotics, 2012, Georgia Institute of Technology.

[76] Chu, W. S., Lee, K. T., Song, S. H., Han, M. W., Lee, J. Y., Kim, H. S., Kim, M. S., Park, Y. J., Cho, K. J., and Ahn, S. H., "Review of Biomimetic Underwater Robots Using Smart Actuators (vol 13, pg 1281, 2012)," International Journal of Precision Engineering and Manufacturing. 13(9): 1721-1721 (2012).

[77] Kim, B., Kim, D. H., Jung, J. H., and Park, J. O., "A biomimetic undulatory tadpole robot using ionic polymer-metal composite actuators," Smart Materials & Structures. 14(6): 1579-1585 (2005).

[78] Tan, X. B., Kim, D., Usher, N., Laboy, D., and Jackson, J., "An autonomous robotic fish for mobile sensing," 2006 IEEE/RSJ International Conference on Intelligent Robots and Systems, Vols 1-12: 5424-5429 (2006).

[79] Ye, X. F., Su, Y. D., and Guo, S. X., "A centimeter-scale autonomous robotic fish actuated by IPMC actuator," 2007 Ieee International Conference on Robotics and Biomimetics, Vols 1-5: 262-267 (2007).

[80] Ye, X. F., Su, Y. D., Guo, S. X., and Wang, L. Q., "Design and Realization of a Remote Control Centimeter-Scale Robotic Fish," 2008 Ieee/Asme International Conference on Advanced Intelligent Mechatronics, Vols 1-3: 25-30 (2008).

[81] Mbemmo, E., Chen, Z., Shatara, S., and Tan, X. B., "Modeling of biomimetic robotic fish propelled by an ionic polymer-metal composite actuator," 2008 Ieee International Conference on Robotics and Automation, Vols 1-9: 689-694 (2008).

[82] Aureli, M., Kopman, V., and Porfiri, M., "Free-Locomotion of Underwater Vehicles Actuated by Ionic Polymer Metal Composites," Ieee-Asme Transactions on Mechatronics. 15(4): 603-614 (2010).

[83] Chen, Z., Shatara, S., and Tan, X. B., "Modeling of Biomimetic Robotic Fish Propelled by An Ionic Polymer-Metal Composite Caudal Fin," Ieee-Asme Transactions on Mechatronics. 15(3): 448-459 (2010).

[84] Wilkie, W. K., Bryant, R. G., High, J. W., Fox, R. L., Hellbaum, R. F., Jalink Jr., A., Little, B. D., and Mirick, P. H., "Low-Cost Piezocomposite Actuator for Structural Control Applicaitons," (2000).

[85] Nagata, Y., Park, S., Ming, A., and Shimojo, M. "Development of underwater robot using Macro Fiber Composite," in Advanced Intelligent Mechatronics, 2008. AIM 2008. IEEE/ASME International Conference on. IEEE 2008.

[86] Ming, A., Park, S., Nagata, Y., and Shimojo, M. "Development of underwater robots using piezoelectric fiber composite," in Robotics and Automation, 2009. ICRA'09. IEEE International Conference on. IEEE 2009.

[87] Shintake, J., Ming, A., and Shimojo, M. "Development of flexible underwater robots with caudal fin propulsion," in Intelligent Robots and Systems (IROS), 2010 IEEE/RSJ International Conference on. IEEE 2010.

[88] Kancharala, A. and Philen, M., "Enhanced hydrodynamic performance of flexible fins using macro fiber composite actuators," Smart Materials and Structures. 23(11): 115012 (2014).

[89] Erturk, A. and Inman, D. J., "An experimentally validated bimorph cantilever model for piezoelectric energy harvesting from base excitations," Smart Materials and Structures. 18(2): 025009 (2009).

[90] Erturk, A. and Inman, D. J., "A distributed parameter electromechanical model for cantilevered piezoelectric energy harvesters," Journal of Vibration and Acoustics. 130(4): 041002 (2008).

[91] Troesch, A. W. and Kim, S., "Hydrodynamic forces acting on cylinders oscillating at small amplitudes," Journal of Fluids and Structures. 5(1): 113-126 (1991).

[92] Keulegan, G. H. and Carpenter, L. H., Forces on cylinders and plates in an oscillating fluid: US Department of Commerce, National Bureau of Standards (1956).

[93] Ihara, A. and Watanabe, H., "On the flow around flexible plates, oscillating with large amplitude," Journal of Fluids and Structures. 8(6): 601-619 (1994).

[94] Jalalisendi, M., Panciroli, R., Cha, Y., and Porfiri, M., "A particle image velocimetry study of the flow physics generated by a thin lamina oscillating in a viscous fluid," Journal of Applied Physics. 115(5): 054901 (2014).

[95] Phan, C. N., Aureli, M., and Porfiri, M., "Finite amplitude vibrations of cantilevers of rectangular cross sections in viscous fluids," Journal of Fluids and Structures. 40: 52-69 (2013).

[96] Van Eysden, C. A. and Sader, J. E., "Small amplitude oscillations of a flexible thin blade in a viscous fluid: Exact analytical solution," Physics of Fluids. 18: 123102 (2006).

[97] Lighthill, M., "Note on the swimming of slender fish," Journal of fluid Mechanics. 9(02): 305-317 (1960).

[98] Lighthill, M., "Hydromechanics of aquatic animal propulsion," Annual review of fluid mechanics. 1(1): 413-446 (1969).

[99] Lighthill, M., "Aquatic animal propulsion of high hydrodynamic efficiency," J. Fluid Mech. v44: 265-301

[100] Anton, S. R. and Sodano, H. A., "A review of power harvesting using piezoelectric materials (2003–2006)," Smart materials and Structures. 16(3): R1 (2007).

[101] Cook-Chennault, K., Thambi, N., and Sastry, A., "Powering MEMS portable devices—a review of non-regenerative and regenerative power supply systems with special emphasis on piezoelectric energy harvesting systems," Smart Materials and Structures. 17(4): 043001 (2008).

[102] Elvin, N. and Erturk, A., Advances in Energy Harvesting Methods: Springer (2013).

[103] Harne, R. and Wang, K., "A review of the recent research on vibration energy harvesting via bistable systems," Smart materials and structures. 22(2): 023001 (2013).

[104] Daqaq, M., Masana, R., Erturk, A., and Quinn, D. D., "On the Role of Nonlinearities in Vibratory Energy Harvesting: A Critical Review and Discussion," Applied Mechanics Reviews. 66: 040801 (2014).

[105] Roes, M. G. L., Duarte, J. L., Hendrix, A. M., and Lomonova, E. A., "Acoustic Energy Transfer: A Review," IEEE Trans. Ind. Electron. 60(1): 242 (2013).

[106] Amin Karami, M. and Inman, D. J., "Powering pacemakers from heartbeat vibrations using linear and nonlinear energy harvesters," Applied Physics Letters. 100(4): 042901-042901-4 (2012).

[107] Fahy, F. J. and Gardonio, P., Sound and structural vibration: radiation, transmission and response: Academic press (2007).

[108] Kornbluh, R. D., Pelrine, R., Prahlad, H., Wong-Foy, A., McCoy, B., Kim, S., Eckerle, J., and Low, T. "From boots to buoys: promises and challenges of dielectric elastomer energy harvesting," in SPIE Smart Structures and Materials+ Nondestructive Evaluation and Health Monitoring. International Society for Optics and Photonics 2011.

[109] McKay, T. G., O'Brien, B. M., Calius, E. P., and Anderson, I. A., "Soft generators using dielectric elastomers," Applied Physics Letters. 98(14): 142903 (2011).

[110] Dogruer, D., Tiwari, R., and Kim, K. "Ionic polymer metal composites as energy harvesters," in The 14th International Symposium on: Smart Structures and Materials & Nondestructive Evaluation and Health Monitoring. International Society for Optics and Photonics 2007.

[111] Brown, W. C., "The history of power transmission by radio waves," IEEE Transactions on Microwave Theory and Techniques. 32(9): 1230-1242 (1984).

[112] Brown, W. C., "The history of wireless power transmission," Solar Energy. 56(1): 3-21 (1996).

[113] Dickinson, R. M., "Wireless power transmission technology state of the art the first Bill Brown lecture," Acta Astronomica. 53(4): 561-570 (2003).

[114] Cochran, G. V., Johnson, M., Kadaba, M., Vosburgh, F., Ferguson-Pell, M., and Palmeiri, V., "Piezoelectric internal fixation devices: A new approach to electrical augmentation of osteogenesis," J. Orthop. Res. 3(4): 508-513 (1985).

[115] Cochran, G. V., Kadaba, M. P., and Palmieri, V. R., "External ultrasound can generate microampere direct currents in vivo from implanted piezoelectric materials," J. Orthop. Res. 6(1): 145-147 (1988).

[116] Kawanabe, H., Katane, T., Saotome, H., Saito, O., and Kobayashi, K., "Power and information transmission to implanted medical device using ultrasonic," Jpn. J. Appl. Phys. 40: 3865 (2001).

[117] Suzuki, S.-n., Kimura, S., Katane, T., Saotome, H., Saito, O., and Kobayashi, K., "Power and interactive information transmission to implanted medical device using ultrasonic," Jpn. J. Appl. Phys. 41(5B): 3600-3603 (2002).

[118] Ozeri, S. and Shmilovitz, D., "Ultrasonic transcutaneous energy transfer for powering implanted devices," Ultrasonics. 50(6): 556-566 (2010).

[119] Ozeri, S., Shmilovitz, D., Singer, S., and Wang, C.-C., "Ultrasonic transcutaneous energy transfer using a continuous wave 650kHz Gaussian shaded transmitter," Ultrasonics. 50(7): 666-674 (2010).

[120] Maleki, T., Cao, N., Song, S. H., Kao, C., Ko, S.-C., and Ziaie, B., "An ultrasonically powered implantable micro-oxygen generator (IMOG)," IEEE Trans. Biomed. Eng. 58(11): 3104-3111 (2011).

[121] Olivo, J., Carrara, S., and De Micheli, G., "Energy harvesting and remote powering for implantable biosensors," IEEE Sensors Journal. 11(7): 1573-1586 (2011).

[122] Kurs, A., Karalis, A., Moffatt, R., Joannopoulos, J. D., Fisher, P., and Soljačić, M., "Wireless power transfer via strongly coupled magnetic resonances," Science. 317(5834): 83-86 (2007).

[123] Cannon, B. L., Hoburg, J. F., Stancil, D. D., and Goldstein, S. C., "Magnetic resonant coupling as a potential means for wireless power transfer to multiple small receivers," IEEE Transactions on Power Electronics. 24(7): 1819-1825 (2009).

[124] Karalis, A., Joannopoulos, J. D., and Soljačić, M., "Efficient wireless non-radiative mid-range energy transfer," Annals of Physics. 323(1): 34-48 (2008).

[125] Sample, A. P., Meyer, D. A., and Smith, J. R., "Analysis, experimental results, and range adaptation of magnetically coupled resonators for wireless power transfer," IEEE Transactions on Industrial Electronics. 58(2): 544-554 (2011).

[126] Zhang, F., Hackworth, S. A., Fu, W., Li, C., Mao, Z., and Sun, M., "Relay effect of wireless power transfer using strongly coupled magnetic resonances," IEEE Transactions on Magnetics. 47(5): 1478-1481 (2011).

[127] Sahai, A. and Graham, D. "Optical wireless power transmission at long wavelengths," in Space Optical Systems and Applications (ICSOS), 2011 International Conference on. IEEE 2011.

[128] Denisov, A. and Yeatman, E. "Ultrasonic vs. inductive power delivery for miniature biomedical implants," in Body Sensor Networks (BSN), 2010 International Conference on. IEEE 2010.

[129] ter Haar, G. and Coussios, C., "High intensity focused ultrasound: physical principles and devices," International Journal of Hyperthermia. 23(2): 89-104 (2007).

[130] Carrara, M., Cacan, M., Leamy, M., Ruzzene, M., and Erturk, A., "Dramatic enhancement of structure-borne wave energy harvesting using an elliptical acoustic mirror," Applied Physics Letters. 100(20): 204105 (2012).

[131] Carrara, M., Cacan, M., Toussaint, J., Leamy, M., Ruzzene, M., and Erturk, A., "Metamaterial-inspired structures and concepts for elastoacoustic wave energy harvesting," Smart Materials and Structures. 22(6): 065004 (2013).

[132] Carrara, M., Kulpe, J., Leadenham, S., Leamy, M., and Erturk, A., "Fourier transform-based design of a patterned piezoelectric energy harvester integrated with an elastoacoustic mirror," Applied Physics Letters. 106(1): 013907 (2015).

[133] Canney, M. S., Bailey, M. R., Crum, L. A., Khokhlova, V. A., and Sapozhnikov, O. A., "Acoustic characterization of high intensity focused ultrasound fields: A combined measurement and modeling approach," J. Acoust. Soc. Am. 124(4): 2406-2420 (2008).

[134] O'Neil, H., "Theory of focusing radiators," The Journal of the Acoustical Society of America. 21(5): 516-526 (1949).

[135] Kennedy, J., Wu, F., Ter Haar, G., Gleeson, F., Phillips, R., Middleton, M., and Cranston, D., "High-intensity focused ultrasound for the treatment of liver tumours," Ultrasonics. 42(1): 931-935 (2004).

[136] Hynynen, K. and Clement, G., "Clinical applications of focused ultrasound-the brain," International Journal of Hyperthermia. 23(2): 193-202 (2007).

[137] Carrara, M., Cacan, M., Leamy, M., Ruzzene, M., and Erturk, A., "Dramatic enhancement of structure-borne wave energy harvesting using an elliptical acoustic mirror," Appl. Phys. Lett. 100(20): 204105 (2012).

[138] Carrara, M., Kulpe, J., Leadenham, S., Leamy, M., and Erturk, A., "Fourier transform-based design of a patterned piezoelectric energy harvester integrated with an elastoacoustic mirror," Appl. Phys. Lett. 106(1): 013907 (2015).

[139] Beckert, W. and Kreher, W. S., "Modelling piezoelectric modules with interdigitated electrode structures," Computational Materials Science. 26: 36-45 (2003).

[140] Bowen, C., Nelson, L., Stevens, R., Cain, M., and Stewart, M., "Optimisation of interdigitated electrodes for piezoelectric actuators and active fibre composites," Journal of Electroceramics. 16(4): 263-269 (2006).

[141] DuToit, N. E. and Wardle, B. L., "Experimental verification of models for microfabricated piezoelectric vibration energy harvesters," AIAA Journal. 45(5): 1126-1137 (2007).

[142] Cacan, M. and Erturk, A. "Comparative investigation of the electroelastic dynamics of piezoceramics with interdigitated and uniform electrodes," in ASME 2012 Conference on Smart Materials, Adaptive Structures and Intelligent Systems. American Society of Mechanical Engineers 2012.

[143] Agarwal, B. D., Broutman, L. J., and Chandrashekhara, K., Analysis and performance of fiber composites: John Wiley & Sons (2006).

[144] Shu, Y. and Lien, I., "Analysis of power output for piezoelectric energy harvesting systems," Smart Materials and Structures. 15(6): 1499 (2006).

[145] Erturk, A. and Inman, D., "Parameter identification and optimization in piezoelectric energy harvesting: analytical relations, asymptotic analyses, and experimental validations," Proceedings of the Institution of Mechanical Engineers, Part I: Journal of Systems and Control Engineering. 225(4): 485-496 (2011).

[146] Lesieutre, G. A., "Vibration damping and control using shunted piezoelectric materials," The Shock and Vibration Digest. 30(3): 187-195 (1998).

[147] Lesieutre, G. A., Ottman, G. K., and Hofmann, H. F., "Damping as a result of piezoelectric energy harvesting," Journal of Sound and Vibration. 269(3): 991-1001 (2004).

[148] Shahab, S. and Erturk, A. "Experimentally Validated Nonlinear Electrohydroelastic Euler-Bernoulli-Morison Model for Macro-Fiber Composites with Different Aspect Ratios," in Proceedings of the ASME 2015 IDETC 27th Biennial Conference on Mechanical Vibration and Noise, Boston, MA, 2-5 August 2015. 2015.

[149] Shahab, S. and Erturk, A., "Experimentally validated electrohydroelastic Euler-Bernoulli-Morison model for underwater resonant actuation of macro-fiber composite piezoelectric cantilevers ", Journal of Fluid and Structures. Submitted., (2015).

[150] Meirovitch, L., Fundamentals of vibrations: Waveland Press (2010).

[151] Nayfeh, A. H., Perturbation methods: John Wiley & Sons (2008).

[152] Leadenham, S. and Erturk, A., "M-shaped asymmetric nonlinear oscillator for broadband vibration energy harvesting: Harmonic balance analysis and experimental validation," Journal of Sound and Vibration. 333(23): 6209-6223 (2014).

[153] Leadenham, S. and Erturk, A., "Unified Nonlinear Electroelastic Dynamics of a Bimorph Piezoelectric Cantilever for Energy Harvesting, Sensing, and Actuation," Nonlinear Dynamics (in press) (2014).

[154] Anton, S., Erturk, A., and Inman, D., "Multifunctional self-charging structures using piezoceramics and thin-film batteries," Smart Materials and Structures. 19(11): 115021 (2010).

[155] Taylor, G., "Analysis of the swimming of microscopic organisms," Proceedings of the Royal Society of London. Series A. Mathematical and Physical Sciences. 209(1099): 447-461 (1951).

[156] Taylor, G., "The action of waving cylindrical tails in propelling microscopic organisms," Proceedings of the Royal Society of London. Series A. Mathematical and Physical Sciences. 211(1105): 225-239 (1952).

[157] Hill, M. L., "Aquatic animal propulsion of high hydrodynamic efficiency," Journal of fluid Mechanics. 44: 256-301 (1970).

[158] Chen, Z., Shatara, S., and Tan, X., "Modeling of biomimetic robotic fish propelled by an ionic polymer–metal composite caudal fin," Mechatronics, IEEE/ASME Transactions on. 15(3): 448-459 (2010).

[159] Wolf, K. and Gottlieb, O., "Nonlinear dynamics of a noncontacting atomic force microscope cantilever actuated by a piezoelectric layer," Journal of Applied Physics. 91(7): 4701-4709 (2002).

[160] Usher, T. and Sim, A., "Nonlinear dynamics of piezoelectric high displacement actuators in cantilever mode," Journal of Applied Physics. 98(6) (2005).

[161] Stanton, S. C., Erturk, A., Mann, B. P., Dowell, E. H., and Inman, D. J., "Nonlinear nonconservative behavior and modeling of piezoelectric energy harvesters including proof mass effects," Journal of Intelligent Material Systems and Structures. 23(2): 183-199 (2012).

[162] Aureli, M., Basaran, M. E., and Porfiri, M., "Nonlinear finite amplitude vibrations of sharp-edged beams in viscous fluids," Journal of Sound and Vibration. 331(7): 1624-1654 (2012).

[163] Abdelnour, K., Mancia, E., Peterson, S. D., and Porfiri, M., "Hydrodynamics of underwater propulsors based on ionic polymer–metal composites: a numerical study," Smart Materials and Structures. 18(8): 085006 (2009).

[164] Lighthill., M. J., "Hydromechanics of Aquatic Animal Propulsion," Annual Review of Fluid Mechanics. 1: 413-& (1969).

[165] Lighthill., M. J., "Aquatic Animal Propulsion of High Hydromechanical Efficiency," Journal of Fluid Mechanics. 44(Nov11): 265-& (1970).

[166] Lighthill., M. J., "Large-Amplitude Elongated-Body Theory of Fish Locomotion," Proceedings of the Royal Society of London Series B-Biological Sciences. 179(1055): 125-& (1971).

[167] Leo, D. J., Introduction to Smart Material Systems. Engineering Analysis of Smart Material Systems: Wiley (2007).

[168] Sherman, C. H. and Butler, J. L., Transducers and arrays for underwater sound: Springer (2007).

[169] Stanton, S. C., Erturk, A., Mann, B. P., and Inman, D. J., "Nonlinear piezoelectricity in electroelastic energy harvesters: modeling and experimental identification," Journal of Applied Physics. 108(7): 074903 (2010).

[170] Stanton, S. C., Erturk, A., Mann, B. P., and Inman, D. J., "Resonant manifestation of intrinsic nonlinearity within electroelastic micropower generators," Applied Physics Letters. 97(25): 254101 (2010).

[171] Leadenham, S. and Erturk, A. "Global nonlinear electroelastic dynamics of a bimorph piezoelectric cantilever for energy harvesting, sensing, and actuation," in SPIE Smart Structures and Materials+ Nondestructive Evaluation and Health Monitoring. International Society for Optics and Photonics 2014.

[172] Kinsler, L. E., Frey, A. R., Coppens, A. B., and Sanders, J. V., Fundamentals of acoustics. Vol. 1. Wiley-VCH (1999).

[173] Pierce, A. D., Acoustics: an introduction to its physical principles and applications: Acoustical Soc of America (1989).

[174] Renno, J. M., Daqaq, M. F., and Inman, D. J., "On the optimal energy harvesting from a vibration source," Journal of sound and vibration. 320(1): 386-405 (2009).

[175] Zhao, S. and Erturk, A., "Deterministic and band-limited stochastic energy harvesting from uniaxial excitation of a multilayer piezoelectric stack," Sensors and Actuators A: Physical. 214: 58-65 (2014).

[176] Fleming, A., Behrens, S., and Moheimani, S., "Synthetic impedance for implementation of piezoelectric shunt-damping circuits," Electronics Letters. 36(18): 1525-1526 (2000).

[177] Luo, C., Whitehead, M., and Hofmann, H., "Design and testing of a power electronic synthetic inductor," International Journal of Electronics. 96(12): 1249-1264 (2009).

[178] Cao, H., Schmidt, V. H., Zhang, R., Cao, W., and Luo, H., "Elastic, piezoelectric, and dielectric properties of 0.58Pb (Mg 1/3 Nb 2/3) O 3-0.42PbTiO 3 single crystal," Journal of applied physics. 96(1): 549-554 (2004).

[179] Zhang, S., Lee, S.-M., Kim, D.-H., Lee, H.-Y., and Shrout, T. R., "Characterization of mn-modified Pb (Mg 1/3 Nb 2/3) O 3–PbZrO 3–PbTiO 3 single crystals for high power broad bandwidth transducers," Applied Physics Letters. 93(12): 122908-122908-3 (2008).

[180] Russell, D. A., Titlow, J. P., and Bemmen, Y.-J., "Acoustic monopoles, dipoles, and quadrupoles: An experiment revisited," Am. J. Phys. 67(8): 660-664 (1999).

[181] Rupp, C. J., Dunn, M. L., and Maute, K., "Analysis of piezoelectric energy harvesting systems with non-linear circuits using the harmonic balance method," Journal of Intelligent Material Systems and Structures. 21(14): 1383-1396 (2010).

[182] Chen, C. T. and Millero, F. J., "Speed of sound in seawater at high pressures," J. Acoust. Soc. Am. 62(5): 1129-1135 (1977).

[183] Luker, L. and Van Buren, A., "Phase calibration of hydrophones," J. Acoust. Soc. Am. 70(2): 516-519 (1981).

[184] Perreira, N. D. and Dawe, D., "An analytical model for noise generated by axial oscillations of unbaffled cylindrical elements," The Journal of the Acoustical Society of America. 75(1): 80-87 (1984).

[185] Sommerfeld, A. J. W., Partial differential equations in physics: Academic press (1949).

[186] Sherman, C. H., "Special relationships between the farfield and the radiation impedance of cylinders," The Journal of the Acoustical Society of America. 43(6): 1452-1454 (1968).

[187] Rschevkin, S. N. and Blunn, O., The theory of sound: Pergamon press (1963).

[188] Hamilton, M. F. and Blackstock, D. T., Nonlinear acoustics. Vol. 237. Academic press San Diego (1998).

[189] Ottman, G. K., Hofmann, H. F., Bhatt, A. C., and Lesieutre, G. A., "Adaptive piezoelectric energy harvesting circuit for wireless remote power supply," Power Electronics, IEEE Transactions on. 17(5): 669-676 (2002).

[190] Guyomar, D., Badel, A., Lefeuvre, E., and Richard, C., "Toward energy harvesting using active materials and conversion improvement by nonlinear processing," Ultrasonics, Ferroelectrics and Frequency Control, IEEE Transactions on. 52(4): 584-595 (2005).

[191] Shu, Y., Lien, I., and Wu, W., "An improved analysis of the SSHI interface in piezoelectric energy harvesting," Smart Materials and Structures. 16(6): 2253 (2007).

[192] Lallart, M. and Guyomar, D., "An optimized self-powered switching circuit for non-linear energy harvesting with low voltage output," Smart Materials and Structures. 17(3): 035030 (2008).

[193] Kong, N., Ha, D. S., Erturk, A., and Inman, D. J., "Resistive impedance matching circuit for piezoelectric energy harvesting," Journal of Intelligent Material Systems and Structures. 21(13): 1293-1302 (2010).

[194] Szarka, G. D., Stark, B. H., and Burrow, S. G., "Review of power conditioning for kinetic energy harvesting systems," Power Electronics, IEEE Transactions on. 27(2): 803-815 (2012).